
Optical and transport properties of quantum impurity models – an NRG study of generic models and real physical systems

Markus Johannes Hanl



München 2014

Optical and transport properties of quantum impurity models – an NRG study of generic models and real physical systems

Markus Johannes Hanl

Dissertation
an der Fakultät für Physik
der Ludwig–Maximilians–Universität
München

vorgelegt von
Markus Johannes Hanl
aus Ulm

München, den 25. Juni 2014

Erstgutachter: Prof. Dr. Jan von Delft

Zweitgutachter: Prof. Dr. Alexander Högele

Tag der mündlichen Prüfung: 23. Juli 2014

Contents

Deutsche Zusammenfassung	vii
Abstract	ix
I. General Introduction	1
1. Introduction	3
2. Quantum dots and iron impurities in bulk metals	7
2.1. Quantum dots	7
2.2. Anderson model	8
2.3. Kondo model	10
2.4. Kondo effect	10
2.5. Transport for impurity systems	12
2.6. Impurity models with several channels	15
3. Absorption and emission spectra of self-assembled quantum dots	17
3.1. Theoretical description of absorption for weak optical coupling	17
3.2. Anderson orthogonality and Fermi-edge singularity	19
3.3. Absorption in the presence of Kondo correlations	23
3.4. Emission for strong optical coupling	27
3.4.1. Mollow triplet	27
3.4.2. Two-level system tunnel-coupled to a Fermi reservoir	28
4. Numerical renormalization group	31
4.1. NRG algorithm	31
4.2. Spectral functions	36
4.2.1. Definition	36
4.2.2. Impurity spectral function	37
4.2.3. Smoothing of discrete data	37
4.2.4. Matrix product states	38
4.2.5. FDM-NRG	38
4.3. Fermionic signs	42
4.3.1. Fermionic signs for the NRG diagonalization	42
4.3.2. Fermionic signs for spectral functions	44

4.4. Abelian symmetries and the NRG	45
4.5. Non-abelian symmetries and the NRG	46
4.5.1. MPS and operators	46
4.5.2. Operations on MPS	48
II. Results	49
5. Optics for impurity models	51
5.1. Quantum quench of Kondo correlations in optical absorption	51
5.2. Rabi-Kondo Correlated State in a Laser-Driven Quantum Dot	84
5.3. Fermi edge singularity at the absorption spectrum of a quantum dot	102
6. Transport for impurity models	117
6.1. Kondo effect in an InAs nanowire quantum dot	117
6.2. Transport at gold and silver with iron impurities	129
6.3. Local susceptibility and Kondo scaling with finite bandwidth	140
6.4. Equilibrium Fermi Liquid coefficients for fully screened Kondo models	157
7. Conclusions	169
III. Appendix	171
A. NRG Hamiltonian of impurity and hybridization in matrix form	173
B. Publication for absorption in the presence of Kondo correlations	175
IV. Miscellaneous	185
List of Figures	187
Bibliography	189
List of Publications	197
Acknowledgements	199

Deutsche Zusammenfassung

Die vorliegende Arbeit trägt zum Verständnis von Störstellenmodellen bei. Sie ist in zwei Hauptteile aufgeteilt, mit einer allgemeinen Einleitung in Teil I und den damit verbundenen Untersuchungen in Teil II, wobei der zweite Teil in zwei Hauptprojekte aufgeteilt ist.

Das erste Projekt untersucht den Einfluss von zwei Vielteilcheneffekten, dem Kondo-Effekt und der Singularität der Fermi-Kante, auf die Absorptions- und Emissionsspektren von selbstgebildeten Quantenpunkten (QPs). Obgleich der Kondo-Effekt bis jetzt immer mit Transportexperimenten untersucht wurde, zeigen wir, dass er das erste Mal mit optischen Methoden beobachtet worden ist, indem wir die experimentellen Daten für die Linienform der Absorptionsspektren von QPs mit Berechnungen mittels der numerischen Renormierungsgruppe vergleichen. Wir fahren fort mit der Untersuchung eines QP mit starker optischer Kopplung der Energieniveaus. Das sich ergebende Zusammenspiel von Rabi-Oszillationen und Kondo-Effekt führt zu einem neuen Vielteilchenzustand, einem sekundären, äußeren Kondo-Effekt, mit Kondo-artigen Korrelationen zwischen dem Spin-Kondo- und dem Trionzustand. Die letzte Studie, die Optik an einem QP betrifft, behandelt die Singularität der Fermi-Kante. Wir zeigen, dass dieses Phänomen bei QPs numerisch auf einem quantitativen Level beschrieben werden kann.

Das zweite Projekt betrifft die Transporteigenschaften von Störstellenmodellen. Zunächst zeigen wir eine umfassende Studie des Kondo-Effekts für einen aus einem InAs-Nanodraht bestehenden QP, ein System bei dem der Kondo-Effekt erst vor ein paar Jahren das erste Mal beobachtet wurde. Die zweite Studie, die den Transport betrifft, betrachtet den Kondo-Effekt in Massenmetallen mit magnetischen Störstellen. Obwohl der Kondo-Effekt heutzutage oft an QPs untersucht wird, wurde er bei Eisenstörstellen in Edelmetallen wie Gold und Silber entdeckt. Es war jedoch für lange Zeit nicht bekannt, welche genaue mikroskopische Realisierung des Kondo-Modells diese Systeme beschreibt. Wir identifizieren das Modell eindeutig, indem wir numerische Berechnungen für den spezifischen Magnetowiderstand und die Dephasierungsrate für unterschiedliche Modelle mit experimentellen Ergebnissen vergleichen. Die dritte Studie, die sich mit Transport befasst, behandelt das Phänomen, dass für einen festgelegten Typ von Kondo-Modell Größen wie der spezifische Magnetowiderstand, bzw. die spezifische Leitfähigkeit, für unterschiedliche Parameter auf eine universelle Kurve skaliert werden können, wenn die Energien mit der Kondo-Temperatur T_K reskaliert werden, was die einzige relevante Energieskala des Problems ist. Bei endlicher Bandbreite führen unterschiedliche Definitionen von T_K (die im Limes unendlicher Bandbreite zusammenfallen) allerdings zu unterschiedlichen T_K -Werten. Wir zeigen, dass bei einer weit verbreiteten Definition von T_K die endliche Bandbreite, die bei numerischen Rechnungen immer vorhanden ist, die Universalität kompromittiert, und wir zeigen eine alternative Definition von T_K auf, die richtiges Skalieren sicherstellt.

In der letzten Studie dieser Arbeit berechnen wir die Fermiflüssigkeitskoeffizienten für voll abgeschirmte Mehrkanal-Kondo-Modelle. Für Temperaturen unterhalb von T_K zeigen diese Modelle Fermiflüssigkeitsverhalten und die Zustandsdichte der Störstelle und bestimmte Größen, die davon abhängen, wie der spezifische Widerstand, zeigen quadratisches Verhalten in Bezug auf Parameter wie Temperatur oder Magnetfeld, welches durch die Fermiflüssigkeitskoeffizienten beschrieben wird. Wir berechnen diese Koeffizienten sowohl analytisch als auch numerisch.

Abstract

This thesis contributes to the understanding of impurity models. It is divided into two main parts, with a general introduction given in Part I and the research related to it presented in Part II, with the second part being subdivided into two main projects.

In the first project, the influence of two many-body effects, the Kondo effect and the Fermi edge singularity, on the absorption and emission spectra of self-assembled quantum dots (QDs) is examined. Whereas the Kondo effect so far was always examined with transport experiments, we show that it has been observed with optical methods for the first time, by comparing experimental data for the absorption line shapes of QDs to calculations with the numerical renormalization group. We continue by examining a QD with strong optical coupling of the energy levels. The resulting interplay of Rabi-oscillations and Kondo effect leads to a new many-body state, a secondary, outer Kondo effect, with Kondo-like correlations between the spin-Kondo and the trion state. The last work regarding optics at QDs addresses the Fermi edge singularity. We show that for QDs this phenomenon can be described numerically on a quantitative level.

The second project concerns transport properties of impurity models. First, we present a comprehensive study of the Kondo effect for an InAs-nanowire QD, a system for which the Kondo effect was observed only a few years ago. The second study regarding transport concerns the Kondo effect in bulk metals with magnetic impurities. Although nowadays the Kondo effect is often studied with QDs, it was discovered for iron impurities in noble metals like gold and silver. However, it was unknown for a long time which exact realization of Kondo model describes these systems. We identify the model by comparing numerical calculations for the magnetoresistivity and the dephasing rate for different models to experimental results. The third work about transport concerns the phenomenon that for a fixed type of Kondo model quantities like the magnetoresistivity or the conductivity, respectively, can be scaled onto a universal curve for different parameters, when energies are rescaled with the the Kondo temperature T_K , since it is the only relevant low energy scale of the problem. For finite bandwidth, however, different definitions of T_K (which coincide in the limit of infinite bandwidth) lead to different T_K -values. We show that with a very common definition of T_K , finite bandwidth, which is always present at numerical calculations, can deteriorate the universality of rescaled curves, and we offer an alternative definition of T_K which ensures proper scaling. In the last study presented in this thesis we calculate the Fermi-liquid coefficients for fully screened multi-channel Kondo models. For temperatures below T_K , these models show Fermi-liquid behavior, and the impurity density of states and certain quantities which depend on it, like resistivity, show quadratic dependencies on parameters like temperature or magnetic field, described by the Fermi-liquid coefficients. We calculate these coefficients both analytically and numerically.

Part I.

General Introduction

1. Introduction

The aim of physics is to understand and predict the observable processes in nature on a quantitative level and to constantly extend the current understanding with experimental and theoretical methods. While the experiment tries to improve measurement techniques and control of physical processes, theory tries to find adequate models and methods to treat them. At the process of research it is thereby essential that theory and experiment are continuously compared to each other, the mutual feedback consolidates the prevailing knowledge, so that further research can build on it. Regarding experiments, one can distinguish between three main kinds in the field of condensed matter physics: experiments probing thermodynamic coefficients, transport experiments, and spectroscopy [1]. Whereas thermodynamic experiments give static information on systems, which is quite universal for very different kind of systems, transport and spectroscopy experiments, which are considered in this thesis, can be used to obtain more system-specific and dynamical information, which allows to identify individual energy levels or eigenstates.

Although in condensed matter physics the physical laws that govern single particles are known, predicting the collective behavior that determines an energy level or another measurable quantity is far from trivial [2]. This is not primarily because of the large particle numbers one encounters here, but due to the fact that (i) the particles do not behave independently of each other because of their mutual interactions, and (ii) quantum mechanical superpositions of states have to be taken into account. The system therefore has to be treated as a whole, where all possible *combinations* of single particle states have to be considered. Since the Hilbert space grows exponentially with the number of particles, an exact theoretical description is impossible since one would have to keep track of every possible state of the system, however, even a system as small as 300 atoms with two states per atom, has more possible global states than there are atoms in the observable universe! Therefore theoretical methods always consider an effective system where the number of degrees of freedom is drastically reduced.

Instead of simply being a necessary approximation that accompanies every theoretical description, the reduction of degrees of freedom is the central paradigm of the renormalization group, which, based on previous ideas of renormalization, was developed by K. G. Wilson in the 1970's [3, 4, 5, 6]. The main idea of the renormalization group is to set up a sequential transformation where a Hamiltonian with many degrees of freedom is transformed into a Hamiltonian with new effective parameters and less degrees of freedom. Today there exist many methods which are based on renormalization ideas, which have different strengths and drawbacks and are suited for different kinds of problems. The numerical renormalization group (NRG) [4, 7, 8, 9] is one of the earliest renormalization methods and is the method of choice for impurity problems. Its power was first demon-

strated in one of Wilson's seminal publications on this method [4], where it was used to solve a many-body problem which had been unsolved for decades at that time: the Kondo problem [10, 11].

This problem emerged from the observation in the 1930s that the resistivity of gold shows an anomalous rise at low temperatures [12], which was later discovered to be due to magnetic impurities. J. Kondo explained the increase of the resistivity [13] as spin-flip scattering of conduction electrons off the impurities, which sets in below a certain energy scale, the Kondo temperature T_K . However, his perturbative solution diverged for zero temperature, a phenomenon which became known as the Kondo problem. The NRG as a non-perturbative method on the other hand could solve the problem. In this thesis, the NRG method is used to extend the knowledge of impurity models with Kondo correlations and related many-body effects, like the Fermi-edge singularity [14, 15] and Anderson orthogonality [16], by examining optical and transport properties of these models.

When it comes to experiments on the Kondo effect, so far, Kondo correlations were always examined with transport experiments. However, the possibility to perform optical experiments with Kondo correlated systems opens up a whole new field of experiments. We show that for self-assembled quantum dots (QDs) Kondo correlations have been observed with optical methods for the first time, by comparing NRG calculations to experimental data, giving a proof of concept of optical experiments with Kondo correlated systems. But light can not only be used to examine a Kondo state, it can also be used to create new physical processes within a system. For example, since two optically coupled discrete energy levels show Rabi-oscillations, the local energy level of the impurity, which is necessary to realize Kondo correlations, can be strongly optically coupled to a second level, so that an interplay between Rabi and Kondo correlations emerges. Optical experiments with quantum dots also allow the study of many-body effects beyond Kondo correlations, like the Fermi edge singularity or Anderson orthogonality. Being able to perform optical experiments with quantum dots, for which most model parameters are tunable, allows for a controlled setting in which these effects can be studied, in contrast to prior experiments with bulk materials, where the model parameters were given by material constants. We compare numerical to experimental data and show that the Fermi-edge singularity can be observed for quantum dots and can be understood theoretically on a quantitative level.

The second kind of the projects presented in this thesis concerns transport experiments. We present a study of the Kondo effect at an InAs-nanowire QD, an experimental system of increasing interest, where the Kondo effect was first observed a few years ago. Although nowadays many experiments regarding the Kondo effect consider QDs, it was first observed at iron impurities in gold and silver. However, despite the fact that the discovery of the Kondo effect dates back roughly 80 years, it was unclear until very recently, which exact type of Kondo model describes these systems. Here we identify the correct model by comparing calculations of the resistivity [17] depending on temperature and magnetic field and of the dephasing rate [18] for different models to experimental data. We thereby make use of non-abelian symmetries of the models to make the calculations feasible. One characteristic feature of the Kondo effect is that energy dependent quantities like the magnetoresistivity collapse onto a universal curve for different model parameters, when the

energy is rescaled with T_K . At numerical calculations, however, T_K can be influenced by the finite bandwidth, which is always present there, and special care must therefore be taken at the definition of T_K . We investigate how the magnetic impurity susceptibility, which can be used to define T_K , must be calculated correctly to account for finite bandwidth. The correct definition of T_K is of special importance in the last study of this thesis, where we calculate several Fermi liquid coefficients for multi-channel Kondo models with different number of channels. At low temperatures ($T \ll T_K$), fully screened Kondo models can be described by Fermi liquid theory [19], at which the local density of states and related quantities, like the resistivity, show quadratic behavior with respect to some parameters, like temperature or magnetic field.

This thesis is organized as follows: Part I gives an introduction to the topics which are examined in this thesis, as well as an introduction to the applied numerical method, the NRG. Part II shows the results of these examinations and consists mainly of the published papers. Three publications consider the topic of absorption and emission at quantum dots and four publications consider transport experiments at quantum impurity models. Part III contains an appendix and part IV contains the list of figures, the bibliography, the list of publications and some acknowledgements.

Part I consists of four chapters: After this introduction follows Chap. 2 about quantum dots and iron impurities in bulk metals. There we sketch the experimental systems and explain the models used to describe them. We give a short introduction to quantum dots (Sec. 2.1) and the Anderson and Kondo model (Secs. 2.2 and 2.3). Further we describe the Kondo effect (Sec. 2.4) and give a summary of the physics of electron transport through QDs (Sec. 2.5). We also mention multi-channel models, which are relevant for magnetic impurities in bulk metals (Sec. 2.6). Chap. 3 describes the basic physics of optical experiments at self-assembled quantum dots. We explain the physical processes at weak optical coupling (Sec. 3.1), the relevant many-body effects like Anderson orthogonality and the Fermi-edge singularity (Sec. 3.2), absorption in the presence of Kondo correlations (Sec. 3.3), and the basic processes of emission at strong optical coupling (Sec. 3.4). Chap. 4 describes the NRG method, which is used to iteratively diagonalize the system. It starts with the description of the NRG algorithm (Sec. 4.1) and continues with a description how dynamic quantities like spectral functions can be calculated from the eigenstates (Sec. 4.2). Additional sections explain the correct treatment of fermionic signs (Sec. 4.3) and describe how symmetries, both abelian and non-abelian, can be used to speed up the calculations (Secs. 4.4 and 4.5).

Part II contains the results of this work. In Sec. 5.1, NRG calculations of the absorption spectrum of a QD with Kondo correlations are compared to experimental results. Sec. 5.2 describes the emission spectrum from resonance fluorescence of a QD with strong optical coupling, which is examined with both numerical and analytical methods. In Sec. 5.3, the Fermi-edge singularity of a QD is examined by comparing experimental data for the absorption spectrum to NRG calculations. In Sec. 6.1 we present a study of the Kondo effect at an InAs-nanowire QD, before we identify the correct model to describe iron impurities in noble metals in Sec. 6.2. Sec. 6.3 examines how to calculate the magnetic susceptibility and the Kondo temperature, which is derived from it, correctly in the presence of finite

bandwidth, so that observable quantities show a scaling collapse, when energies are rescaled with the Kondo temperature. The results of this work are a necessary requirement for Sec. 6.4, where the Fermi liquid coefficients for a fully screened N -channel Kondo model are calculated, both numerically and analytically. Finally, Chap. 7 completes this thesis by giving a summary of the presented work and an outlook to future research.

2. Quantum dots and iron impurities in bulk metals

Impurity models describe systems where few microscopic degrees of freedom are coupled to a non-interacting macroscopic continuum. Being originally intended to describe magnetic impurities in bulk metals, they received increased attention with the progress of nanotechnology since the 1990s, since they also describe the physics of quantum dots. In this section we introduce the most important impurity models and address the Kondo effect, a many-body effect that occurs in these models.

2.1. Quantum dots

Quantum dots are physical systems, made from a semiconductor material or a metal, which are confined in all three dimensions to such small length scales that quantum effects of the electrons populating the quantum dot become relevant. This means that the extent of the QD is comparable or smaller than the de Broglie wavelength of the electron. The de Broglie wavelength, on the other hand, is proportional to the inverse of the velocity v_F of the electrons close to the Fermi energy, and since v_F in semiconductors is much smaller than it is for metals, semiconductor quantum dots can be made larger than metal QDs, while still allowing the study of quantum effects, which makes them experimentally easier accessible than metal QDs.

One can distinguish according to the method of fabrication between electrostatically defined QDs, QDs that resemble etched heterostructures and self-assembled QDs [20]. Electrostatically QDs are created by applying a voltage to electrodes that are on top of a two-dimensional electron gas (2DEG), thus depleting the 2DEG region beneath the electrodes of electrons and creating a quantum dot in the 2DEG-area surrounded by the electrodes. The gate electrodes are defined by a lithographical pattern and are created by an etching process. To produce heterostructure QDs, the QDs themselves are created by an etching procedure. Like other lithographically produced devices, the final QDs can consist of several layers of different material. Self-assembled QDs are created by growing nanometer-sized crystals from a precursor in a solvent, a method known as colloidal synthesis or by growing a material on a substrate whose lattice constant is different from the growth material. With the latter method, due to the strain induced by the different lattice constants, the material on the substrate will not grow homogeneously, but there will be large areas with less material and small areas with more material, the final result of the growing process is often compared to islands in an ocean. This kind of self-assembled

QDs were used for the experiments described in Chaps. 5.1 and 5.3.

A less coarse classification scheme is to distinguish QDs according to their systematic structure of energy levels. Due to this structure, which depends mainly on the physical dimensions of the QD, QDs are often considered as artificial atoms, i. e. atoms with tailor-made properties. There exist even a periodic table and magic numbers [21], comparable to atom shells and atomic nuclei.

Depending on their specific properties, the different type of QDs have different applications. Self-assembled QDs are much smaller (~ 10 nm) than lithographically produced QDs. Because of that, they contain only very few electrons with a large energy level spacing. The difference in energy is on the order of magnitude of optical wavelengths, which makes these QDs ideally suited for optical experiments [22, 23, 24]. Lithographic QDs, on the other hand, have a larger spatial extent (~ 100 nm), however they have other advantages: For electrostatically defined QDs many parameters are experimentally accessible, for example the tunnel-barrier between the dot and the surrounding reservoir can be tuned by electrodes. This property, together with the fact that single lateral QDs are experimentally accessible in transport experiments, makes it possible to study certain phenomena, e. g. the Kondo effect (see Sec. 2.4), in much more detail than this was possible before the development of QDs. For heterostructure QDs on the other hand, less parameters can be tuned experimentally. However, these QDs can be produced on a larger scale, which allows for experiments involving many QDs simultaneously.

Besides their application in research, practical applications for QDs become visible in the future. By including self-assembled QDs into displays, computer screens are able to cover a greater range of the electromagnetic spectrum, while at the same time consuming less energy. They even seem to have the potential to improve lasers and solar-cells in the more distant future. For lithographic QDs, applications in electronics are very likely, which is a logical consequence of the continuous miniaturization process of electronic devices and which can be directly seen in the term “single-electron transistor”, which was formerly used for QD.

A system which has great similarities with QDs coupled to a Fermionic reservoir are magnetic impurities in bulk metals. The remainder of this chapter, where we present the models used to describe QDs and give an explanation of the Kondo effect, is therefore valid for both systems, since they show the similar physics. When this is not the case, it will explicitly be pointed out.

2.2. Anderson model

One of the most basic impurity models is the Single Impurity Anderson model (SIAM), which was proposed by Anderson in 1961 [25]. Although Anderson used it originally to describe magnetic impurities in metals, nowadays it is also used to describe electrons in a QD which is coupled to a Fermi reservoir. The SIAM Hamiltonian can be divided into three parts, H_{imp} , H_{res} and H_{hyb} , which describe dot, reservoir electrons of the conduction

band and the hybridization via tunnel-coupling between them:

$$H_{\text{SIAM}} = H_{\text{imp}} + H_{\text{res}} + H_{\text{hyb}}, \quad (2.1)$$

with

$$H_{\text{imp}} = \sum_{\sigma=\uparrow,\downarrow} \varepsilon_e n_{e\sigma} + U n_{e\uparrow} n_{e\downarrow}, \quad (2.2a)$$

$$H_{\text{res}} = \sum_{k\sigma} \varepsilon_{k\sigma} c_{k\sigma}^\dagger c_{k\sigma}, \quad (2.2b)$$

$$H_{\text{hyb}} = V_k \sum_{k\sigma} (e_\sigma^\dagger c_{k\sigma} + \text{h.c.}), \quad (2.2c)$$

where ε_e is the energy of an electron localized at the dot, U is the Coulomb repulsion between the dot electrons, e_σ (e_σ^\dagger) and $c_{k\sigma}$ ($c_{k\sigma}^\dagger$) are the annihilation (creation) operators of an electron with spin σ on the dot or in the reservoir with momentum k , respectively, $n_{e\sigma}$ is the number operator for a localized dot-electron with spin σ , and V_k is the k -dependent coupling strength between dot and reservoir. For simplicity, we assume that the coupling is the same for each electronic spin σ . We use a one-dimensional momentum representation which is sufficient for all impurity systems that we analyze, QDs and magnetic impurities in bulk metals, since one deals either with one dimensional reservoirs directly (e. g. the leads of a QD), or with higher dimensional reservoirs, where s-wave scattering is the predominant scattering mechanism, which again can be described with an effective one-dimensional momentum representation.

Quite generally, the influence of the reservoir on the dot can be fully characterized by the spectral function of the bath, the so called ‘‘hybridization function’’ [9],

$$\Gamma(\varepsilon) = \pi \sum_k V_k^2 \delta(\varepsilon - \varepsilon_k), \quad (2.3)$$

which describes hybridization with respect to energy ε , and which contains information of both the tunnel coupling V_k and the reservoir density of states $\rho(\varepsilon) = \sum_k \delta(\varepsilon - \varepsilon_k)$. The hybridization $\Gamma(\varepsilon)$ fully determines the dynamics of the impurity. This reflects the fact, that the tunneling rate between the dot and a certain energy interval of the FR depends both on the tunneling strength and on the density of states. For practical purposes, it is therefore always possible to make at least either V_k or $\rho(\varepsilon)$ k -independent, by including the k -dependence completely into the respective other quantity.

Although there are impurity problems for which a non-constant hybridization function is crucial, e. g. for applications of dynamical mean field theory (DMFT) [9, 26], it is often sufficient to consider a constant hybridization function, especially if one is interested only in the low-energy behavior, as it is the case for the problems considered in this thesis. For the examinations in part II we will therefore always assume a k -independent coupling strength and a constant density of states with bandwidth $2D$, $\rho(\varepsilon) = \Theta(D - |\varepsilon|) \cdot 1/(2D)$. According to Eq. (2.3) the prefactor of the tunneling term is then given by $V = \sqrt{\Gamma/\pi\rho}$, where Γ corresponds to the width of the dot energy level due to hybridization with the reservoir.

2.3. Kondo model

The Kondo model was proposed by J. Kondo in 1964 [13] in order to describe the resistivity increase of noble metals for low temperatures (Sec. 2.4). The model is given by

$$H_{\text{Kondo}} = 2J\vec{S} \cdot \vec{s} + \sum_{k\sigma} \varepsilon_{k\sigma} c_{k\sigma}^\dagger c_{k\sigma}, \quad (2.4)$$

where J is the coupling constant between the spin \vec{S} of the dot-electron and the spin \vec{s} of the conduction band at the position of the dot, which is given by

$$\vec{s} = \sum_{kk'\sigma\sigma'} \frac{1}{2} c_{k\sigma}^\dagger \vec{\tau}_{\sigma\sigma'} c_{k'\sigma'}, \quad (2.5)$$

where $\vec{\tau}$ are the Pauli matrices. The prefactor of 2 in the coupling term of Eq. (2.4), is a widely used convention, however, there exist also publications, where $J\vec{S} \cdot \vec{s}$ is used to describe the coupling. Although the spin-spin coupling of the Kondo model might look more complicated to describe than the plain Coulomb repulsion of the Anderson model, the opposite is the case. In fact, the physics of the Kondo model is a subset of the richer physics of the Anderson model, which becomes visible by the Schrieffer-Wolff transformation [27]. This transformation maps the low energy subspace of the Anderson model, for which the dot is always occupied by a single electron, to the Kondo model.

2.4. Kondo effect

The Kondo effect was discovered in 1934, when de Haas et al. discovered an anomalous behavior of the resistivity for gold at low temperatures [12], namely that below a certain temperature, which became later known as the Kondo temperature T_K , the resistivity starts to increase again and then saturates at a finite value. Later it was discovered that this increase in the resistance arises from impurities with a magnetic moment (e. g. iron atoms) in the metal. At the time of observation, however, the origin of this effect was completely unknown and it was about 30 years later J. Kondo who explained this behavior using perturbation theory, as the result of electrons spin-flip-scattering off the impurities [13]. However, it turned out that his solution diverged for zero temperature, a feature which became known as the Kondo problem.

After Kondo's perturbative calculations, it was discovered that renormalization group approaches yielded results that pointed into the right direction [11]. It was then already expected, that a theoretical approach which can solve the Kondo problem, in some way must include renormalization ideas. In 1975 then, K. G. Wilson published a seminal paper describing the solution of the Kondo problem with the numerical renormalization group [4] (c. f. Chap. 4). After this breakthrough, the Kondo problem was essentially solved, but together with impurity models, the Kondo effect again attracted increasing interest with the progress of nanotechnology [28, 29, 30].

Nowadays, there are several methods to derive the low energy scale T_K . For most of these methods, the results differ by a prefactor of order 1, since T_K defines a crossover scale and not a sharp transition. One basic yet insightful method is the poor man scaling approach [31, 32] which shows how the coupling is renormalized when going to ever lower energy scales. T_K is then defined as the energy scale for which the renormalized coupling diverges. Other methods would be perturbation theory or Bethe ansatz [33].

A common analytical expression of T_K is (for all chapters of part I we set $k_B, \mu_B, \hbar = 1$ unless indicated otherwise) for the Kondo model [11]:

$$T_K = D|2\rho J|^{1/2}e^{-1/(2\rho J)}, \quad (2.6)$$

and for the Anderson model,

$$T_K = \sqrt{\frac{\Gamma U}{2}} e^{\pi \varepsilon_d (\varepsilon_d + U) / 2\Gamma}. \quad (2.7)$$

In numerical calculations, T_K is often defined via the impurity contribution to the magnetic susceptibility χ [34],

$$T_K = \frac{1}{4\chi}. \quad (2.8)$$

This definition is particularly useful, when it comes to Fermi liquid theory, since it directly relates T_K to analytically calculable quantities.

Characteristic features of the Kondo state

For $T < T_K$ when a system shows Kondo correlations, there are several interesting features [11]:

- **Enhanced local density of states:**
Due to the large phase space of the virtual excited states, that arise as intermediate states at spin-flip scattering, the system shows an enhanced impurity density of states. Most quantities which are measured at transport experiments in some way reflect the existence of this enhanced spectral density, or its behavior when parameters like temperature, magnetic field or source drain voltage are changed.
- **Spin screening and Kondo cloud:**
When there exist Kondo correlations in the system, the impurity spin is screened by the Kondo screening cloud [35]. This means that the electrons surrounding the impurity within a distance of $\sim v_F/T_K$ have slight preference of the opposite spin, with a total cloud-spin of 1/2, so that the system which consists of impurity and cloud, forms a Kondo singlet with net spin zero.
- **Scaling collapse:**
When the system is in a universal Kondo regime, T_K is the smallest energy scale in the system by far and therefore it is the only relevant energy scale of the problem.

Energy dependent quantities for different model parameters thus collapse onto a single universal curve, when the energy is rescaled with T_K . Examples are the impurity density of states with respect to energy or the resistivity with respect to temperature or magnetic field.

- Fermi liquid behavior and phase shift:
Nozières [36, 37] showed that when being in a Kondo state, the whole system can be considered as a Fermi liquid where the electrons at the Fermi surface have a phase shift of $\pi/2$. Because of the single-particle nature of the Fermi liquid description, this connection allows for an analytic treatment of the low-energy regime.

For more information on the Kondo effect, there is the popular review by Kouwenhoven and Glazman [10], a detailed discussion in the book of Hewson [11] and Pustilnik and Glazman describe the Kondo effect in QDs [38, 39]. For the numerical treatment of the Kondo effect see Wilson for calculations on the Kondo model [4] and Krishna-Murthy and Wilson for calculations on the Anderson model [7, 8].

2.5. Transport for impurity systems

Transport through quantum dots

In the field of low temperature physics, traditionally, quantum dots are subject to transport experiments. Due to the quantum effects at low temperatures, the behavior of a QD is qualitatively different from that at higher energies. For a QD whose single-particle level spacing δ is much smaller than the Coulomb repulsion, $\delta \ll U$, the effective level spacing is given by U and the quantized structure of the energy levels therefore becomes visible, when the temperature is lowered so that $T \ll U$, when Coulomb blockade effects [40] set in. Then, only the two energy levels that are closest to the Fermi energy are relevant, so that the system can be described by a SIAM. Here, it can be seen that transport through the dot is not possible because an electron would be required to have a charging energy $E = U + \varepsilon_e \gg T$ to occupy the dot. When plotting the conductance with respect to source-drain voltage V_{sd} and gate voltage $V_g \propto \varepsilon_e$ this leads to diamond-shaped areas of zero conductance, the so called Coulomb diamonds. For temperatures and source-drain voltages below the Kondo scale, $T, V_{sd} \ll T_K$, one can observe increased conductance, since transport is now possible via Kondo states (Fig. 2.1).

In general, the conductance G in the linear response regime can be calculated with the Kubo formula [41] (in the following three equations, we include h or \hbar , respectively, to make the quantization of the conductance in units of e^2/h explicit):

$$G(T) = \lim_{\omega \rightarrow 0} \frac{1}{\hbar\omega} \int_0^\infty dt e^{i\omega t} \langle [I(t), I] \rangle, \quad (2.9)$$

with I being the current through the dot. A special case of the Kubo formula is the

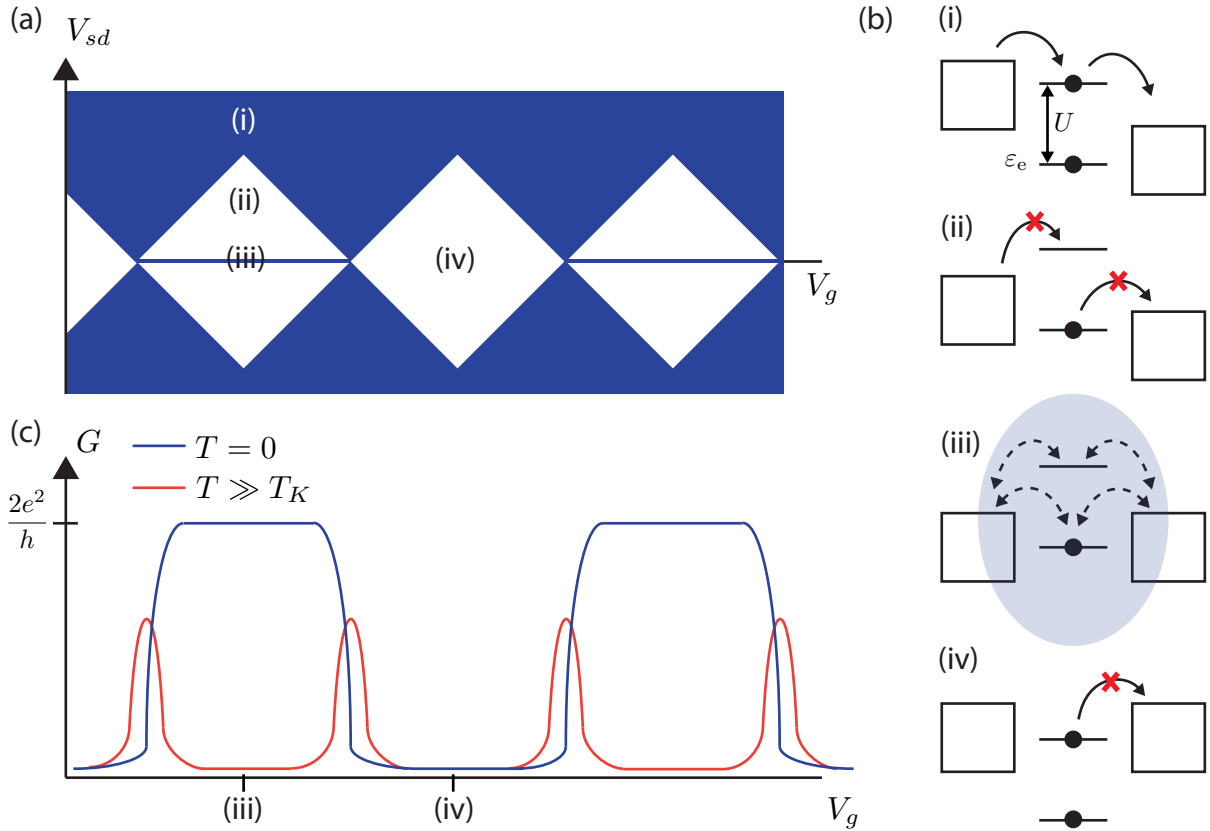


Figure 2.1.: (a) Schematic picture of the differential conductance depending on V_g and V_{sd} for $T \ll T_K$ through a quantum dot with single-particle level-spacing $\delta \ll U$. Conductance is finite for the blue areas and vanishes for the white areas. (b) Energetically possible and impossible processes for different configurations of $\epsilon_e \propto V_g$ and V_{sd} . For configurations (ii) and (iv) the dot is in the Coulomb blockade regime and conduction is not possible. At configuration (i) conduction through the dot is possible via sequential tunneling, i. e. the electrons have enough energy to hop on and off the local energy level. At configuration (iii) the electrons are in a Kondo correlated state, transport takes place via higher order tunneling processes. (c) Schematic picture of the behavior of the conductivity on gate voltage for two different temperatures. For temperatures $U \gg T \gg T_K$ conduction is only possible if an energy level of the dot is close to the Fermi energy. For $T \ll T_K$ the conduction increases for situations where the local level is in a position where it is clearly below the Fermi energy for single occupation, but clearly above the Fermi energy for double occupation. In that case electron transport is mediated by Kondo correlated states (iii). If an energy level is doubly occupied, Kondo correlations are absent and transport through the QD is no longer possible (iv).

Meir-Wingreen formula for the case of a QD with a left and a right lead [42, 43],

$$G(T) = \frac{dI}{dV_{sd}} = \frac{e^2}{h} \sum_{\sigma} \int d\omega \left(-\frac{df(\omega, T)}{d\omega} \right) 4\pi^2 \rho \frac{|V_L|^2 |V_R|^2}{|V_L|^2 + |V_R|^2} A_{\sigma}(\omega, T), \quad (2.10)$$

with $\partial f(\omega, T)/\partial\omega$ the derivative of the Fermi function, $A_{\sigma}(\omega, T)$ the impurity density of states, and where V_L and V_R are the hybridization parameters between the impurity and the left or right lead, respectively. It can be shown that a QD with two symmetric leads can be mapped onto a single impurity Anderson model with a single reservoir [44], and the conductance is then given by

$$G(T) = \frac{e^2}{h} \sum_{\sigma} \pi\Gamma \int d\omega \left(-\frac{df(\omega, T)}{d\omega} \right) A_{\sigma}(\omega, T), \quad (2.11)$$

where $\Gamma = \pi\rho(V_L^2 + V_R^2)$.

Transport in bulk metals in the presence of magnetic impurities

When investigating the Kondo effect at magnetic impurities in bulk metals instead of QDs, one looks at the resistivity instead of the conductance. The reason for this is that here the resistivity, like the conductance at QDs, is directly linked to the impurity density of states by an integral over energy,

$$\rho(T) \propto \int d\omega \left(-\frac{\partial f(\omega, T)}{\partial\omega} \right) \sum_{\sigma} A_{\sigma}(\omega, T). \quad (2.12)$$

The explanation for the correspondence between the conductance of QDs and the resistivity of magnetic impurities in bulk metals starts from the Drude conductivity of a disordered metal:

$$\rho_{\text{tot}}(T)^{-1} \propto \int d\omega \tau(\omega, T) \left(-\frac{\partial f(\omega, T)}{\partial\omega} \right), \quad (2.13)$$

with scattering time $\tau(\omega, T)$. The total scattering rate $1/\tau(\omega, T)$ consists of the scattering rates due to static disorder and due to magnetic impurities, $1/\tau(\omega, T) = 1/\tau_{\text{st}} + 1/\tau_{\text{mag}}(\omega, T)$ with $1/\tau_{\text{mag}}(\omega, T) \propto \sum_{\sigma} A_{\sigma}(\omega, T)$. Eq. (2.12) can then be obtained [45], by expanding $\tau(\omega, T)$ in $\tau_{\text{st}}/\tau_{\text{mag}}(\omega, T) \ll 1$, and expanding the resistivity as $\rho_{\text{tot}} = \rho_{\text{st}} + \rho(T)$, where the second contribution due to magnetic impurities is much smaller than the first.

Heuristically, this correspondence can be understood by the different geometries of the two systems: for a QD, with the current flowing in one direction through the leads, an increased density of states leads to increased forward scattering and therefore to increased conductivity. For a bulk metal with magnetic impurities, however, electrons can be scattered in all directions, and an increased density of states therefore leads to an increased resistivity.

2.6. Impurity models with several channels

Real physical systems of magnetic impurities in bulk metals are in general more complex than the Kondo model in Eq. (2.4). A magnetic impurity can have several inner shell orbitals with magnetic moments and the bulk metal can have several conduction bands. For the Kondo model this means that the impurity can contain several electrons and is coupled to several Fermi reservoirs (usually referred to as “channels” in this context).

The Hamiltonian for the general multi-channel Kondo model with n channels and m dot electrons is given by

$$H = \sum_{\alpha=1}^n \left(2J \vec{S}_m \cdot \vec{s}_\alpha + \sum_{k\sigma} \varepsilon_{k\alpha\sigma} c_{k\alpha\sigma}^\dagger c_{k\alpha\sigma} \right), \quad (2.14)$$

where $c_{k\alpha\sigma}$, ($c_{k\alpha\sigma}^\dagger$) are the annihilation (creation) operators of an electron in channel α with momentum k and spin σ , \vec{s}_α (see Eq. (2.5)) is the spin of the electrons in channel α at the position of the impurity, and \vec{S}_m are the spin matrices for impurity spin $S = m/2$.

Multi-channel Kondo models of the form of Eq. (2.14) can be classified in fully-screened, overscreened and underscreened Kondo models, depending on whether the number of channels is equal, larger or smaller than the number of impurity electrons [46].

Fully screened Kondo models ($n = m$)

The fully screened Kondo model for n channels shows qualitatively the same physics as the single channel case (i. e. $n = 1$). This is supported by the fixed point spectra (see Sec. 4.1 for an explanation of fixed point spectra) of fully screened multi-channel Kondo models, which are qualitatively equal to those of the single channel case. In particular, this means, that their low energy regimes can be described by Fermi liquid theory. However for models with several channels, although there exist exact solutions [47, 48, 49], the theoretical treatment, both analytically and numerically, is more involved than for the one-channel model.

Overscreened Kondo models ($n > m$)

In contrast to the fully screened case, an overscreened Kondo model shows a non-Fermi liquid low-temperature behavior [50]. The non-Fermi liquid properties can be observed through different quantities, such as the impurity spectral function or the impurity contribution to the entropy [51]. The best studied multi-channel Kondo model is the overscreened two-channel Kondo model, which is therefore sometimes simply referred to as “the two-channel Kondo model”. For an analysis of the overscreened two-channel Kondo model, see [52], detailed numerical calculations, including dynamical quantities, for overscreened models with several channels can be found in [51].

Underscreened Kondo models ($n < m$)

The underscreened Kondo model shows singular Fermi liquid behavior for $T \rightarrow 0$. This means, that when the energy of the reservoir electrons approaches the Fermi energy, the S-matrix, that describes scattering of the reservoir electrons off the impurity, approaches the unit circle in the complex plane non-analytically [53]. Due to their unusual scattering processes, singular Fermi liquids show singular thermodynamic behavior that is usually not associated with Fermi liquids, like a divergent specific heat [53].

Different realizations of multi-channel impurity models

There exists a variety of different physical realizations of impurity models whose effective low-temperature behavior results in one of the multi-channel Kondo models described above. For example, the impurity electrons can be tunnel-coupled to the Fermi reservoirs, they can be coupled to each other via Hund's coupling, they can occupy energy levels with different energies, there can be a Coulomb repulsion on the impurity, or the model can have Kondo correlations not with respect to spin, but with respect to impurity orbitals or charge.

In Chap. 6.2, we will consider the following Kondo-Anderson hybrid Hamiltonian:

$$H = -J_H \sum_{\alpha, \beta=1}^n \vec{S}_\alpha \cdot \vec{S}_\beta + \sum_{\alpha=1}^n \sum_{k\sigma} \left(V^2 (e_{\alpha\sigma}^\dagger c_{k\alpha\sigma} + \text{h.c.}) + \varepsilon_{k\alpha\sigma} c_{k\alpha\sigma}^\dagger c_{k\alpha\sigma} \right). \quad (2.15)$$

There the impurity is tunnel-coupled to the FR, as is the case for the Anderson model, but with an additional Hund's coupling term $-J_H \sum_{\alpha, \beta=1}^n \vec{S}_\alpha \cdot \vec{S}_\beta$ on the impurity. The Hund's coupling favors parallel alignment of the spins of the impurity electrons, so that the impurity exhibits a single spin of $n/2$ [54, 55], as is the case for the fully screened multi-channel Kondo model.

3. Absorption and emission spectra of self-assembled quantum dots

This chapter presents the basic models and physical processes to describe optical experiments at self-assembled quantum dots, which are examined in detail in part II. Since these systems exhibit many-body correlations, examining them with optical methods builds a bridge between the field of quantum optics and many-body physics. This becomes directly visible for the model we use for the calculations, which is a combination of an optically coupled two-level system, a system very common in quantum optics, and a single impurity Anderson model, which is one of the basic models of many-body theory.

For optical experiments, information about the system is obtained from transition amplitudes between different states, which are experimentally determined by measuring the absorption or emission rate with respect to photon energy. We will consider the absorption spectrum in Secs. 5.1 and 5.3, whereas we will consider the emission spectrum in Sec. 5.2. The type of spectrum usually depends on the experimental setup.

When calculating absorption or emission spectra of the system sketched above, one has to distinguish whether the electromagnetic coupling of the two discrete levels by the incident photons is weak (Secs. 3.1, 3.2, 3.3) or strong (Sec. 3.4) with respect to their difference in energy. When we investigate the spectrum for strong optical coupling in detail in part II, we will examine how the line shape changes as optical coupling is increased. The physics of weak optical coupling is therefore a necessary prerequisite for the discussion of strong optical coupling, which leads to the following relations between the chapters concerning optical spectra:

Weak optical coupling:	sections 3.1, 3.2, 3.3	→ relevant for sections 5.1, 5.2, 5.3
Strong optical coupling:	section 3.4	→ relevant for sections 5.2

3.1. Theoretical description of absorption for weak optical coupling

To describe absorption for weak optical coupling we start from the excitonic Anderson model, which consists of the Anderson model and an additional energy level, which is energetically located far below the Fermi level ε_F . The energies of the lower and upper level correspond to the energies of the valence and the conduction band of the dot material, and since they allow for the creation of an exciton at photon absorption, the model is referred

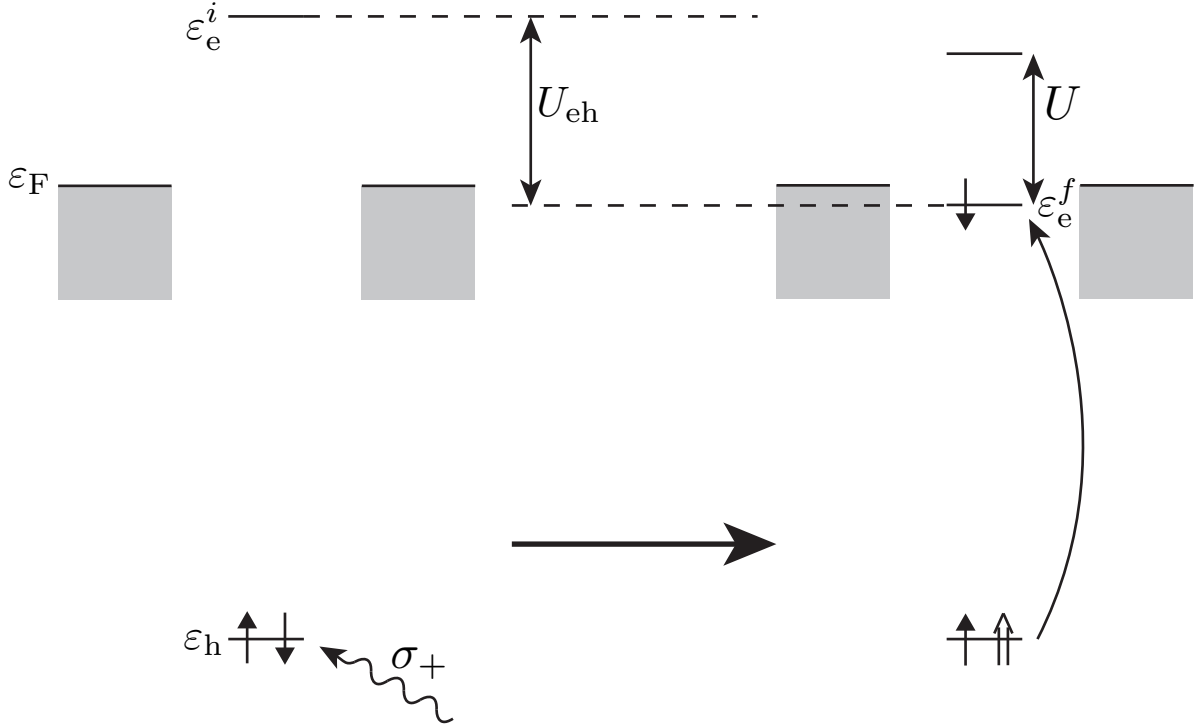


Figure 3.1.: Schematic picture of the excitonic Anderson model (EAM). The usual Anderson model, consisting of the local energy level of the dot and the Fermi reservoir (upper part), is extended by an energy level in the valence band with hole-energy ε_h (lower part). When a photon is absorbed, the local level with energy ε_e^i is pulled down to ε_e^f by U_{eh} due to the attraction of the hole. Because the electrons in the lower level have pseudo-spin 3/2, the spin of the excited electron has the opposite direction as the hole spin.

to as the excitonic Anderson model (EAM). Its Hamiltonian is given by

$$H_{\text{EAM}} = H_{\text{SIAM}} + n_h \varepsilon_h - \sum_{\sigma} n_h n_{e\sigma} U_{eh}, \quad (3.1)$$

with ε_h the energy of the hole and n_h the number operator for the hole. At the presence of a hole, which can be created by absorption of a photon, the local level is pulled down by the excitonic Coulomb attraction U_{eh} (c. f. Fig. 3.1).

In the case of weak optical coupling, the laser can be considered as a perturbation $V(t)$ to the unperturbed Hamiltonian H_{EAM} and the transition rate between two eigenstates $|m\rangle, |m'\rangle$ of H_{EAM} can in first order perturbation theory be calculated through Fermi's Golden Rule:

$$p_{mm'} = 2\pi |\langle m'|V|m\rangle|^2. \quad (3.2)$$

In second quantization, the perturbation Hamiltonian in rotating wave approximation is given by $V = g(a_{\bar{\sigma}}e^{-i\omega_L t}e_{\sigma}^{\dagger}h_{\bar{\sigma}}^{\dagger} + \text{h.c.})$, with coupling strength g , laser frequency ω_L , and photon annihilation operator $a_{\bar{\sigma}}$ with polarization $\bar{\sigma}$, where the first and second term describe absorption and emission, respectively. Because the electrons in the lower level have pseudo-spin 3/2, the spin of the excited electron has opposite direction as the hole spin. By switching to a rotating frame and by looking only at single transition events that are induced by single photons so that the photon creation and annihilation operators can be neglected, the perturbation operator simplifies to: $V = g(e_{\sigma}^{\dagger}h_{\bar{\sigma}}^{\dagger} + \text{h.c.})$. For weak optical coupling, we will restrict our theoretical and experimental examinations to the absorption spectrum and the perturbation term is therefore given by: $V = ge_{\sigma}^{\dagger}h_{\bar{\sigma}}^{\dagger}$.

Since $h_{\bar{\sigma}}^{\dagger}$ relates two decoupled parts of the Hamiltonian, the Hamiltonian can be divided into an initial ($n_h = 0$) and a final part ($n_h = 1$) with states $\{|i\rangle\}$ and $\{|f\rangle\}$, respectively, (see Eq. (3.1)):

$$H_{\text{EAM}} = \begin{pmatrix} H_i & 0 \\ 0 & H_f \end{pmatrix}, \quad H^i = H_{\text{SIAM}}, \quad H^f = H^i - \left(\sum_{\sigma} U_{\text{eh}} n_{e\sigma} - \varepsilon_h \right). \quad (3.3)$$

H^i and H^f correspond to Anderson models with level positions ε_e^i and $\varepsilon_e^f = \varepsilon_e^i - U_{\text{eh}}$, and with an energy offset ε_h for H^f . The states $|m\rangle$ and $|m'\rangle$ of Eq. (3.2) are then replaced by eigenstates of the Hamiltonians H_i and H_f and the transition probability is given by:

$$p_{if} = 2\pi g^2 |\langle f | e_{\sigma}^{\dagger} | i \rangle|^2. \quad (3.4)$$

The absorption spectrum is then given by the frequency resolved sum of all possible transitions, where the initial system is in thermal equilibrium,

$$A(\nu) = 2\pi \sum_{if} \frac{e^{-\beta E_i}}{Z} |\langle f | e_{\sigma}^{\dagger} | i \rangle|^2 \delta(\nu - (E_f - E_i)), \quad (3.5)$$

where we have set $g = 1$ and where $\nu = \omega_L - \omega_{\text{th}}$ is the photon energy with respect to the threshold frequency $\omega_{\text{th}} = E_{G,f} - E_{G,i}$, which is given by the difference of the ground state energies $E_{G,i}$ and $E_{G,f}$ of initial and final Hamiltonian, respectively. It describes the frequency above which (for $T = 0$) absorption sets in.

3.2. Anderson orthogonality and Fermi-edge singularity

In all parts of this thesis that consider absorption or emission spectra of quantum dots, the Fermi edge singularity (FES) is always present and hence needs to be kept in mind. The term Fermi edge singularity is closely related to the terms Anderson orthogonality (AO), Hopfield's rule, Friedel sum rule and Mahan contribution. This section has the purpose to explain these terms and show how they are interconnected. In this section we use the most basic model for which the absorption spectrum exhibits the FES, the Fermi edge Hamiltonian. The results, however, equally apply to the EAM introduced in Sec. 3.1.

The Fermi edge singularity was first observed in the absorption of x-rays at metals and is therefore also called the x-ray edge singularity. This is the physical system that underlies the Fermi edge Hamiltonian [14]:

$$H_{\text{FES}} = \sum_k \varepsilon_k c_k^\dagger c_k + \varepsilon_h h^\dagger h + \sum_{kk'} V c_k^\dagger c_{k'} h^\dagger h. \quad (3.6)$$

It consists of a Fermi sea with energies ε_k , annihilation (creation) operators c_k (c_k^\dagger), and an energy level well below the Fermi energy, described by a hole with energy ε_h and annihilation (creation) operator h (h^\dagger). The hole is created at photon absorption, which turns on a scattering term of strength V of reservoir electrons off the localized hole.

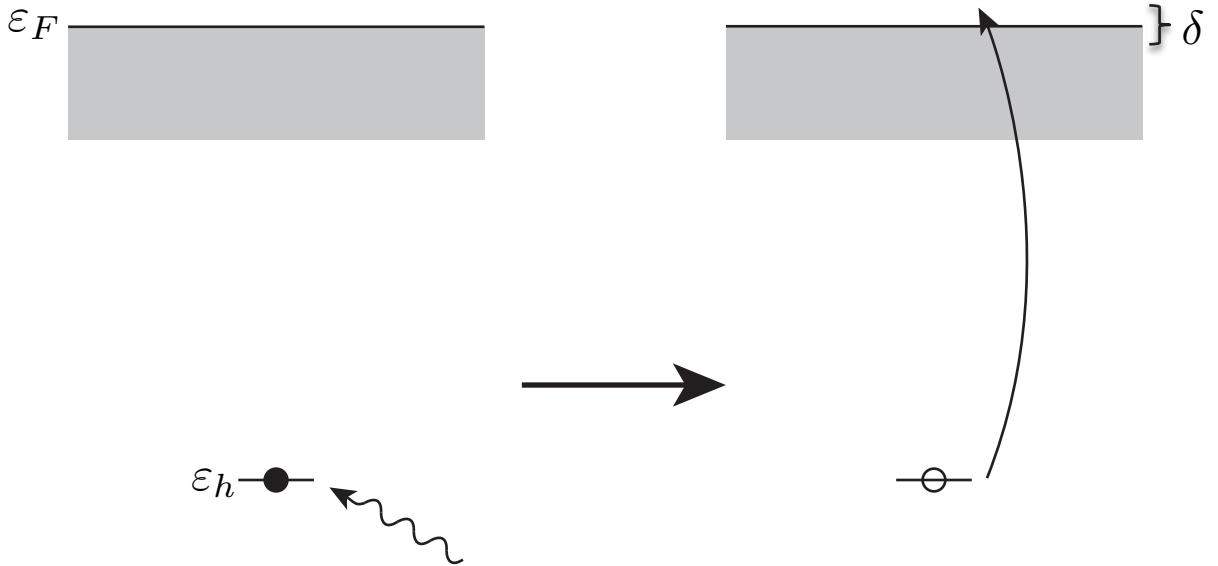


Figure 3.2.: Schematic picture of the absorption process which leads to the Fermi edge singularity. At absorption of a photon, an electron from an inner shell is lifted above the Fermi level. Due to the potential of the resulting core hole, the electrons at the Fermi level acquire a phase shift and the resulting (divergent) absorption spectrum can be explained by Anderson orthogonality.

At an absorption process, an electron is lifted from the lower level above the Fermi energy into the conduction band (Fig. 3.2). Similar to absorption at a QD, the Hamiltonian can be divided into a final and an initial Hamiltonian with and without a hole, respectively, and analogous to Eq. (3.5) the absorption spectrum is given by Fermi's Golden Rule:

$$A(\nu) = 2\pi \sum_f |\langle f | f_0^\dagger | G_i \rangle|^2 \delta(\nu - (E_f - E_i)), \quad (3.7)$$

where we assumed $T = 0$. $|G_i\rangle$ is the ground state of the initial Hamiltonian and $f_0^\dagger = \sum_k c_k^\dagger$ is the operator that creates an electron in the conduction band with bandwidth $2D$ at the position $\vec{r} = 0$ of the hole.

Since at the time the model was developed it was not clear how the corresponding absorption spectrum can be calculated explicitly, the x-ray edge problem caught the attention of theoretical physicists. Nozières and de Dominicis [14] calculated the correlator

$$\mathcal{G}(t) = -i\theta(t)\langle G_i|f_0(t)f_0^\dagger|G_i\rangle = -i\theta(t)\langle G_i|e^{iH^i t}f_0e^{-iH^f t}f_0^\dagger|G_i\rangle \quad (3.8)$$

whose imaginary part is proportional to the Fourier transform of the absorption spectrum,

$$A(\nu) = -2\text{Im}\left(\int_{-\infty}^{\infty} dt e^{i(\nu+i0^+)t}\mathcal{G}(t)\right), \quad (3.9)$$

to show that $A(\nu)$ diverges according to the non-universal power law,

$$A(\nu) \sim \nu^{-2\delta/\pi+(\frac{\delta}{\pi})^2}, \quad (3.10)$$

where δ is the phase shift of the scattered electrons. After their rather abstract derivation, Schotte and Schotte [15] gave a much more stringent explanation for this behavior and related it to the effect of Anderson orthogonality: Anderson [16] stated that the overlap of the ground state $|G_i\rangle$ of a Fermi sea and the ground state $|G_f\rangle$ of a Fermi sea with a local and finite ranged scattering potential decreases exponentially with system size,

$$|\langle G_i|G_f\rangle| \sim N^{-\frac{1}{2}\Delta_{\text{AO}}^2}, \quad (3.11)$$

with N the particle number of the system and Δ_{AO} the so called AO-exponent, which depends only on the phase difference between $|G_i\rangle$ and $|G_f\rangle$.

Hopfield then made the connection, that in the correlator of Eq. (3.8), which is the overlap between $f_0^\dagger|G_i\rangle$ and $f_0^\dagger|G_i\rangle$ time-evolved with the final Hamiltonian, the time-evolved state can be equated with the ground state of the final Hamiltonian, which yields an equation similar to Eq. (3.11). Identifying these states with phase shifts of π and δ , the AO-origin of the divergence of Eq. (3.10) becomes evident, if it is written in the form

$$A(\nu) \sim \nu^{-1+((\pi-\delta)/\pi)^2}, \quad (3.12)$$

where π is the phase shift of $f_0^\dagger|G_i\rangle$ and δ is the phase-shift of the ground state of the final Hamiltonian [56]. Combining Eq. (3.12) with Friedel's sum rule [57, 58, 59], which can be used to relate the phase shift to the change of occupation of the dot, one obtains

$$A(\nu) \sim \nu^{-1+(\Delta n')^2}, \quad (3.13)$$

which relates the exponent of the divergence to the occupation difference $\Delta n'$ between $f_0^\dagger|G_i\rangle$ and $|G_f\rangle$, and is known as ‘‘Hopfield’s rule of thumb’’.

It is a priori not clear, how Anderson *orthogonality*, which originates from vanishing overlap between different states, leads to a *divergence*, which corresponds to large transition

matrix elements in Eq. (3.6). This can be understood by looking at $\mathcal{G}(t)$ which vanishes in the long time limit [15], with its decay governed by the AO-exponent,

$$\mathcal{G}(t) \sim t^{-\Delta_{\text{AO}}^2}, \quad (3.14)$$

and by recalling that according to Eq. (3.9) $A(\nu)$ is given by the Fourier transform of $\mathcal{G}(t)$, which yields [60]

$$A(\nu) \sim \nu^{-1+\Delta_{\text{AO}}^2}. \quad (3.15)$$

In the context of Anderson orthogonality, the first part of the exponent in Eq. (3.10), $-2\delta/\pi$, is often referred to as the Mahan contribution, whereas the second part is called the AO contribution [60]. These definitions, however, are somehow misleading, since the whole exponent can be explained by the phenomenon of AO as shown above. The term ‘‘Mahan contribution’’ originates from the fact that Mahan determined the exponent using perturbation theory, but summed up only lower-order terms, which only gave a premature result, namely the first part of the exponent [61].

An NRG treatment of the Fermi-edge Hamiltonian can be found in [62], for AO with NRG calculations see [63], and a detailed discussion of AO after quantum quenches is given in [60].

Generalized Hopfield’s rule

The AO-physics also governs the absorption spectrum of a quantum dot for low energies, given by Eq. (3.5), for which the whole system consisting of dot and reservoir can be described as a Fermi liquid whose states have acquired a phase shift, analogous to the phase shift which is acquired by the scattered states at the x-ray problem.

Although Hopfield’s rule was originally formulated for the case of spinless fermions of the Fermi edge Hamiltonian, it can readily be generalized to spinful fermions of the Anderson model. First, note since the spin degrees of freedom decouple in a Fermi liquid, the states $|G_i\rangle$ and $|G_f\rangle$ in Eq. (3.11) can be written as product states of a spin up and a spin down part, $|G_a\rangle = |G_{a\uparrow}\rangle|G_{a\downarrow}\rangle$, with $a = i, f$. The exponent in Eq. (3.11) then also consists of a spin up and a spin down part,

$$|\langle G_i|G_f\rangle| \sim N^{-\frac{1}{2}(\Delta_{\text{AO}\uparrow}^2 + \Delta_{\text{AO}\downarrow}^2)}. \quad (3.16)$$

and the exponent in Eq. (3.13) is determined by the sum of the squared occupation differences for both spin directions (see Eq. (3.18) below). Because the excited electron has a certain spin σ , the correlator $\mathcal{G}(t)$ is given by the overlap of $e_{\sigma}^{\dagger}|G_i\rangle$ and $e_{\sigma}^{\dagger}|G_i\rangle$ time-evolved with the final Hamiltonian, which introduces a spin asymmetry in the change of occupation. In addition, for the Anderson model one must take into account, that the impurity can have a finite occupation $\langle G_i|n_{e\sigma'}|G_i\rangle$ before absorption. So for an absorption process, the occupation difference for electrons with spin σ' is

$$\Delta n'_{e\sigma'} = \delta_{\sigma\sigma'} - \Delta n_{e\sigma'} \quad (3.17)$$

with $\Delta n_{e\sigma'} = \langle G_f | n_{e\sigma'} | G_f \rangle - \langle G_i | n_{e\sigma'} | G_i \rangle$ the difference of the local occupation of the final and initial Hamiltonian. This results in the generalized Hopfield's rule for absorption spectra of the Anderson model:

$$A_\sigma(\nu) \sim \nu^{-1 + \sum_{\sigma'} (\Delta n'_{e\sigma'})^2}. \quad (3.18)$$

3.3. Absorption in the presence of Kondo correlations

In this section we answer the following question: *How does the absorption spectrum according to Eq. (3.5) of an initially empty dot look like if the final state shows Kondo correlations (Fig. 3.3)?*

This section therefore summarizes the work of my Diploma thesis, which has been pub-

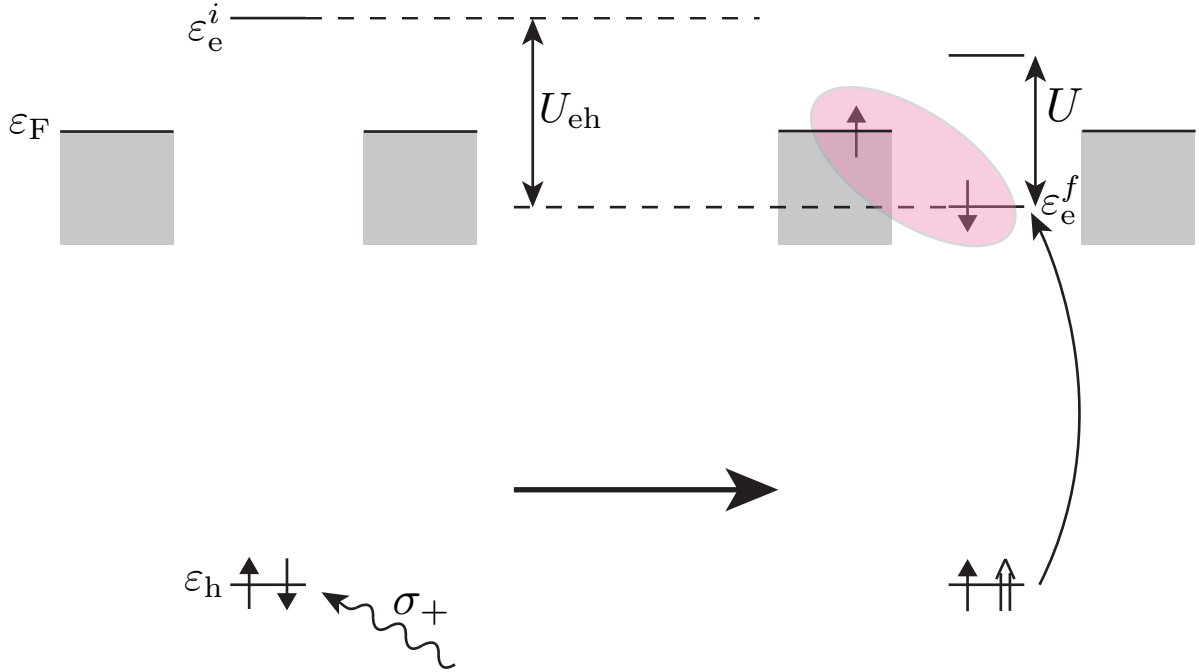


Figure 3.3.: Schematic picture of the excitonic Anderson model with Kondo correlations in the final state. After absorption, the local level is in a position such that it is occupied by a single electron, which can build a Kondo state with the surrounding reservoir electrons.

lished in Ref. [64] (see appendix B for Ref. [64]), where this problem is examined. This section presents the theory that underlies part II, Sec. 5.1, which describes the observation of the Kondo exciton and compares experimental to numerical data.

The main result from Ref. [64] is that the lineshape for an absorption process according to Fig. 3.3 where the dot is initially empty and in a Kondo state afterwards, can be divided

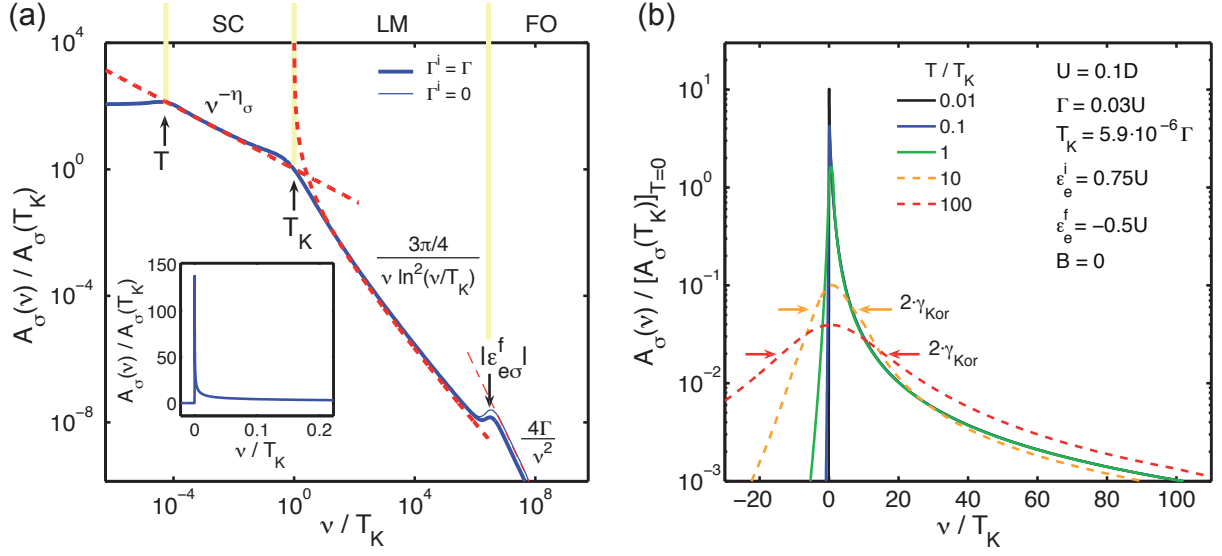


Figure 3.4.: (a) Absorption lineshape on a double logarithmic scale. The blue line corresponds to the NRG-calculated absorption spectrum, the dashed red lines correspond to the analytic expressions from Eq. (3.19a-3.19c), for the three different energy regimes which correspond to the fixed points of the Anderson model (indicated by thick yellow lines). The absorption lineshape is also shown for the case of $\Gamma^i = 0$ (thin blue line), which corresponds to zero occupancy before absorption which is assumed for the analytic expressions. Apart from a slight deviation in the FO-regime, the spectra are equal. The inset shows the absorption spectrum on a linear scale, which demonstrates AO divergence close to the threshold frequency that is only cut off by temperature. Model parameters are shown in panel (b). (b) Absorption lineshapes for different temperatures on a logarithmic y-scale. For $T \gg T_K$ the threshold behavior of the spectrum becomes smeared out, but the width of the peak, determined by the Korrington rate, is significantly narrower than temperature.

into three distinct regimes that correspond to the different fixed points (free orbital (FO), local moment (LM) and strong coupling (SC) fixed point, see Sec. 4.1) of the SIAM. Fig. 3.4a shows the numerically calculated line shape, where the regimes are divided by thick yellow lines. For the three different regimes, the line shape can be approximated by analytic expressions, which for the symmetric case with $\varepsilon_e^f = -U/2$ are given by:

$$|\varepsilon_e^f| \lesssim \nu \lesssim D : \quad A_\sigma^{\text{FO}}(\nu) = \frac{4\Gamma}{\nu^2} \theta(\nu - |\varepsilon_e^f|), \quad (3.19a)$$

$$T_K \lesssim \nu \lesssim |\varepsilon_e^f| : \quad A_\sigma^{\text{LM}}(\nu) = \frac{3\pi}{4\nu} \ln^{-2}(\nu/T_K), \quad (3.19b)$$

$$T \lesssim \nu \lesssim T_K : \quad A_\sigma^{\text{SC}}(\nu) \propto T_K^{-1} (\nu/T_K)^{-\eta_\sigma}, \quad (3.19c)$$

shown as red dashed lines in Fig. 3.4a. For the FO- and the LM-regime, the analytic

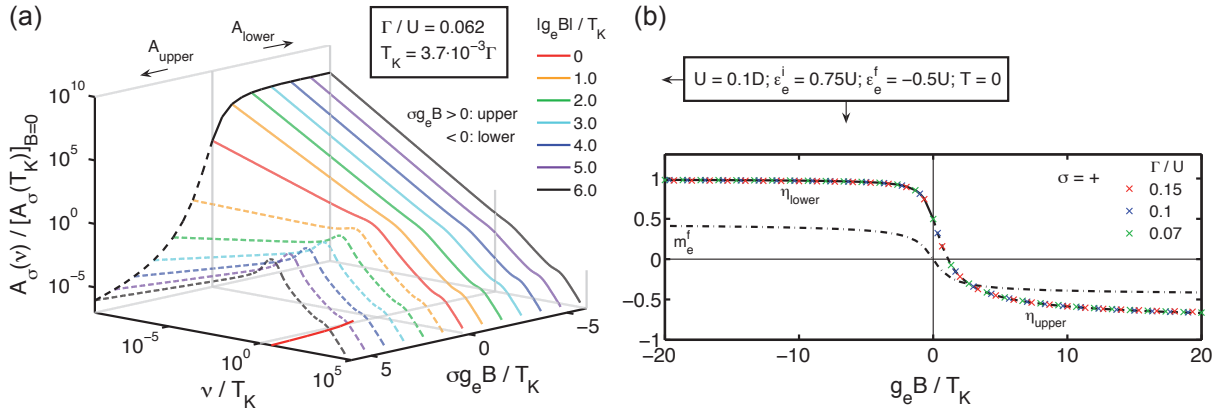


Figure 3.5.: (a) Absorption lineshapes for different magnetic fields. The different colors correspond to different values of the magnetic field, the linestyle (solid or dashed) indicates the orientation of the magnetic field. Changing the orientation of magnetic field is equivalent to considering both absorption into the upper and into the lower Zeeman-split level, as indicated by A_{upper} and A_{lower} , which can be tuned via the polarization of the incident photons. For absorption into the upper level, the AO divergence is suppressed and the peak position is no longer at the threshold frequency (indicated by the red line in the $\sigma g_e B / T_K$ -plane). (b) B-field dependence of the local magnetization and the low-energy exponent. The dashed and dashed-dotted lines show the universal curves of the low-energy exponents and the magnetization, respectively, with respect to $g_e B / T_K$. The colored crosses correspond to the exponents extracted for low frequencies from the NRG-calculated absorption spectra for different parameters.

expressions are obtained with fixed point perturbation theory (FPPT). At FPPT one makes use of the fact, that for $T = 0$ the absorption spectrum can be written as

$$\begin{aligned} A_\sigma(\nu) &= 2\text{Re} \int_0^\infty dt e^{it\nu_+} \langle G_i | e^{i\bar{H}^i t} e_\sigma e^{-i\bar{H}^f t} e_\sigma^\dagger | G_i \rangle \\ &= -2\text{Im} \langle G_i | e_\sigma \frac{1}{\nu_+ - \bar{H}^f} e_\sigma^\dagger | G_i \rangle, \end{aligned} \quad (3.20)$$

with $\bar{H}^a = H^a - E_G^a$ for $a = i, f$ and $\nu_+ = \nu + i0_+$. The final Hamiltonian $\bar{H}^f = H_r^* + H_r'$ can be represented by a fixed point Hamiltonian H_r^* of the SIAM and a perturbative term H_r' , with $r = \text{FO, LM}$, respectively. This allows an expansion of the resolvent in powers of H_r' which leads to:

$$A_\sigma^r(\nu) \simeq -\frac{2}{\nu^2} \text{Im} \langle G_i | e_\sigma H_r' \frac{1}{\nu_+ - H_r^*} H_r' e_\sigma^\dagger | G_i \rangle. \quad (3.21)$$

For the FO-regime, the excitation energies are high enough to allow charge fluctuations on the impurity, whereas for the LM-regime, the excitation energies are lower, so that real charge fluctuations are frozen out and a local moment forms at the impurity. In this energy regime, only virtual charge fluctuations are possible, which results in spin fluctuations of the local moment. The fixed point Hamiltonians and the perturbations are therefore given by:

$$H_{\text{FO}}^* = H_{\text{res}} + H_{\text{imp}}^f + \text{const.}, \quad H_{\text{FO}}' = H_{\text{hyb}}, \quad (3.22a)$$

$$H_{\text{LM}}^* = H_{\text{res}} + \text{const.}, \quad H_{\text{LM}}' = \frac{J(\nu)}{\rho} \vec{S} \cdot \vec{s}, \quad (3.22b)$$

with H_{imp} , H_{res} and H_{hyb} as in Eqs. (2.1) with (3.3) and where in Eq. (3.22b), \vec{S} is the impurity spin, \vec{s} is the spin of the reservoir electrons at the position of the impurity, ρ is the reservoir density of states and $J(\nu) = \ln^{-1}(\nu/T_K)$ is an effective, scale-dependent, dimensionless coupling constant. FPPT can be generalized to finite temperatures according to [65]. For the local moment regime one obtains:

$$A_\sigma^{\text{LM}}(\nu) = \frac{3\pi}{4} \frac{\nu/T}{1 - e^{-\nu/T}} \frac{\gamma_{\text{Kor}}(\nu, T)/\pi}{\nu^2 + \gamma_{\text{Kor}}^2(\nu, T)}, \quad (3.23)$$

where γ_{Kor} is the Korringa relaxation rate, given by $\gamma_{\text{Kor}} = \pi T / \ln^2[\max(|\nu|, T)/T_K]$. Since for the local moment regime $\max(|\nu|, T)/T_K \gg T_K$, γ_{Kor} is smaller than temperature and the absorption peak is narrower than one would expect from simple thermal broadening (e. g. see red dashed line in Fig. 3.4).

For frequencies $\nu < T_K$, the spectrum can be described by a power law (Eq. (3.19c)), where the exponent is given by the generalized Hopfield's rule, $\eta_\sigma = 1 - \sum_{\sigma'} (\Delta n'_{e\sigma'})^2$ (Sec. 3.2). Since the occupation can be changed not only by varying the position of the local level via gate voltage, but also by applying a magnetic field (which corresponds to a

spin-dependent splitting of the energy level: $\varepsilon_e^{i/f} \rightarrow \varepsilon_e^{i/f} + \frac{1}{2}\sigma g_e B$, the exponent is B -field dependent. The B -field dependence can be made explicit by expressing the exponent in terms of the final magnetization for the case of zero occupancy before absorption $n^i = 0$ and half occupancy afterwards, $n^f = 1$: $\eta_\sigma = \frac{1}{2} + 2m_e^f \sigma - 2(m_e^f)^2$, with the final magnetization $m_e^f = \frac{1}{2}(n_{e\uparrow}^f - n_{e\downarrow}^f)$ being a universal function of $g_e B/T_K$. By varying the magnetic field, Anderson orthogonality can therefore be tuned between being maximal ($\Delta n'_{e\sigma'} = 1$, $\eta_\sigma = -1$) and being completely absent ($\Delta n'_{e\sigma'} = 0$, $\eta_\sigma = 1$) (Fig. 3.5).

3.4. Emission for strong optical coupling

3.4.1. Mollow triplet

In this section we explain the qualitative features of the resonance fluorescence (RF) spectrum, which originates from spontaneous emission of an optically strongly coupled two-level system, before we add the FR and the tunnel-coupling to the impurity in the next section.

A two-level system with one optical mode, as it is the case for a laser, can be described with the Jaynes-Cummings Hamiltonian:

$$H_{JC} = \frac{1}{2}\omega_{eg}|e\rangle\langle e| - \frac{1}{2}\omega_{eg}|g\rangle\langle g| + \omega_L \left(a^\dagger a + \frac{1}{2} \right) + g (|e\rangle\langle g|a + a^\dagger|g\rangle\langle e|), \quad (3.24)$$

where $|e\rangle$ and $|g\rangle$ are the excited and the ground state of the two-level system, a (a^\dagger) are the annihilation (creation) operators of a photon, ω_{eg} is the transition frequency, ω_L is the frequency of the laser, and g the coupling constant for the laser with the two-level system. Because the energy ω_{eg} of the excited state and the energy ω_L of a photon are comparable, the Hilbert space can be divided according to the number of excitations into so called excitation manifolds. If one looks at the bare states $|e, n\rangle, |g, n+1\rangle$ of the $n+1$ -manifold, with n and $n+1$ photons, respectively, one can observe the well-known Rabi oscillations between these states with Rabi frequency $\Omega = g\sqrt{n+1}$. These occur since the bare states are not eigenstates of the Hamiltonian due to the coupling described by the last term in Eq. (3.24). Transforming the bare state basis to the eigenbasis of the Hamiltonian yields the so called "dressed states", $|+, n+1\rangle$ and $|-, n+1\rangle$ of the $n+1$ -manifold, with eigenenergies $E_{+,n+1} = (n+1)\omega_L + g\sqrt{n+1}$ and $E_{-,n+1} = (n+1)\omega_L - g\sqrt{n+1}$, having assumed $\omega_{eg} = \omega_L$ [66].

For an excitation number $n \gg 1$ of the manifold, the energy splitting between the two dressed states becomes $2g\sqrt{n+1} \simeq 2g\sqrt{n}$. Therefore, the transition energies from $|+, n+1\rangle$ to $|+, n\rangle$ and from $|-, n+1\rangle$ to $|-, n\rangle$ can be considered approximately degenerate. For $T \gg \Omega$ this results in three peaks in the emission spectrum, the Mollow triplet, where the side-peaks are separated from the peak in the middle by $2g\sqrt{n}$ and the middle peak is twice as high as the outer peaks [67] (Fig. 3.6), since it is associated with two equivalent transitions. The Mollow Triplet can also be observed if the light constitutes a coherent state (as it is the case for a laser) instead of a photon-number eigenstate. This is because

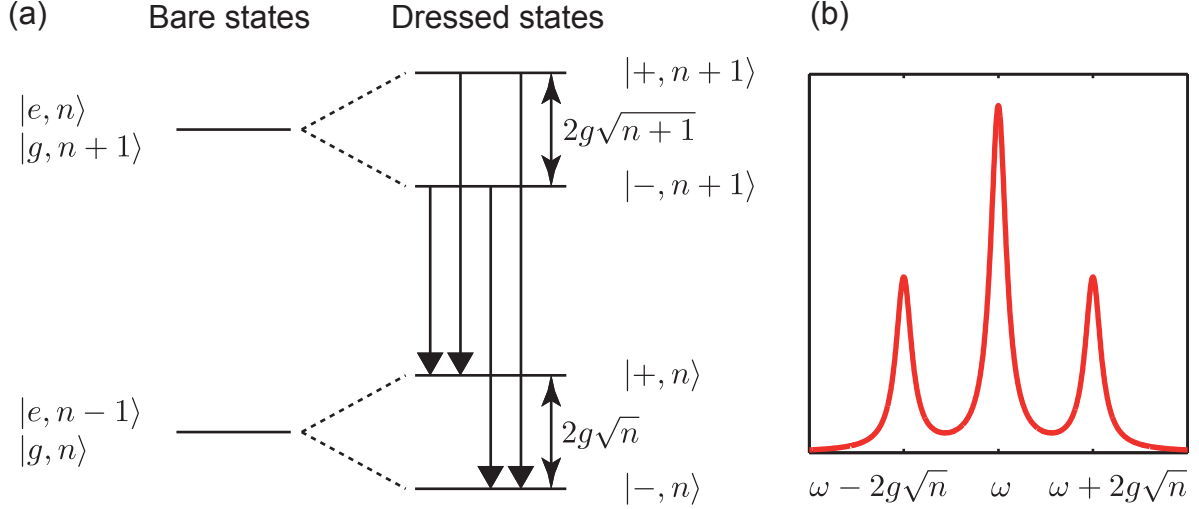


Figure 3.6.: Schematic of the transitions that yield the Mollow triplet and qualitative behavior of the RF spectrum. (a) shows the possible transitions between the dressed states of two neighboring manifolds. Two of the four possible transitions have the same frequency, which for $T \gg \Omega$ causes the emission to be twice as strong for this frequency as for the other transitions (b). Figure adapted from [66].

the photon number of a coherent state $|\alpha\rangle$ follows a Poisson distribution which in the case of a laser is rather narrow compared to its average value $|\alpha|^2$ [66].

The above derivation for the Mollow triplet is valid if the temperature is high enough that both dressed states of a manifold are occupied, which means that $T \gg \Omega$. In Sec. 5.2 we will examine, how the shape of the RF spectrum changes if the temperature is lowered below the Kondo temperature, $T \ll T_K$, so that Kondo correlations emerge between the upper level and the Fermi reservoir.

3.4.2. Two-level system tunnel-coupled to a Fermi reservoir

This subsection derives the formula which is used to calculate the emission spectrum with strong optical coupling with NRG in part II. It is a short summary of the detailed explanation of Ref. [68].

If the coupling between the two energy levels of the dot, ε_e and ε_h (see Fig. 3.1) is large, which corresponds to a large laser intensity, it cannot be treated as a perturbation which connects two different Hamiltonians, but one has to consider a Hamiltonian, where the optical coupling is explicitly included. Adding the radiative Hamiltonian and the optical coupling of the two-level system in rotating wave approximation to H_{EAM} (Eq. (3.1))

yields in the rotating frame:

$$\begin{aligned}
H' = H_{\text{EAM}} + \omega_L a_L^\dagger a_L &+ g \left(a_L e_{\downarrow}^\dagger h_{\uparrow}^\dagger + \text{h. c.} \right) \\
+ \sum_{q\sigma} \omega_q a_{q\sigma}^\dagger a_{q\sigma} &+ g \sum_{q\bar{\sigma}} \left(a_{q\bar{\sigma}} e_{\sigma}^\dagger h_{\bar{\sigma}}^\dagger + \text{h. c.} \right)
\end{aligned} \tag{3.25}$$

with g the coupling strength of the photons to the electrons and $a_{q\bar{\sigma}}$ ($a_{q\bar{\sigma}}^\dagger$) the annihilation (creation) operator of optical mode q with polarization $\bar{\sigma}$. The last two terms in the first line describe the laser photons and their coupling to the electrons, whereas the last two terms in the second line describe the modes of the radiative reservoir and their coupling to the electrons, with the last term being responsible for spontaneous emission.

Starting from the optical Bloch equations, the RF spectrum can be derived as (e. g. see [69]):

$$S(\omega) = \frac{\gamma_{\text{SE}}}{2\pi} \int_{-\infty}^{\infty} d\tau \langle \sigma_+(\tau) \sigma_- \rangle_{ss} e^{-i\omega\tau}, \tag{3.26}$$

with γ_{SE} being the rate for spontaneous emission and where

$$\langle \sigma_+(\tau) \sigma_- \rangle_{ss} = \text{Tr}(e^{iH'\tau} \sigma_+ e^{-iH'\tau} \sigma_- \rho_{ss}), \tag{3.27}$$

with $\sigma_+ = e_{\downarrow}^\dagger h_{\uparrow}^\dagger$ and $\sigma_- = h_{\uparrow} e_{\downarrow}$ creating or annihilating, respectively, an electron-hole pair and with $\langle \rangle_{ss}$ denoting the expectation value with respect to the steady state density matrix.

By assuming $\gamma_{\text{SE}} \propto g^2$ to be very small compared to the other rates of H' , we can then neglect the modes of the radiative reservoir in H' whose frequency is different from the laser frequency, which results in the following Hamiltonian for the time evolution in Eq. (3.27):

$$H'' = H_{\text{EAM}} + \omega_L a_L^\dagger a_L + g(a_L e_{\downarrow}^\dagger h_{\uparrow}^\dagger + h e_{\downarrow} a_L^\dagger), \tag{3.28}$$

so that

$$\langle \sigma_+(\tau) \sigma_- \rangle_{ss} \simeq \text{Tr}(e^{iH''\tau} \sigma_+ e^{-iH''\tau} \sigma_- \rho_{ss}). \tag{3.29}$$

After the reduction of the radiative modes to those with a single frequency, the Hamiltonian can be divided into excitation manifolds and it can be written as a sum of the Hamiltonians for the different manifolds $H'' = \sum_n H_n''$, with:

$$H_n'' = \omega_L(n-1) + \tilde{H}. \tag{3.30}$$

Here, \tilde{H} is Hamiltonian, which describes the two level system with one excitation, which can be a photon or a hole or a superposition thereof and $\omega_L(n-1)$ describes the additional $n-1$ excitations of the n -manifold. \tilde{H} is given by:

$$\begin{aligned}
\tilde{H} = \sum_{\sigma} (\varepsilon_e - U_{\text{eh}} n_h) n_{e\sigma} + U n_{e\uparrow} n_{e\downarrow} + \sum_{k\sigma} \varepsilon_k n_{k\sigma} + V \sum_{k\sigma} (e_{\sigma}^\dagger c_{k\sigma} + \text{h.c.}) \\
+ \varepsilon_h n_h + \omega_L(1 - n_h) + \Omega \left(e_{\downarrow}^\dagger h_{\uparrow}^\dagger + h_{\uparrow} e_{\downarrow} \right),
\end{aligned} \tag{3.31}$$

where the first line describes the SIAM and the second line describes the hole, the photon, and the optical coupling of the two levels, where $\Omega = g\sqrt{n}$ is the Rabi frequency for excitation manifold n , which can be assumed constant for a given laser intensity.

The connection to weak optical coupling (which corresponds to $\Omega = 0$) can be seen by writing \tilde{H} in the form of Eq. (3.3). For the case of strong optical coupling, the initial and final Hamiltonians from Eq. (3.3) are connected by the term $\Omega(e_{\downarrow}^{\dagger}h_{\uparrow}^{\dagger} + h_{\uparrow}e_{\downarrow})$, so that one obtains:

$$\tilde{H} = \begin{pmatrix} H_{\text{SIAM}} + \omega_{\text{L}} & \Omega h_{\uparrow}e_{\downarrow} \\ \Omega e_{\downarrow}^{\dagger}h_{\uparrow}^{\dagger} & H_{\text{T}} \end{pmatrix}, \quad H_{\text{T}} = H_{\text{SIAM}} - \sum_{\sigma=\uparrow,\downarrow} U_{\text{eh}}n_{\text{e}\sigma} + \varepsilon_{\text{h}}, \quad (3.32)$$

where for H_{T} the photon has been absorbed and has created an electron-hole pair, so that the system is in a trion state (assuming that the QD was singly occupied before photon absorption).

It can be shown [68] that in Eq. (3.29) H'' can be approximated by \tilde{H} , so that

$$\langle \sigma_{+}(\tau)\sigma_{-} \rangle_{ss} = \text{Tr} \left(e^{i\tilde{H}\tau} \sigma_{+} e^{-i\tilde{H}\tau} \sigma_{-} \rho_{ss} \right), \quad (3.33)$$

where the excitation manifold degree of freedom has been eliminated. With this simplification, and by normalizing with respect to γ_{SE} , Eq. (3.26) becomes

$$S(\omega) = \frac{1}{2\pi} \int_{-\infty}^{\infty} d\tau \langle \sigma_{+}(\tau)\sigma_{-} \rangle_{ss} e^{-i\omega\tau}. \quad (3.34)$$

Writing Eq. (3.34) in Lehmann representation and approximating the steady-state density matrix by the Boltzmann weights ρ_m , we obtain:

$$S(\nu) = \sum_{mn} \rho_m |\langle \psi_n | \sigma_{-} | \psi_m \rangle|^2 \delta(\nu - (E_m - E_n)), \quad (3.35)$$

with $\nu = \omega - \omega_{\text{L}}$. Interestingly, Eq. (3.35) is mathematically very similar to Eq. (3.5) and can be seen as an application of Fermi's Golden Rule, however, the states $|\psi_n\rangle$ and $|\psi_m\rangle$ are *dressed* states, and they are both eigenstates of the *same* Hamiltonian, that consists of H_i , H_f and the coupling term, (see Eq. (3.32)). By convention, Eq. (3.5) differs from Eq. (3.35) by a factor of 2π . This way, the formulas are in accordance with those of part II. The eigenstates and -energies can be obtained via NRG, and Eq. (3.35) can then be used to calculate the RF spectrum, as will be done in Sec. 5.2.

4. Numerical renormalization group

This chapter explains the basic ideas behind the iterative diagonalization of impurity models via NRG and the subsequent calculation of spectral functions. Although the Anderson model is more complex than the Kondo model, in the following sections, the NRG algorithm will be explained for the case of the Anderson model, because first, for most of the calculations presented in part II, we use Anderson-like models and second, dynamical quantities for the impurity (c. f. Sec. 4.2) are then more straightforward to obtain than is the case for the Kondo model [70, 71].

4.1. NRG algorithm

For convenience, we repeat the SIAM-Hamiltonian from Eq. (2.1):

$$H = \sum_{\sigma} \varepsilon_{\sigma} e_{\sigma}^{\dagger} e_{\sigma} + U n_{\uparrow} n_{\downarrow} + \sum_{k\sigma} \varepsilon_{k\sigma} c_{k\sigma}^{\dagger} c_{k\sigma} + \sum_{k\sigma} V_k \left(e_{\sigma}^{\dagger} c_{k\sigma} + c_{k\sigma}^{\dagger} e_{\sigma} \right). \quad (4.1)$$

Since the conduction band will be discretized according to *energy* below, we switch from the momentum (k) to an energy representation (ε) where the conduction band energies lie within an interval $[-D, D]$. In the following we set the half-bandwidth $D = 1$ and the Hamiltonian is thus given by:

$$H = H_{imp} + \sum_{\sigma} \int_{-1}^1 d\varepsilon \varepsilon a_{\varepsilon\sigma}^{\dagger} a_{\varepsilon\sigma} + \sum_{\sigma} \int_{-1}^1 d\varepsilon V_{\varepsilon} \left(e_{\sigma}^{\dagger} a_{\varepsilon\sigma} + a_{\varepsilon\sigma}^{\dagger} e_{\sigma} \right), \quad (4.2)$$

where $a_{\varepsilon\sigma}$ ($a_{\varepsilon\sigma}^{\dagger}$) are the annihilation (creation) operators of the reservoir electrons with energy ε and spin σ ,

To perform numerical calculations, the energy continuum of the conduction band has to be discretized (Fig. 4.1a,b). Since the renormalization algorithm, which is explained below, subsequently includes exponentially decaying energy scales, the continuum is discretized logarithmically. First one chooses a discretization parameter Λ , which is a dimensionless number $\Lambda > 1$, typically $\Lambda \simeq 2$, and divides the bath into intervals $\pm[\Lambda^{-(n+1)}, \Lambda^n]$ with $n \in \mathbb{N}_0$.

For each interval one can define a complete set of orthonormal functions

$$\psi_{np}^{\pm}(\varepsilon) = \begin{cases} \frac{1}{\sqrt{\Lambda^{-n}(1-\Lambda^{-1})}} e^{\pm i\omega_n p \varepsilon} & \text{for } |\pm \Lambda^{-(n+1)}| < |\pm \varepsilon| < |\pm \Lambda^{-n}| \\ 0 & \text{otherwise.} \end{cases} \quad (4.3)$$

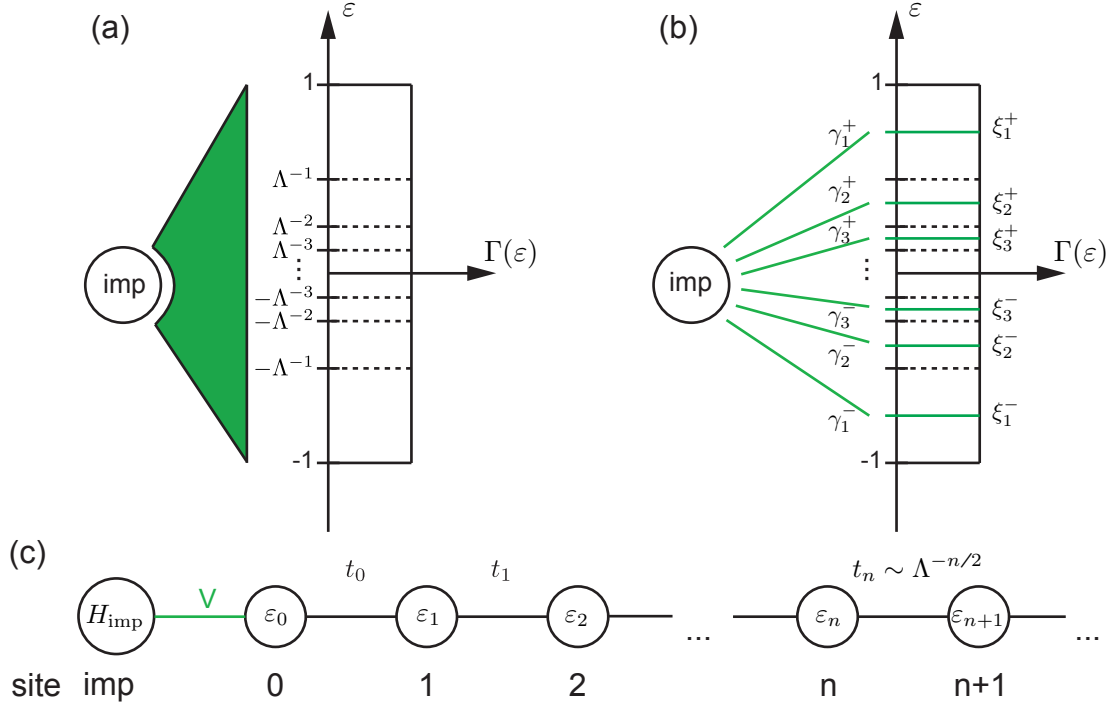


Figure 4.1.: (a) Impurity, Fermi reservoir and coupling. The Fermi reservoir is discretized logarithmically, with the resolution increasing towards the Fermi level. (b) An energy value is assigned to each interval, which corresponds to the mean values of the energy within the interval. The couplings are given by the length of the interval. (c) Wilson chain with impurity and sites describing the reservoir. Due to the logarithmic discretization in (b) the couplings decrease exponentially. Figure adapted from [9].

ω_n is thereby defined as $\omega_n = 2\pi/[\Lambda^{-n}(1 - \Lambda^{-1})]$ and p runs over all integers between $-\infty$ and $+\infty$. This basis defines the operators

$$a_{n\sigma} = \int_{-1}^1 d\varepsilon [\psi_{n0}^+(\varepsilon)]^* a_{\varepsilon\sigma}, \quad b_{n\sigma} = \int_{-1}^1 d\varepsilon [\psi_{n0}^-(\varepsilon)]^* a_{\varepsilon\sigma}. \quad (4.4)$$

This definition corresponds to performing a Fourier transformation on each interval of the hybridization and keeping only the lowest mode of each transformation.

Then two energies ξ_n and γ_n are assigned to each interval, which correspond to the average energy of the interval and to the coupling of the interval to the impurity, respectively,

$$\xi_n^\pm = \frac{\int^{\pm,n} d\varepsilon \Gamma(\varepsilon) \varepsilon}{\int^{\pm,n} d\varepsilon \Gamma(\varepsilon)}, \quad \gamma_n^{\pm 2} = \int^{\pm,n} d\varepsilon \Gamma(\varepsilon), \quad (4.5)$$

where $\int^{\pm,n}$ denotes the integral over the energy interval $\pm[\Lambda^{-(n+1)}, \Lambda^n]$, and where $\Gamma(\varepsilon)$ is the hybridization function from Eq. (2.3). (A slightly improved way to perform the

discretization is described in [72], which minimizes discretization artifacts. For a constant hybridization, as assumed in part II, however, this is equal to using the more illustrative discretization scheme described here, and multiplying the hybridization with a Λ -dependent prefactor.)

The discretized Hamiltonian is then given by:

$$H = H_{imp} + \sum_{n\sigma} (\xi_n^+ a_{n\sigma}^\dagger a_{n\sigma} + \xi_n^- b_{n\sigma}^\dagger b_{n\sigma}) + \frac{1}{\sqrt{\pi}} \sum_{\sigma} e_{\sigma}^\dagger \sum_n (\gamma_n^+ a_{n\sigma} + \gamma_n^- b_{n\sigma}) + \frac{1}{\sqrt{\pi}} \sum_{\sigma} \left(\sum_n (\gamma_n^+ a_{n\sigma}^\dagger + \gamma_n^- b_{n\sigma}^\dagger) \right) e_{\sigma}. \quad (4.6)$$

The reservoir is non-interacting, and hence its Hamiltonian is quadratic. Together with the hybridization to the impurity, it can be described in matrix notation by

$$H_{res} + H_{hyb} = \sum_{\sigma} [(e_{\sigma}^\dagger, a_{0\sigma}^\dagger, \dots, a_{M\sigma}^\dagger, b_{0\sigma}^\dagger, \dots, b_{M\sigma}^\dagger) \begin{pmatrix} 0 & \gamma_0^+ & \cdots & \gamma_M^+ & \gamma_0^- & \cdots & \gamma_M^- \\ \gamma_0^+ & \xi_0^+ & \cdots & 0 & 0 & \cdots & 0 \\ \vdots & \vdots & \ddots & & & & \vdots \\ \gamma_M^+ & 0 & & \xi_M^+ & & & 0 \\ \gamma_0^- & 0 & & & \xi_0^- & & 0 \\ \vdots & \vdots & & & & \ddots & \vdots \\ \gamma_M^- & 0 & \cdots & 0 & 0 & \cdots & \xi_M^- \end{pmatrix} \begin{pmatrix} e_{\sigma} \\ a_{0\sigma} \\ \vdots \\ a_{M\sigma} \\ b_{0\sigma} \\ \vdots \\ b_{M\sigma} \end{pmatrix}], \quad (4.7)$$

where we accounted for the fact that in practice it suffices to consider a finite number of intervals $M + 1$ above and below the Fermi energy. The matrix in between can be tridiagonalized using the Lanczos algorithm. Here the impurity level remains untouched, which implies that the starting vector into the Lanczos algorithm is given by $[1, 0, 0, \dots]$. The tridiagonalization corresponds to a basis transformation of the bath and results in

$$H_{res} + H_{hyb} = \sum_{\sigma} [(e_{\sigma}^\dagger, f_{0\sigma}^\dagger, f_{1\sigma}^\dagger, \dots, f_{2M+1\sigma}^\dagger) \begin{pmatrix} 0 & V & 0 & \cdots & 0 \\ V & \varepsilon_0 & t_0 & & 0 \\ 0 & t_0 & \varepsilon_1 & \ddots & 0 \\ \vdots & & \ddots & \ddots & t_{2M} \\ 0 & 0 & 0 & t_{2M} & \varepsilon_{2M+1} \end{pmatrix} \begin{pmatrix} e_{\sigma} \\ f_{0\sigma} \\ f_{1\sigma} \\ \vdots \\ f_{2M+1\sigma} \end{pmatrix}], \quad (4.8)$$

where the operators $f_{n\sigma}^{(\dagger)}$ fulfill fermionic commutation relations, $\{f_{n\sigma}, f_{n'\sigma'}^\dagger\} = \delta_{nn'}\delta_{\sigma\sigma'}$. For some special cases of the hybridization, the couplings ξ_n and on-site energies ε_n can be calculated analytically. E. g. for a constant hybridization Γ in $[-1, 1]$, one gets [4]:

$$t_n = \frac{(1 + \Lambda^{-1})(1 - \Lambda^{-n-1})}{2\sqrt{1 - \Lambda^{-2n-1}}\sqrt{1 - \Lambda^{-2n-3}}} \Lambda^{-n/2}, \quad \varepsilon_n = 0. \quad (4.9)$$

The final Hamiltonian contains the impurity which is coupled to a chain with $2M + 2$ sites, with on-site energies ε_n and couplings t_n (Fig. 4.1c). The chain is then truncated to

size $N \lesssim M$, and since the truncation in the number of sites eventually occurs at the level of the chain, rather than in the discretization in Eq. (4.7), the couplings t_n do not depend on M . The length N of the chain is chosen such that $\Lambda^{-N/2}$ corresponds to the lowest energy scale one wants to examine. The Hamiltonian then reads:

$$H = H_{imp} + \sum_{\sigma} V(e_{\sigma}^{\dagger} f_{0\sigma} + f_{0\sigma}^{\dagger} e_{\sigma}) + \sum_{\sigma} \sum_{n=0}^N [t_n (f_{n\sigma}^{\dagger} f_{n+1\sigma} + f_{n+1\sigma}^{\dagger} f_{n\sigma}) + \varepsilon_n f_{n\sigma}^{\dagger} f_{n\sigma}]. \quad (4.10)$$

Note that for the assumed case of a constant density of states, the ε_n are zero due to the particle-hole symmetry of the bath. For the recursive NRG procedure, we define for each chain of length $k \leq N \lesssim M$ a rescaled Hamiltonian

$$H_k = \Lambda^{(k-1)/2} \left(H_{imp} + H_{hyb} + \sum_{\sigma} \sum_{n=0}^{k-1} t_n (f_{n\sigma}^{\dagger} f_{n+1\sigma} + f_{n+1\sigma}^{\dagger} f_{n\sigma}) + \varepsilon_n f_{n\sigma}^{\dagger} f_{n\sigma} \right), \quad (4.11)$$

where we introduced the scaling factor $\Lambda^{(k-1)/2}$ to make the energy spectra of the different iterations comparable. Two successive Hamiltonians are therefore related to each other via the recursion relation

$$H_{k+1} = \sqrt{\Lambda} H_k + \Lambda^{k/2} \left(\sum_{\sigma} t_k (f_{k\sigma}^{\dagger} f_{k+1\sigma} + f_{k+1\sigma}^{\dagger} f_{k\sigma}) + \varepsilon_n f_{k+1\sigma}^{\dagger} f_{k+1\sigma} \right). \quad (4.12)$$

The Hamiltonian is now in a form in which it can be diagonalized iteratively. Starting from the impurity, we successively add a new site to the chain and diagonalize the new Hamiltonian. However, since the state space increases exponentially with the length of the chain (i. e. $\propto d^k$ with site dimension $d = 4$ for the SIAM), after the first few iterations it has to be reduced after the diagonalization. This is done by keeping only the states with the lowest energies, with the truncation criterion being either a fixed number of states or a certain (rescaled) energy value, below which all states are kept. States with higher energy are discarded and are no more refined at the next iteration. This leads to the following procedure for the iterative diagonalization of the Hamiltonian (App. A shows the Hamiltonian of the first iteration written out explicitly):

- Diagonalize H_k to obtain energies E_k^s and eigenstates $|s\rangle_k$. At the first iteration diagonalize $H_{imp} + H_{hyb}$.
- Shift the energy spectrum by the ground state energy E_k^0 such that the lowest energy of E_k^s lies at zero.
- Truncate the state space according to energy or number of kept states. For $k = N$ at the end of the chain, truncate all states and stop the iterative procedure.
- Add the next site according to Eq. (4.12) and express the Hamiltonian H_{k+1} in the product basis $|s\rangle_k \otimes |\sigma\rangle$ of the eigenstates $|s\rangle_k$ of Hamiltonian H_k and of local basis $|\sigma\rangle$ of the new site. Set $k \rightarrow k + 1$ and repeat from point one above.

For the application of this procedure, it is crucial, that both, coupling elements and on-site energies of the Wilson chain decay exponentially. With an appropriate criterion for truncation, discarding states introduces only tiny errors, since due to the energy scale separation of the problem, the influence of high-energy states on low-energy states is essentially negligible. To be sure that the number of kept states is high enough, a quantitative measure of the truncation-error can be obtained by calculating the 'discarded weight' according to [73].

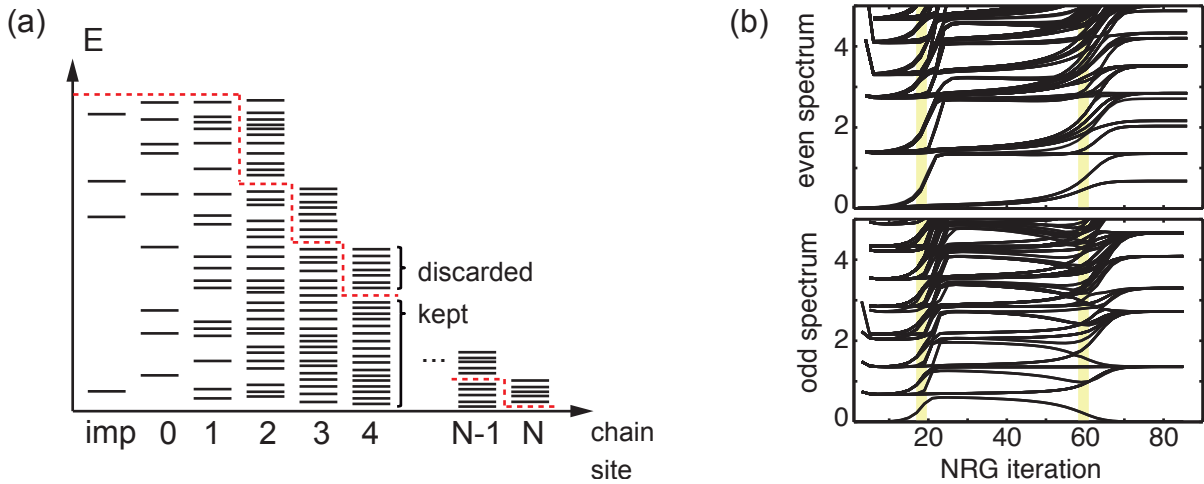


Figure 4.2.: (a) Energy spectra for several NRG iterations. The states above a certain number of kept states or above a certain rescaled energy are discarded. Panel (a) adapted from [43]. (b) Example of an energy flow diagram for the SIAM in the symmetric case. The different fixed point regimes (free orbital (FO), local moment (LM) and strong coupling (SC)) can be identified clearly from the flow-diagrams alone, their borders are indicated by thick yellow bars. Due to even-odd oscillations, it is necessary to examine the energy flow for even and odd iterations separately.

Flow diagrams

Significant physical information can be obtained directly from the energy spectrum. To make the energy spectra of different iterations comparable to each other, one uses the spectra of the rescaled Hamiltonians Eq. (4.11), shifted by their respective ground state energies. By plotting the energy spectra vs. iteration, one obtains the so called energy flow diagrams (Fig. 4.2), which show how the energy spectra develop (flow) with increasing iteration. Flow diagrams always have to be considered for even and odd iterations separately, due to the even-odd oscillations which occur at the iterative diagonalization of the Wilson chain. The origin of these oscillations is that the free electron Hamiltonian (chain without impurity) in its diagonalized form has either only free particle levels with negative energy (occupied) and free particle levels with positive energy (unoccupied), which results in a

non-degenerate ground state and which is the case for an even number of sites; or it has an additional free particle level with zero energy, which results in a four-fold degenerate ground state and which is the case for an odd number of sites. For a detailed discussion see [7], chapter III.

By looking at the energy flow diagrams, the various stable or unstable fixed points of the model become visible, at which the model is governed by different physics. For the symmetric SIAM, going from high to low energies, these are [7] (i) the free orbital (FO) fixed point, for which the energy level of the impurity behaves as a free orbital, where electrons can hop onto and off the impurity, (ii) the local moment (LM) fixed point, for which the impurity level is occupied by a single electron with a magnetic moment (iii) the strong coupling (SC) fixed point for which there are Kondo correlations and where the localized impurity spin is screened by the electrons from the surrounding reservoir. The name of the strong coupling fixed point originates from the fact that in this energy regime, the effective coupling of the impurity to the reservoir is divergent.

Moreover, one can determine from the energy spectra thermodynamic quantities like the specific heat or the magnetic susceptibility. It is even possible to obtain certain non-thermodynamic quantities (like scattering phase shifts) from the spectrum alone [60]. However, although more difficult to obtain, one is often interested in dynamical quantities which contain information about scattering processes and the time-evolution of the system. Sec. 4.2 will show how dynamical quantities can be calculated from the eigenenergies and eigenstates.

4.2. Spectral functions

4.2.1. Definition

Calculating dynamic quantities like spectral functions requires more work than calculating static quantities directly from the energy spectra, since spectral functions involve not just the plain energies, but also transition matrix elements for combinations of eigenstates. In general, the spectral function for two operators \mathcal{B} and \mathcal{C} [74] is given by:

$$\mathcal{A}_{\mathcal{B}\mathcal{C}}(\omega) = \int \frac{dt}{2\pi} e^{i\omega t} \langle \mathcal{B}(t)\mathcal{C} \rangle_T. \quad (4.13)$$

Using the explicit expression for the time dependence $\mathcal{B}(t) = e^{iHt}\mathcal{B}e^{-iHt}$ and writing the spectral function in Lehmann representation, this reads:

$$\mathcal{A}_{\mathcal{B}\mathcal{C}}(\omega) = \int \frac{dt}{2\pi} e^{i\omega t} \sum_{ij} \frac{e^{-\beta E_i}}{Z} \langle i | e^{iHt}\mathcal{B}e^{-iHt} | j \rangle \langle j | \mathcal{C} | i \rangle. \quad (4.14)$$

Performing the Fourier transformation results in:

$$\mathcal{A}_{\mathcal{B}\mathcal{C}}(\omega) = \sum_{ij} \frac{e^{-\beta E_i}}{Z} \langle i | \mathcal{B} | j \rangle \langle j | \mathcal{C} | i \rangle \delta(\omega - (E_j - E_i)). \quad (4.15)$$

4.2.2. Impurity spectral function

A spectral function which is of special interest at impurity problems, is the 'impurity spectral function', i. e. the local density of states of the impurity, which for the SIAM is given by

$$A_\sigma(\omega) = \sum_{ij} \frac{e^{-\beta E_i} + e^{-\beta E_j}}{Z} |\langle j | e_\sigma^\dagger | i \rangle|^2 \delta(\omega - (E_i - E_j)). \quad (4.16)$$

This spectral function consists of two spectral functions of the type of Eq. (4.15): $A_\sigma(\omega) = \mathcal{A}_\sigma^>(\omega) + \mathcal{A}_\sigma^<(\omega)$, with $\mathcal{A}_\sigma^>(\omega) = \mathcal{A}_{e_\sigma^\dagger e_\sigma}(-\omega)$ and $\mathcal{A}_\sigma^<(\omega) = \mathcal{A}_{e_\sigma e_\sigma^\dagger}(\omega)$. The impurity spectral function is related to the retarded Green's function via

$$A_\sigma(\omega) = -\frac{1}{\pi} \text{Im}[\mathcal{G}_\sigma^R(\omega)], \quad (4.17)$$

with the Green's function defined by $\mathcal{G}_\sigma^R(t) = -i\theta(t)\langle\{e_\sigma(t), e_\sigma^\dagger\}\rangle_T$.

4.2.3. Smoothing of discrete data

Eq. (4.15) yields discrete raw data $\mathcal{A}_{\text{disc}}$, which, in practice, are stored in binned form with typically 256 bins per decade (which renders further numerical processing more efficient). These data are then smoothed [74] according to $\mathcal{A}(\omega) = \int d\omega' K(\omega, \omega') \mathcal{A}_{\text{disc}}(\omega')$. For the broadening kernel $K(\omega, \omega')$ we use

$$K(\omega, \omega') = L(\omega, \omega') h(\omega') + G(\omega, \omega') [1 - h(\omega')], \quad (4.18)$$

with

$$L(\omega, \omega') = \frac{\theta(\omega\omega')}{\sqrt{\pi}\alpha|\omega|} e^{-\left(\frac{\log|\omega/\omega'|}{\alpha} - \gamma\right)^2} \quad (4.19)$$

$$= \frac{\theta(\omega\omega')}{\sqrt{\pi}\alpha|\omega'|} e^{-\left(\frac{\log|\omega'/\omega|}{\alpha} + \gamma - \alpha/2\right)^2} e^{-\alpha(\gamma - \alpha/4)}, \quad (4.20)$$

$$G(\omega, \omega') = \frac{1}{\sqrt{\pi}\omega_0} e^{-(\omega - \omega')^2/\omega_0^2}, \quad (4.21)$$

$$h(\omega') = \begin{cases} 1, & |\omega'| \geq \omega_0 \\ e^{-\left(\frac{\log|\omega'/\omega_0|}{\alpha}\right)^2}, & |\omega'| < \omega_0. \end{cases} \quad (4.22)$$

$L(\omega, \omega')$ and $G(\omega, \omega')$ describe log-gaussian and gaussian functions with width α . The parameter $\gamma = \alpha/4$ ensures that the log-gaussians conserve peak height, e. g. such that a constant function would be mapped onto itself [74]. For $\omega > \omega_0$ we strictly use a log-gaussian because it is naturally adapted to the logarithmic spread of the raw data, which results from the NRG-inherent logarithmic discretization. However, since a log-gaussian vanishes for $\omega \rightarrow 0$, one uses a normal (linear) gaussian for $\omega \ll \omega_0$, to avoid an artificial gap at $\omega = 0$. The function $h(\omega')$ smoothly interpolates between $L(\omega, \omega')$ and $G(\omega, \omega')$ and is

chosen also of log-gaussian type. For functions which still change strongly for $|\omega| \lesssim \omega = 0$, an appropriately adapted $h(\omega')$ and $G(\omega, \omega')$ may be required to reduce possible emerging artifacts. ω_0 is typically chosen to be $T/2$ for temperatures $T > \Lambda^{-N/2}$, with N being the chain length, and $\Lambda^{-N/2}/2$ otherwise, when the length of the chain determines the effective temperature $T \approx \Lambda^{-N/2}$.

Typical values of the broadening parameter are $\alpha \simeq 0.86 \cdot \log \Lambda$, i. e. $\alpha \in [0.5; 1.2]$ for $\Lambda \in [1.8; 4]$. Smaller values for α can be achieved with z-averaging [75] or by calculating the spectral function with the use of the correct self-energy [76].

4.2.4. Matrix product states

The eigenstates as generated by the iterative NRG diagonalization, have the form of matrix product states [77]. This means they are stored as a sequence of rank-3 tensors $A_{KX}^{[n]}$ with elements $[A_{KX}^{[n]}]_{ss'}$ which describe how the product basis $|\sigma\rangle_n \otimes |s\rangle_{n-1}^K$ of site n and the chain up to site $n-1$ transforms into the eigenbasis $|s'\rangle_n^X$ of the chain with n sites:

$$|s'\rangle_n^X = \sum_{\sigma_n s}^K [A_{KX}^{[n]}]_{ss'} |\sigma\rangle_n \otimes |s\rangle_{n-1}^K. \quad (4.23)$$

The tensors $A_{KX}^{[n]}$ are divided into two parts, $A_{KK}^{[n]}$ and $A_{KD}^{[n]}$, depending on whether the state $|s'\rangle_n^X$ belongs to the kept ($X = K$) or to the discarded ($X = D$) states of iteration n . The tensors $A_{KX}^{[n]}$ can also be considered as a set of d matrices $A_{KX}^{[\sigma_n]}$ and are therefore often simply being referred to as A-matrices.

By inserting the definition of a Matrix Product State (MPS) repeatedly in Eq. (4.23) for $|s\rangle_{n-1}^K$, we obtain:

$$|s'\rangle_n^X = \sum_{\sigma_n \dots \sigma_1 \sigma_{imp}} [A_{KK}^{[\sigma_0]} \dots A_{KK}^{[\sigma_{n-1}]} A_{KX}^{[\sigma_n]}]_{\sigma_{imp} s'} |\sigma_n\rangle \otimes |\sigma_{n-1}\rangle \otimes \dots \otimes |\sigma_0\rangle \otimes |\sigma_{imp}\rangle. \quad (4.24)$$

Here, the origin of the term MPS becomes visible, since the coefficients of the eigenstates when expressed in the product basis, are given by a product of A-matrices. It is interesting to note that for the states $|s'\rangle_n^X$, Eq. (4.24) yields d^n coefficients, which, however, are not all independent, given that they are encoded as MPS.

4.2.5. FDM-NRG

For the calculation of spectral functions, there exist different approaches, which differ in the way how they combine states from different iterations. For the first calculations of dynamical quantities [78], the spectral data in Eq. (4.15) was computed on a by-shell basis, where the weights of the states were given by plain Boltzmann factors. This data was then patched together to the full spectral function. This approach faces two problems: (i) since the kept states of high energy shells are further refined at the NRG procedure at later iterations, the contribution of some states is counted more than once: at the iteration

they are eventually discarded, and at the kept states of the previous iterations, (ii) for shells with energy $E \gg T$, the correct density matrix is given by the reduced density matrix where higher iterations have been traced out, instead of the Boltzmann factors.

The first problem had been addressed by using a special patching scheme that reduces the double counting errors [79]. The second problem was solved by Hofstetter with density matrix NRG (DM-NRG) [80], where the reduced density matrix is used for each iteration. It was shown by Weichselbaum and von Delft [74] and Peters, Pruschke, Anders and Schiller [81, 82, 83], that it is possible to completely avoid double countings (and use the reduced density matrix) by using a basis which consists solely of the discarded states of all iterations. This method, the full density matrix NRG (FDM-NRG) will be explained in the remainder of this section. There exist different notations to handle the various indices that occur with FDM-NRG. We use the description from [74, 84] which is very clearly arranged.

Complete basis

To compute spectral functions, all states must be defined within the same Hilbert space. Since the Wilson chain is extended by one site at a time, a common Hilbert space can be obtained by extending all states to the Hilbert space that corresponds to the Hamiltonian H_N of the full chain. This is achieved by complementing the states $|s\rangle_n^X$ of iteration n by the environmental states $|e_n\rangle$ (Fig. 4.3):

$$|se\rangle_n^X = |e_n\rangle \otimes |s\rangle_n^X \quad (4.25)$$

with

$$|e_n\rangle \equiv |\sigma_N\rangle \otimes |\sigma_{N-1}\rangle \otimes \cdots \otimes |\sigma_{n+1}\rangle \quad (4.26)$$

simply the Fock space for the remainder of the chain.

The eigenenergies E_s^n of the Hamiltonian H_n can then be seen as approximate eigenenergies of the Hamiltonian of the full chain:

$$H_N |se\rangle_n^X \simeq E_s^n |se\rangle_n^X. \quad (4.27)$$

With these definitions, the discarded states by Anders and Schiller [81] form an approximate but complete and orthogonal basis of the full Hamiltonian,

$$\mathbb{1} = \sum_{n>n_0}^N \sum_{se} |se\rangle_n^D \langle se|, \quad (4.28)$$

$${}^D_n \langle se|s'e'\rangle_m^D = \delta_{nm} \delta_{ss'} \delta_{e_n e'_n}, \quad (4.29)$$

where n_0 is the last iteration where no truncation occurred. A kept state can therefore be fully expressed as a linear combination of discarded states, and the overlap between a discarded and a kept state is given by

$${}^D_n \langle se|s'e'\rangle_m^K = \begin{cases} [A_{KK}^{[\sigma_{m+1}]} \cdots A_{KD}^{[\sigma_n]}]_{ss'} \delta_{e_n e'_n} & n > m \\ 0 & n \leq m. \end{cases} \quad (4.30)$$

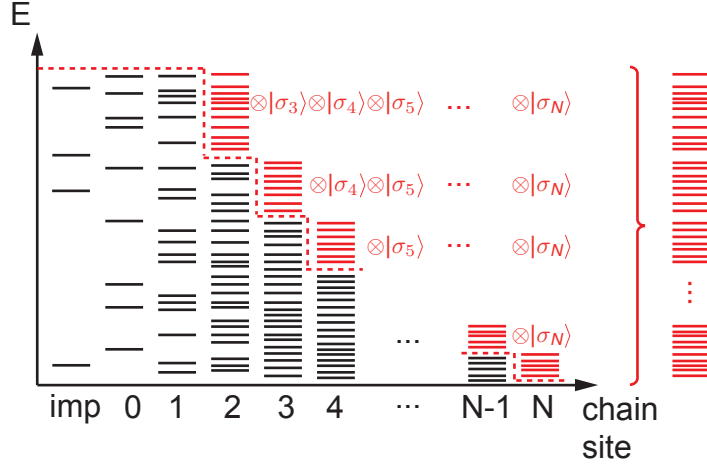


Figure 4.3.: Eigenenergies obtained from the NRG algorithm. The discarded states (red) constitute a complete and orthonormal basis. The environmental states $|\sigma_n\rangle$ indicate that the discarded states are no longer refined but that they are considered to be appropriately degenerate instead, which is reflected in their weighting factors at the calculation of the spectral function (c. f. Eq. (4.31)). Figure adapted from [43].

Density matrix

The density matrix ρ of the Wilson chain Hamiltonian can be expressed as a sum of density matrices, the states of which correspond to different iterations:

$$\rho(T) = \sum_{n>n_0}^N \sum_{se} \frac{e^{-\beta E_s^n}}{Z} |se\rangle_n^D \langle se|_n^D = \sum_{n>n_0}^N w_n \rho_{DD}^{[n]} \quad (4.31)$$

with

$$\rho_{DD}^{[n]} = \frac{1}{Z_n} \sum_s e^{-\beta E_s^n} |s\rangle_n^D \langle s|_n^D, \quad (4.32)$$

$$w_n = \frac{Z_n d^{N-n}}{Z}, \quad (4.33)$$

$$Z_n = \sum_s^D e^{-\beta E_s^n}. \quad (4.34)$$

w_n are the weighting factors which are determined by temperature and the degeneracy due to the environmental states of iteration n . The w_n 's are peaked at a certain iteration n_T (the energy of which corresponds to temperature) and are essentially zero for iterations $n \ll n_T$ or $n \gg n_T$. At early iterations the reason for this is that the Boltzmann weights are vanishingly small. At later iterations, the occupation is essentially 1, but the degeneracy

d^{N-n} of these states is exponentially smaller than the degeneracy of the states at earlier iterations, so that these states effectively also have no contribution.

Spectral functions with FDM-NRG

At FDM-NRG the general expression for the spectral function is (sum over s , s' and local site indices σ implied for this section)

$$\mathcal{A}^{\mathcal{B}\mathcal{C}}(\omega) = \sum_{n>n_0}^N w_n \mathcal{A}_n^{\mathcal{B}\mathcal{C}}(\omega) = \sum_{n>n_0}^N w_n \sum_{m>n_0}^n \sum_{XX'}^{\neq KK} [\mathcal{C}_{X'X}^{[m]} \rho_{XX}^{[mn]}]_{s's} [\mathcal{B}_{XX'}^{[m]}]_{ss'} \delta(\omega - E_{s's}^m) \quad (4.35)$$

with

$$[\rho_{DD}^{[m=n]}]_{ss'} = \delta_{ss'} \frac{e^{-\beta E_s^n}}{Z_n}, \quad (4.36)$$

$$[\rho_{KK}^{[m<n]}]_{ss'} = [A_{KK}^{[\sigma_{m+1}]} \dots A_{KD}^{[\sigma_n]} \rho_{DD}^{[nn]} A_{DK}^{[\sigma_n]\dagger} \dots A_{KK}^{[\sigma_{m+1}]\dagger}]_{ss'}, \quad (4.37)$$

$$[\mathcal{B}_{KD}^{[m]}]_{ss'} = [A_{KD}^{[\sigma_m]} \dots A_{KK}^{[\sigma_{n_0+1}]} \mathcal{B}_{KK}^{[n_0]} A_{KK}^{[\sigma_{n_0+1}]} \dots A_{KK}^{[\sigma_m]}]_{ss'}, \quad (4.38)$$

$$[\mathcal{B}_{DK}^{[m]}]_{ss'} = [A_{KK}^{[\sigma_m]} \dots A_{KK}^{[\sigma_{n_0+1}]} \mathcal{B}_{KK}^{[n_0]} A_{KK}^{[\sigma_{n_0+1}]} \dots A_{DK}^{[\sigma_m]}]_{ss'}, \quad (4.39)$$

$$[\mathcal{B}_{DD}^{[m]}]_{ss'} = [A_{KD}^{[\sigma_m]} \dots A_{KK}^{[\sigma_{n_0+1}]} \mathcal{B}_{KK}^{[n_0]} A_{KK}^{[\sigma_{n_0+1}]} \dots A_{DK}^{[\sigma_m]}]_{ss'}, \quad (4.40)$$

where we assumed, that the operators \mathcal{B} and \mathcal{C} only act on the impurity or within the beginning of the chain and can therefore be expressed in the basis of iteration n_0 . The left hand side of Eqs. (4.36)-(4.40) are the matrix elements for the density matrix and the operator \mathcal{B} , expressed in the basis of iteration m . They are obtained by using MPS to transform them into the basis of iteration m , as described on the right hand side. The definition of the matrix elements of \mathcal{C} is analogous to the definition of \mathcal{B} .

In Eq. (4.35), the terms $\mathcal{A}_n^{\mathcal{B}\mathcal{C}}(\omega)$ are the contributions to the spectral function of all states of a single shell, where the matrix elements of two kept states are successively refined and expressed in terms of the discarded states of all later iterations. However, instead of transforming the kept states into the space of all discarded states, it is more convenient to start from the end of the chain and to iteratively generate the density matrices while going backwards. This yields the reduced density matrix for each iteration, where the later iterations have been traced out. This way the refinement of the kept states is taken into account by the reduced density matrix and it is sufficient to calculate only the matrix elements where both states s and s' belong to the same shell. This corresponds to changing the order of summation for n and m compared to Eq. (4.35):

$$\mathcal{A}^{\mathcal{B}\mathcal{C}} = \sum_{m>n_0}^N \sum_{n \geq m}^N w_n \sum_{XX'}^{\neq KK} [\mathcal{C}_{X'X}^{[m]} \rho_{XX}^{[mn]}]_{s's} [\mathcal{B}_{XX'}^{[m]}]_{ss'} \delta(\omega - E_{s's}^m). \quad (4.41)$$

With the (non-normalized) reduced density matrix for shell m ,

$$\rho_{XX}^{[m],red} = \sum_{n \geq m}^N w_n \rho_{XX}^{[mn]}, \quad (4.42)$$

this becomes

$$\mathcal{A}^{BC} = \sum_{m > n_0}^N \sum_{XX'}^{\neq KK} [\mathcal{C}_{X'X}^{[m]} \rho_{XX}^{[m],red}]_{s's} [\mathcal{B}_{XX'}^{[m]}]_{ss'} \delta(\omega - E_{s's}^m). \quad (4.43)$$

In practice, the reduced density matrices $\rho_{XX}^{[m],red}$ are first calculated in a “backward run“ by going from the end of the chain to the beginning. The calculation of the transition matrix elements $[\mathcal{B}_{XX'}^{[m]}]_{ss'}$ and $[\mathcal{C}_{X'X}^{[m]}]_{s's}$ and the actual evaluation of Eq. (4.43) is then performed in a “forward run“ by going from the beginning of the chain to the end (Fig. 4.4). Calculating the spectral function this way has the additional benefit that one naturally obtains the reduced density matrices, which are interesting quantities themselves [73].

4.3. Fermionic signs

4.3.1. Fermionic signs for the NRG diagonalization

During the NRG diagonalization, states are determined by the subsequent application of raising and lowering operators. Since the sign of a state depends on the order in which these fermionic operators act, it is necessary to define an order for these operators, both, for different sites and for the states on a certain site. We therefore define the fully occupied state and thus the fermionic order as:

$$f_{N\uparrow}^\dagger f_{N\downarrow}^\dagger f_{N-1\uparrow}^\dagger f_{N-1\downarrow}^\dagger \cdots f_{0\uparrow}^\dagger f_{0\downarrow}^\dagger e_\uparrow^\dagger e_\downarrow^\dagger |\text{vac}\rangle, \quad (4.44)$$

with $|\text{vac}\rangle$ being the vacuum state.

This convention, together with the commutation relations of the operators determines the fermionic signs of the states. We thereby call the sign that arises due to the spin order of a certain site the “intra-site” fermionic sign and the sign that arises due to the order of different sites the “inter-site” fermionic sign. Since the intra-site fermionic sign is determined solely by the operators that act on this single site and because the creation and annihilation operators are *always* either given in the local basis directly or are transformed from the local basis to another basis via the MPS contraction, it is possible to incorporate the intra-site fermionic sign into the definitions of the operators $f_{n\sigma}$ in the local basis:

$$f_{n\uparrow,loc} = \begin{pmatrix} |0\rangle & |\uparrow\rangle & |\downarrow\rangle & |\uparrow\downarrow\rangle \\ 0 & 1 & 0 & 0 \\ 0 & 0 & 0 & 0 \\ 0 & 0 & 0 & 1 \\ 0 & 0 & 0 & 0 \end{pmatrix}, \quad f_{n\downarrow,loc} = \begin{pmatrix} |0\rangle & |\uparrow\rangle & |\downarrow\rangle & |\uparrow\downarrow\rangle \\ 0 & 0 & 1 & 0 \\ 0 & 0 & 0 & -1 \\ 0 & 0 & 0 & 0 \\ 0 & 0 & 0 & 0 \end{pmatrix}. \quad (4.45)$$

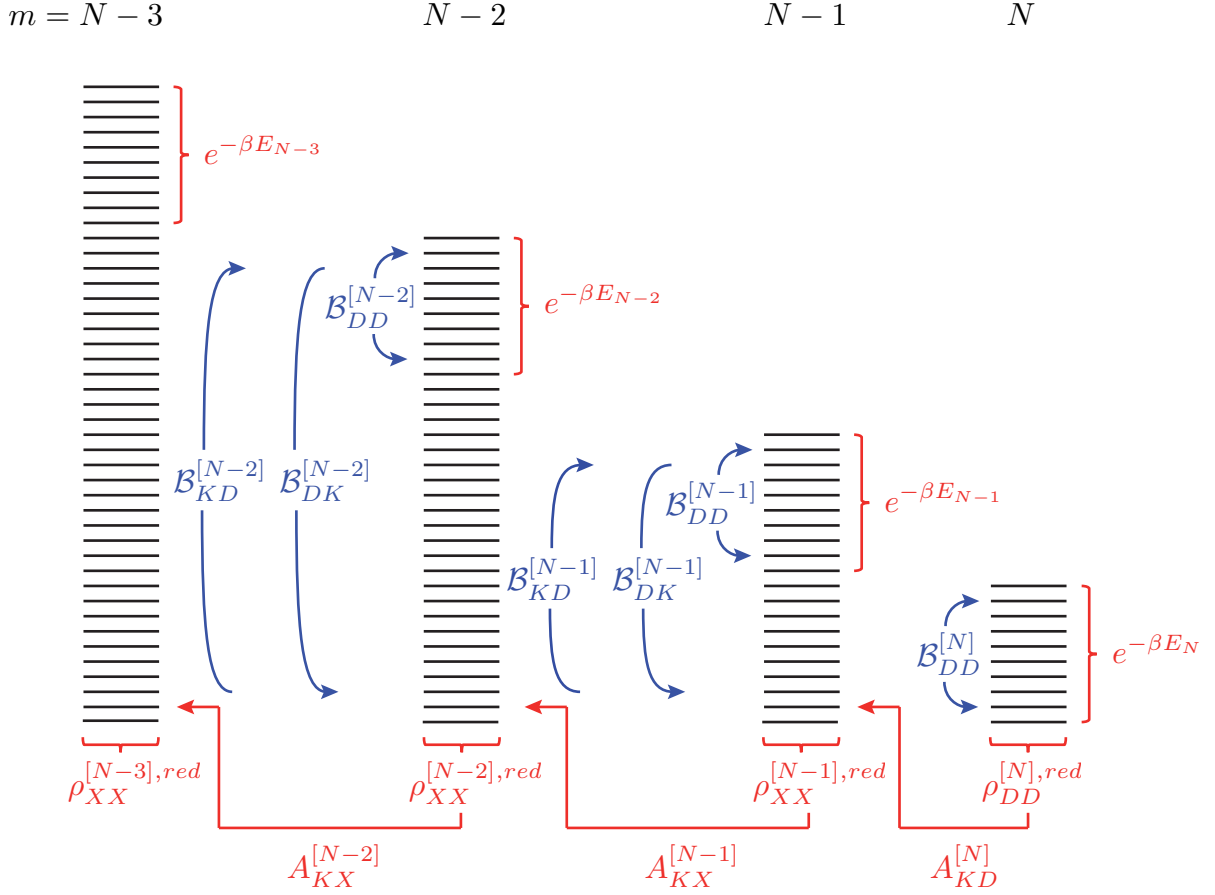


Figure 4.4.: Beginning of the backward run to calculate the reduced density matrices (red) and end of the following forward run for calculating the spectral function as described by Eq. (4.43) (blue). At the iteration of the backward run which corresponds to shell m , the reduced density matrix $\rho_{XX}^{[m],red}$ is calculated from the Boltzmann weights of shell m and from the reduced density matrix of shell $m+1$ by back transforming the latter with $A_{KK}^{[m+1]}$ and $A_{KD}^{[m+1]}$, respectively. The three contributions of the spectral function which are calculated at iteration m of the forward run correspond to different XX' in the summation of Eq. (4.43) and are denoted by $\mathcal{B}_{DK}^{[m]}$, $\mathcal{B}_{KD}^{[m]}$ and $\mathcal{B}_{DD}^{[m]}$ ($\mathcal{C}_{X'X}^{[m]}$ is calculated analogously and is therefore not indicated here for better readability). The origin of the blue arrows indicates whether the reduced density matrix corresponds to the kept or to the discarded states of iteration m . Since the summation over XX' does not include KK , there is no $\mathcal{B}_{KK}^{[m]}$ indicated here. The part of the spectral function that would correspond to $\mathcal{B}_{KK}^{[m]}$ is already taken into account by the entirety of $\mathcal{B}_{DK}^{[m']}$, $\mathcal{B}_{KD}^{[m']}$ and $\mathcal{B}_{DD}^{[m']}$ with $m' \geq m + 1, \dots, N$.

With these definitions the intra-site fermionic sign has been fully taken care of and does not need to be regarded anymore.

During the NRG diagonalization the inter-site fermionic sign comes in through the four tunneling terms at Eq. (4.12) which occur when a new site is added at the iteration procedure: $f_{n+1\sigma}^\dagger f_{n\sigma}$ and $f_{n\sigma}^\dagger f_{n+1\sigma}$, each for both spin directions σ , respectively. By looking at the tunneling terms and at Eq. (4.44), we see that due to the commutation relations of the $f_{n\sigma}^{(\dagger)}$ -operators, the state acquires an additional minus sign for each electron that occupies site $n + 1$, when acting on the state with $f_{n\sigma}^{(\dagger)}$. The inter-site fermionic sign can therefore be taken care of by replacing $f_{n+1\sigma} \rightarrow Z f_{n+1\sigma}$, so that the hopping terms become $(Z f_{n+1\sigma})^\dagger f_{n\sigma}$ and $f_{n\sigma}^\dagger (Z f_{n+1\sigma})$, where the operator $Z = (-1)^{n_{n+1}}$ determines the sign due to the occupation n_{n+1} of site $n + 1$.

4.3.2. Fermionic signs for spectral functions

When calculating spectral functions, the situation with fermionic signs is different. The operator e_σ^\dagger which acts on a state like in Eq. (4.16), does not act on the end, but on the beginning of the chain, i. e. the impurity. To respect the fermionic order in Eq. (4.44), the operator therefore is not only moved past the electrons of the last site, but past the electrons of *every* chain site (apart from the impurity). However, it is not necessary to evaluate the occupation for every site of the chain, but it is rather sufficient to determine the occupancy of the impurity instead, as will be shown in the following.

Let $|s\rangle$ and $|\tilde{s}\rangle$ be two eigentstates of the chain, $\{|d\rangle\}$ a basis of the impurity state space and $\{|r\rangle\}$ a basis of the chain without the impurity. The state $|s\rangle$ can therefore be written as:

$$|s\rangle = \sum_{rd} s_{rd} |r\rangle |d\rangle. \quad (4.46)$$

When calculating spectral functions, one calculates matrix elements of the following type:

$$\langle s | e_\sigma | \tilde{s} \rangle \langle \tilde{s} | e_\sigma^\dagger | s \rangle = \sum_{rr'\tilde{r}\tilde{r}' dd'\tilde{d}\tilde{d}'} s_{r'd'}^* s_{\tilde{r}'\tilde{d}} s_{\tilde{r}\tilde{d}'}^* s_{rd} \langle d' | \langle r' | e_\sigma | \tilde{r}' \rangle | \tilde{d}' \rangle \langle \tilde{d} | \langle \tilde{r} | e_\sigma^\dagger | r \rangle | d \rangle. \quad (4.47)$$

When the operator e_σ^\dagger acts on the state $|r\rangle |d\rangle$ (similar when e_σ acts on $\langle d' | \langle r' |$ from the right), one obtains a minus sign for each electron of $|r\rangle$. Therefore, the operator e_σ^\dagger can be replaced by an operator $e_{\sigma,\text{loc}}^\dagger$ which is given in the local basis of the impurity, together with an operator $(-1)^{n_r} = (-1)^{n_s - n_d} = (-1)^{n_s + n_d}$, which determines the sign due to the electrons of $|r\rangle$, with n_s , n_d and n_r the number operators of the full chain, the impurity and the chain without the impurity, respectively. The last equality is true, because it only matters whether the exponent is even or odd, and this in turn depends only on the occupancy of the impurity n_d but not on whether n_d is added or subtracted to n_s . One

obtains

$$\begin{aligned} \langle s|e_\sigma|\tilde{s}\rangle\langle\tilde{s}|e_\sigma^\dagger|s\rangle = \\ \sum_{rr'\tilde{r}\tilde{r}'dd'\tilde{d}'} s_{r'd'}^* s_{\tilde{r}'\tilde{d}'} s_{\tilde{r}\tilde{d}}^* s_{rd} \langle d'|\langle r'|(-1)^{n_s}(-1)^{n_d}e_{\sigma,\text{loc}}|\tilde{r}'\rangle|\tilde{d}'\rangle\langle\tilde{d}|\langle\tilde{r}|e_{\sigma,\text{loc}}^\dagger(-1)^{n_s}(-1)^{n_d}|r\rangle|d\rangle. \end{aligned} \quad (4.48)$$

Because $|s\rangle$ is an eigenstate of n_s , the occurrences of the term $(-1)^{n_s}$ can be factorized out and cancel, so that and $Z_{\text{imp}}^\dagger \equiv Z_{\text{imp}} \equiv (-1)^{n_d}$ remains:

$$\langle s|e_\sigma|\tilde{s}\rangle\langle\tilde{s}|e_\sigma^\dagger|s\rangle = \langle s|Z_{\text{imp}}e_{\sigma,\text{loc}}|\tilde{s}\rangle\langle\tilde{s}|(Z_{\text{imp}}e_{\sigma,\text{loc}})^\dagger|s\rangle. \quad (4.49)$$

For other operators than e_σ^\dagger or for composite operators which act on several sites, the considerations above can easily be generalized.

4.4. Abelian symmetries and the NRG

In all fields of physics, calculations can be simplified by making use of the symmetries of the system under consideration. The following two sections will give an overview of how abelian and non-abelian symmetries are exploited within NRG calculations.

For each abelian symmetry of the Hamiltonian, there exists a corresponding physical quantity which is conserved, and for each eigenstate the conserved quantity has a well defined value that can be assigned to the state in form of a quantum number. Since the Hamiltonian only connects states with equal quantum numbers, it can be made block-diagonal where each block is associated with a certain quantum number. Operators that do not conserve quantum numbers can also be divided into symmetry blocks, since all operators that occur in practice have clearly defined selection rules which describe how the quantum number changes at a transition. The difference to quantum number preserving operators like the Hamiltonian, is that the blocks are not on the diagonal.

For numerical calculations one makes use of the fact, that apart from the blocks which describe allowed transitions, all other parts of the matrix are zero and one thus deals with sparse matrices. Hence, it is sufficient to reduce numerical operations to the non-zero parts of the tensor, and therefore there is not a single index running over all states, but instead there is the quantum number Q which identifies the different non-zero blocks, and an index n , which specifies a state within a block. A matrix product state, as from Eq. (4.23), is therefore written as:

$$|\tilde{Q}\tilde{n}\rangle = \sum_{Qn} \sum_{ql} (A_{Q\tilde{Q}}^{[q]})_{n\tilde{n}}^{[l]} |Qn\rangle |ql\rangle, \quad (4.50)$$

where Q, n and q, l are the quantum numbers and state indices of the states that are combined to the state with quantum number \tilde{Q} and index \tilde{n} . For better clarity we omitted the indices which refer to iteration and to the kept or discarded part of the state space, which will also be the case in Sec. 4.5.

Although there is some small numerical overhead due to the bookkeeping of the non-zero blocks, the use of abelian symmetries results in a great computational speed-up, since computations with several smaller matrices require much less numerical resources than computations with a single large one.

4.5. Non-abelian symmetries and the NRG

This section briefly describes the main aspects of how non-abelian symmetries enter the NRG. For a detailed introduction to the usage of non-abelian symmetries, see Ref. [85]. The non-abelian symmetry used most often in calculations is the SU(2) symmetry. This symmetry is well known from the quantum theory of angular momentum and it has been used in NRG calculations from the very beginning [7, 86]. The implementation of other symmetries, however, is more involved, with the SU(3) symmetry, for example, being treated only recently [87, 88]. Note that the subsections about symmetries at the NRG concern the symmetries of the model. However, in the context of symmetries and the Kondo effect, it is important to distinguish between the *symmetry of the Kondo effect* and the *symmetry of the model*. A generalization of the Kondo effect which may involve impurity states not only with different spins, but also with different orbitals, can have SU(n) symmetry [89], which means that the low-energy effective Hamiltonian features an exchange coupling that is described by generalized SU(n) spin matrices. But on the other hand, the multi-channel Kondo model from Eq. (2.14), for example, always has an SU(2) (spin-)Kondo effect, while the Hamiltonian has SU(2) particle-hole, SU(2) spin and SU(n) channel symmetry.

Computational effort can be reduced even more at the presence of non-abelian symmetries, even though the relations between the group elements are more complicated than for the abelian case. The reason for this is that every non-abelian symmetry group contains an abelian subgroup and the non-abelian commutation relations do therefore not exist instead, but *in addition* to the abelian commutation relations of this subgroup.

4.5.1. MPS and operators

Matrix product states

When exploiting non-abelian symmetries, first, there are the same benefits as when making use of abelian symmetries: MPS can be split into blocks that can be associated with quantum numbers, and it is sufficient to consider only the non-vanishing blocks of the MPS. In addition, however, the elements of a block are dependent on each other. The states of a block with certain quantum numbers can therefore be gathered to multiplets, where the index n from Eq. (4.50) now labels the multiplets (within a block) and an additional quantum number Q_z labels the states within a multiplet (the quantum numbers Q and Q_z which label blocks and the states within a multiplet, respectively, will also be referred to as q - and z -labels below). The states within a multiplet are then related to each other via the (generalized) Clebsch-Gordan coefficients (CGC) of the respective symmetry.

The CGCs can be factorized out and it is therefore sufficient to store only one number (the reduced matrix element) for each multiplet together with the CGCs necessary to construct the states of the multiplet. A matrix product state, as from Eq. (4.23) can therefore be written as

$$|\tilde{Q}\tilde{n}; \tilde{Q}_z\rangle = \sum_{Qn; Q_z} \sum_{ql; q_z} (A_{Q\tilde{Q}}^{[q]})^{[l]} \cdot C_{Q_z \tilde{Q}_z}^{[q_z]} |Qn; Q_z\rangle |ql; q_z\rangle, \quad (4.51)$$

with $C_{Q_z \tilde{Q}_z}^{[q_z]} \equiv \langle Q\tilde{Q}_z; qq_z | \tilde{Q}\tilde{Q}_z \rangle$ the Clebsch-Gordan coefficients. When comparing Eq. (4.51) to Eq. (4.23), it becomes visible that from a numeric point of view, an abelian symmetry can be treated in exactly the same way as a non-abelian symmetry, yet with multiplet dimension 1.

Operators

In the presence of non-abelian symmetries, one has to distinguish between scalar operators and tensor operators. A tensor operator transforms like a higher order tensor and is therefore related to nontrivial CGC spaces. Tensor operators can be characterized in a similar way as MPS: they have three q -labels and corresponding CGC spaces, which can be factorized out. According to the Wigner-Eckhart theorem [90], the matrix element of a tensor operator is given by:

$$\langle Q'n'; Q'_z | F_{q_z}^q | Qn; Q_z \rangle = \langle Q'n'; Q'_z | (F_{q_z}^q | Qn; Q_z \rangle) = \langle Q'n' || F^q || Qn \rangle \cdot C_{Q_z Q'_z}^{[q_z]}, \quad (4.52)$$

where $C_{Q_z Q'_z}^{[q_z]}$ are again the Clebsch Gordan coefficients and $\langle Q'n' || F^q || Qn \rangle$ are the reduced matrix elements, which do not depend on any z -labels. In practice, the reduced matrix element can be determined by calculating $\langle Q'n'; Q'_z | F_{q_z}^q | Qn; Q_z \rangle$ and the corresponding Clebsch Gordan coefficient for one combination of z -labels.

An example of a tensor operator $F_{q_z}^q$ is the creation operator of an electron with SU(2) spin symmetry. If it acts on $|Qn; Q_z\rangle$, i. e. if an additional electron with spin quantum number $q = 1/2$ is added to the state $|Qn; Q_z\rangle$, the Clebsch-Gordan coefficients determine how the spins with quantum numbers Q , Q_z and q, q_z couple to the new spin with Q' , Q'_z .

A scalar operator, such as the Hamiltonian, on the other hand, transforms like a scalar under symmetry transformations. It has only two indices and the CGC spaces therefore simply are identity matrices.

Multiplicity

When combining two quantum numbers Q and q to a quantum number \tilde{Q} , in the case of the SU(2) symmetry group, for each combination of the q - and z -labels, the corresponding CGC, $C_{Q_z \tilde{Q}_z}^{[q_z]}$, is a single number. For the general case of an arbitrary non-abelian symmetry, however, this is no longer the case, i. e. it is possible to have inner and outer multiplicity. Inner multiplicity means that for a given quantum number q , several states with the same z -label can exist, i. e. for a single q -value there are at least two states with one or more identical z -labels. To treat inner multiplicity in a simple manner, one may introduce an

additional index α_z where $\alpha_z = 1, \dots, m_z^q$ specifies which state within the multiplet one refers to, so that the z -label becomes an extended index: $q_z \rightarrow (q_z, \alpha_z)$. Inner multiplicity therefore leaves the multiplets untouched.

Outer multiplicity means that when combining states with quantum numbers Q and q , the resulting quantum number \tilde{Q} can show up several times, but with different CGC spaces. In contrast to inner multiplicity, outer multiplicity also affects the tensors on the multiplet level. So to treat outer multiplicity in a simple manner, one may introduce an additional index α to label different multiplets with the same q -label: $q \rightarrow (q, \alpha)$. Inner and outer multiplicity are not present for every non-abelian symmetry. For example, they do not occur for $SU(2)$ as mentioned above, however they are present e. g. for $SU(n \geq 3)$.

4.5.2. Operations on MPS

Combining state spaces

When combining the effective state space of a chain with the state space of a new site, as is done repeatedly during the NRG procedure, the new states are given by the product space of the states of the new site and the states of the chain without it. During the following determination of the eigenstates, on the multiplet level the new Hamiltonian is diagonalized, whereas on the CGC-level, the new CGCs are solely determined by the q - and q_z -labels of the states which are combined.

The CGC spaces which emerge when the state-spaces of the chain and the new site are combined, can be determined deterministically by repeatedly applying lowering operators on a seed state, which usually is the state with the highest q_z within a multiplet. For a detailed description of the calculation procedure of the CGCs, see [85], Appendix B. A closed analytic formula for the CGCs is only known for special symmetries, e. g. the $SU(2)$ symmetry, and a formula for $SU(n)$ for arbitrary $n > 2$ does not exist. In the case of inner and outer multiplicity, special care has to be taken that the CGCs are treated consistently.

During the NRG algorithm, the truncation which follows the diagonalization happens only on the multiplet level, since truncation within the degenerate CGC space would introduce an artificial symmetry breaking.

Contractions

When using non-abelian symmetries, a contraction of two tensors involves a contraction both on the multiplet and on the CGC level. The CGC spaces are thereby contracted in exactly the same way as the tensors on the multiplet level. If one of the two tensors to be contracted is a scalar operator, performing only the contraction on the multiplet level is sufficient, since the CGC spaces of a scalar operator are identities and will therefore leave the CGC spaces of the other tensor unaffected.

Part II.

Results

5. Optics for impurity models

5.1. Quantum quench of Kondo correlations in optical absorption

The observation of Kondo correlations has been predicted in the context of optical experiments with self-assembled, tunable QDs [91, 92, 93, 64]. In this section the absorption spectra of self-assembled QDs are examined both numerically and experimentally. We first use the gate voltage dependence of the spectra's threshold frequency to determine the values of the model-parameters and then compare the lineshapes calculated with these values to the experimental spectra. We compare the absorption spectra for different gate voltages and also for finite magnetic field and observe very good agreement between experiment and theory. Although the temperature is not sufficiently far below the Kondo temperature to clearly observe the power-law behavior described in section 3.3, the results show that Kondo correlations are present and are observed with optical methods for the first time. Compared to section 3.3, here, the initial state shows Kondo correlations instead of the final state, however, the absorption spectrum can in both cases be calculated according to Eq. (3.5) and we checked that the line shapes for both cases are similar.

LETTER

doi:10.1038/nature10204

Quantum quench of Kondo correlations in optical absorption

C. Latta¹, F. Haupt¹, M. Hanl², A. Weichselbaum², M. Claassen¹, W. Wuester¹, P. Fallahi¹, S. Faelt¹, L. Glazman³, J. von Delft², H. E. Türeci^{1,4} & A. Imamoglu¹

The interaction between a single confined spin and the spins of an electron reservoir leads to one of the most remarkable phenomena of many-body physics—the Kondo effect^{1,2}. Electronic transport measurements on single artificial atoms, or quantum dots, have made it possible to study the effect in great detail^{3–5}. Here we report optical measurements on a single semiconductor quantum dot tunnel-coupled to a degenerate electron gas which show that absorption of a single photon leads to an abrupt change in the system Hamiltonian and a quantum quench of Kondo correlations. By inferring the characteristic power-law exponents from the experimental absorption line shapes, we find a unique signature of the quench in the form of an Anderson orthogonality catastrophe^{6,7}, induced by a vanishing overlap between the initial and final many-body wavefunctions. We show that the power-law exponent that determines the degree of orthogonality can be tuned using an external magnetic field⁸, which unequivocally demonstrates that the observed absorption line shape originates from Kondo correlations. Our experiments demonstrate that optical measurements on single artificial atoms offer new perspectives on many-body phenomena previously studied using transport spectroscopy only.

Optical spectroscopy of single quantum dots has demonstrated its potential for applications in quantum information processing, particularly in the realization of single- and entangled-photon sources^{9,10}, coherent spin qubits^{11,12} and a spin-photon interface^{13,14}. Although recent experiments have established this system as a new model for solid-state quantum optics, all of the striking experimental observations made so far can be understood within the framework of single- or few-particle physics enriched by perturbative coupling to reservoirs involving phonons, a degenerate electron gas^{15–17} or nuclear spins^{18,19}.

We present differential transmission experiments²⁰ on single, charge-tunable quantum dots that reveal optical signatures of the Kondo effect. By contrast with prior experiments^{17,21}, the tunnel coupling between the quantum dot and a nearby degenerate electron gas, which we refer to as the fermionic reservoir, is engineered to be so strong that the resulting exchange interactions cannot be treated using a perturbative system–reservoir theory: in the initial state, the ‘system’—quantum dot spin—is maximally entangled with the fermionic reservoir, forming a singlet. Various settings have been proposed for finding optical signatures of Kondo physics^{8,22–25}; our work is most closely related to the theoretical investigation of refs 8, 25.

The feature that differentiates our results from all prior transport-based investigations of the Kondo effect^{3–5} is the realization of a quantum quench of the local Hamiltonian; in our experiments, photon absorption abruptly turns off the exchange interaction between the quantum dot electron and the fermionic reservoir, leading to the destruction of the correlated dot–reservoir singlet that otherwise acts as a local scattering potential for all reservoir electrons. The overlap between *N*-electron fermionic reservoir states with and without a local scattering potential scales as $N^{-\alpha}$, with $\alpha > 0$ (refs 6, 7). This reduced overlap, called an Anderson orthogonality catastrophe (AOC), leads to

a power-law tail in absorption if the scattering potential is turned on or off by photon absorption. Here we determine the AOC-induced power-law exponents in the absorption line shape that uniquely characterize the quench of Kondo correlations. Moreover, by tuning the applied laser frequency, we observe both the perturbative and the non-perturbative regimes of the Kondo effect in one absorption line shape, without having to change the fermionic reservoir (electron) temperature, T_{FR} . The AOC after a Kondo quench can, in principle, also be probed by core-level X-ray absorption spectroscopy of suitable bulk materials²⁶, but optical studies of quantum dots offer higher resolution and a tunable local Hamiltonian.

The quantum dot sample we study is shown schematically in Fig. 1a: a gate voltage, V_g , applied between a top Schottky gate and the degenerate electron gas, allows us to tune the charging state of the quantum dot²⁷. Figure 1b shows the photoluminescence spectrum of a particular quantum dot (dot 1), as a function of V_g , where different discrete ‘charging plateaux’ are clearly observable. The dependence of the photoluminescence energy on the quantum dot charging state originates from a Coulomb renormalization of the optical transition energy. In addition to photoluminescence lines (for example X^0) associated with a fixed charging state (for example neutral) of the quantum dot, we also observe spatially indirect transitions with a strong dependence on V_g (refs 8, 17; see Fig. 1b, red arrow).

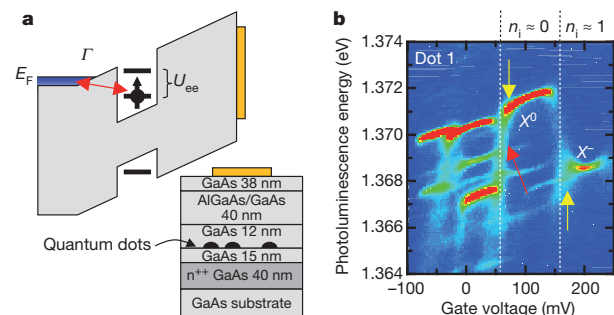


Figure 1 | Single quantum dot strongly coupled to a fermionic reservoir.

a, Band structure of the device. The quantum dots are separated by a 15-nm tunnel barrier from an n^{++} -doped GaAs layer (fermionic reservoir). A voltage, V_g , applied between the electron gas and a semi-transparent NiCr gate on the sample surface controls the relative value of the quantum dot single-particle energy levels with respect to the Fermi energy, E_F . **b**, Low-temperature (4 K) photoluminescence spectrum of a single quantum dot (dot 1) as a function of V_g ; n_i denotes the initial state electron occupancy of the quantum dot. The interaction of the quantum dot electron with the Fermi sea leads to a broadening of the photoluminescence lines at the plateau edges (yellow arrows) and indirect recombinations of a quantum dot hole and a Fermi sea electron (red arrow). Indirect transitions are identified by the stronger V_g dependence of the transition energy, compared with that for direct transitions. A detailed discussion of the origin of various photoluminescence lines can be found in ref. 17.

¹Institute of Quantum Electronics, ETH-Zürich, CH-8093 Zürich, Switzerland. ²Arnold Sommerfeld Center for Theoretical Physics, Ludwig-Maximilians-Universität München, D-80333 München, Germany. ³Sloane Physics Laboratory, Yale University, New Haven, Connecticut 06520, USA. ⁴Department of Electrical Engineering, Princeton University, Princeton, New Jersey 08544, USA.

RESEARCH LETTER

In this Letter, we focus on the X^- plateau, for which the quantum dot carries the charge of a single electron and the influence of the fermionic reservoir on the quantum dot photoluminescence dispersion and linewidth is strongest. The X^- optical transition couples the initial configuration, containing on average one electron in the quantum dot, to a final configuration, containing on average two electrons and a valence-band hole (a negatively charged trion). This transition can be described within the framework of an excitonic Anderson model^{8,25} (EAM), depicted schematically in Fig. 2c (and described explicitly in Supplementary Information). It is parameterized by the energy, ε , of the quantum dot electron level with respect to the Fermi level; the on-site Coulomb repulsion, U_{ee} ; the tunnelling rate, Γ , between quantum dot and fermionic reservoir; the half-bandwidth, D , of the fermionic reservoir; and the electron–hole Coulomb attraction, U_{eh} . The last is relevant only in the final configuration, where it effectively lowers the electron level energy to $\varepsilon - U_{eh}$, thus ensuring the double occupancy of the electron level. An estimate from the photoluminescence data in Fig. 1b yields $U_{eh} \approx U_{ee} + 4$ meV.

The inset of Fig. 2a shows high-resolution laser absorption spectroscopy on dot 1 across the X^- single-electron charging plateau

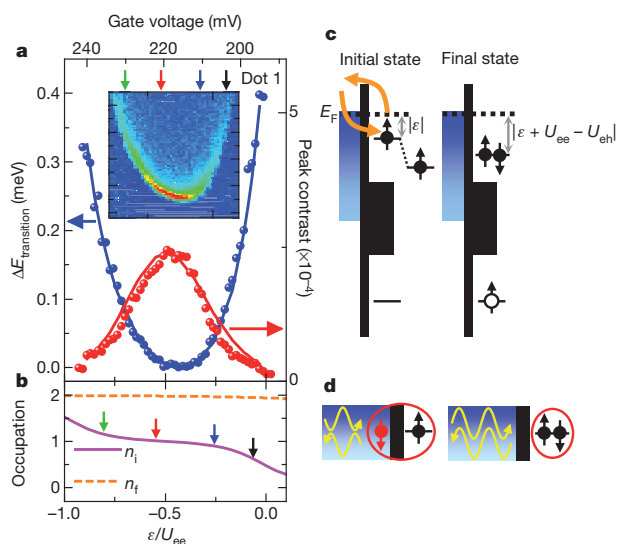


Figure 2 | Gate voltage dependence of the peak absorption strength.

a, Experimental data (symbols) for the ε dependence of the shift in the resonance energy, $\Delta E_{\text{transition}}$ (blue, left axis), and the absorption contrast (red, right axis) are well reproduced by NRG calculations (solid lines) for the following parameters: $U_{ee} = 7.5$ meV, $\Gamma = 0.7$ meV, $D = 3.5$ meV, $U_{eh} = 11$ meV, $T_{\text{FR}} = 180$ mK. Inset, absorption on the negatively charged exciton X^- transition of dot 1 as a function of the gate voltage, measured at $T_{\text{FR}} = 180$ mK. **b**, NRG results for the respective occupancies, n_i and n_f , of the quantum dot electron level in the initial and final ground states. **c**, Energy renormalization process: the initial configuration (left) features a single electron in the quantum dot, whose energy is lowered by virtual tunnelling between the dot and the fermionic reservoir. Because virtual excitations with energy ΔE contribute a shift proportional to $-\Gamma/\Delta E$, the total shift (involving a sum over all possible values of ΔE), is strongest near the edges of the X^- plateau. Towards the right-hand edge (ε near zero), the dominant contribution comes from virtual tunnelling of the quantum dot electron into the fermionic reservoir (as depicted); towards the left-hand edge (ε near $-U_{ee}$), it comes from virtual tunnelling of a fermionic reservoir electron into the quantum dot (not depicted). In the final configuration (right), the quantum dot contains two electrons and a hole. The electron–hole Coulomb attraction, U_{eh} , effectively lowers the quantum dot electron level energy to $\varepsilon - U_{eh}$. This raises the energy cost, ΔE , for virtual excitations by $U_{eh} - U_{ee}$ (which is $\gg \Gamma$), such that the final-state energy renormalization is negligible. The renormalization of the transition energy, probed by a weak laser, is thus mainly due to initial-state energy renormalization. **d**, Anderson orthogonality: the Kondo cloud (left-hand diagram) and local singlet (right-hand diagram) of the initial and final configurations produce strong or weak scattering phase shifts, respectively.

(Supplementary Information). Here we parameterize V_g in terms of ε , normalized and shifted such that $\varepsilon = -U_{ee}/2$ for the gate voltage at which the absorption contrast is maximal. Instead of the usual linear d.c. Stark shift of the absorption peak that is characteristic of charge-tunable quantum dots, we find a strongly nonlinear, ε -dependent shift of the X^- transition energy^{15,17}, which measures the energy difference between the final and initial ground states. As shown in Fig. 2c, this energy shift arises from a renormalization of the initial state energy²⁸ due to virtual tunnelling between the singly occupied quantum dot and the fermionic reservoir (analogous to the Lamb shift of atomic ground states). The final trion state energy, on the other hand, is hardly affected by virtual tunnelling processes, owing to $U_{eh} - U_{ee}$ being large. This renormalization-induced redshift of the initial state is strongest at the plateau edges and leads to an ε -dependent blueshift of the optical resonance frequency. The latter can be used to determine the EAM parameters for dot 1: $U_{ee} = 7.5$ meV, $\Gamma = 0.7$ meV and $D = 3.5$ meV. Numerical renormalization-group (NRG) calculations for the transition energy (Fig. 2a, blue line) give excellent agreement with the experimental data (blue symbols).

We now consider the detailed form of the absorption line shape, $A(\nu)$, as function of the detuning, ν , between the applied laser frequency and the transition threshold. Figure 3a shows, on a log–log scale, the blue ($\nu > 0$) tail of $A(\nu)$ for dot 1, for the four values of gate voltage indicated by arrows in the inset of Fig. 2a. The inset of Fig. 3a compares the full, un-normalized absorption line shapes for the same gate voltages on a linear scale; the red ($\nu < 0$) absorption tail allows us to determine the temperature of the fermionic reservoir to be

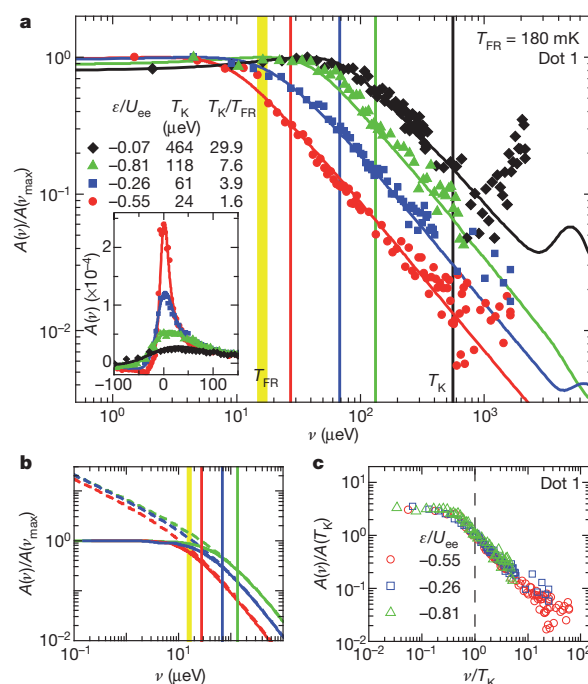


Figure 3 | The absorption line shape $A(\nu)$. **a**, Blue tail of $A(\nu)/A(\nu_{\text{max}})$ for dot 1, plotted versus the laser detuning, ν , on a log–log scale. Here ν_{max} is the threshold frequency for which the absorption strength is maximal. The experimental data were measured at an electron temperature of $T_{\text{FR}} = 180$ mK for the four values of gate voltage, ε , indicated by arrows in Fig. 2a; the corresponding Kondo temperatures, $T_K(\varepsilon)$, are indicated by vertical lines in matching colours. The yellow line indicates T_{FR} . NRG results (solid lines), obtained using the parameters from the fit in Fig. 2a, are in remarkable agreement with experiment. Inset, the measured full (un-normalized) absorption line shape for the same ε values, plotted on a linear scale. **b**, NRG results for $T = T_{\text{FR}}$ (solid lines) and $T_{\text{FR}} = 0$ (dashed lines); the latter show the $\nu^{-0.5}$ behaviour expected in the strong-coupling regime, $T_{\text{FR}} \ll \nu \ll T_K$. **c**, The rescaled line shape, $A(\nu)/A(T_K)$, versus ν/T_K shows a universal scaling collapse characteristic of Kondo physics.

$T_{\text{FR}} = 180$ mK, equivalent to $15.6 \mu\text{eV}$ (Supplementary Information). The strong variation of the peak absorption strength and width shown in the inset of Fig. 3a is a consequence of the exponential dependence of the Kondo temperature on the gate voltage ε :

$$T_{\text{K}}(\varepsilon) = \sqrt{TD} \exp \left[- \left(1 - \left(\frac{2\varepsilon}{U_{\text{ce}}} + 1 \right)^2 \right) \frac{\pi U_{\text{ce}}}{8\Gamma} \right] \quad (1)$$

For dot 1, T_{K} varies between 24 and $118 \mu\text{eV}$; we emphasize that even though $T_{\text{K}} = 464 \mu\text{eV}$ for the black curve (Fig. 3a, inset), the dot–reservoir system is no longer in the local moment regime for this gate voltage. All line shapes carry the signatures of an optical interference effect induced by the sample structure (causing some line shapes to become negative for small red detunings), and of independently measured fluctuations in gate voltage; both effects have been taken into account in the calculated line shapes (Supplementary Information). Calculating the line shapes using NRG (solid lines) without any further fit parameters, we find remarkable agreement with experiment for all four line shapes shown in Fig. 3a, demonstrating the validity of the EAM⁸ for the coupled dot–reservoir system.

For blue detunings satisfying $\nu > \max(T_{\text{FR}}, T_{\text{K}})$, a perturbative description for $A(\nu)$ is possible. The frequency scale for which the perturbative $\sim \nu^{-1}$ dependence in Fig. 3a sets in and the peak absorption contrast itself both strongly depend on gate voltage. Remarkably, for gate voltages such that the initial ground state is a Kondo singlet, this dependence is such that it permits a scaling collapse: Fig. 3c shows the normalized absorption line shape, $A(\nu)/A(T_{\text{K}}(\varepsilon))$, as a function of ν/T_{K} for the red, green and blue curves of Fig. 3a (but omitting the black curve, which is in the mixed valence regime). We find that all three curves collapse to a universal scaling function of ν/T_{K} , as expected⁸ for the regime $T_{\text{FR}} \ll \nu \ll U_{\text{ce}}$. Thus, the ε dependence of the crossover scale is captured by equation (1) for T_{K} ; this observation is unequivocal proof that the Kondo effect is indeed present in our system.

In the limit $T_{\text{FR}} < \nu < T_{\text{K}}$, a perturbative description of the line shape is no longer valid. In the initial configuration, the exchange interaction between the quantum dot and the fermionic reservoir induces a ‘Kondo screening cloud’ that forms a singlet with the quantum dot spin. This acts as a scattering potential that induces strong phase shifts for those low-energy fermionic excitations whose energies differ from the Fermi level by T_{K} or less. In the final configuration after photon absorption, the quantum dot has two electrons in a local singlet state. Therefore, the Kondo screening cloud, and the scattering potential that it constitutes for reservoir electrons, disappears in the long-time limit: the corresponding ground-state wavefunction is a tensor product of the local singlet and free electronic states, with only weak phase shifts. Because the initial and final fermionic reservoir phase shifts differ (as depicted schematically in Fig. 2d), the fermionic reservoir does not remain a spectator during the X^- transition; instead, the transition matrix element between the ground states of the initial and final configurations is vanishingly small. This leads to an AOC that manifests itself by transforming a delta-function resonance (of an uncoupled quantum dot) into a power-law singularity⁶ of the form $\nu^{-\eta}$, where the exponent η characterizes the extent of the AOC. For $T_{\text{FR}} \ll \nu \ll T_{\text{K}}$, the absorption line shape of the X^- transition is expected to show an analogous power-law singularity. The exponent η is predicted^{8,25} to range between 0 and 0.5 (assuming no magnetic field), with $\eta \approx 0.5$ being characteristic for a Kondo-correlated initial state and an uncorrelated final state. This line shape modification is a consequence of a redistribution of the optical oscillator strength, associated with the fact that the fermionic reservoir wavefunction in the Kondo-correlated initial state has finite overlap with a range of final states consisting of electron–hole pair excitations out of a non-interacting fermionic reservoir.

If $T_{\text{FR}} \ll T_{\text{K}}$ and the optical detuning is reduced below T_{K} , the line shape is predicted to cross over smoothly from the perturbative $1/\nu$ tail to the strong-coupling $1/\nu^{0.5}$ power law just discussed. This crossover is illustrated in Fig. 3b (dashed lines) by NRG calculations, performed at $T_{\text{FR}} = 0$ for the three ε values of Fig. 3c: Remarkably, despite drastic

differences in the $\nu > T_{\text{K}}$ tails due to different values of $T_{\text{K}}(\varepsilon)$, all three line shapes show similar power-law exponents, of around $\eta \approx 0.5$, for $\nu \ll T_{\text{K}}$. For non-zero temperature, however, the $1/\nu^{0.5}$ power law is cut off and saturates once ν decreases past T_{FR} (Fig. 3b, solid lines), because of thermal averaging over initial states with excitation energies $\leq T_{\text{FR}}$.

A direct extraction of the $1/\nu^{0.5}$ power law from the measured data is difficult owing to the small accessible experimental window, $T_{\text{FR}} < \nu < T_{\text{K}}$. Nevertheless, we are able to determine the power-law exponent accurately for a more strongly coupled quantum dot (dot 2) by using the fact that the detailed form of the line shape sensitively depends on the exponent η , which can be tuned using an external magnetic field⁸. This tunability arises because the magnetic field, B_{ext} , changes the initial dot occupancies, favouring spin up over spin down, and hence affects the overlap between the initial and final states of the transition (Supplementary Information). Figure 4a shows the $B_{\text{ext}} = 0$ absorption line shape for dot 2 with parameters $U_{\text{ce}} = 7.5$ meV, $\Gamma = 1$ meV, $D = 6.5$ meV and $U_{\text{ch}} = (3/2)U_{\text{ce}}$, measured at $\varepsilon/U_{\text{ce}} = -0.43$ (where $T_{\text{K}} = 140 \mu\text{eV}$) and $T_{\text{FR}} = 15.6 \mu\text{eV}$. An attempt to obtain a fit to the experimental absorption line shape using a perturbative formula⁸

$$A(\nu) \propto \frac{\nu/T_{\text{FR}}}{1 - e^{-\nu/T_{\text{FR}}}} \frac{\gamma}{\nu^2 + \gamma^2/4}$$

where $\gamma \leq T_{\text{FR}}$ denotes a phenomenological relaxation rate, fails markedly for dot 2 (Fig. 4a, red curve). By striking contrast, Fig. 4b shows that an excellent fit is obtained for a weakly coupled dot (dot 3; Supplementary Information).

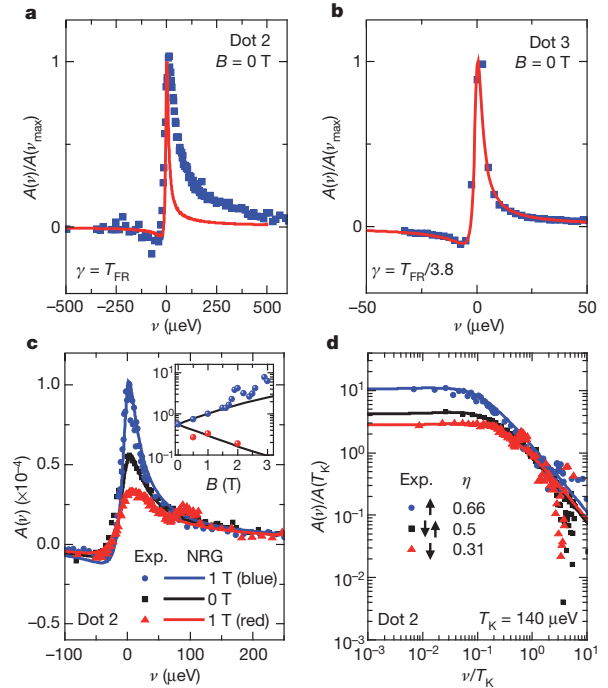


Figure 4 | Magnetic field dependence of the absorption. **a**, The absorption line shape of dot 2 for $B = 0$ (symbols) cannot be fit by the perturbative formula (red line) given in the text. **b**, By contrast, for dot 3 such a fit works well. **c**, Absorption line shapes for dot 2, at $B_{\text{ext}} = 0$ and 1 T, for the blue–red trion transition. The magnetic field changes the strength of the AOC and the line shape. The small peak that appears at $\nu \approx 80 \mu\text{eV}$ in the red trion absorption is due to incomplete suppression of the laser polarization that couples to the blue trion transition. Inset, the peak absorption contrast shows good agreement with the NRG calculations for $B_{\text{ext}} \leq 1.5$ T. **d**, Normalized absorption line shape for dot 2 in a log–log plot. These measurements pin the value of $\eta(B_{\text{ext}} = 0)$ to ~ 0.5 , which is a direct signature of a Kondo singlet in the absorption line shape. In addition, they demonstrate the tunability of an orthogonality exponent.

RESEARCH LETTER

Figure 4c shows the magnetic field dependence of the line shape of dot 2, measured in Faraday geometry, where quantum dot optical selection rules¹³ ensure that by choosing right- or left-handed circular polarization of the laser field, it is possible to probe selectively the blue or, respectively, red trion transition that couples exclusively to the spin-up or, respectively, spin-down initial state. In comparison with the $B_{\text{ext}} = 0$ (Fig. 4c, black squares) results, the absorption line shapes for the blue (Fig. 4c; blue dots) and red (Fig. 4c; red triangles) trion transitions at $B_{\text{ext}} = 1$ T exhibit two striking features: the peak contrast increases (blue) or decreases (red) by a factor of ~ 2 , and the area under the absorption curve increases (blue) or decreases (red) by less than 20%. These observations indicate that the change in the $B_{\text{ext}} \leq 1.5$ T line shapes is predominantly due to a line narrowing associated with an increase in the AOC power-law exponent, η , of the blue trion transition and a line broadening associated with a decrease in η for the red trion transition. To quantify the field-induced change in η , we plot in Fig. 4d the corresponding normalized line shapes, $A(\nu)/A(T_{\text{K}})$, as functions of ν/T_{K} in a log-log plot, together with the corresponding NRG results (solid lines): the latter yield $\eta = 0.5$ at $B_{\text{ext}} = 0$ and $\eta = 0.31$ (red trion) and $\eta = 0.66$ (blue trion) at $B_{\text{ext}} = 1$ T, proving the remarkable sensitivity of the measured line shapes to the AOC-determined power-law exponents. By contrast with Fig. 3c, the line shapes in Fig. 4d do not show a scaling collapse. We emphasize that qualitatively similar features are observed for all field values $B_{\text{ext}} \leq 1.5$ T; for $B_{\text{ext}} > 1.5$ T, the blue trion absorption contrast has oscillations (Fig. 4c, inset), most probably stemming from the modification of the fermionic reservoir density of states at high fields in Faraday geometry.

The area under the (un-normalized) absorption line shape is proportional to the initial occupancy, n_{\uparrow} or n_{\downarrow} , of the spin-up or, respectively, spin-down state. The small ($\leq 20\%$) field-induced change in the measured areas in Fig. 4c implies a small magnetization, $m = (n_{\uparrow} - n_{\downarrow})/2 \approx 0.16$ (Supplementary Information). By contrast, the corresponding magnetization for a free spin would have been $m = 0.40$. This measurement confirms that the static spin susceptibility of the initial configuration is substantially reduced relative to that of a free spin, providing yet another optical signature of the Kondo screening.

The remarkable agreement between our experimental data depicted in Figs 2–4 and the NRG calculations demonstrates Kondo correlations between a quantum dot electron and the electrons in a fermionic reservoir. The optical probe of these correlations unequivocally shows the signatures of Anderson orthogonality physics associated with the quantum quench of Kondo correlations, with field-tunable power-law exponents. Our experiments establish the potential of single, optically active quantum dots in investigating many-body physics. In addition, they pave the way for a new class of quantum optics experiments in which the influence of the simultaneous presence of non-perturbative cavity or laser coupling and Kondo correlations on electric field and photon correlations could be investigated.

METHODS SUMMARY

The InGaAs quantum dots studied in this work were grown by molecular beam epitaxy; the quantum dot layer was separated by a nominally 15-nm-thick GaAs tunnel barrier from a back gate consisting of a 40-nm-thick n^{++} -doped GaAs layer. This back gate serves as an electron reservoir. The distance from the quantum dot layer to the sample surface was 90 nm. A voltage applied between a 5-nm-thick NiCr top gate and the n^{++} GaAs back gate allows for discrete charging of the quantum dots. The sample was placed inside a fibre-based confocal microscope embedded in a dilution refrigerator with a base temperature of 20 mK in the mixing chamber. The objective was mounted on a stack of low-temperature x - y - z positioners. The cryostat was equipped with a 7-T magnet. The absorption experiments were performed by focusing on a single quantum dot a power- and frequency-stabilized, single-mode tunable laser with an intensity of 15 nW. The objective had a numerical aperture of 0.6, yielding a diffraction-limited spot size. The change in transmission through the sample was recorded using a silicon photodiode. To increase the signal-to-noise ratio, a lock-in technique was used whereby the gate voltage was modulated at 187.195 Hz with a modulation amplitude of 50 mV.

The calculations were carried out using the NRG. The continuous energy spectrum of the Fermi reservoir was logarithmically discretized and mapped onto a semi-infinite chain with exponentially decaying hopping amplitudes. In each

iteration, a new site was added to the chain, which corresponds to including ever lower energy scales of the system. By combining NRG data from all iterations, it was possible to construct a complete set of approximate many-body eigenstates of the full Hamiltonian, which could be used to calculate the physical quantities using the full-density-matrix NRG (Supplementary Information).

Received 1 January; accepted 16 May 2011.

- Kondo, J. Resistance minimum in dilute magnetic alloys. *Prog. Theor. Phys.* **32**, 37–49 (1964).
- Kouwenhoven, L. P. & Glazman, L. Revival of the Kondo effect. *Phys. World* **14**, 33–38 (January 2001).
- Goldhaber-Gordon, D. *et al.* Kondo effect in a single-electron transistor. *Nature* **391**, 156–159 (1998).
- Cronenwett, S. M., Oosterkamp, T. H. & Kouwenhoven, L. P. A tunable Kondo effect in quantum dots. *Science* **281**, 540–544 (1998).
- van der Wiel, W. G. *et al.* The Kondo effect in the unitary limit. *Science* **289**, 2105–2108 (2000).
- Mahan, G. *Many-Particle Physics* 612–621 (Kluwer, 2000).
- Anderson, P. W. Infrared catastrophe in Fermi gases with local scattering potentials. *Phys. Rev. Lett.* **18**, 1049–1051 (1967).
- Türeci, H. E. *et al.* Many-body dynamics of exciton creation in a quantum dot by optical absorption: a quantum quench towards Kondo correlations. *Phys. Rev. Lett.* **106**, 107402 (2011).
- Michler, P. *et al.* A quantum dot single-photon turnstile device. *Science* **290**, 2282–2285 (2000).
- Dousse, A. *et al.* Ultrabright source of entangled photon pairs. *Nature* **466**, 217–220 (2010).
- Press, D., Ladd, T. D., Zhang, B. & Yamamoto, Y. Complete quantum control of a single quantum dot spin using ultrafast optical pulses. *Nature* **456**, 218–221 (2008).
- Kim, D. *et al.* Ultrafast optical control of entanglement between two quantum-dot spins. *Nature Phys.* **7**, 223–229 (2011).
- Yilmaz, S. T., Fallahi, P. & Imamoglu, A. Quantum-dot-spin single-photon interface. *Phys. Rev. Lett.* **105**, 033601 (2010).
- Claassen, M., Türeci, H. & Imamoglu, A. Solid-state spin-photon quantum interface without spin-orbit coupling. *Phys. Rev. Lett.* **104**, 177403 (2010).
- Dalgarno, P. A. *et al.* Optically induced hybridization of a quantum dot state with a filled continuum. *Phys. Rev. Lett.* **100**, 176801 (2008).
- Hilario, L. M. L. & Aligia, A. A. Photoluminescence of a quantum dot hybridized with a continuum of extended states. *Phys. Rev. Lett.* **103**, 156802 (2009).
- Kleemann, N. A. J. M. *et al.* Many-body exciton states in self-assembled quantum dots coupled to a Fermi sea. *Nature Phys.* **6**, 534–538 (2010).
- Latta, C. *et al.* Confluence of resonant laser excitation and bidirectional quantum-dot nuclear-spin polarization. *Nature Phys.* **5**, 758–763 (2009).
- Xu, X. *et al.* Optically controlled locking of the nuclear field via coherent dark-state spectroscopy. *Nature* **459**, 1105–1109 (2009).
- Högele, A. *et al.* Voltage-controlled optics of a quantum dot. *Phys. Rev. Lett.* **93**, 217401 (2004).
- Atatüre, M. *et al.* Quantum-dot spin-state preparation with near-unity fidelity. *Science* **312**, 551–553 (2006).
- Shahbazyan, T. V., Perakis, I. E. & Raikh, M. E. Spin correlations in nonlinear optical response: light-induced Kondo effect. *Phys. Rev. Lett.* **84**, 5896–5899 (2000).
- Kikoin, K. & Avishai, Y. Many-particle resonances in excited states of semiconductor quantum dots. *Phys. Rev. B* **62**, 4647–4655 (2000).
- Govorov, A. O., Karrai, K. & Warburton, R. J. Kondo excitons in self-assembled quantum dots. *Phys. Rev. B* **67**, 241307(R) (2003).
- Helmes, R. W., Sindel, M., Borda, L. & von Delft, J. Absorption and emission in quantum dots: Fermi surface effects of Anderson excitons. *Phys. Rev. B* **72**, 125301 (2005).
- Gunnarsson, O. & Schönhammer, K. Electron spectroscopies for Ce compounds in the impurity model. *Phys. Rev. B* **28**, 4315–4341 (1983).
- Warburton, R. J. *et al.* Optical emission from a charge-tunable quantum ring. *Nature* **405**, 926–929 (2000).
- Anderson, P. W. Localized magnetic states in metals. *Phys. Rev.* **124**, 41–53 (1961).

Supplementary Information is linked to the online version of the paper at www.nature.com/nature.

Acknowledgements This work was supported by Swiss NSF under grant no. 200021-121757 and an ERC Advanced Investigator Grant (A.I.). J.v.D. acknowledges support from the DFG (SFB631, SFB-TR12, De730/3-2, De730/4-1), the Cluster of Excellence ‘Nanosystems Initiative Munich’. H.E.T. acknowledges support from the Swiss NSF under grant no. PPO0P2-123519/1. L.G. acknowledges support from NSF DMR under grant no. 0906498.

Author Contributions C.L., F.H., W.W. and P.F. carried out the experiments. M.H. and A.W. performed the numerical analysis. The samples were grown by S.F. C.L. and A.I. planned the experiment. H.E.T., M.C., L.G., A.I. and J.v.D. developed the theoretical framework. C.L., J.v.D. and A.I. supervised the project, carried out the analysis of the data and wrote the manuscript.

Author Information Reprints and permissions information is available at www.nature.com/reprints. The authors declare no competing financial interests. Readers are welcome to comment on the online version of this article at www.nature.com/nature. Correspondence and requests for materials should be addressed to C.L. (clatta@phys.ethz.ch) or A.I. (imamoglu@phys.ethz.ch).

SUPPLEMENTARY INFORMATION

doi:10.1038/nature10204

The following supplementary material is divided into ten sections. Each section provides background information related to specific topics of the main text. The sections are not built upon each other and can be read independently. Section S1 provides details on how the electron temperature is obtained. The influence of the optical interference and the gate voltage fluctuations are analyzed in Sections S2 and S3, respectively. In Section S4, we analyze the influence of experimental parameters on the line shape. Theoretical background for the underlying excitonic Anderson model and the numerical renormalization group technique is given in Sections S5 and S6, respectively. In Section S7 we detail how we determine the parameters of the Anderson model. A discussion of the quantum dot optical spectra is presented in Section S8. Section S9 outlines the effect of an applied magnetic field on the line shapes, and, in particular, on the QD magnetization in the initial configuration. Finally, Section S10 shows the limitation of a fully perturbative description of the observed line shapes.

S1 Electron temperature

All experiments were carried out in a dilution refrigerator with a base temperature of 20 mK in the mixing chamber. From fits to experimental data, we find, that the (relevant) electron temperature is around 180 mK. The optical transitions were probed by focussing a weak single-mode (intensity and frequency stabilized) laser on a single quantum dot (QD). We recorded the intensity transmitted through the sample with a silicon photo diode. In order to increase the signal-to-noise ratio, a lock-in technique was used where the gate voltage was modulated[1].

For red detunings, such that $\nu < -T$, the number of electron-hole pairs that could provide the energy necessary for FR-assisted laser absorption scales exponentially with ν due to Fermi statistics: as a consequence, the absorption line shape shows an exponential tail (see Eq. (7) of [2]), whose slope gives us the electron temperature T . For very large red detunings, the dominant line broadening is due to spontaneous emission and we recover the associated Lorentzian tail. To determine T , we actually fit the NRG line shape for red detunings, taking into account optical interference (as described in Section S2 below).

S2 Influence of optical interference on measured line shapes

All the measured line shapes carry the signatures of an optical interference effect induced by the sample structure[1]. The experimental situation is depicted in Fig. S2a. The laser field is incident onto the QD through the top gate, and the light transmitted at the other side of the structure is detected. The response of the QD to the laser field is $E_{\text{QD}} = \chi(\nu)E_{\text{L}}$, where E_{L} is the laser field at the position of the quantum dot, while $\chi(\nu) = \chi'(\nu) + i\chi''(\nu)$ is the

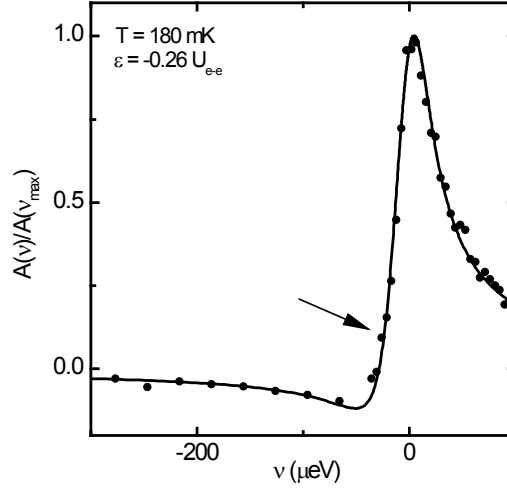


Figure S1: For $\nu < -T$, the red side (arrow) of the absorption resonance has a strong dependence on the temperature T . Dots: experimental data. Line: NRG prediction, obtained via Eq. (S2) as described in Sec. S2, using the temperature T as fit parameter.

susceptibility of the QD with an absorptive part $\chi''(\nu) < 0$ and a dispersive part $\chi'(\nu)$. The total field at the detector position has three components:

$$E_{\text{tot}} = E_L e^{i\pi/2} + E_{\text{QD},f} + E_{\text{QD},b}. \quad (\text{S1a})$$

The first term is the laser field at the detector position, which features a Gouy phase (an additional phase shift occurring in the propagation of focused Gaussian beams) of $\pi/2$ relative to the QD field as it propagates from the QD position to the detector position. $E_{\text{QD},f} = \chi(\nu)E_L$ is the field of photons scattered from the QD into the *forward* direction. $E_{\text{QD},b} = r e^{i\phi} E_{\text{QD},f}$ is the field of photons scattered from the QD into the *backward* direction, which are then reflected from the sample surface (combination of top gate and dielectric interface) and thereby are redirected into the forward direction. Here r is the reflectivity at the sample surface, and the additional phase factor for $E_{\text{QD},b}$ has the form $\phi = \frac{2\pi n}{\lambda} 2L$, where L is the QD-surface distance, n the refractive index of the sample (GaAs) and λ the laser wavelength. E_{tot} can then we

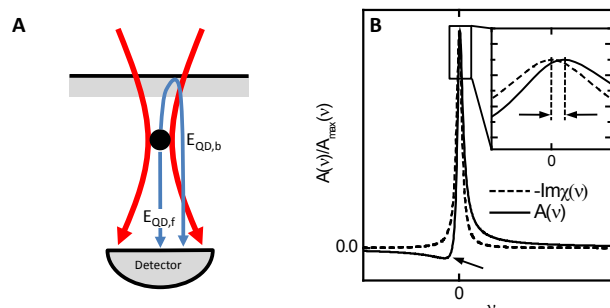


Figure S2: **a**, Schematic of the origin of the interference effect. **b** Effect of the interference on a Lorentzian line shape. NRG results for the $T = 0$ line shapes of Fig. 3b shown with interference effect as in the main text (dashed lines), and without (solid lines).

expressed as

$$E_{\text{tot}} = iE_L [1 - i\chi(\nu)(1 + re^{i\phi})] . \quad (\text{S1b})$$

The transmitted intensity reaching the detector is $\propto |E_{\text{tot}}|^2$. Since the laser intensity is constant in time, it contributes only a (large) offset $I = E_L^2$ to the measured signal. The measured “absorption rate” $A(\nu)$ (experimental data in Figures 3 and 4) is the differential transmission signal relative to this offset, $A(\nu) = \Delta I/I = 1 - |E_{\text{tot}}|^2/E_L^2$. Hence $A(\nu)$ is given by the interference of the field $E_L e^{i\pi/2}$ from the laser photons and the field $E_{\text{QD}}(1 + re^{i\phi})$ from the scattered QD photons:

$$A(\nu) \simeq \text{Re} [i\chi(\nu)(1 + re^{i\phi})] , \quad (\text{S2})$$

where we neglect the vanishingly small contribution from the QD resonance fluorescence. The reflection at the sample surface causes a mixing of the absorptive and the dispersive part of $\chi(\nu)$.

For our sample structure, $L = 90$ nm, $\lambda = 904$ nm and $r = 0.67$ and $n = 3.5$, so that $\phi = 1.4\pi$. If the absorptive part $-\chi''(\nu)$ were purely Lorentzian, the interference effect would modify the line shape in the way depicted in Fig. S2b and S2c: the mixing of the absorptive and

dispersive part of $\chi(\nu)$ leads to a shift of the absorption peak to blue laser detunings and causes the signal to become negative for small red detunings. Moreover, tails that decay faster than $1/\nu$ are changed by the interference effect to decay as $1/\nu$, as discussed in more detail below.

In order to compare the results of numerical calculations with experimental data, we calculated interference-modified versions of the former, by proceeding as follows: state-of-the-art full density matrix (FDM) numerical renormalization group (NRG) techniques for calculating (nonequilibrium) spectral functions $A_{\text{NRG}}(\nu)$ (see section S6 below) give us the absorptive part of the susceptibility, $\chi''_{\text{NRG}}(\nu) \equiv A_{\text{NRG}}(\nu)$. From this we calculate the dispersive part using the Kramers-Kronig relation, $\chi'_{\text{NRG}}(\nu) = -\mathcal{P} \int \frac{d\bar{\nu}}{\pi} \frac{\chi''_{\text{NRG}}(\bar{\nu})}{\nu - \bar{\nu}}$. Inserting $\chi_{\text{NRG}}(\nu) = [\chi'_{\text{NRG}}(\nu) + i\chi''_{\text{NRG}}(\nu)]$ into Eq. (S2) we obtain the interference-corrected prediction for the absorption line shape, $A_{\text{int}}(\nu)$. We note that the numerical absorption line shape plotted in the main text also takes into account the influence of gate voltage fluctuations as discussed in the next section.

In order to clarify the role of optical interference on the power-law exponents associated with the Kondo correlations, we compare the NRG results of Figs. 3b from the main text (dashed lines), which take into account interference, to their counterparts in the absence of optical interference (solid lines). Fig. S3 shows that in the large detuning (perturbative) limit ($\nu \gg T_{\text{K}}$), the faster-than- $1/\nu$ decay expected due to logarithmic corrections is modified by interference towards a slower $1/\nu$ decay. Crucially, however, in the strong-coupling regime ($\nu \lesssim T_{\text{K}}$) the slower-than- $1/\nu$ AOC power law decay (i.e. $\nu^{-1/2}$) is *not* affected by the optical interference.

S3 Gate voltage fluctuations

In contrast to conventional quantum dot samples, even small fluctuations $\delta\varepsilon$ in the effective applied gate voltage ε , originating from voltage fluctuations at the output of the function generator and charge fluctuations in the QD environment, have an impact on the absorption line shapes due

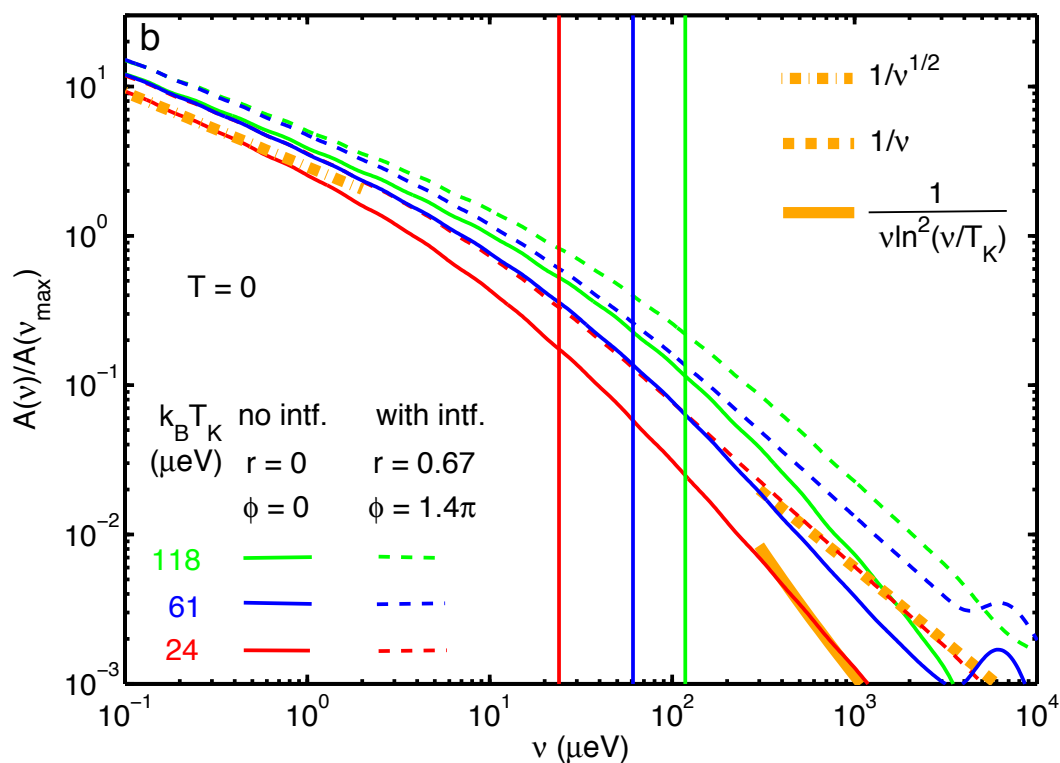


Figure S3: NRG results for the $T = 0$ line shapes of Fig. 3b shown with interference effect as in the main text (dashed lines), and without (solid lines).

to the strong non-linear dependence of the transition energy on the gate voltage. In the plateau center, where a small change $\delta\varepsilon$ in gate voltage corresponds to a negligible change in transition energy, fluctuations do not affect the line shape. However, at the plateau edges, even small fluctuations $\delta\varepsilon$ cause measurable energy shifts of the threshold frequency $\omega_{\text{th}}(\varepsilon)$, and hence of the detuning $\nu = \omega - \omega_{\text{th}}(\varepsilon)$ of the laser (with frequency ω) from the QD resonance. After having determined the temperature from the red tail of the line shape in the plateau center, we find that the line shapes at the plateau edges are modified by gate voltage fluctuations. We take these fluctuations into account phenomenologically by convoluting the interference-corrected

line shape $A_{\text{int}}(\nu)$ with a Gaussian,

$$A_{\text{predicted}}(\nu) = \int dx A_{\text{int}}(\nu + x) p(x, \varepsilon), \quad p(x, \varepsilon) = \frac{e^{-(x/\sigma(\varepsilon))^2/2}}{\sqrt{2\pi}\sigma(\varepsilon)}, \quad (\text{S3})$$

with a gate-voltage dependent width $\sigma(\varepsilon)$. Here $\sigma(\varepsilon) = \langle [\omega_{\text{th}}(\varepsilon + \delta\varepsilon) - \omega_{\text{th}}(\varepsilon)]^2 \rangle^{1/2}$ represents the standard deviation of the fluctuations around the mean threshold frequency $\omega_{\text{th}}(\varepsilon)$, under fluctuations $\delta\varepsilon$ arising from fluctuations in the gate voltage, $\delta\varepsilon \sim \delta V_g$. The fluctuations δV_g are assumed to Gaussian distributed, with a standard deviation of $10\mu\text{V}$. These fluctuations predominantly alter the red tail of the absorption resonance away from the plateau center. We emphasize that our approach accounts only for fluctuations in the threshold frequency; it neglects the changes in the actual line *shape* induced by the fluctuations in ε .) $A_{\text{predicted}}$ is the quantity plotted in the main text when comparing “NRG results for line shape $A(\nu)$ ” to data.

S4 Dependence of the line shape on experimental parameters

We have carried out experiments to confirm that the measured absorption line shapes do not depend on the gate voltage modulation amplitude, the lock-in modulation frequency and the laser intensity. The measurements described below were carried out on “dot 4” which exhibited strong coupling to the FR, similar to dot 1 and dot 2. The modulation frequency $f = 497.197\text{ Hz}$ and the intensity $I = 10\text{ nW}$ used to obtain the absorption line shape for dot 1 and dot 2 were identical.

- **Modulation Amplitude:** For a better signal-to-noise ratio during data acquisition, we use a lock-in amplifier and modulate the gate voltage [1]. Let us assume that a X^- resonance in the absence of modulation would appear at an energy E_{X^-} and a voltage V_{X^-} . In the measurements using a lock-in amplifier with a voltage modulation ΔV which is added to V_{gate} , the very same resonance would appear at the same energy but at two different gate voltages $V_{X^-,1} = V_{X^-} - \Delta V/2$ and $V_{X^-,2} = V_{X^-} + \Delta V/2$. In principle,

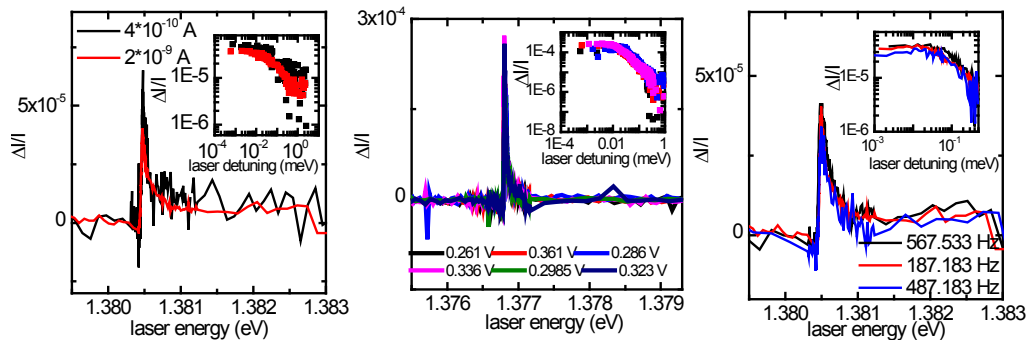


Figure S4: Dependence of the line shape on measurement parameters: Left: intensity dependence of the line shape; the intensity I is depicted in terms of the current it produces in the photodiode; an incident intensity of 10 nW produces a current of 4 nA. Middle: modulation voltage dependence. The gate voltage is modulated with a square-wave between 0.311 V and the values depicted in the figure. Right: lock-in modulation frequency dependence of the absorption line shape.

both signals are identical. However, a large modulation amplitude could be a potential source of degenerate electron gas heating. In order to rule out a change in line shape due to heating or other unknown effects, we measured the dependence of the line shape (proportional to the differential transmission signal $\Delta I/I$) on the modulation amplitude ΔV . Experimentally, we could not find any dependence for $-50\text{mV} \geq \Delta V \geq 50\text{mV}$, as shown in Fig. S4 (middle panel). The measurements were obtained for a center gate voltage of $V_{\text{gate}} = 311\text{mV}$. While the actual gate voltages used for different dots were different, the modulation amplitude for the experiments depicted in Fig. 2-4 of the main text were -50mV .

- Modulation Frequency:** As stated earlier, we used a modulation frequency of $f = 497.197\text{ Hz}$ for the measurements depicted in the main text. When we repeated the measurements for $f = 187.183\text{ Hz}$ and $f = 567.533\text{ Hz}$, we did not observe an appreciable change in the line shape, as is shown in Fig. S4 (right panel).

- **Laser intensity:** Since the experimental measurements are compared to theoretical predictions that assume a perturbative laser field, we made sure that the QD is not saturated for the applied laser intensity (see Fig. S5 below). To demonstrate the insensitivity of the absorption line shape on small variations of the laser intensity, we have plotted the complete line shape at two different laser intensities for dot 4: we observed that, despite $\sim 40\%$ reduction in contrast due to partial saturation, the line shape remained unchanged (see Fig. S4, left panel).

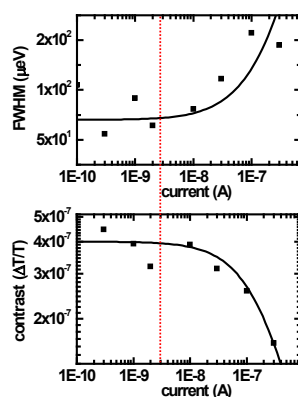


Figure S5: The peak contrast and linewidth of dot 1 as a function of the laser intensity.

While we do not have high signal-to-noise data (that would allow for a comparison with FDM-NRG calculations) for various laser intensities for dot 1 and 2, we did carry out saturation measurements on all dots before we took slow scans to determine the absorption line-shape. Figure S5 shows the peak absorption contrast and the full-width half maximum linewidth of the absorption for dot 1; the dashed red line indicates the intensity used to carry out the measurements depicted in Figs. 2-3 of the main text.

S5 Excitonic Anderson Model (EAM)

The coupled QD-FR system is described by an extension of the Single Impurity Anderson Model, which we call Excitonic Anderson Model (EAM) [2]: The Hamiltonian is given by $H = H_{\text{eh}} + H_c + H_t$, where

$$H_{\text{eh}} = \sum_{\sigma} (\varepsilon_{e\sigma} n_{e\sigma} + \varepsilon_{h\sigma} n_{h\sigma}) + U_{ee} n_{e\uparrow} n_{e\downarrow} - \sum_{\sigma\sigma'} U_{\text{eh}} n_{e\sigma} n_{h\sigma'} \quad (\text{S4})$$

describes the dot, with electron number $n_{e\sigma} = e_{\sigma}^{\dagger} e_{\sigma}$ and hole number $n_{h\sigma} = h_{\sigma}^{\dagger} h_{\sigma}$. The Coulomb repulsion U_{ee} , excitonic attraction U_{eh} and hole energy $\varepsilon_{h\sigma}$ are taken to be positive. The energies $\varepsilon_{e\sigma}$ and $\varepsilon_{h\sigma}$ both shift linearly with gate voltage V_g , with a slope of opposite sign, but same magnitude,

$$\Delta\varepsilon_{e\sigma} = -\frac{|e|}{\alpha_g} \Delta V_g, \quad \Delta\varepsilon_{h\bar{\sigma}} = \frac{|e|}{\alpha_g} \Delta V_g, \quad (\text{S5})$$

where $|e|$ is the unit of charge and α_g the lever arm. For dot 1, whose gate-voltage dependence we studied in detail, the lever arm is given by $\alpha_g = 7$.

$H_c = \sum_{k\sigma} \varepsilon_{k\sigma} c_{k\sigma}^{\dagger} c_{k\sigma}$ represents the FR, which consists of non-interacting electrons with energies $-D < \varepsilon_{k\sigma} < +D$, with reservoir bandwidth $2D = 1/\rho$ and constant density of states per spin ρ . $H_t = \sqrt{\Gamma/\pi\rho} \sum_{\sigma} (e_{\sigma}^{\dagger} c_{\sigma} + \text{h.c.})$ describes the tunnel-coupling between local level and reservoir, determined by the level-width Γ .

When an incident photon is absorbed by the semiconductor quantum dot, it creates a particle-hole pair. The interaction between photon and dot is given by $H_L \propto (e_{\sigma}^{\dagger} h_{\bar{\sigma}}^{\dagger} e^{-i\omega_L t} + \text{h.c.})$, where e_{σ}^{\dagger} and $h_{\bar{\sigma}}^{\dagger}$ create a QD electron and a hole, with well defined spins σ and $\bar{\sigma} = -\sigma$. For the experimental situation of present interest, the average valence band hole occupations of the initial configuration are given by $\bar{n}_{h\sigma}^i = \bar{n}_{h\bar{\sigma}}^i = 0$, and for the final configuration by $\bar{n}_{h\sigma}^f = 0$ and $\bar{n}_{h\bar{\sigma}}^f = 1$. It is therefore convenient to define two different Hamiltonians, $H^{i/f} = H_e^{i/f} + H_c + H_t$,

describing the system before and after absorption, where

$$H_e^a = \sum_{\sigma} \varepsilon_{e\sigma}^a n_{e\sigma} + U_{ee} n_{e\uparrow} n_{e\downarrow} + \delta_{af} \varepsilon_{h\bar{\sigma}} \quad (a = i, f). \quad (\text{S6})$$

These Hamiltonians differ (i) in the position of their e-levels ($\varepsilon_{e\sigma}^i$ and $\varepsilon_{e\sigma}^f = \varepsilon_{e\sigma}^i - U_{eh}$), where the e-level of the final Hamiltonian is pulled down by the excitonic Coulomb attraction and (ii) in the term $\delta_{af} \varepsilon_{h\bar{\sigma}}$ which accounts for the energy of the hole.

The absorption spectrum for the X^- transition can then be calculated according to Fermi's golden rule

$$A_{\sigma}(\nu) = 2\pi \sum_{mm'} \rho_m^i |f \langle m' | e_{\bar{\sigma}}^{\dagger} | m \rangle_i|^2 \delta(\omega_L - E_{m'}^f + E_m^i) \quad (\text{S7})$$

where $|m\rangle_a$ and E_m^a are the eigenstates and -energies of H^a . The detuning $\nu = \omega_L - \omega_{th}$ is defined relative to the threshold frequency $\omega_{th} \equiv E_G^f - E_G^i$ below which at $T = 0$ no photons can be absorbed, which is given by the difference of the ground state energies E_G^a of H^a . The positive hole is taken as a static spectator, interacting with the dot through Coulomb interaction U_{eh} only. We remark that the definition of $A_{\sigma}(\nu)$ in Eq. (S7) contains a creation operator $e_{e\bar{\sigma}}^{\dagger}$ of *opposite* spin (in contrast to the convention used in Ref. [2] for the X^0 transition, which contains $e_{e\sigma}^{\dagger}$). The convention used here ensures that $A_{\sigma}(\nu)$ describes the transition with highest weight for an initial configuration containing a spin- σ electron ($n_{e\sigma}^i \simeq 1$), which requires the added electron from the exciton to have opposite spin, $\bar{\sigma}$.

S6 Numerical Renormalization Group approach for spectral functions

The quantities $|m\rangle_a$ and E_m^a occurring in Eq. S7 can be calculated using the numerical renormalization group [3] (NRG). This is an iterative method for numerically diagonalizing quantum

impurity models, which also applies to the EAM Hamiltonians H^a ($a = i, f$) specified around Eq. (S6).

The spectrum of states of the Fermi reservoir is coarse-grained using a logarithmic discretization scheme governed by a parameter $\Lambda > 1$ (we typically use $\Lambda = 1.8$), followed by an exact mapping of the discretized model onto a semi-infinite chain, the so-called Wilson chain, whose hopping amplitudes decay exponentially along the chain, as $t_k \sim \Lambda^{-k/2}$. This produces a separation of energy scales and makes it possible to diagonalize the Hamiltonian iteratively: knowing the eigenstates of a chain of length $k - 1$, one adds site k and calculates the “shell” of eigenenergies of the Hamiltonian for the chain of length k . The high-lying eigenstates of that shell are “discarded”, while the low-lying states are “kept” and used for the next iteration. The spectrum of eigenenergies so obtained typically flows past one or more non-stable fixed-points and finally converges towards a stable fixed point, whereupon the iterative procedure can be stopped. In practice one thus deals with a finite Wilson chain, whose length is set by the smallest energy scale in the system (e.g. the Kondo temperature, temperature, or magnetic field). By combining NRG data from all iterations, it is possible to construct a *complete* set [4] of approximate many-body eigenstates of the full Hamiltonian. These can be used to evaluate equilibrium spectral functions via their Lehmann-representations; at finite temperatures, this can be done using the full density matrix (FDM)-NRG [5].

Since Eq. (S7) expresses the Fermi golden rule absorption rate via a Lehmann representation, it, too, can be evaluated using NRG [6], systematically so at finite temperatures by using complete basis sets using a FDM-NRG approach [2]. However, it contains matrix elements between initial and final states that are eigenstates of different Hamiltonians, H^i and H^f . Hence, two separate NRG runs are required to calculate these (similar in spirit to what is done for time-dependent NRG [4]). The strategy is then as follows:

- NRG run #1 generates a complete set of approximate eigenstates $|m\rangle_i$ and eigenenergies

E_m^i for the initial Hamiltonian H^i (without exciton).

- NRG run #2 generates a complete set of approximate eigenstates $|n\rangle_f$ and eigenenergies E_m^f for the final Hamiltonian H^f (with exciton).
- The double sum in Eq. (S7), over all initial and final eigenstates, is performed in two steps. First we perform a *backward* run, with site index k running from the end to the beginning of the Wilson chain[4], and calculate for each shell k the contribution ρ_k^i towards the initial density matrix from that shell (obtained using data from NRG run #1). This is followed by the usual *forward* run, in which the matrix elements $|\langle n|e_\sigma^\dagger|m\rangle_i|^2$ between shell- k eigenstates from NRG runs #2 and NRG #1 are calculated, combined with ρ_k^i , and binned (see below) according to the corresponding frequency difference $E_n^f - E_m^i$.
- The $T = 0$ threshold frequency for the onset of absorption is given by the difference of ground state energies of NRG runs #2 and #1, $\omega_{\text{th}} \equiv E_G^f - E_G^i$. The absorption spectrum is expected to have divergences at the threshold ω_{th} , hence all frequency data are shifted by the overall threshold energy ω_{th} prior to binning. (For finite temperature, the sharp onset is broadened and divergences are cut off.)
- The discrete eigenenergies of shell k are spread over an energy range comparable to the characteristic energy $\Lambda^{-k/2}$ scale of that iteration, which decreases exponentially with k . Thus, the bins used for collecting the discrete data are likewise chosen to have widths decreasing exponentially with decreasing energy. The discrete, binned data are subsequently broadened using a log-Gaussian broadening scheme, characterized by a broadening parameter α as described in Ref. [5], here taken as $\alpha = 0.4$.

S7 Fitting model parameters

To determine the values of Γ , U_{ee} and D , we fit the numerical predictions for the gate-voltage dependence of the transition energy $\Delta E_{\text{transition}}$ to the experimental data (Fig. 2A, blue symbols, which give the frequency where the absorption spectrum reaches its maximum).

Within our model the transition energy $E_{\text{transition}} = \omega_{\text{th}} + E_{\text{Stark}}$ is given by the sum of the threshold frequency $\omega_{\text{th}} = E_{\text{G}}^{\text{f}} - E_{\text{G}}^{\text{i}}$ and a linear Stark shift, $E_{\text{Stark}} \propto \varepsilon$.

The threshold frequency ω_{th} is obtained numerically by simply calculating the ground state energies E_{G}^{i} and E_{G}^{f} of the two Anderson Hamiltonians H^{i} and H^{f} specified around Eq. (S6), taking care to incorporate the gate-voltage dependence of the electron and hole levels, according to Eq. (S5). When comparing experimental data with NRG-results, E_{Stark} is treated as fit parameter, together with Γ , D and U_{ee} . Since only relative changes in gate voltage have physical relevance, the horizontal offset of the experimental data is chosen such that the value of V_{g} for which the absorption contrast is strongest corresponds to the specific level-position $\varepsilon \equiv \varepsilon_{e\sigma}^{\text{i}}$ given by $\varepsilon = -U/2$. Since the band gap, which contributes to $\varepsilon_{h\bar{\sigma}}$ and hence to E_{G}^{f} , is not precisely known, the experimental and theoretical data are both shifted along the values of their minima are $\Delta E_{\text{transition}} = 0$.

S8 Fitting experimental lineshapes to perturbative formula

It is instructive to gauge the effect of Kondo correlations in the measured line shapes by comparing them to cases for which the Kondo effect is absent, so that the absorption line shape lends itself to a perturbative description (based on the Anderson model). To show how the line shapes differ in the absence of Kondo correlations, we here present a comparison of the X^- line of dot 2 (used to obtain the line shapes depicted in Fig. 4 of the main text), and another dot (referred to as dot 3) from the same sample. Dot 3 has a trion emission wavelength

of 955 nm (as opposed to ~ 900 nm for dots 1 and 2); we observe that the dots emitting at this wavelength have much sharper lines, indicating weak coupling to the FR; this is a consequence of lower conduction band electron energy, which in turn increases the effective tunnel barrier to the FR.

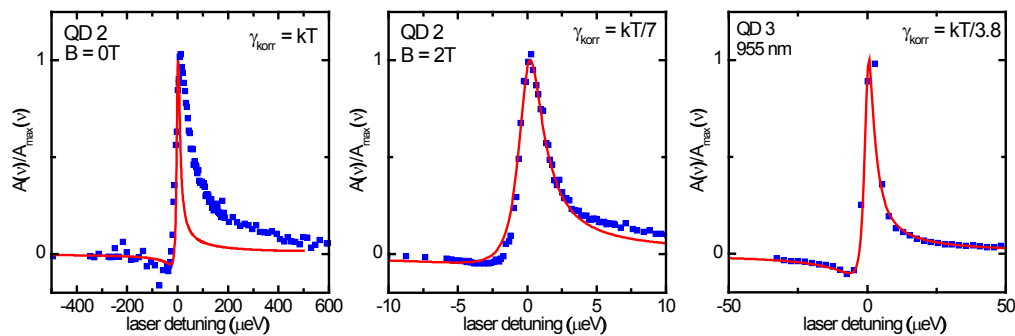


Figure S6: Perturbative fits to absorption line shapes measured for (a) dot 2 at $B = 0$ Tesla, (b) dot 2 at $B = 2$ Tesla, (c) dot 3 at $B = 0$ Tesla.

Figure S6c shows that the line shape of this weakly coupled dot 3 can be perfectly fit using a perturbative absorption line shape:

$$A(\nu) \propto \frac{\nu/T}{1 - e^{-\nu/T}} \frac{\gamma}{\nu^2 + \gamma^2/4}, \quad (\text{S8})$$

where $\gamma < T$ is a phenomenological relaxation rate. This line shape is a simplified version of the one derived in Ref. [23], where γ was given by the scale-dependent Korringa relaxation rate $\gamma_{\text{Kor}}(\nu, T) = 2\pi T / \ln^2[\max(|\nu|, T)/T_K]$. As was argued in [2], this line shape is strictly valid only in the limit $\max[|\nu|, T] \gg T_K$. Instead of the scale-dependent Korringa relaxation rate, we choose to use a constant γ in our fits. We do however, take into account that the relaxation is stemming from the Anderson model, which restricts $\gamma < T$ (for $B = 0$) and introduces the $\frac{\nu/T}{1 - e^{-\nu/T}}$ factor, that accounts for the asymmetry between the FR electron-hole pair generation and annihilation processes.

In contrast to dot 3, an attempt to use Eq. (S8) with $\gamma \leq T$ to fit the line shape of the strongly coupled dot 2 at $B_{\text{ext}} = 0$ fails dramatically, as shown in Fig. S6a.

Interestingly, the situation is different for $B_{\text{ext}} = 2$ Tesla, where the absorption line shape of dot 2 can be fitted reasonably well with Eq. (S8), as shown in Fig. S6b. The reason for this striking change is related to the onset of the oscillations in peak contrast observed for the blue transition in the inset of Fig. 4c: as mentioned in the main text, a magnetic field exceeding 1 Tesla causes oscillations in the FR density of states, ρ_{FR} . The Kondo temperature, which depends exponentially on ρ_{FR} , will thus experience strong oscillations as well, which explains the observed strong oscillations in the peak contrast. Thus, the maximum in peak contrast observed at $B_{\text{ext}} = 2$ Tesla corresponds to a *minimum* for T_{K} , i.e. at $B_{\text{ext}} = 2$ Tesla we have, in effect, a *weakly* coupled dot, explaining why its line shape can be fit reasonably well with the perturbative Eq. (S8).

In summary, the striking difference seen in Figs. S6a and S6b between the $B_{\text{ext}} = 0$ and 2 Tesla line shapes of dot 2 confirms our interpretation that for $B_{\text{ext}} = 0$, Kondo correlations are at the heart of the observed line shapes.

S9 Quantum dot optical transitions

In the main text we focus exclusively on the X^- transition; in this section, we comment on some of its similarities and differences with respect to the neighboring X^0 transition.

Figs. S7a and S7c show the PL spectra as a function of gate voltage for the QDs that are discussed in the main text, dot 1 and dot 2, respectively. Both are strongly coupled to the FR, as is evident from the rather strong curvature of their respective X^- and X^0 plateaus, which is superimposed on the expected linear DC Stark shift. The reason for this curvature has been discussed in the main text: when the QD's localized conduction-band level, $\varepsilon_{e\sigma}$, is singly-occupied, its energy is renormalized (lowered) due to charge fluctuations (virtual tun-

neling processes described by the Anderson model), and this renormalization is strongest near the edges of a plateau, where charge fluctuations are strong. The sign of the curvature of the threshold frequency, $\omega_{\text{th}} = E_G^f - E_G^i$, is positive for X^- , where the singly-occupied e-level occurs in the initial configuration, and negative for X^0 , where it occurs in the final configuration (as illustrated schematically in Figs. 2c of the main text and Fig. S7b, respectively). Since the dominant transitions on the left of X^0 in Figs. S7a and S7c also have negative curvature, they presumably also involve a singly-occupied electron state in their final configurations. We have not attempted to identify the nature of these transitions in detail, however; a detailed discussion of a very similar spectrum may be found in Ref. [7].

For strongly coupled dots, the exchange interaction between the singly-occupied electron state and the FR in the initial configuration gives rise to Kondo correlations. In the main text, we showed that this affects the line shape of the X^- transition, due to Kondo correlations in the *initial* configuration. Similarly, one may expect that the line shape of the X^0 transition should be affected as well, due to Kondo correlations in the *final* configuration of X^0 . However, the latter also contains a hole (in contrast to the initial configuration of X^- , compare Fig. 2c of the main text and Fig. S7c), which leads to a complication: the QD electron and hole will experience an exchange interaction, which will tend to counteract the formation of a Kondo singlet between the QD electron and Fermi sea. Due to large confinement- and strain-induced spin splitting of the hole states, we expect the dominant electron-hole exchange interaction to be of the form $H_{\text{exch}} = -J_{\text{eh}}S_e^z S_h^z$, involving only the z -components of the e-level spin operator and local heavy-hole pseudo-spin operator, respectively.

Figure S8a shows the absorption of the X^0 resonance of another strongly coupled QD, dot 4. When we take a line cut through this plot at the gate voltage indicated by the vertical yellow line, we note that the line shape is broad yet qualitatively different from that of X^- . We also note that unlike X^- , the peak of the absorption line shape can be modified by changing the polarization of

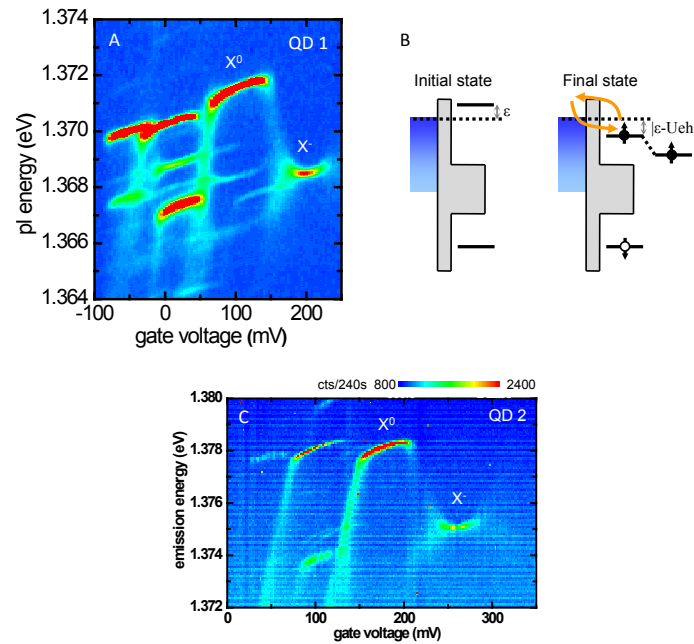


Figure S7: (a) Photoluminescence as a function of V_g for dot 1: this is the same plot as in Fig. 1b of the main text. (b) Schematic of the X^0 transition. The X^0 plateau has a curvature with a different sign as compared to X^- , since the renormalization of the electron level energy $\epsilon_{e\sigma}$ by hybridization with the FR is relevant only in the final state. (c) Photoluminescence as a function of V_g for dot 2.

the incident light (Fig.S8b), suggesting a large anisotropic electron-hole exchange interaction. We note however, that the splitting inferred from the polarization dependent absorption is large compared to the typical values of bright exciton (anisotropic electron-hole exchange) splitting and small compared to the bright-dark (isotropic electron-hole exchange) splitting. Remarkably, our attempts to fit the observed line shape with a perturbative formula (discussed in Section S8) failed drastically (Fig.S8 c), indicating the importance of Kondo correlations despite the presence of electron-hole exchange interaction. A detailed analysis of this line shape would

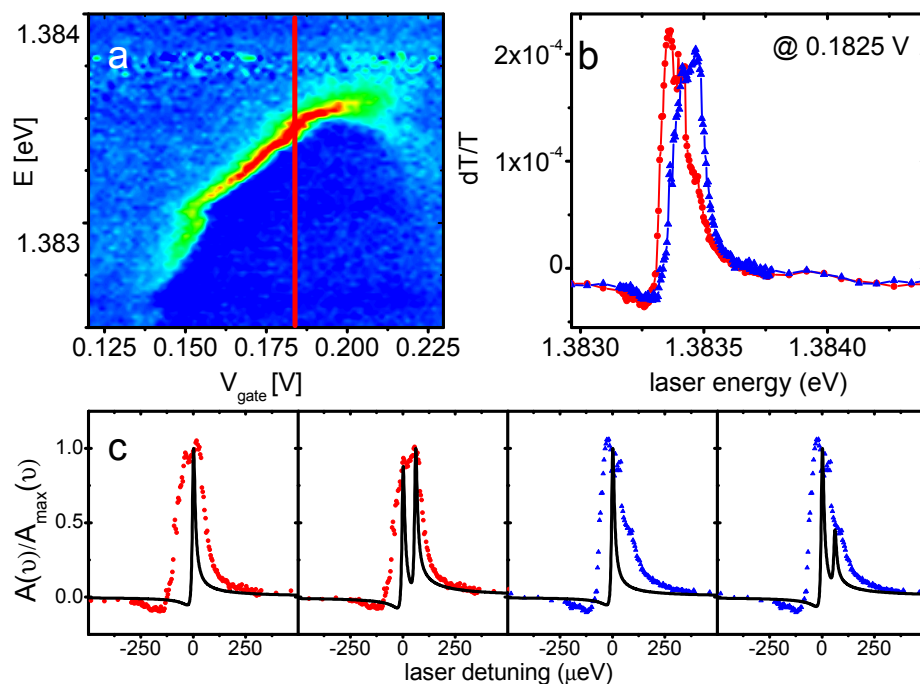


Figure S8: (a) Absorption of the neutral exciton (X^0) as a function of V_g for dot 4. (b) The absorption line shape of the $V_g = 0.1825$ V for two different incident laser polarizations. (c) Attempted fits to the absorption line shape in (b) using one or two (modified) Lorentzians, given in Eq. (S8), assuming $\gamma = T$.

require an accurate identification of the isotropic as well as anisotropic electron-hole exchange interaction strengths, and is beyond the scope of this work.

S10 Magnetization and line shapes at finite magnetic field

One of the most striking ways to identify the presence of Kondo correlations is to study how they are reduced by applying an external magnetic field. In this section, we outline what is expected to happen in some detail, based on NRG calculations and analytical arguments. We also show data that nicely illustrates the difference between dots with or without Kondo correlations.

In the presence of an external magnetic field B_{ext} applied along the growth axis of the heterostructure (Faraday configuration), the electron and hole level energies will be Zeeman-shifted according to ($a = i, f$):

$$\varepsilon_{e\sigma}^a = \varepsilon_e^a + \frac{1}{2}\sigma g_e \mu_B B_{\text{ext}} = \varepsilon_e^a - \frac{1}{2}\sigma B, \quad (\text{S9})$$

$$\varepsilon_{h\sigma} = \varepsilon_h + \frac{1}{2}\sigma g_h \mu_B B_{\text{ext}} = \varepsilon_h + \frac{1}{2} \frac{g_h}{|g_e|} \sigma B, \quad (\text{S10})$$

where $g_e \simeq -0.6$ and $g_h \simeq 1.1$ for our dots, $\mu_B = 58 \mu\text{eV/Tesla}$, and we have defined $B = |g_e| \mu_B B_{\text{ext}}$.

Creation of a trion, described by $H_L \propto (e_{\sigma}^{\dagger} h_{\sigma}^{\dagger} e^{-i\omega_L t} + \text{h.c.})$, can be induced in a *spin-selective* way [8]: by choosing right (left) circularly polarized laser field, one can exclusively couple to the state with initial electron spin-up $\sigma = +$ (spin-down $\sigma = -$). For $B > 0$ (assumed henceforth), the spin-up (spin-down) electron has lower (higher) energy and the corresponding optical transitions are conventionally referred to as blue (red) trion, with line shapes $A_+(\nu)$ ($A_-(\nu)$), since the B -induced shift in threshold frequency $\omega_{\text{th}}^{\sigma}(B) = E_G^f - E_G^i$ is positive (negative), as elaborated below.

We will discuss the effect of $B \neq 0$ on (i) the initial e-level magnetization $m_e^i(B, T) = \frac{1}{2}(n_{e+}^i - n_{e-}^i)$, (ii) the absorption line shape $A_{\sigma}(\nu)$, and (iii) the threshold frequency $\omega_{\text{th}}^{\sigma}(B)$, all for the X^- transition. Our discussion is very similar to that of Ref. [2], which analyzes analogous questions for the X^0 transition.

(i) Magnetization: The magnetization $m(B, T)$ of a free, localized spin, at finite temperature T , evolves in a magnetic field with Zeeman energy $H_{\text{Zeeman}} = -BS_z$ according to $m_{\text{free}} = \frac{1}{2} \tanh(B/2T)$. Thus, $m(B, T)$ crosses over from 0 to $\frac{1}{2}$ on the scale $B \gtrsim T$. In contrast, if the spin is exchanged-coupled to a FR, and the temperature is low enough that Kondo-screening occurs ($T \ll T_K$), the crossover scale increases to $|B| \simeq T_K$. Thus, the magnetization for a Kondo-screened spin evolves much slower with applied field than it does for a

free spin, as illustrated in Fig. S9a. The reason is that Kondo screening of the local spin by the FR causes a strong reduction in the static spin susceptibility.

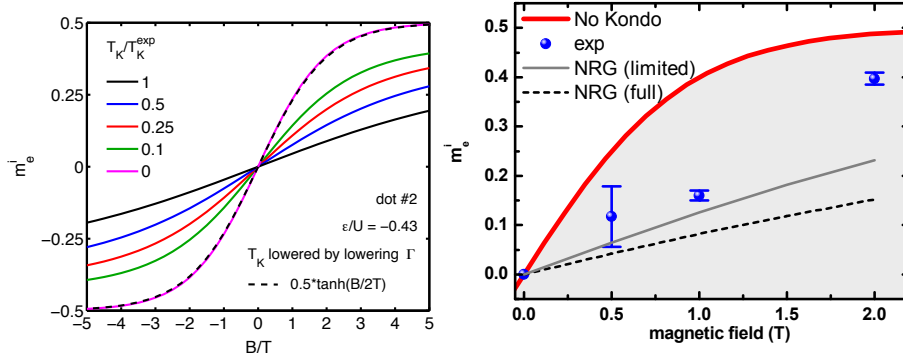


Figure S9: **a**, The calculated magnetization $m(B, T)$ of a localized spin coupled to a FR, with Zeeman energy $H_{\text{Zeeman}} = -B_{\text{ext}}S_z$, plotted as a function of B/T for several values of T_K . We assumed $n_h = 0$, $\Gamma = 1$ meV, $D = 6.5$ meV, $U_{ee} = 7.5$ meV, $\varepsilon = -0.43U_{ee}$ (such that $n_e^i \simeq 1$ and $T_K^{\text{exp}} = 140$ μeV), and $T = T_{\text{FR}} = 15.6$ μeV . Thus, the black curve with $T_K = T_K^{\text{exp}}$ corresponds to the experimental situation of dot 2. For the other curves, we (only) changed Γ , to obtain smaller T_K . **b** The experimental magnetization of dot 2 at $B_{\text{ext}} = 0, 0.5, 1$ and 2 Tesla, determined by directly integrating the area under the measured blue and red trion absorption line shapes. For comparison, the predictions of NRG for the "full area" as well as "limited area" (i.e. integration of the area up to $\nu_{\text{max}} = 3T_K$, as was done for the experimental points) cases are shown, along with a case where T_K is vanishingly small (red curve). The data points at $B_{\text{ext}} = 0.5$ and 1 Tesla lie far below the red curve, indicating a reduced magnetization consistent with Kondo screening. In contrast, the magnetization at $B_{\text{ext}} = 2$ Tesla lies close to the red curve: we argue that this increase in magnetization is related to the oscillations in peak contrast visible in the inset of Fig. 4c of the main text.

Since the area under the absorption curve $A_\sigma(\nu)$,

$$W_\sigma = \int_{-\infty}^{\infty} d\nu A_\sigma(\nu), \quad (\text{S11})$$

is proportional to $(1 - n_{e\sigma}^i)$ [by Eq. (S7)], the initial magnetization can be extracted from the normalized difference in areas under the blue and red shapes:

$$m_e^i(B) = \frac{1}{2}(n_{e+}^i - n_{e-}^i) = \frac{W_+(B) - W_-(B)}{2(W_+(0) + W_-(0))}. \quad (\text{S12})$$

The second equality assumes that the total initial occupancy is one, $n_{e+}^i + n_{e-}^i = 1$, which, to very good approximation, is the case for dot 2 of Fig. 4 (main text). We have confirmed numerically that $W_+(B) + W_-(B) = W_+(0) + W_-(0)$, even in the presence of optical interference induced modification of the absorption line shape.

In practice, the determination of m_e^i from experimental line shapes using Eq. (S12) is complicated by (a) the difficulty in ensuring perfect circular polarization of the incident laser field, (b) the low signal-to-noise ratio for the red trion transition due to its enhanced broadening (arising from a magnetic-field induced reduction in its power-law exponent), (c) the low signal-to-noise ratio in the tails of the absorption line-shape which have a sizeable contribution to the area, and (d) the modification of the FR density of states for $B > 1$ Tesla. Despite these complications, the results shown in Fig. S9b demonstrate unambiguously that the crossover scale for the initial magnetization to change significantly from 0 is not $B \simeq T$ but $B \simeq T_K$, implying that the initial state of dot 2 is a screened Kondo singlet. To determine the magnetization from the area of the experimental line shapes, we have integrated the line shapes in the interval $-3T_K \leq \nu \leq 3T_K$. The dominant contribution to the error bars comes from the fact that with the limited integral, we find that sum of the area under the blue and red trion transitions is not equal to the area under the $B = 0$ line shape. In addition, the additional peak visible at high frequency tail of the red trion transition depicted in Fig. 4c suggests that the suppression of the orthogonal polarization is incomplete: these two factors give rise to the error bars indicated in Fig. S9b.

(ii) Absorption line shape: Fig. S10 illustrates the influence of Kondo correlations in the initial configuration of the X^- transition on the absorption line shape. The line shapes in the top (bottom) panels were calculated for $T \ll T_K$ ($T_K \ll T$), so that Kondo correlations are strong (weak). Evidently, Kondo correlations cause the peaks to be much broader and less high, in effect redistributing oscillator strength over a larger frequency range.

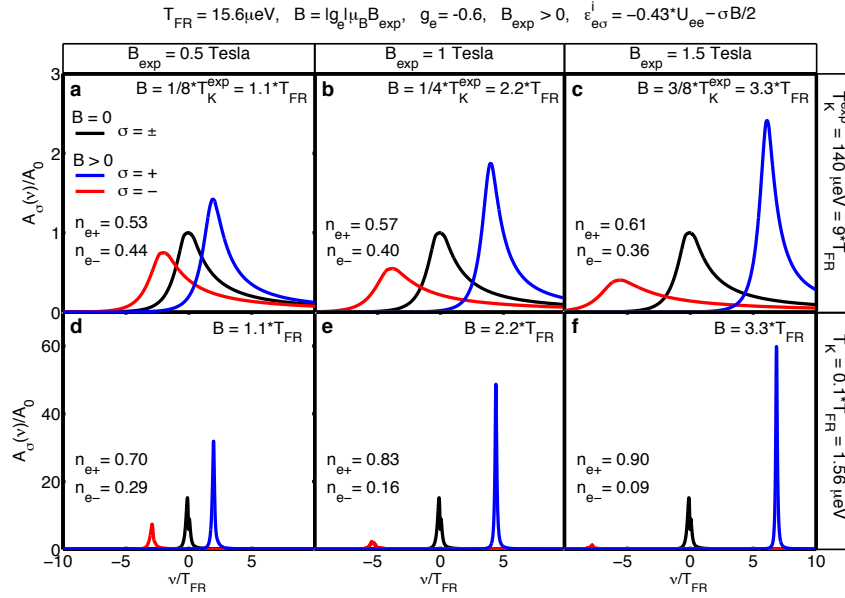


Figure S10: NRG calculations for the line shapes $A_{\pm}(\nu)$, where ν is the detuning w.r.t. to the absorption threshold at zero field, $\omega_{\text{th}}^{\sigma}(B=0)$. For the upper panels, all parameters were chosen as for the black curve of Fig. S9a. Lower panels differ from upper ones only in a 90 times smaller choice of T_K , namely $T_K = 0.1 T_{\text{FR}} = 1.56 \mu\text{eV}$ instead of $T_K = T_K^{\text{exp}} = 140 \mu\text{eV}$. Thus upper and lower panels correspond to the black or pink curves of Fig. S9a, featuring strong or no Kondo correlations, respectively. The data in panel b correspond to the NRG lines shown in Fig. 4c of the main text.

In both upper and lower panels, a magnetic field splits the peak into two separate ones, whose areas W_{\pm} reflect the spin-dependent occupations $1 - \bar{n}_{e\mp}^i \simeq \bar{n}_{e\pm}^i$ of the Zeeman-split initial e-levels. The difference in areas between the blue and red transitions, $W_+ - W_-$, which is a measure of the initial magnetization m_e^i [see Eq. (S12)], changes much more slowly with increasing field for the upper than the lower panels, in accord with the behavior shown in Fig. S9a. We emphasize that the splitting of the trion transitions with the applied magnetic field is primarily due to the hole-Zeeman effect as we discuss below.

(iii) Spin-dependent threshold frequency: The *shift* of the (zero temperature) absorption

threshold frequency $\omega_{\text{th}}^\sigma(B) = E_G^f - E_G^i$ with magnetic field can be written as

$$\omega_{\text{th}}^\sigma(B) - \omega_{\text{th}}(0) = \frac{1}{2} \frac{g_h}{|g_e|} \sigma B + \delta\omega_{\text{th}}^e(B). \quad (\text{S13})$$

The first term reflects the Zeeman energy of the photo-excited hole, the second the B -dependence of the ground-state energy of the electron system. In our situation, $\bar{n}_e^i \simeq 1$ and $\bar{n}_e^f \simeq 2$. The asymptotic behavior of the initial magnetization is $m_e^i = \chi_0 B$ for small fields, where the linear static susceptibility χ_0 is of order $1/T_K$, and $|m_e^i| = \frac{1}{2}$ for large fields. This implies

$$\delta\omega_{\text{th}}^e = \begin{cases} \frac{1}{2} \chi_0 B^2 & (|B| \ll T_K), \\ \frac{1}{2} |B| & (T_K \ll |B| \ll |\varepsilon_e^i|). \end{cases} \quad (\text{S14})$$

In our experiment for dot 2, $|B| \lesssim T_K$, hence the dominant contribution to the threshold shift will be the $\frac{1}{2} \frac{g_h}{|g_e|} \sigma B$ term from the hole. This shift is evident in the calculated NRG absorption spectra shown in Fig. S9. For the B -dependent spectra displayed in Fig. 4 of the main text and in Fig. S3 of Section S2, the B -dependent shift in the position $\omega_{\text{th}}^\sigma(B)$ of the peak maximum is subtracted out, i.e. the detuning refers to the $\nu = \omega - \omega_{\text{th}}^\sigma(B)$.

(iv) Modification of Anderson orthogonality exponents with magnetic field: To understand the dependence of the power-law exponents on the magnetic field, we first recall that in the strong-coupling regime, the absorption line shape exhibits a power-law divergence of the form [2],

$$A_\sigma(\nu) \sim \nu^{-\eta_\sigma}, \quad (T \ll \nu \ll T_K). \quad (\text{S15})$$

The value of the exponent η_σ is governed by Anderson orthogonality between the initial state $e_{\bar{\sigma}}^\dagger |G_i\rangle$, obtained by adding a photo-excited spin- $\bar{\sigma}$ electron to the initial ground state, and the final ground state $|G_f\rangle$. This exponent depends on gate voltage and magnetic field in a way that has been worked out in Ref. [2], for the case of the X^0 transition. Adapting the arguments given there to the X^- transition of present interest, the exponent can be expressed as

$$\eta_\sigma = 1 - \sum_{\sigma'} (\delta_{\bar{\sigma}\sigma'} + \bar{n}_{e\sigma'}^i - \bar{n}_{e\sigma'}^f)^2, \quad (\bar{\sigma} = -\sigma) \quad (\text{S16})$$

where $\bar{n}_{e\sigma'}^i$ and $\bar{n}_{e\sigma'}^f$ are the initial and final occupancies of the QD e-level for spin σ' . This is a generalization [2] of Hopfield's rule [9]. It has an instructive physical interpretation [9, 2]. The “1” represents a ν^{-1} power law divergence: it may be thought of as arising from a detuned, virtual transition into a narrow e-level situated at $\nu = 0$ (giving a Lorentzian detuning factor $1/\nu^2$), followed by the creation of particle-hole pairs (with phase space ν) to carry off the excess energy ν , resulting in a lineshape scaling as $\nu/\nu^2 = \nu^{-1}$. The second term of Eq. (S16) reflects Anderson orthogonality.

According to Eq. (S16), η_σ can be tuned experimentally by varying either gate voltage or magnetic field, since both modify the initial and final occupancies $\bar{n}_{e\sigma'}^i$ and $\bar{n}_{e\sigma'}^f$ (see Fig. 2b of main text). This *tunability* can be exploited to study universal aspects of Anderson orthogonality physics that had hitherto been inaccessible. Let us focus on the case (relevant for dot 2 of Fig. 4) that the QD is tuned to the center of a charging plateau, where $\bar{n}_e^i = 1$ (initial Kondo singlet) and $\bar{n}_e^f = 2$ (final local doublet). Then Eq. (S16) can be expressed as

$$\eta_\sigma = \frac{1}{2} + 2m_e^i\sigma - 2(m_e^i)^2, \quad (\text{S17})$$

where $m_e^i = \frac{1}{2}(\bar{n}_{e+}^i - \bar{n}_{e-}^i)$ is the initial local moment of the QD. The latter is a universal function of B/T_K , which changes from 0 to $\frac{1}{2}$ as the field increases from 0 to $B \gg T_K$. Thus, the exponents η_σ are universal functions of B/T_K , too, with simple limits for small and large fields

$$\eta_\sigma \rightarrow \begin{cases} \frac{1}{2} & (B \ll T_K), \\ \sigma & (B \gg T_K). \end{cases} \quad (\text{S18})$$

The reason why η_+ increases while η_- decreases with increasing field can be understood qualitatively by considering the limit of large fields: for $B \gg T_K$, the QD initially contains a single spin-up electron in the lower of the Zeeman-split levels ($n_{e+}^i = 1$, $\bar{n}_{e-}^i = 0$), whereas the final local doublet contains both a spin-up and spin-down electron ($\bar{n}_{e\sigma'}^f = 1$). For $\sigma = +$, corresponding to the photo-excitation of a spin-down electron into the upper of the Zeeman-split QD

levels, Anderson orthogonality is completely *absent* (the second term in Eq. (S16) vanishes, thus $\eta_+ = 1$), since the state $e_-^\dagger|G_i\rangle$ describes a doubly occupied QD, just as the final ground state $|G_f\rangle$. In contrast, for $\sigma = -$, corresponding to the photo-excitation of a spin-up electron into the lower of the Zeeman-split levels, Anderson orthogonality is *maximal* (the second term in Eq. (S16) equals 2, thus $\eta_- = -1$); the reason is that for the initial ground state the QD already contains a spin-up electron, hence this transition is possible only if accompanied by at least one virtual spin-flip exchange transition, causing $e_+^\dagger|G_i\rangle$ to be orthogonal to $|G_f\rangle$.

Fig. 4d of the main text shows the onset of the B -dependent changes in η_σ discussed above. Since at $B_{\text{ext}} = 1$ T the ratio $B/T_K = 0.25$ is still small, the field is too weak to modify the ($\sigma = -$) lineshape in the perturbative regime ($\nu > T_K$). However, it is large enough to already affect the Anderson orthogonality exponents in the strong-coupling regime ($\nu \lesssim T_K$), and the trend $\eta_-(B) < \eta_\sigma(0) < \eta_+(B)$ is clearly observed.

References and Notes

- [1] Karrai, K., Warburton, R. Optical transmission and reflection spectroscopy of single quantum dots, *Superlattice Microst.* **33**, 311 (2003)
- [2] Türeci, H. E. *et al.* Many-Body Dynamics of Exciton Creation in a Quantum Dot by Optical Absorption: A Quantum Quench towards Kondo Correlations. *Phys. Rev. Lett.* **106**, 107402 (2011).
- [3] Krishna-murthy, H. R., Wilkins J. W. & Wilson, K. G. Renormalization-group approach to the Anderson model of dilute magnetic alloys. II. static properties for the asymmetric case. *Phys. Rev. B* **21**, 1044-1083 (1980)
- [4] Anders, F. B. & Schiller, A. Real-time dynamics in quantum-impurity systems: a time-dependent numerical renormalization-group approach. *Phys. Rev. Lett.* **95**, 196801 (2005).
- [5] Weichselbaum, A. & von Delft, J. Sum-rule conserving spectral functions from the numerical renormalization group. *Phys. Rev. Lett.* **99**, 076402 (2007).
- [6] Helmes, R. W., Sindel, M., Borda, L. & von Delft, J. Absorption and emission in quantum dots: Fermi surface effects of Anderson excitons. *Phys. Rev. B* **72**, 125301 (2005).
- [7] Kleemans, N. A. J. M. *et al.* Many-body exciton states in self-assembled quantum dots coupled to a Fermi sea. *Nature Physics* **6**, 534 (2010).
- [8] Yilmaz, S. T., Fallahi, P. & Imamoglu, A. Quantum-Dot-Spin Single-Photon Interface. *Phys. Rev. Lett.* **105**, 033601 (2010).
- [9] Hopfield, J. J. Infrared divergences, X-ray edges, and all that. *Comments on Solid State Phys.* **2**, 40 (1969).

Comment: After publication we found the following errors in the supplementary information: (i) The reflectivity of the top surface should be $r = 0.35$ rather than $r = 0.67$. This value is quoted in Fig. S3. (ii) In Fig. S6 middle panel, the best fitting Korringa relaxation rate should be $\gamma_{\text{korr}} = kT/1.4$, rather than $\gamma_{\text{korr}} = kT/7$. The conclusions on pages 6 and 15 of the supplementary information remain unchanged. The corrected errors are not relevant for the main text of the letter.

5.2. Rabi-Kondo Correlated State in a Laser-Driven Quantum Dot

In the following section, we theoretically examine a QD which is subject to strong optical coupling. Contrary to the previous section, we will look at the emission instead of the absorption spectrum, since strong optical coupling requires a laser, and a second laser would be needed for measuring absorption, which would render the experiment rather difficult. We observe the emergence of a new energy scale which depends on the Rabi frequency of the system and which can be understood as a Kondo temperature for a secondary Kondo effect which occurs at the system. There, spin up and down, the two degrees of freedom which are usually required for Kondo correlations, are replaced by two many-body states: a (spin-) Kondo state and a trion state.

Proposed Rabi-Kondo Correlated State in a Laser-Driven Semiconductor Quantum Dot

B. Sbierski,^{1,2} M. Hanl,³ A. Weichselbaum,³ H. E. Türeci,^{1,4} M. Goldstein,⁵ L. I. Glazman,⁵
J. von Delft,³ and A. Imamoglu¹¹Institute for Quantum Electronics, ETH Zürich, CH-8093 Zürich, Switzerland²Dahlem Center for Complex Quantum Systems and Institut für Theoretische Physik, FU Berlin, D-14195 Berlin, Germany³Arnold Sommerfeld Center for Theoretical Physics and Center for NanoScience, LMU München, D-80333 München, Germany⁴Department of Electrical Engineering, Princeton University, Princeton, New Jersey 08544, USA⁵Department of Physics, Yale University, 217 Prospect Street, New Haven, Connecticut 06520, USA

(Received 28 November 2012; published 10 October 2013)

Spin exchange between a single-electron charged quantum dot and itinerant electrons leads to an emergence of Kondo correlations. When the quantum dot is driven resonantly by weak laser light, the resulting emission spectrum allows for a direct probe of these correlations. In the opposite limit of vanishing exchange interaction and strong laser drive, the quantum dot exhibits coherent oscillations between the single-spin and optically excited states. Here, we show that the interplay between strong exchange and nonperturbative laser coupling leads to the formation of a new nonequilibrium quantum-correlated state, characterized by the emergence of a laser-induced secondary spin screening cloud, and examine the implications for the emission spectrum.

DOI: 10.1103/PhysRevLett.111.157402

PACS numbers: 78.60.Lc, 72.10.Fk, 78.40.Fy, 78.67.Hc

Introduction.—Exchange interactions between a singly occupied quantum dot (QD) and a fermionic bath (FB) of itinerant electrons in the bulk lead to the formation of a Kondo state $|K\rangle$ [1–3]. When this many-body ground state is coupled by a laser field of vanishingly small Rabi frequency Ω to an optically excited trion state $|T\rangle$ with an additional QD electron-hole pair [see Fig. 1(a)], the resulting emission spectrum at low FB temperatures T is highly asymmetric [4,5]. Within the energy range defined by Kondo temperature $T_K \gg T$, the spectral line shape is characterized by a power-law singularity. Anderson orthogonality (AO) determines the corresponding noninteger exponent and precludes any coherent light scattering in this limit. In the opposite limit of large Ω and vanishing exchange interaction ($T_K \rightarrow 0$), the emission spectrum consists of a Mollow triplet and an additional δ -function peak [6–8]. While the latter stems from coherent Rayleigh scattering, the Mollow triplet originates from incoherent transitions between dressed states which are superpositions of the original excited trion and the singly charged ground states.

In this Letter, we analyze the interplay between strong exchange and nonperturbative laser couplings. By using a combination of numerical and analytical techniques, we find that the emission line shape for $T \ll \Omega \ll T_K$ differs drastically from both the above limits. We demonstrate the emergence of a new quantum-correlated many-body state, which is a laser-induced, coherent superposition of the Kondo singlet state $|K\rangle$ and the trionic state $|T\rangle$ [see Fig. 1(a)]. The Kondo state involves a spin 1/2 on the dot, screened by a spin cloud in the FB which is formed within distance $\propto 1/T_K$ from the dot, while the FB is trivial in the bare trion state. The new quantum-correlated state is

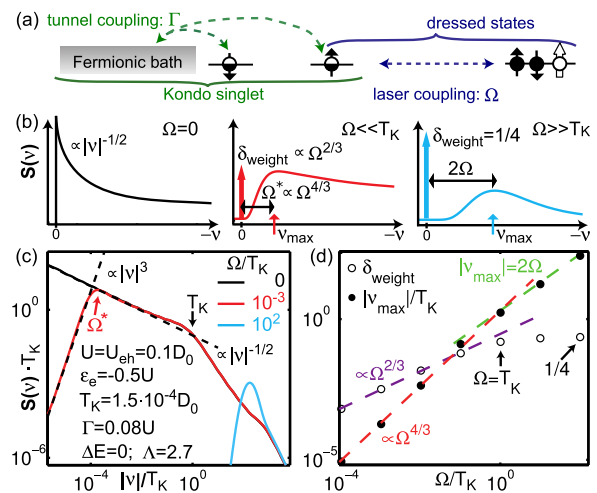


FIG. 1 (color online). (a) Competition between tunnel and laser coupling on the QD. While tunnel coupling favors a Kondo singlet state correlated with the FB, laser coupling favors dressed QD states. The characteristic energy scales are the Kondo temperature T_K and Rabi frequency Ω , respectively. (b) Schematic plots of emission spectra $S(\nu)$ from the Rabi-Kondo model Eq. (1) for $\Delta E = 0$ and three characteristic choices for Ω/T_K . For $\Omega = 0$, $S(\nu)$ shows a power-law divergence (left-hand panel). With increasing laser intensity ($\Omega \neq 0$, other two panels) it transforms to a δ peak at $\nu = 0$ (thick arrows) and a broad maximum at the (renormalized) Rabi frequency. (c),(d) NRG results with power-law asymptotes denoted as dashed lines: Log-log plot of the broad emission peak [$S(\nu < 0)$] (c), its position $|\nu_{\max}|$ (dots) and the δ -peak weight (circles) vs Ω/T_K (d). We have confirmed similar results for the nonsymmetric case $\varepsilon_e \neq -U/2$ and $U \neq U_{e-h}$ as long as $n_{e1} + n_{e1} - n_h \simeq 1$.

associated with the formation of an additional “secondary” screening cloud at larger distances that compensates for the differences in local occupancies between $|K\rangle$ and $|T\rangle$. The secondary screening process is also of the Kondo type, and sets in below a secondary Kondo temperature, the renormalized Rabi frequency $\Omega^* \propto \Omega^{4/3}$. This new energy scale manifests itself in the location of a broad peak in the emission spectrum. The peak’s red and blue tails follow power-law functions corresponding to the primary and secondary Kondo correlations, respectively. The emergence of the secondary screening cloud coincides with the recovery of the δ -function peak in the emission spectrum, with weight scaling as $\Omega^{2/3}$. Measuring these effects should be possible in a setting similar to the one recently employed in Ref. [5]. There the effects of Kondo correlations on the absorption spectrum of self-assembled QDs were measured in the limit $\Omega < T$, and the ability to resolve spectral features at $T < T_K$ was demonstrated. Starting from this system one would need to increase the laser power to reach $\Omega > T$ while measuring the resulting resonance fluorescence spectrum, or, alternatively, employ a continuous-wave laser pump-probe setup.

Model.—We consider a self-assembled QD in a semiconductor heterostructure, tunnel coupled to a FB. We assume laser light propagating along the heterostructure growth direction with right-handed circular polarization $\sigma_L = +1$ and a frequency ω_L close to the QD trion (X^-) resonance. We model the system by an excitonic Anderson model [4,9] augmented by a nonperturbative laser-QD interaction in the rotating wave approximation. We set $\hbar = k_B = 1$ and assume zero magnetic field. Optical selection rules imply that only the spin-down valence electron state will be optically excited, leading to the generation of a trion state involving a spin-up hole [Fig. 1(a)]. The spontaneous emission rate γ_{SE} is assumed to be negligibly small compared to all other energy scales. In the rotating frame, the Hamiltonian, to be called the “Rabi-Kondo model,” thus reads

$$\begin{aligned}
 H = & \sum_{\sigma} (\varepsilon_e - U_{e-h} \hat{n}_h) \hat{n}_{e\sigma} + U \hat{n}_{e\uparrow} \hat{n}_{e\downarrow} + (\varepsilon_h - \omega_L) \hat{n}_h \\
 & + \sum_{k\sigma} \varepsilon_{k\sigma} c_{k\sigma}^{\dagger} c_{k\sigma} + \sqrt{\Gamma/(\pi\rho)} \sum_{k\sigma} (e_{\sigma}^{\dagger} c_{k\sigma} + \text{H.c.}) \\
 & + \Omega e_{\downarrow}^{\dagger} h_{\uparrow}^{\dagger} + \text{H.c.}
 \end{aligned} \quad (1)$$

The first line defines the QD Hamiltonian, where $\hat{n}_{e\sigma} = e_{\sigma}^{\dagger} e_{\sigma}$, $\hat{n}_h = h_{\uparrow}^{\dagger} h_{\uparrow}$, while e_{σ}^{\dagger} and h_{\uparrow}^{\dagger} are, respectively, creation operators for QD spin- σ electrons ($\sigma = \uparrow, \downarrow$ or ± 1) and spin-up holes, ε_e and ε_h being the corresponding energies. We account for intradot Coulomb interaction by $U_{e-h} > 0$ and $U > 0$. To ensure a separated low-energy subspace formed by the states in Fig. 1(a), the laser detuning from the bare QD transition, $\delta_L = \omega_L - \varepsilon_e - U - \varepsilon_h + 2U_{e-h}$, has to be small in the sense defined below.

The second line of Eq. (1) models a noninteracting conduction band (the FB) of energies $\varepsilon_{k\sigma} \in [-D_0, D_0]$, with $\varepsilon_F = 0$ and constant density of states $\rho \equiv 1/(2D_0)$ per spin, tunnel coupled to the QD’s e level, giving it a width Γ . We assume $T \ll \Gamma \ll U \simeq U_{e-h} \ll D_0 \ll \varepsilon_h, \omega_L$ and investigate a situation where the QD carries one negative charge on average, $n_{e\uparrow} + n_{e\downarrow} - n_h \simeq 1$ [10]. The QD-laser coupling of strength Ω [last term of Eq. (1)] connects the trion and Kondo subspaces, with projectors $P_T = \hat{n}_h$ or $P_K = 1 - \hat{n}_h$. When $\Omega = 0$, these subspaces have hole and e -level occupancies $n_h^T = 1$ and $n_{e\sigma}^T \simeq 1$ or $n_h^K = 0$ and $n_{e\sigma}^K \simeq 1/2$, respectively, and ground states $|T\rangle$ and $|K\rangle$ with energy difference $\Delta E = E_{0,T} - E_{0,K}$.

Emission spectrum.—The emission spectrum at detuning ν from the laser frequency ω_L is proportional to the spectral function

$$S(\nu) = \sum_{n,m} \varrho_m |\langle n | h_{\uparrow} e_{\downarrow} | m \rangle|^2 \delta(E_n - E_m + \nu), \quad (2)$$

where $|m\rangle$ and E_m are eigenstates and eigenenergies of the Rabi-Kondo model. We assume that spontaneous emission has a negligible effect on the system’s steady state, which is taken to be a thermal state in the rotating frame at the temperature T of the solid state environment, $\varrho_m = Z^{-1} e^{-E_m/T}$ [9], and concentrate on $T = 0$. To simplify the discussion we will address mostly the $\Delta E = 0$ case below (achieved by properly tuning the laser frequency ω_L to resonance), where the secondary screening effect is most pronounced, and defer the treatment of finite ΔE to the Supplemental Material [9]. Figure 1(b) schematically summarizes the main features of typical numerical renormalization group (NRG) [11–13] results for the emission spectrum in Figs. 1(c) and 1(d).

For $\Omega \gg T_K$, no signatures of Kondo physics are expected. The emission spectrum can be completely understood in terms of a dressed state ladder with the assumption $\gamma_{SE} = 0$ and an intramanifold, FB-induced decay process [14,15]. The spectrum has two peaks: a broad peak at $|\nu_{\max}| = 2\Omega$ and a δ peak at $\nu = 0$, both with equal weight 0.25 [see Fig. 1(b), blue line].

The situation is much more interesting for the Kondo-dominated regime, $\Omega \ll T_K$, which we consider henceforth. Here one might attempt to treat the QD-laser coupling [last term in Eq. (1)] as a perturbation. This would yield a spectrum that is essentially the same as the $\Omega = 0$ spectrum calculated in Ref. [4]. However, we will show momentarily that this is correct only if the frequency $|\nu|$ is larger than a new energy scale $\Omega^* \ll T_K$.

Effective model.—In order to understand this restriction on the perturbative treatment of the QD-laser coupling, as well as to derive the low-frequency behavior, we introduce an effective Hamiltonian H' , which captures the essential physics of H in the entire regime $|\nu| < T_K$. It can be thought of as the result of integrating out the degrees of freedom in the Rabi-Kondo model H with energies larger

than T_K . We can concentrate on just two states of the QD together with the surrounding FB degrees of freedom: the Kondo singlet state restricted (subscript r) to a FB region of screening cloud size $\lesssim 1/T_K$, $|K\rangle_r$, and the trion state $|T\rangle_r$, with no screening cloud. We thus replace the QD and the nearby degrees of freedom of the FB by a two level system (TLS) whose $\sigma'_z = \pm 1$ (σ'_i being the Pauli matrices) eigenstates correspond to the $|T\rangle_r$ and $|K\rangle_r$, respectively. These are coupled by the laser and are split in energy. Furthermore, the outer electrons with energies $\lesssim T_K$ experience different scattering phase shifts depending on the state of the TLS. Taking $|K\rangle_r$ as reference state relative to which phase shifts are measured, we have $\delta_\sigma^K = 0$ and, by the Friedel sum rule [16], $\delta_\sigma^T = \Delta_\sigma \pi$, where $\Delta_\sigma = (n_{e\sigma}^T - \delta_{\sigma 1}) - n_{e\sigma}^K = \sigma/2$ is the total dot charge difference per spin between $|T\rangle_r$ and $|K\rangle_r$. All this is captured by the following Hamiltonian:

$$H' = \sum_{k\sigma} \varepsilon'_{k\sigma} c'_{k\sigma} c'_{k\sigma} + \Omega' \sigma'_x + \frac{\Delta E'}{2} \sigma'_z + P'_T \sum_{\sigma,k,k'} U'_\sigma c'_{k\sigma} c'_{k'\sigma} \quad (3)$$

The first term describes the FB degrees of freedom whose distance from the QD is larger than $\sim 1/T_K$, corresponding to a reduced half-bandwidth $D'_0 \sim T_K$. The second term describes optical excitations, with $\Omega' = \Omega_r \langle K|h_{\uparrow 1}e_1|T\rangle_r \propto \Omega$. The third term is the detuning, $\Delta E' = \Delta E$ [17]. Finally, the last term accounts for the scattering of the FB electrons by the TLS, where $P'_T = (1 + \sigma'_z)/2$ is a projector onto the trion sector. To reproduce the phase shifts mentioned above, we choose U'_σ equal to $-\sigma$ times a large positive numerical value ($\gg D'_0$) which satisfies $\pi \rho' U'_\sigma = -\tan(\Delta_\sigma \pi)$. NRG energy flow diagrams confirm that H' is a good description of the system below T_K [9]. For $|\nu| < T_K$, the emission spectrum $S(\nu)$ for the Rabi-Kondo model is reproduced qualitatively by $S'(\nu)$ computed as in Eq. (2), with H' and σ'_- replacing H and $h_{\uparrow 1}e_1$, respectively, [9].

Intermediate-frequency behavior and emergence of a new energy scale.—To lowest order in Ω' , the behavior of $S'(\nu)$ is governed by the AO between the TLS states $|K\rangle_r$ and $|T\rangle_r$, caused by the difference in phase shifts the FB electrons experience in the two states. The spectrum thus behaves as a power law, $S'(\nu) \sim |\nu|^{2\eta'_x - 1}$, with AO exponent $2\eta'_x = [\delta_\uparrow^K - \delta_\uparrow^T]^2/\pi^2 + [\delta_\downarrow^K - \delta_\downarrow^T]^2/\pi^2 = 1/2$ [13,18], in agreement with the $\Omega = 0$ results of Ref. [4]. This implies that the hybridization operator σ'_x has a scaling dimension $\eta'_x = 1/4 < 1$ and is thus a relevant perturbation near the fixed point $\Omega' = 0$. Thus the leading-order renormalization group flow equation for Ω' as one decreases the cutoff D' from its bare value D'_0 is [19]

$$D' \frac{d}{dD'} \left(\frac{\Omega'}{D'} \right) = (\eta'_x - 1) \frac{\Omega'}{D'} \quad (4)$$

The dimensionless coupling Ω'/D' therefore grows and becomes of order 1 when the cutoff reaches the scale

$$\Omega^* = D'_0 \left(\frac{\Omega'}{D'_0} \right)^{1/(1-\eta'_x)} \sim T_K \left(\frac{\Omega}{T_K} \right)^{4/3} \ll T_K \quad (5)$$

Hence, one may treat the term $\Omega' \sigma'_x$ [corresponding to the last term in Eq. (1)] as a perturbation only if $|\nu| \gg \Omega^*$. The power law $S(\nu) \sim |\nu|^{-1/2}$ thus applies at intermediate frequencies, $\Omega^* \ll |\nu| \ll T_K$. The power-law divergence of the spectrum is cut off around $|\nu| \sim \Omega^*$ [13], resulting in a maximum in the spectrum at this scale, as confirmed by the NRG data shown in Fig. 1. The emergence of this new energy scale is one of our central results. At low frequencies, $|\nu| \ll \Omega^*$, the physics is governed by a new fixed point, which we now discuss.

Secondary Kondo screening.—To understand this new fixed point we formally argue below that H' can be mapped onto the anisotropic Kondo model. This “secondary” Kondo model should not be confused with the original “primary” isotropic Kondo model for the QD spin. The role of the secondary Kondo temperature is played by Ω^* ; at energies below Ω^* , the original system flows to a strong-coupling fixed point featuring strong hybridization of Kondo and trion sectors, as confirmed by NRG level-flow data [9]. The low-energy behavior is universal when energies are measured in units of Ω^* .

One of the predictions of this secondary Kondo picture is that the ground state of H for $\Omega \ll T_K$ and $\Delta E = 0$ is an equal-amplitude superposition of the Kondo and trion states, with some secondary screening cloud, whose distance from the QD is larger than the primary Kondo length $\propto 1/T_K$. To understand this nested screening cloud structure, consider $|K\rangle$ (ground state for $\Omega = 0$, $\Delta E > 0$) as a reference state where the QD valence levels are filled and its conduction levels carry half an electron of each spin. Since the total spin is zero, the correlation function between the QD spin and the total FB spin is $\langle S_{\text{QD}}^z S_{\text{FB}}^z \rangle = \langle S_{\text{QD}}^z (S_{\text{FB}}^z + S_{\text{QD}}^z) \rangle - \langle (S_{\text{QD}}^z)^2 \rangle = -\langle (S_{\text{QD}}^z)^2 \rangle = -1/4$. This implies that when projecting into the subspace with spin-up (spin-down) in the QD, the FB has a net additional single spin-down (spin-up) electron [20] within a screening cloud up to a distance $\propto 1/T_K$ from the QD [indicated by ellipses in Fig. 2(a)]. If, on the other hand, $\Omega = 0$ but $\Delta E < 0$, the system is in the trion state $|T\rangle$ with two QD electrons and a spin-up hole, and no screening cloud [Fig. 2(b)]. The absorbed $\sigma_L = +1$ photon induces a change in QD charge per spin of Δ_σ , thus causing the phase shifts $\delta_\sigma^T = \sigma\pi/2$ with respect to the reference state, as mentioned above. Turning on the laser source Ω , when $\Delta E = 0$, the ground state is an equal-amplitudes superposition of the Kondo and trion states ($\langle P_T \rangle = \langle P_K \rangle = 1/2$), as depicted in Fig. 2(c). In analogy with the screening of a QD spin in a Kondo singlet, the FB screens the spin configurations of the $|T\rangle_r$ and $|K\rangle_r$ states, which, respectively, have spin $\sigma/4$ or $-\sigma/4$ with respect to their mutual average of $\sigma/4$, by

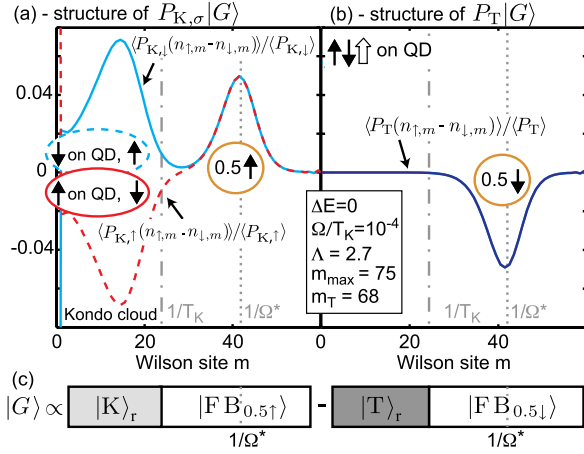


FIG. 2 (color online). NRG results for the Rabi-Kondo model Eq. (1). Distribution of magnetization $n_{1,m} - n_{1,m}$ along the Wilson chain, obtained after acting with QD projectors (a) $P_{K,\sigma} = P_K \hat{n}_{e,\sigma} (1 - \hat{n}_{e,\bar{\sigma}})$ and (b) P_T , for $\Omega/T_K = 10^{-4}$ and $\Delta E = 0$ at $T = 2 \times 10^{-14} D_0$ (corresponding to the energy scale of Wilson site $m_T = 68$). Even-odd oscillations have been averaged out. The QD is represented by site zero. In (a), the Kondo state, restricted to a region of size $\lesssim 1/T_K$ (subscript r), approximately $|K\rangle_r \propto |\uparrow\rangle|FB\rangle_r - |\downarrow\rangle|FB\rangle_r$, features a singlet configuration with FB magnetization opposite to that of the QD (left dip or peak structure). In (b) the $|T\rangle_r$ trivial FB configuration appears within the same length scale. The presence of a laser ($\Omega > 0$) combines the states $|K\rangle_r$ and $|T\rangle_r$ into a new ground state shown in (c), where FB states $|FB_{0.5\sigma}\rangle$ carry a magnetization of half a spin σ at distance $1/\Omega^*$ [peak in (a), dip in (b)]. The spin orientation of this secondary screening cloud is controlled by the laser polarization $\sigma_L = +1$.

creating FB spin configurations with an opposite spin of $-\sigma/4$ or $\sigma/4$ (i.e., half an electron spin) within distance $\sim 1/\Omega^*$ of the QD, respectively, [21]. This nested screening cloud indeed appears in the NRG results in Fig. 2, further confirming our effective low-energy description.

Low-frequency behavior and δ peak.—To derive the low-frequency behavior of the spectrum, as well as the appearance of the elastic δ peak mentioned in the introduction, we make the notion of “secondary Kondo effect” more precise. This can be done formally by transforming H' into a secondary Kondo model in two stages: (i) Upon bosonization of the FB [22] H' becomes the spin-boson model with Ohmic dissipation [23,24], the basic idea behind this mapping being that the low-lying particle-hole excitations of the FB are bosonic in nature, with a linear (Ohmic) density of states, and (ii) the spin-boson model can be mapped onto the anisotropic Kondo model [1,2]:

$$H'_K = -iv_F \sum_{\sigma=\pm 1} \int dx \psi_{\sigma}^{\dagger}(x) \partial_x \psi_{\sigma}(x) + \frac{J_z}{2} S'_z s'_z(0) + \frac{J_{xy}}{2} S'_z s'_z(0) + \text{H.c.} - \Delta E_z S'_z, \quad (6)$$

where $v_F = 1/(\pi\rho')$ is the Fermi velocity, S'_i are the components of the secondary Kondo impurity spin, and $s'_i(0) = \sum_{\sigma,\sigma'} \psi_{\sigma}(0)^{\dagger} \tau_i^{\sigma\sigma'} \psi_{\sigma'}(0)/2$ (τ_i being the Pauli matrices) are the FB spin density components in the vicinity of the impurity. Under this mapping $\sigma'_z = 2S'_z$ (hence, $\Delta E_z \propto \Delta E'$), but $\sigma'_+ \rightarrow S'_+ s'_-(0)$.

One can now use known results on H'_K to find the low-frequency ($|\nu| \ll \Omega^*$) behavior of the emission spectrum of H' . By the above mapping $S'(\nu)$ is proportional to the spectral function of the retarded correlator of $S'_+ s'_-(0)$ with its conjugate in H'_K . Since the anisotropic antiferromagnetic Kondo problem flows to the same strong-coupling fixed point as the isotropic version, the calculation of low-frequency power-law exponents can be done in the isotropic case $J_z = J_{xy}$, where the $S'_+ s'_-(0)$ correlator can be replaced by the $S'_z s'_z(0)$ correlator. At low energies, after the impurity spin is screened by the FB, $S'_z s'_z(0)$ can be replaced by the square of the local density of the z component of the electronic spin, which is a four-fermion operator. Thus, if the effective magnetic field vanishes, $\Delta E_z = 0$, its correlation function scales at long times ($t > 1/\Omega^*$) as t^{-4} , leading to a $\sim |\nu|^3$ low-frequency behavior of the corresponding spectral function. The same then applies to $S^{(l)}(\nu)$ in the regime $|\nu| \ll \Omega^*$. This is indeed the behavior of the NRG results, cf. Fig. 1(c) and Ref. [9].

The above picture leads to another implication for the spectrum: Since the relevant perturbation $\Omega' \sigma'_x$ strongly hybridizes, and thus cuts off the AO between the $|K\rangle$ and $|T\rangle$ states at energy scales smaller than Ω^* [13], a Dirac δ peak is now allowed to appear in the spectrum at $\nu = 0$. By the definition of $S'(\nu)$, its weight is $\delta_{\text{weight}} = |\langle \sigma'_x \rangle|^2$. Since Ω^* is the only low-energy scale, we expect that $\Omega' \langle \sigma'_x \rangle \propto \Omega^* \propto \Omega^{4/3}$. Hence, $\langle \sigma'_x \rangle \propto \Omega^{1/3} \propto \Omega^{1/3}$, leading to $\delta_{\text{weight}} \propto \Omega^{2/3}$, which is in excellent agreement with the NRG results, Fig. 1(d) [25,26].

Conclusions.—Laser excitation of a QD in the Kondo regime leads to a new correlated state featuring a nested spin screening cloud in the FB (Fig. 2) and gives rise to a specific double-peaked emission line shape (Fig. 1): (i) a broad peak centered at a renormalized Rabi frequency Ω^* [Eq. (5)], with a $\sim |\nu|^{-1/2}$ red tail, resulting from the AO between ground and postemission states resembling $|T\rangle$ and $|K\rangle$ at length scales $\ll 1/\Omega^*$. A Fermi-liquid-type blue tail stems from the cutoff of the AO by the relevant Rabi coupling, as ground and postemission states share a “common” FB configuration at length scales $\gg 1/\Omega^*$ due to the secondary screening cloud. (ii) This common FB region leads to a δ peak at $\nu = 0$ with weight $\propto \Omega^{2/3}$. The Ω dependence of the coherent Rayleigh scattering strength in the presence of a finite spontaneous emission rate γ_{SE} remains an open question.

We acknowledge helpful discussions with A. Rosch. This work was supported by an ERC Advanced

Investigator Grant (B. S. and A. I.). H. E. T. acknowledges support from the Swiss NSF under Grant No. PP00P2-123519/1. M. G. is supported by the Simons Foundation and the BIKURA (FIRST) program of the Israel Science Foundation, L. I. G. by NSF DMR Grants No. 0906498 and No. 1206612, and J. v. D., M. H., and A. W. by the DFG via NIM, SFB631, SFB-TR12, and WE4819/1-1.

- [1] A. Hewson, *The Kondo Problem to Heavy Fermions* (Cambridge University Press, Cambridge, England, 1993).
- [2] D. L. Cox and A. Zawadovski, *Adv. Phys.* **47**, 599 (1998).
- [3] L. Kouwenhoven and L. Glazman, *Phys. World* **14**, 33 (2001).
- [4] H. E. Türeci, M. Hanl, M. Claassen, A. Weichselbaum, T. Hecht, B. Braunecker, A. Govorov, L. Glazman, A. Imamoglu, and J. von Delft, *Phys. Rev. Lett.* **106**, 107402 (2011).
- [5] C. Latta *et al.*, *Nature (London)* **474**, 627 (2011).
- [6] B. R. Mollow, *Phys. Rev.* **188**, 1969 (1969).
- [7] E. B. Flagg, A. Muller, J. W. Robertson, S. Founta, D. G. Deppe, M. Xiao, W. Ma, G. J. Salamo, and C. K. Shih, *Nat. Phys.* **5**, 203 (2009).
- [8] C. Matthiesen, A. N. Vamivakas, and M. Atatüre, *Phys. Rev. Lett.* **108**, 093602 (2012).
- [9] See Supplemental Material at <http://link.aps.org/supplemental/10.1103/PhysRevLett.111.157402> for additional discussion of the Rabi-Kondo model H , the case of finite ΔE , the effective model H' with its emission spectrum, NRG flow diagrams and the theory of quantum quenches.
- [10] This requires $\Gamma \ll -\varepsilon_e, \varepsilon_e + U, -(2\varepsilon_e - 2U_{e-h} + U), -\varepsilon_e + U_{e-h} - U$.
- [11] R. Bulla, T. A. Costi, and T. Pruschke, *Rev. Mod. Phys.* **80**, 395 (2008).
- [12] A. Weichselbaum and J. von Delft, *Phys. Rev. Lett.* **99**, 076402 (2007); A. Weichselbaum, *Phys. Rev. B* **86**, 245124 (2012).
- [13] W. Munder, A. Weichselbaum, M. Goldstein, Y. Gefen, and J. von Delft, *Phys. Rev. B* **85**, 235104 (2012).
- [14] B. Sbierski and A. Imamoglu (to be published).
- [15] In the more realistic situation of a finite rate γ_{SE} , a Mollow triplet with a broadened peak at $\nu = 0$ and a blue detuned peak at $\nu = 2\Omega$ may develop.
- [16] J. Friedel, *Philos. Mag.* **43**, 153 (1952); *Can. J. Phys.* **34**, 1190 (1956); D. C. Langreth, *Phys. Rev.* **150**, 516 (1966).
- [17] More precisely, an offset is added to $\Delta E'$ such that $H'|\Omega', \Delta E'=0\rangle$ has a ground state degenerate in the two TLS sectors.
- [18] B. Roulet, J. Gavoret, and P. Nozieres, *Phys. Rev.* **178**, 1072 (1969); P. Nozieres, J. Gavoret, and B. Roulet, *ibid.* **178**, 1084 (1969); P. Nozieres and C. T. De Dominicis, *ibid.* **178**, 1097 (1969).
- [19] J. Cardy, *Scaling and Renormalization in Statistical Physics* (Cambridge University Press, Cambridge, England, 1996).
- [20] I. Affleck, [arXiv:0911.2209](https://arxiv.org/abs/0911.2209).
- [21] The total electron number is of course integer; if the screening cloud contains fractions of electrons, the rest is spread over the entire system, and thus does not contribute to the charge and spin distributions in the thermodynamic limit.
- [22] A. Gogolin, A. A. Nersesyan, and A. M. Tsvelik, *Bosonization and Strongly Correlated Systems* (Cambridge University Press, Cambridge, England, 1998).
- [23] U. Weiss, *Quantum Dissipative Systems* (World Scientific, Singapore, 1999).
- [24] A. Leggett, S. Chakravarty, A. Dorsey, M. Fisher, A. Garg, and W. Zwerger, *Rev. Mod. Phys.* **59**, 1 (1987).
- [25] The Ω scaling of the δ -peak weight can also be found as follows: it scales as the spectral weight that goes missing from the $\Omega = 0$ emission spectrum $\propto |\nu|^{-1/2}$ when the latter is cut off at $\nu \simeq \Omega^*$: $\int_0^{\Omega^{4/3}} d\nu \nu^{-1/2} \propto \Omega^{2/3}$.
- [26] However, further work including spontaneous emission in the theoretical treatment would have to revisit the actual form of the spectrum for $|\nu| < \gamma_{SE}$ and the distribution of δ_{weight} into an elastic and inelastic contribution.

Supplemental Material: “Proposed Rabi-Kondo Correlated State in a Laser-Driven Semiconductor Quantum Dot”

Discussion of the Hamiltonian H and Born-Markov approximation

Here we discuss the form of the Rabi-Kondo model Hamiltonian H , Eq. (1) in the main text, in more detail. The QD part reads $H_{\text{QD}} = \sum_{\sigma} (\varepsilon_e - U_{\text{eh}} n_h) n_{e\sigma} + U n_{e\uparrow} n_{e\downarrow} + \varepsilon_h n_h$. The eigenenergies are conveniently displayed vs. the gate voltage which controls ε_e and ε_h , in Fig. S1(a). The lowest energy QD state in the subspace with hole number $n_h = 0$ or 1 is denoted by a purple or blue solid line, respectively. We focus on a gate voltage regime around V_0 , as marked in Fig. S1(a). In this regime the lowest energy QD states carry one negative charge. Applying a monochromatic laser with photon energy $\omega_L \simeq \varepsilon_h$ leads to the rotating frame Hamiltonian $H_{\text{QD,L}} = \sum_{\sigma} (\varepsilon_e - U_{\text{eh}} n_h) n_{e\sigma} + U n_{e\uparrow} n_{e\downarrow} + (\varepsilon_h - \omega_L) n_h$, effectively shifting the purple line to the vicinity of the blue line. If the detuning δ_L to the bare QD transition is small, then there exists a low energy description of $H_{\text{QD,L}}$ involving only the states $|\uparrow\rangle, |\downarrow\rangle$ and the trion $|\uparrow\downarrow\uparrow\rangle$ shown in Fig. 1(a) of the main text.

We now add to $H_{\text{QD,L}}$ the QD-laser coupling in rotating wave approximation, $H_{\text{QD-L}} = \Omega e^{\dagger} h^{\dagger} + \text{h.c.}$, (we assume a circularly polarized laser and apply optical selection rules to simplify the problem, see main text) and a radiative reservoir H_{rad} (leading to a spontaneous emission rate γ_{SE} on the order of $1\mu\text{eV}$). For $\Omega \gg \gamma_{\text{SE}}$ a three-peak Mollow triplet, similar to the red curve in Fig. S1(b), can be detected in the RF spectrum. The central peak appears at the laser frequency, $\omega = \omega_L$ and the two side peaks at detuning $\nu = \omega - \omega_L = \pm 2\Omega$.

If we now include the fermionic bath (FB), $H_{\text{FB}} = \sum_{k\sigma} \varepsilon_{k\sigma} c_{k\sigma}^{\dagger} c_{k\sigma}$, and the QD-FB hybridization $H_{\text{QD-FB}}$, the Hamiltonian reads $H + H_{\text{rad}}$ with H as in Eq. (1) of the main text. For a weak QD-FB coupling and temperatures $T > T_{\text{K}}$ we make a Born-Markov approximation for the QD-FB coupling [1, 2], the corresponding transition rates in the dressed-QD Master equation crucially rely on the ratio between laser Rabi frequency Ω and sample temperature T . While $\Omega \ll T$ leads to a broadening of the ordinary Mollow RF-spectrum by symmetric thermal rates γ_{T} in each dressed-state manifold, a dominant laser $\Omega \gg T$ results in asymmetric intra-manifold rates γ_{Ω} and an asymmetric doublet in the RF spectrum, see Fig. S1(b), along with the dressed-state schematics. In this case, the FB cannot provide the energy difference for an upward transition between the dressed states. In experiment, the formation of an asymmetric doublet would have to be carefully distinguished from the effect of a finite laser detuning [which we have set to zero in Fig. S1(b)].

To access Kondo physics, $T < T_{\text{K}}$ is required and the Born-Markov treatment of the dressed QD-FB interaction is no longer valid. With the spectral function defined as

$$S(\nu) = \frac{1}{2\pi} \int_{-\infty}^{\infty} d\tau \langle \langle (he_{\downarrow})^{\dagger}(\tau) (he_{\downarrow}) \rangle \rangle_{\text{ss}} e^{-i\nu\tau}. \quad (\text{S1})$$

the RF-spectrum is given by $\gamma_{\text{SE}} \cdot S(\nu)$ [3]. Here, the occurrence of γ_{SE} shows that H_{rad} has explicitly been used in the derivation. If the coupling to the radiative reservoir is weak (i.e. γ_{SE} smaller than all other energy scales), we neglect H_{rad} to higher order in Eq. (S1), i.e. we approximate $(he_{\downarrow})^{\dagger}(\tau) \simeq e^{i\tau H} (he_{\downarrow})^{\dagger} e^{-i\tau H}$. Further, a similar approximation is done for the steady state density matrix ρ_{ss} used in

Eq. (S1) ($\langle \dots \rangle_{\text{ss}}$ denotes a trace over ρ_{ss}): We assume that thermalization of the system due to the solid state environment at temperature T takes place on timescales much faster than spontaneous emission. Then, we neglect H_{rad} for ρ_{ss} and assert that

$$\rho_{\text{ss}} = \rho_{\text{eq}} = e^{-H/T} / \text{Tr} \left(e^{-H/T} \right) \quad (\text{S2})$$

serves as a good approximation of the steady state. This leads to a RF spectrum that has support for $\nu \lesssim T$ only. We will further discuss effects related to the neglect of H_{rad} in the last section of this Supplemental Material.

With these two important simplifications, the numerical study is facilitated considerably, Eq. (S1) can be written in Lehmann form and we arrive at Eq. (2) of the main text where the eigenstates and -energies of H (as computed approximately by NRG) are used.

To conclude, the main text investigates how the asymmetric two peak structure (blue line in Fig. S1(b)) for $\Omega \gg T > T_{\text{K}}$ changes when we increase the QD-FB coupling beyond perturbatively weak values, i.e. increase T_{K} above T . We investigate the more interesting regime $T_{\text{K}} \gg \Omega$ in detail and comment briefly on the case $T_{\text{K}} \ll \Omega$.

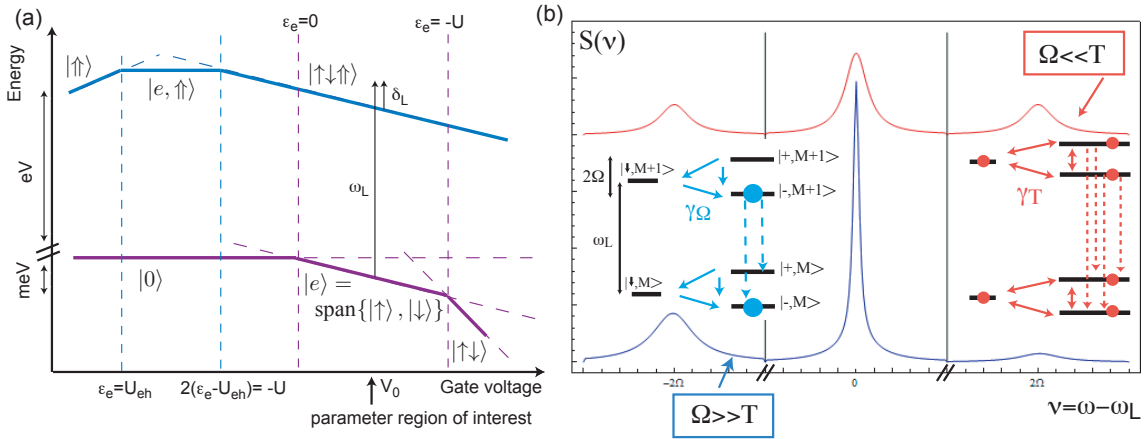


Figure S1: (a) Energy level diagram for H_{QD} vs. gate voltage. We assume that the gate voltage is tuned to the vicinity of V_0 where the ground state of $H_{\text{QD}}|_{n_h=0}$ and $H_{\text{QD}}|_{n_h=1}$ carries one negative charge, ω_L is the laser frequency and δ_L the detuning from the bare QD-transition. (b) Application of a resonant laser ($\delta_L = 0$) and weak coupling to a FB at temperature $T \gg T_{\text{K}}$ leads to formation of QD dressed states $|\pm\rangle = (|\uparrow\downarrow\uparrow\rangle \pm |\uparrow\rangle) / \sqrt{2}$ where $|\uparrow\rangle$ and $|\downarrow\rangle$ denote QD states carrying one electron of spin up or down, respectively, while $|\uparrow\downarrow\uparrow\rangle$ denotes a negatively charged exciton including a hole. The index M or $M - 1$ counts the number of excitations (i.e. laser photons + holes), see [3], Ch. VI. Intra-manifold rates induced by the FB are denoted by solid arrows, steady state population by filled circles and spontaneous emission transitions by dashed arrows. The RF spectrum calculated using a Markovian master equation (neglecting Kondo correlations) shows a broadened Mollow triplet for $T_{\text{K}} \ll \Omega \ll T$ (red) and an asymmetric doublet for $\Omega \gg T \gg T_{\text{K}}$ (blue).

NRG energy flow diagrams for the Rabi-Kondo model H

The numerical renormalization group (NRG) is a method to approximately diagonalize quantum impurity Hamiltonians where a few-level system, described by H_{imp} (the impurity - or, in modern literature, the QD) is coupled to a (fermionic) bath, $H = H_{\text{imp}} + H_{\text{imp-FB}} + H_{\text{FB}}$ [4]. The strategy is to approximate H_{FB} by

a tight-binding (Wilson-)chain where the coupling between two successive sites is exponentially decreasing as $\Lambda^{-n/2}$ for site index n , where $\Lambda > 1$ is a non-physical NRG discretization parameter. The QD is included as a site with index zero, only coupled to the first FB Wilson site (QD plus first FB Wilson site will be called “odd” Wilson chain). Each Wilson site can be identified with an exponentially decreasing energy scale $\Lambda^{-n/2}$, or, by looking at the associated fermionic wavefunction, with an exponentially increasing spatial separation $\Lambda^{n/2}$ from the QD position.

Due to the separation of energy scales along the Wilson chain, the chain Hamiltonian H_N , restricted to the first N sites, can be diagonalized iteratively. After multiplying H_N by $\Lambda^{N/2}$, the lowest eigenenergies can be plotted vs. N in an NRG energy flow diagram, thus showing high to low energy scales of H from left to right. Moreover, as a Wilson site can also be identified with a length scale in the impurity problem, the NRG flow accesses physics at increasing spatial separation from the impurity site with increasing N . Regions in which the rescaled eigenenergies form parallel horizontal lines are called fixed points - they can be described by fixed point Hamiltonians which are invariant under the renormalization group transformation.

Compared to computations of the quench spectral function in Ref. [5] for $\Omega = 0$, there are considerable conceptual changes for the computation in the $\Omega > 0$ case, described by the Rabi-Kondo model Hamiltonian, written as

$$H = \begin{pmatrix} H_T & \Omega e_{\downarrow}^{\dagger} h_{\uparrow}^{\dagger} \\ \Omega h_{\uparrow} e_{\downarrow} & H_K \end{pmatrix}. \quad (\text{S3})$$

Most important is the loss of a quench setup between initial and final Hamiltonian, meaning that the hole is to be treated as a dynamic quantity. The NRG calculation in [5] relied on two separate NRG runs, separately diagonalizing the initial and final Hamiltonian given by $H_K \equiv P_K H P_K$ and $H_T \equiv P_T H P_T$, respectively. Then the corresponding two sets of eigenstates and -energies entered the analogue of Eq. (2). For $\Omega > 0$, however, we have to use only *one* NRG run for the full Hamiltonian H . Since this technical change comes with a number of important consequences, we first discuss these issues in the simple $\Omega = 0$ case.

For $\Omega = 0$, we define the ground state energy difference between H_T and H_K as

$$\Delta E \equiv E_{0,T} - E_{0,K} \quad (\text{S4})$$

which has two contributions: On the one hand, the laser detuning δ_L from the bare QD transition affects ΔE trivially, on the other hand, a hybridization $\Gamma > 0$ causes Kondo correlations in the H_K Kondo singlet ground state $|K\rangle$ that additionally lower its energy. The energy level diagram is shown in Fig. S2(a) for $\Delta E > 0$ (laser tuned to bare QD transition, $\delta_L = 0$) and $\Delta E = 0$ (b). Note that with a single logarithmic discretization, only low-lying eigenstates close to the overall ground state energy are resolved with increasing accuracy (orange rungs in Fig. S2 are NRG energy eigenvalues). This means if we use for example $\delta_L = 0$ ($\Delta E > 0$), as shown in (a), the state $|K\rangle$ is well resolved while the $|T\rangle$ state is not well described in NRG and does not have a reasonable steady state population since $\rho_{ss} \propto e^{-H/T}$. Numerically feasible is the case shown in (b). Using a laser blue-detuned with respect to the bare QD transition ($\delta_L > 0$), one can counteract the correlation energy and push the $|K\rangle$ up (relative to $|T\rangle$) to

adjust $\Delta E = 0$. This leads to good resolution and finite population for both ladders, as the steady state expectation values $\langle P_K \rangle \simeq 0.5 \simeq \langle P_T \rangle$ show.

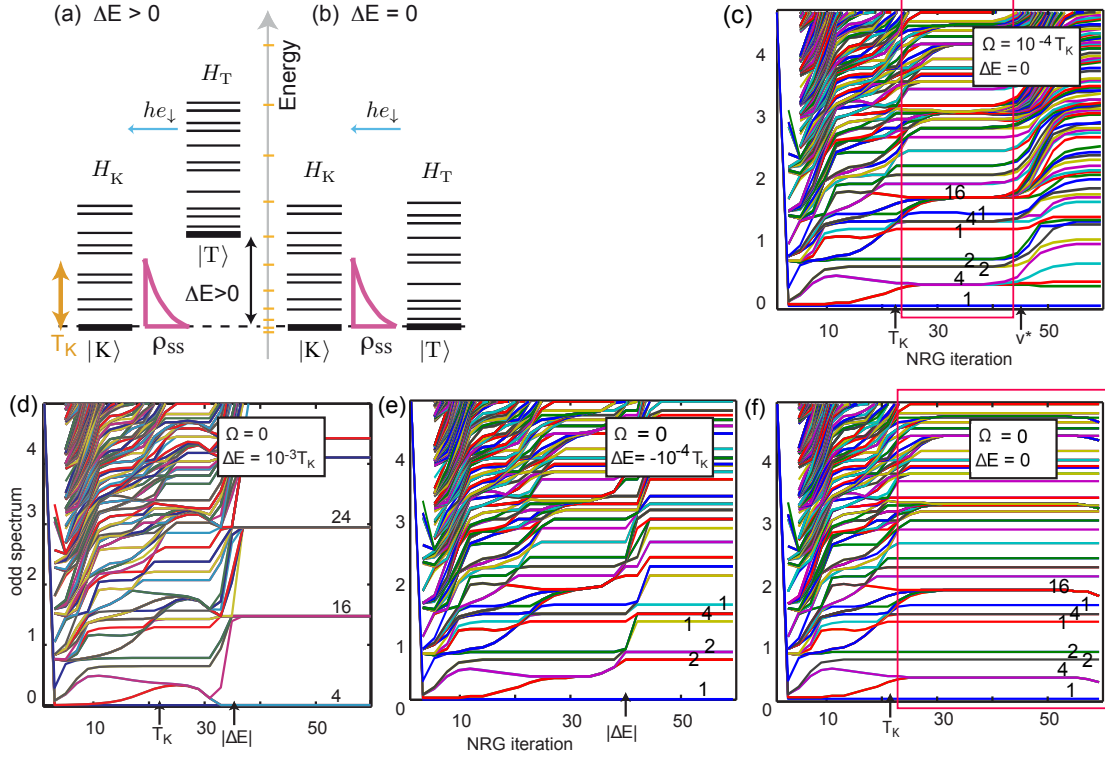


Figure S2: Effect of ΔE for one NRG diagonalization in the $\Omega = 0$ case: (a) $\Delta E > 0$ features a good resolution for the highly-correlated low-energy states above $|K\rangle$, but not for the trionic states above $|T\rangle$ and there is only a very small steady state hole population. (b) For $\Delta E = 0$, a good resolution for both families of states is achieved along with approximately equal steady state population in both ladders. (c) to (f): Flow diagrams for various parameter combinations ΔE and Ω , with the red box showing the intermediate fixed point $H|_{\Omega=0}$. The NRG parameters are: Discretization $\Lambda = 2.7$, number of kept states $N_{\text{keep}} = 1800$ and chain length $N_{\text{max}} = 60$. The model parameters are the same as in Fig. 2 in the main text and the numbers attached to the final fixed point levels denote the degeneracies of the respective eigenenergies.

To find the right laser energy to compensate the ground state energy difference and ensure $\Delta E = 0$, NRG flow diagrams are employed: Both Hamiltonians H_T and H_K have distinct and well understood low energy fixed points: The H_K fixed point [obtained by setting $\Delta E > 0$ and $\Omega = 0$, see Fig. S2 (d)] describes the primary Kondo singlet state and its excitations. The degeneracies for odd Wilson site indices n ('odd spectrum') are 4, 16, The H_T fixed point, describing the trion state and its excitations [$\Delta E < 0$ and $\Omega = 0$, see Fig. S2 (e)] features the degeneracies 1, 2, 2, 1, 4, 1, Consequently, since we still consider the uncoupled $\Omega = 0$ case, the H flow diagram for $\Delta E = 0$ [Fig. S2 (f)] consists of a combination of the flow diagrams of the two decoupled Hamiltonians H_T and H_K . This can be seen in detail by comparing state degeneracies (1, 4, 2, 2, 1, 4, 1, 16, ...) which are a combination of the aforementioned degeneracies of H_K and H_T . We used this fact as a technical trick guiding us how δ_L should be fine-tuned to reach $\Delta E = 0$.

We now turn to the case where the trion and photon subspaces are coupled by stimulated absorption

and emission events for $\Omega > 0$. The parameter ΔE is still defined with respect to the $\Omega = 0$ case. Due to the discretization issues mentioned above, results for $|\Delta E| \gg \Omega$ should be regarded with care. We diagonalize the full Rabi-Kondo model, Eq. (S3). The flow diagram for $\Omega = 10^{-4}T_K$ and $\Delta E = 0$ is shown in Fig. S2(c). We observe the emergence of a new fixed point below an energy scale

$$\nu^* \simeq \max(|\Delta E|, \Omega^*) \quad (\text{S5})$$

which generalizes Ω^* from Eq. (5) for finite ΔE .

Between the scales T_K and ν^* , the fixed point spectrum for $\Omega > 0$ in Fig. S2 (c) has the same structure as the fixed point found for $\Omega = 0$ in Fig. S2 (f), as can be seen by comparison of the red boxes. Hence, the intermediate fixed point for $\Omega > 0$ in Fig. S2 (c) can be understood as a combination of H_K and H_T . This further implies that the QD-perturbation Ω , though local, only affects the system far away from the QD.

Eq. (S5) can be understood by noting that for finite $\Delta E^{(l)}$ the RG flow, Eq. (4), is augmented by a similar equation for $\Delta E'$ which, like the displaced charges, scales with $\Delta E'/D'$ and Ω'/D' in second order. Since $\Delta E'/D'$ and Ω'/D' are small initially compared to unity, $\Delta E'$ and U'_σ do not flow appreciably under RG. Consequently, in the RG flow, the normalized TLS parameters Ω'/D' and $\Delta E'/D'$ increase. As soon as the larger one reaches unity, the scaling equations lose validity. For $|\Delta E'| \ll \Omega^*$, the renormalized Rabi frequency Ω' will increase to the renormalized bandwidth D' before D' reaches $\Delta E'$ and we enter the strong- Ω fixed point below Ω^* , as discussed in the main text. If however $|\Delta E'| \gg \Omega^*$, the TLS energy splitting $\Delta E'$ determines the scale of the uncoupled fixed point, as expressed in Eq. (S5), for the unprimed parameters of the original model H .

The effect of Eq. (S5) on the broad peak position $|\nu_{\max}|$ of the emission spectrum is shown in Fig. S3(a). Analogously, the expression for the weight of the δ -peak is also modified with a cutoff at $|\Delta E| = \Omega^*$ (Fig. S3(b)). For $|\Delta E| \gg \Omega^*$ the ground state contains either the trion or the Kondo state, so that $\delta_{\text{weight}} = |\langle h_\uparrow e_\downarrow \rangle|^2$ vanishes due to AO between ground and post-quench state.

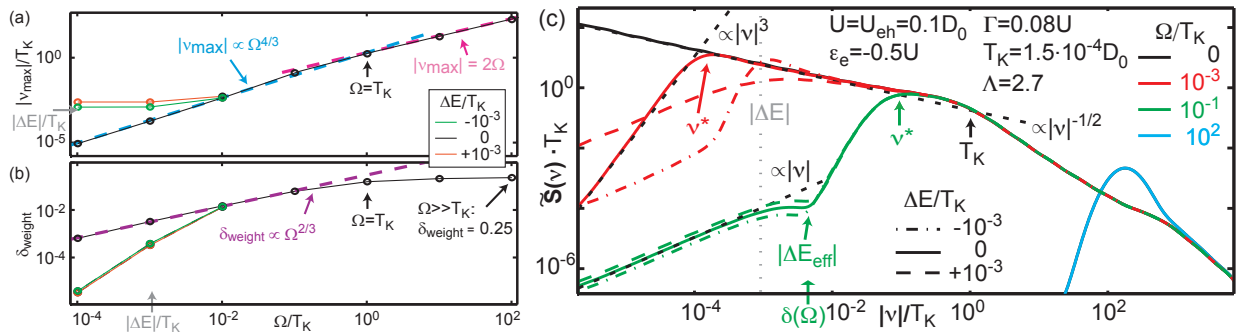


Figure S3: NRG results for the Rabi-Kondo model, Eq. (1), for finite ΔE : The position of broad peak $|\nu_{\max}|$ in (a) and the weight of δ -peak in (b) both deviate from the $\Delta E = 0$ case at $\Omega^* \simeq \Delta E$ where the nature of the low energy fixed point changes according to Eq. (S5). (c) Log-log plot of the normalized broad emission peak ($\tilde{S}(\nu < 0)$, for details on the normalization see below) for various parameters Ω and ΔE . Thick solid lines denote spectra with $\Delta E = 0$, dashed and dash-dotted lines represent $\Delta E = \pm 10^{-3}T_K$, respectively. The straight dashed lines represent power-law functions.

Quantum Quenches and Beyond: Anderson Orthogonality, Hopfield Rule and their application for $S(\nu)$

In this section, we provide some background information on the concept of Anderson Orthogonality (AO), the Hopfield Rule and their application in the discussion of the emission spectrum $S(\nu)$. The basic idea is that for $\Omega = 0$ spontaneous emission can be thought of as a transition corresponding to a quantum quench, showing AO, while for $\Omega \neq 0$, the signatures of AO are cut off at sufficiently low frequencies.

Anderson Orthogonality (AO) and Hopfield Rule (see also Ref. [6] for an extensive discussion): Whenever a quantum quench changes the local scattering potential for a FB, the overlap between the initial and final FB ground states, $|G_i\rangle$ and $|G_f\rangle$, vanishes with increasing electron number N as $|\langle G_i|G_f\rangle| \propto N^{-\frac{1}{2}\Delta_{\text{AO}}^2}$ where Δ_{AO} is called the AO exponent. In the thermodynamic limit $N \rightarrow \infty$, the initial and final ground states are thus orthogonal for $\Delta_{\text{AO}} \neq 0$. There are two important remarks: (i) Anderson [7] showed that the exponent Δ_{AO} equals the displaced electronic charge (in units of e) in the quench, i.e.

$$\Delta_{\text{AO}} = \langle G_f|n_{\text{tot}}|G_f\rangle - \langle G_i|n_{\text{tot}}|G_i\rangle, \quad (\text{S6})$$

where n_{tot} counts the (spinless) electrons in a large volume V_{large} including the scattering site (QD). For spinful fermions, if the spin-channels are decoupled such that the FB ground states factorize, the correspondence is generalized to

$$\Delta_{\text{AO}}^2 = \Delta_{\text{AO},\downarrow}^2 + \Delta_{\text{AO},\uparrow}^2. \quad (\text{S7})$$

Note that by Friedel's sum rule, the displaced charge is connected to the scattering phase shift δ_σ for electrons with spin $\sigma = \pm$ by $\Delta_{\text{AO},\sigma} = \delta_\sigma/\pi$. (ii) AO has important consequences for the low frequency behavior of generic quench spectral functions \mathcal{A} similar to $S(\nu)$ in Eq. (2). AO causes the spectral function to behave as $\mathcal{A}(\nu) \propto \nu^{-1+\Delta_{\text{AO}}^2}$, where ν is measured with respect to a threshold frequency.

Application of AO to emission spectrum $S(\nu)$: We start our discussion with the quench Hamiltonian $H|_{\Omega=0} = H_{\text{QD,L}} + H_{\text{QD-FB}} + H_{\text{FB}} = H_{\text{K}} + H_{\text{T}}$ which we represent schematically in Fig. S4(a). The dashed line between the QD (circle) and the FB (box, in Wilson chain approximation) represents a tunnel coupling, the horizontal axis denotes decreasing energy or increasing length scales as in a NRG flow diagram (see above). If we assume $\Delta E = 0$, the degenerate ground state $|G\rangle|_{\Omega=0}$ is a superposition of the trionic state $|T\rangle$, ground state of H_{T} shown in (b), and the Kondo singlet state $|K\rangle = (|\uparrow\rangle|FB_\downarrow\rangle - |\downarrow\rangle|FB_\uparrow\rangle)/\sqrt{2}$, ground state of H_{K} , depicted in (c). While $|K\rangle$ features strong correlations between QD and FB, the trion state can be well approximated as a simple QD-FB product state $|T\rangle = |\uparrow\downarrow\uparrow\rangle|FB_0\rangle$ where $|FB_0\rangle$ is the unperturbed Fermi sea, i.e. all Wilson sites are half occupied. Let us take the state $|K\rangle$ as reference, where the QD valence levels are filled (no holes present) and its conduction levels harbor half an electron of each spin. The region where the FB parts of the $|K\rangle$ state, $|FB_\sigma\rangle$, support an additional spin σ (the screening cloud) is encircled by a yellow ellipse. Relative to $|K\rangle$, the state $|T\rangle$ features displaced charges $\Delta_{\text{T},\sigma} = \sigma/2$, respectively (the \uparrow -hole counts like a missing \downarrow -electron). Before discussing emission, let us consider an absorption event. Acting on $|G\rangle|_{\Omega=0}$ with the operator $e_{\downarrow}^\dagger h_{\uparrow}^\dagger$, we first project on the component $|K\rangle$ and then create a hole and a spin down electron in the conduction level. The resulting state can “lower its energy” [8] by adjusting its spin configuration to the $|T\rangle$ state (b).

A priori, it is not obvious how an absorption process described by the operator $e_{\downarrow}^\dagger h_{\uparrow}^\dagger$ for Hamiltonian

H can be treated in the framework of AO. First, we recall a non-trivial feature of the Anderson impurity model underlying H_K , namely that the low-energy fixed point below T_K can be described by potential scattering off the complicated Kondo screening cloud structure [5]. This observation implies that AO plays a role only for $|\nu| < T_K$, as documented by an $-1/2$ power-law tail [5] which is explained as follows: Comparing the final state $|T\rangle$, to the initial state $|K\rangle$, the displaced charges (Eq. (S6)) read $\Delta_\sigma \equiv \Delta_{T,\sigma} - \Delta_{K,\sigma} = \sigma/2$. Consequently, for the quench connecting these two ground states in the long time limit, we find from Eq. (S7)

$$\Delta_{\text{AO}}^2 = \Delta_{\text{AO},\downarrow}^2 + \Delta_{\text{AO},\uparrow}^2 = (\Delta_{T,\uparrow} - \Delta_{K,\uparrow})^2 + (\Delta_{T,\downarrow} - \Delta_{K,\downarrow})^2 = 0.5. \quad (\text{S8})$$

Since only the magnitude of the displaced charges, $(\Delta_{T,\sigma} - \Delta_{K,\sigma})^2$, enters this equation, Δ_{AO}^2 and the $-1/2$ power-law tail is the same for the emission process.

The second issue is the presence of the coherent laser drive, $H_{\text{QD-L}} \propto \Omega$ in H leading to stimulated absorption and emission processes. Thus spontaneous emission or absorption does *not* introduce a quantum quench, since the subspaces P_T and P_K are not dynamically decoupled [9]. However, if Ω is small, we can expect that the post-emission dynamics is not affected by the existence of Ω up to some time $\tau = 1/\Omega^*$ (i.e. $e^{i\tau H}(h_\uparrow e_\downarrow)^\dagger e^{-i\tau H} \simeq e^{i\tau H|_{\Omega=0}}(h_\uparrow e_\downarrow)^\dagger e^{-i\tau H|_{\Omega=0}}$ in Eq. (S1) for $\tau < 1/\Omega^*$) and that the spectral function therefore shows AO behavior as in a proper quench situation for $|\nu| > \Omega^*$. The relation between Ω^* , Ω and the displaced charges can be found by a renormalization group analysis as sketched in the main text.

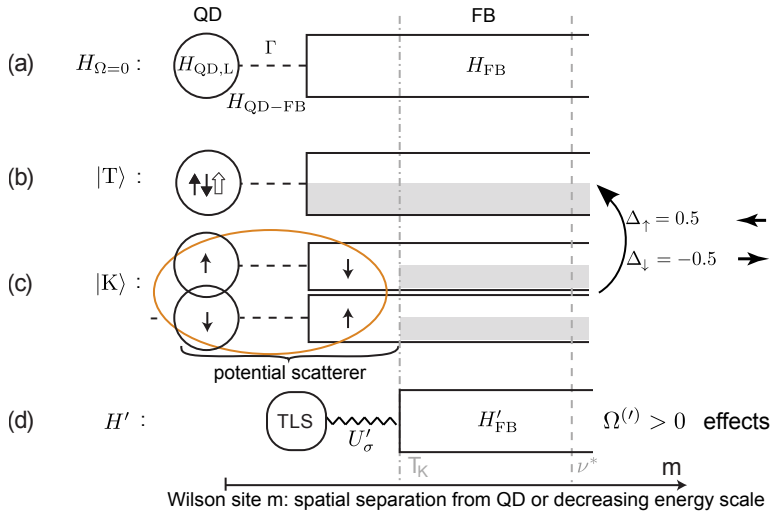


Figure S4: Cartoon of some Hamiltonians and states mentioned in the main text. (a) The quench Hamiltonian $H|_{\Omega=0}$ is of quantum impurity type, featuring a local QD and laser part tunnel coupled to the extended FB. The trionic state (b) can lower its energy after a spontaneous emission process mediated by $h_\uparrow e_\downarrow$ by the formation of correlations (c) between QD and surplus FB spins where the latter are contained in a region of extent $1/T_K$ around the QD (yellow ellipse). The Kondo singlet and trion configuration both act as potential scatterers for the surrounding FB electrons. The effective Hamiltonian H' , which explicitly contains a potential scattering term $\propto U'_\sigma$ in the trion sector, reproduces the respective scattering phase shifts of (b) and (c). In any case, effects due to $\Omega > 0$ are relevant above length scales $1/\nu^*$.

Effective model H'

Considering the NRG energy flow diagrams of the Rabi-Kondo model H in Fig. S2 we noticed that the intermediate fixed point spectrum above ν^* is composed simply of a combination of the spectra of H_K and H_T . This shows that in this intermediate energy range, the spectrum of the full Hamiltonian space can be decomposed into a direct sum of two subspectra, one describing the primary Kondo singlet state and its excitations, the other the trion and its excitations. These get coupled only at energy scales below ν^* . This fact is the main motivation for constructing the effective Hamiltonian H' .

Before comparing H and H' NRG energy flow diagrams, we augment the heuristic derivation of the effective model H' given in the main text in Eq. (3) by an intuitive graphical explanation in Fig. S4. The effective model H' denoted schematically in Fig. S4(d) is designed to describe the effect of the transition between $|T\rangle$ and $|K\rangle$ [from (b) to (c)] on FB electrons beyond a separation $1/T_K$ from the QD. The two-level-system (TLS), representing the QD plus the FB up to distance $1/T_K$, controls the scattering potential U'_σ [wavy line in (d)] for the surrounding FB electrons. If the TLS changes its state, so does the scattering potential – not only after a time scale $1/T_K$ but (within the approximation of replacing H by H') instantaneously like in a X-ray absorption process. For $\Omega' = 0$, σ'_z is conserved and the displaced electronic charge in a transition from $|K\rangle_r$ to $|T\rangle_r$ (TLS raising operators) is $\Delta'_\sigma = -1/\pi \cdot \arctan(\pi\rho U'_\sigma)$ (in units of e , e.g. [6]). To reproduce the displaced charge $\Delta_\sigma = \sigma/2$ as found above, we require $\rho'U'_\sigma$ being equal to $-\sigma$ times a numerical value large compared to unity (we take $\rho'U'_\sigma = -50 \times \sigma$).

Now we can also consider the coherent QD-laser coupling. It is not a priori clear that H' as given in Eq. (3), and the reasoning laid out above, would still be applicable for $\Omega^{(l)} > 0$. However, our NRG calculations show (in accordance with a renormalization analysis and the discussion below Eq. (S5)) that the $H|_{\Omega>0}$ flow diagram does not differ from the $\Omega = 0$ case for energies higher than ν^* (compare Figs. S2(c) and (f)), implying that it is indeed valid to consider the development of potential scattering and the effects of Ω *separately* as long as $\nu^* \ll T_K$.

NRG energy flow comparison for H and H' : One of the implicit assumptions in replacing H by the effective Hamiltonian H' with the scattering phase shifts as given above is that $n_{e\uparrow} + n_{e\downarrow} - n_h$ exactly equals one. With the physical parameters as in Fig. 2 in the main text, this is only approximately true due to $U_{eh} < \infty$. Although this small deviation has no observable consequences in the emission spectrum, turning to NRG energy flow diagrams resolving minute details of eigenstates and -energies, this issue will matter. Therefore, as an intermediate step for a flow diagram bases comparison of H and H' , in Fig. S5 (a)-(c) we show the (odd) flow diagrams for $H|_{U_{eh}=100D_0}$ where, as compared to the original H spectra in Fig. S2, certain degeneracies in the trionic sector are restored. These flow diagrams then indeed agree with those for the effective model H' [panels (d)-(f)].

Discussion of emission spectra for $H^{(l)}$ in the case $\Delta E^{(l)} \neq 0$

In Fig. S3(c), the Rabi-Kondo model emission spectrum, shown in Fig. 2(b,c) of the main text, is repeated for finite ΔE . Since the total spectral weight is given by $\langle n_h n_{e\downarrow} \rangle \simeq O(\langle n_h \rangle)$, it is strongly dependent on ΔE . To enable mutual comparison between results for different values of ΔE we normalize all NRG spectra in this Supplemental Material as $\tilde{S}(\nu) \equiv S(\nu) / \langle n_h \rangle$. Fig. S6(a) schematically summarizes the

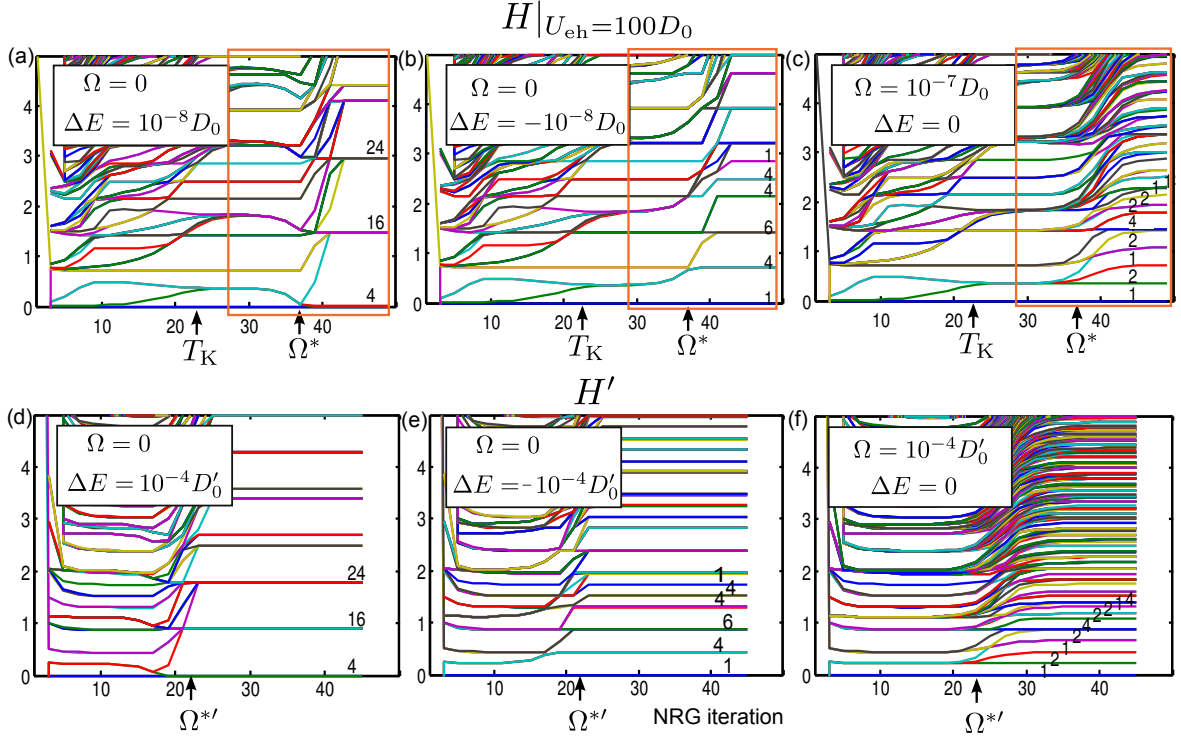


Figure S5: Comparison of NRG energy flow diagrams for $H|_{U_{eh}=100D_0}$ [panels (a)-(c)] and H' [panels (d)-(f)] for $\Delta E^{(\prime)} \leq 0$ and $\Omega^{(\prime)} > 0$. With the QD/TLS defined as Wilson site zero, the $H|_{U_{eh}=100D_0}$ flow diagrams show odd NRG iterations and the H' diagrams even iterations such that an odd number of Wilson sites has been integrated out in going from H to H' . The H' flow diagrams mimic those of portions [boxed] of the $H|_{U_{eh}=100D_0}$ flow diagrams that show the crossover from the intermediate to the strong-coupling fixed point.

generic features of the line shape. Coming from large detunings $|\nu|$, the characteristic power-law tails with exponents -2 (in the free orbital (FO) regime), -1 (in the local moment (LM) regime) and $-1/2$ (in the strong coupling (SC) regime), found and discussed by Türeci *et al.* in Ref. [5], are present also for $\nu^* < T_K$. Curly brackets indicate the range of validity of several Hamiltonians mentioned in the main text. While treating Ω perturbatively using the quench Hamiltonian $H|_{\Omega=0}$ is a valid approximation for $|\nu| > \nu^*$, the effective Hamiltonian in Eq. (3) provides the appropriate approximate description for $|\nu| < T_K$ and can explain the emergence of the low energy fixed point below ν^* . The RF spectrum for the effective Hamiltonian H' , calculated using Eq. (2) but with H' and σ'_- taking the place of H and $h_{\uparrow}e_{\downarrow}$, respectively, is shown in Fig. S7. It indeed correctly reproduces all features of the H spectrum for $|\nu| < T_K$, which we now discuss.

The fixed point at energy ν^* causes a cut-off of the emission line shape; the nature of the line shape below the cut-off energy depends on ΔE and Ω . Fig. S6(b) explains this regime $0 < |\nu| < \nu^*$ in detail, where we find a combination of $+3$ and $+1$ power-law tails as indicated schematically. We consider the two cases $\Omega^* \leq |\Delta E|$ separately.

(i) For $\Omega^* > |\Delta E|$, the transition between the $+3/+1$ power-law tails occurs at a scale

$$\Delta E_{\text{eff}} = \Delta E + \delta(\Omega) > \Delta E, \quad (\text{S9})$$

where $\delta(\Omega)$ denotes an Ω -dependent effective detuning with $0 < \delta(\Omega) \ll \Omega$ that captures the small driving dependence which is attributed to second-order effects in the RG equations for $\Delta E'$ discussed above. The $+3/+1$ crossover is either sharp for $\Delta E_{\text{eff}} > 0$ or gradual in the case $\Delta E_{\text{eff}} < 0$. The analysis for the $+1$ exponent parallels the discussion for the $+3$ exponent in terms of the secondary Kondo model H'_K given in the main text: The presence of an effective magnetic field ($\Delta E_z \neq 0$) in Eq. (6), corresponding to a finite $\Delta E^{(l)}$ in models H and H' , causes the density of the z -component of the spin in H'_K to acquire a nonzero average. Hence, the correlation function $S'_z s'_z(0)$ will have components containing the correlator of just two Fermi operators with their conjugates, which decays as t^{-2} , leading to a $\sim |\nu|^{+1}$ behavior of the spectral function.

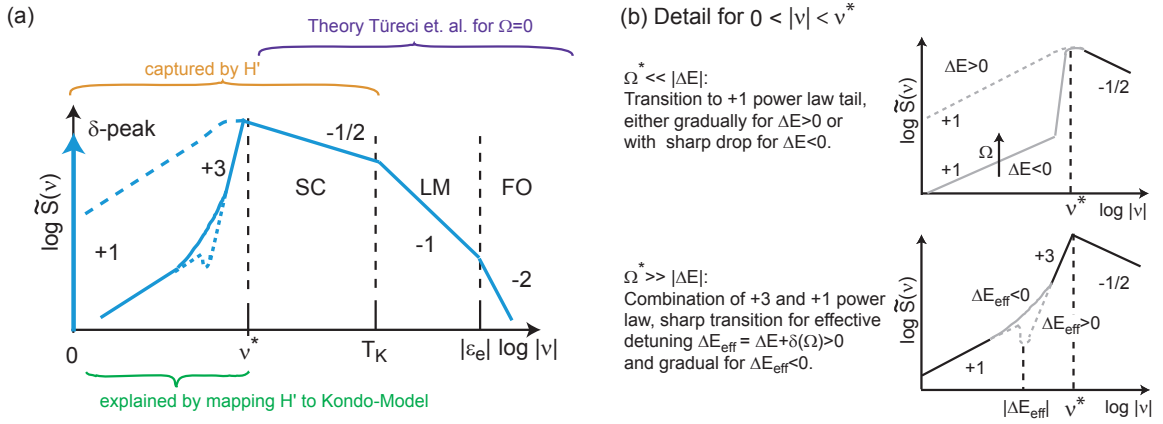


Figure S6: Phenomenological discussion of $\tilde{S}(\nu)$, revealing characteristic power-law tails. The same discussion applies to $\tilde{S}'(\nu)$ (for the effective Hamiltonian H') for $|\nu| < T_K$.

The effect described in Eq. (S9) can be clearly seen in the H spectrum for $\Delta E = 0$ (Fig. S3(c), $\Omega = 10^{-1}T_K$, green solid line) which shows a transition to a $+1$ tail at $\Delta E_{\text{eff}} = \Delta E + \delta(\Omega) = \delta(\Omega)$. Further, the $\Omega = 10^{-1}T_K$ spectra for $\Delta E = \pm 10^{-3}T_K$ (green dashed and dash-dotted lines) do not differ significantly since we have $\delta(\Omega) \gg \Delta E$ and thus, according to Eq. (S9), ΔE_{eff} is virtually equal in both cases.

(ii) Turning to $\Omega^* < |\Delta E|$, (dash and dashed-dotted red lines in Fig. S3(c)) the $+3$ tail is absent; in the case $\Delta E > 0$ a smooth transition to the $+1$ tail occurs while for $\Delta E < 0$ this transition is realized in a steep drop beyond NRG's smoothing resolution limit. This steep drop can be understood in the limiting case $\Omega \rightarrow 0$ as a horizontally displaced $\Omega = \Delta E = 0$ curve which has a threshold at $|\nu| = -\Delta E$.

Implications for an experimental study and outlook

The NRG results shed light on the results of the competition between Kondo physics and the laser coupling. As expected, the ratio of T_K and Ω determines the predominant form of the emission line shape, an asymmetric power-law-divergent peak in the Kondo-dominated regime $\Omega \ll T_K$, and a double

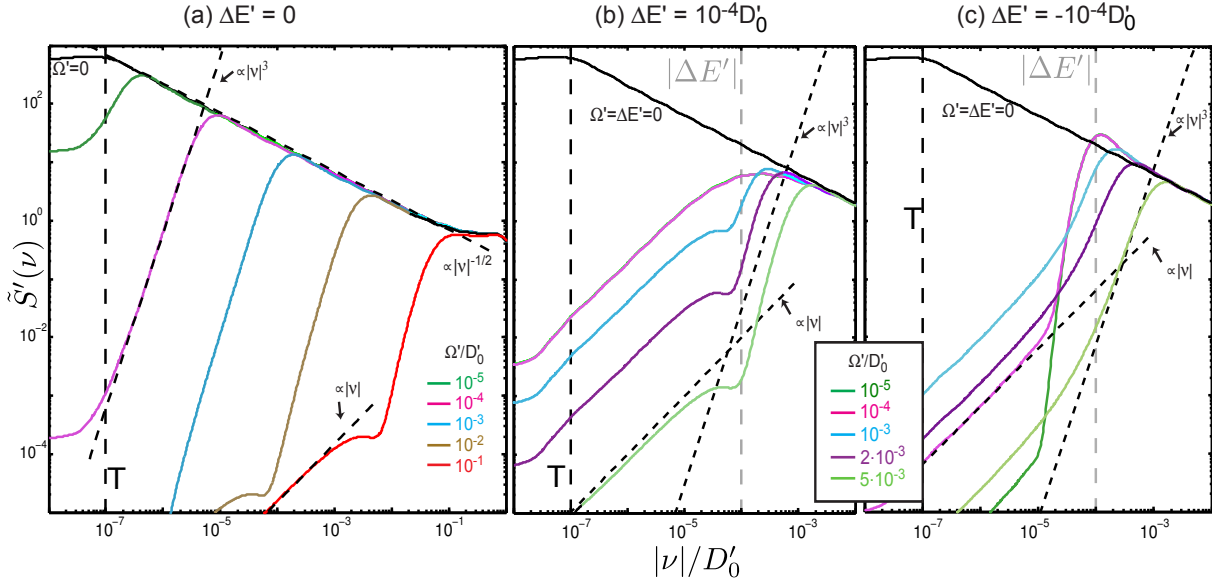


Figure S7: $\tilde{S}'(\nu < 0)$ for H' (without δ -peak). (a) $\Delta E' = 0$, (b) $\Delta E' > 0$ and (c) $\Delta E' < 0$. For reference, the $\Omega' = \Delta E' = 0$ spectrum is repeated in all plots (solid black line).

peak structure in the limit $\Omega \gg T_K$. However, the role of the seemingly weaker effect is interesting: A dominant driving laser leaves no trace of Kondo physics while dominant Kondo physics renormalizes Ω to a smaller value but preserves its characteristic non-trivial double peak feature in the spectrum. This explains our focus on the regime $\Omega < T_K$, which is highly attractive for further experimental study. We remark that the main results should be also valid in a two laser setup (creating dressed states with one laser, probing absorption with another), which might be experimentally more feasible than standard resonance fluorescence.

For a strongly coupled device and temperatures $T \ll T_K$, Kondo signatures in the absorption line shape of a weak laser have already been detected in experiment [10]. An order of magnitude separation between T (which flattens out all spectra for $|\nu| \lesssim T$) and T_K as well as a spontaneous emission rate below T has been achieved. For obtaining the predicted double peak structure in the resonance fluorescence experiment with $\Omega < T_K$, the crucial condition $T \ll \nu^* \ll T_K$ has to be fulfilled. We expect that a non-zero spontaneous emission rate will lead to partial broadening of the δ -peak at zero detuning, separating into an elastic and inelastic component. For the proper inclusion of spontaneous emission in the theoretical treatment, we propose an extension of the current study using the framework of Lindblad-NRG, currently under development [11].

The total area of the peak at the laser frequency and the peak-to-peak separation to the red emission peak are predicted to scale with Ω to the power $2/3$ and $4/3$, respectively. This is valid if ΔE (controlled by the laser detuning) is smaller than the renormalized Rabi frequency Ω^* . Compared to the measurement of power-law tails as signatures of Kondo physics, which require experimental data with sufficiently low noise level, peak areas and peak-to-peak separations can be measured with relative ease. Further, the scaling collapse of the broad emission peak with respect to ν^* , which is theoretically valid only for $S(\nu)$

with $|\Delta E_{\text{eff}}| < |\nu| < T_K$, should be a robust experimental feature since the regions where scaling fails (i.e. $|\nu| > T_K$, $|\nu| < |\Delta E_{\text{eff}}|$) are expected to support only a small spectral signal, effectively well below the noise level.

It is interesting to compare the effect of a laser drive Ω with the consequences of a nonzero magnetic field B (which we have set to zero throughout this work). While a circularly polarized laser coupling in a QD removes the degeneracy of the spin up and down state just like a magnetic field B does, their signatures in the emission spectrum in presence of Kondo physics are strikingly different. While a magnetic field $|B| < T_K$ results in a smooth modification of the $B = \Omega = 0$ fixed point (and consequently changes the $-1/2$ power-law exponent in the RF line shape [5, 10]) a Rabi frequency $\Omega < T_K$ induces a *new* low energy fixed point while keeping the power-law exponent at $-1/2$. For nonzero B and Ω (both $< T_K$) we conclude that a modification of the Ω -scaling dimension η_x (in the original Rabi-Kondo model) due to B would modify the $4/3$ and $2/3$ exponents for the Ω^* and δ_{weight} -scaling with Ω . Thus, application of a magnetic field could enhance the visibility of scaling effects on the emission spectrum in experiment.

References

- [1] B. Sbierski, A. Imamoglu. (to be published).
- [2] H. Breuer, F. Petruccione, *The Theory of Open Quantum Systems* (Oxford, 2002).
- [3] C. Cohen-Tannoudji, J. Dupont-Roc, G. Grynberg, *Atom-Photon Interactions* (Wiley, 1992).
- [4] R. Bulla, T. A. Costi, T. Pruschke, *Rev. Mod. Phys.* **80**, 395 (2008).
- [5] H. E. Türeci, *et al.*, *Phys. Rev. Lett.* **106**, 107402 (2011).
- [6] W. Mündler, A. Weichselbaum, M. Goldstein, Y. Gefen, J. von Delft, *Phys. Rev. B* **85**, 235104 (2012).
- [7] P. W. Anderson, *Phys. Rev. Lett.* **18**, 1049 (1967).
- [8] Of course, unitary evolution cannot change a state's energy and evolve the post quench state to the Kondo singlet state. More precisely, consider the overlap between post-emission state and its time-evolved version in Eq. (S1): Expanding in energy eigenstates, for times larger than $1/T_K$ the overlap has contributions only from strongly correlated eigenstates below energy T_K .
- [9] However, spontaneous emission can be interpreted as a quench between two adjacent excitation manifolds in the dressed state picture of resonance fluorescence.
- [10] C. Latta, *et al.*, *Nature* **474**, 627 (2011).
- [11] I. Weymann, A. Weichselbaum, J. von Delft, (to be published) .

5.3. Fermi edge singularity at the absorption spectrum of a quantum dot

One of the first many-body phenomena observed with optical methods is the Fermi edge singularity. There an electron is lifted from a deep-lying energy level up above the Fermi energy. The hole which is created at this process induces a phase shift of the reservoir electrons close to the Fermi level, and the resulting divergence in the absorption spectrum can be related to phase shift differences and explained with the phenomenon of Anderson orthogonality. Since in the following experiment, the Fermi edge cannot be observed directly, but only via interference of the transition between the dot levels and the transition between dot and reservoir, we will carefully examine the interference effects on the line shape. The following paper describes the first observation of the Fermi edge at quantum dots, that is shown to be in quantitative agreement with numerical calculations. It thus contributes to the understanding and experimental and numerical control of optical experiments at strongly hybridized QDs.

Nonequilibrium dynamics in an optical transition from a neutral quantum dot to a correlated many-body state

F. Haupt,^{1,*} S. Smolka,¹ M. Hanl,² W. Wüster,¹ J. Miguel-Sanchez,¹ A. Weichselbaum,² J. von Delft,² and A. Imamoglu¹

¹*Institute of Quantum Electronics, ETH Zürich, CH-8093, Zürich, Switzerland*

²*Arnold Sommerfeld Center for Theoretical Physics, Ludwig-Maximilians-Universität München, D-80333 München, Germany*

(Received 4 April 2013; revised manuscript received 21 August 2013; published 28 October 2013)

We investigate the effect of many-body interactions on the optical absorption spectrum of a charge-tunable quantum dot coupled to a degenerate electron gas. A constructive Fano interference between an indirect path, associated with an intradot exciton generation followed by tunneling, and a direct path, associated with the ionization of a valence-band quantum dot electron, ensures the visibility of the ensuing Fermi-edge singularity despite weak absorption strength. We find good agreement between experiment and renormalization group theory, but only when we generalize the Anderson impurity model to include a static hole and a dynamic dot-electron scattering potential. The latter highlights the fact that an optically active dot acts as a tunable quantum impurity, enabling the investigation of a new dynamic regime of Fermi-edge physics.

DOI: [10.1103/PhysRevB.88.161304](https://doi.org/10.1103/PhysRevB.88.161304)

PACS number(s): 78.67.Hc, 73.20.-r, 73.21.La, 78.30.Fs

When a fermionic reservoir (FR) experiences a dynamically changing local perturbation, all its eigenstates are modified in response; the resulting Anderson's orthogonality catastrophe¹ plays a central role in the physics of quantum impurity systems. Along with the Kondo effect,^{2–6} the most extensively studied quantum impurity problem is the Fermi-edge singularity (FES):^{7–10} an optical absorption event induces a local quantum quench, causing dynamical changes in reservoir states that lead to power-law tails in the absorption line shape. This has been observed, for example, in the context of x-ray absorption in metals,^{11–13} where a large ensemble of deep-level states were ionized upon absorption and the resulting collective modification of the absorption line shape was measured. A related many-body effect has also been investigated in semiconductor structures incorporating a degenerate electron gas.^{14–16} In these studies, the modification of the absorption line shape is due to a rearrangement of the conduction-band electrons after the creation of an electrostatic potential by photoexcited quasimobile valence-band holes.

In this Rapid Communication, we report the observation of a FES due to a single localized hole in a charge-tunable quantum dot (QD) and a tunnel-coupled FR. In our experiments, the ionization of a QD valence-band electron takes place via two competing paths: (1) excitation of a QD neutral exciton followed by ionization due to tunneling of the conduction-band electron into the FR, and (2) a direct transition from a QD valence band to an electronic state above the Fermi level of the FR. While in the classic x-ray absorption experiments only the latter process is relevant, in our experiments both contribute to single-photon absorption. Since both paths lead to final states of identical structure, involving a single-hole charged QD and a FR whose eigenstates are modified by the QD scattering potential, we observe a Fano interference.¹⁷ Thanks to the constructive nature of this interference we can observe the signature of the FES despite the small transition probability associated with path (2). The presence of path (1) is also responsible for the dynamical local screening of the hole potential. Tuning the energy of the QD electron level with respect to the Fermi energy allows us to change the residual electron charge on the QD continuously, thereby

varying the strength of the effective hole scattering potential. While in earlier optical experiments^{18–23} a FES was observed by creating an undefined number of positive hole charges in the FR, we generate the electrostatic scattering potential by a single localized hole on a QD, defining a spatially well-isolated impurity.^{10,24–26} From resonant absorption measurements we can determine the dynamics of the potential scattering as well as the Fano parameters of the correlated many-body state.

Setup. The quantum impurity system under study,²⁷ consists of a single shallow self-assembled InAs QD with the neutral exciton resonance at $\lambda \approx 891.25$ nm, tunnel coupled to a 40-nm n^{++} back gate and an $\text{In}_{0.08}\text{Ga}_{0.92}\text{As}$ 7 nm quantum well that is 9 nm below the QDs. The system is embedded in a Schottky diode structure, in order to allow continuous tuning between different charging regimes.^{28,29} Resonant laser spectroscopy measurements are carried out with a fiber-based confocal microscope setup (numerical aperture $\text{NA} = 0.55$) that is embedded in a dilution refrigerator. Figure 1(a) shows low-temperature differential transmission measurements of the energy plateaus of the neutral QD exciton (X^0) and single-negatively charged QD exciton (X^-) as a function of applied gate voltage. At the edges of the charging plateaus we observe an energy renormalization towards lower (higher) energies for the neutral (charged) QD transition, which is a hallmark of a strong tunnel coupling to a nearby FR.^{5,30}

Measured absorption spectra. To probe the role of many-body interactions, we carried out high-resolution laser scans for various representative gate voltages in the X^0 plateau [Fig. 1(b)]. Tuning the gate voltage to lower values allows us to increase the energy of the QD electron levels with respect to the Fermi energy. The absorption line shapes $[A(\Delta E)]$ obtained for various gate voltages thus show the gradual evolution of the system from a regime where the final state is an excited QD state [Fig. 1(d)] to the one in which it can be described by an optically excited electron in the FR and a hole trapped in the QD [Fig. 1(j)]. We emphasize that for our sample the latter state has a dipole moment that is approximately a factor of 2 larger than the dipole moment of the X^0 .

When the QD X^0 state approaches the Fermi energy, the absorption line shape consists of two peaks: the

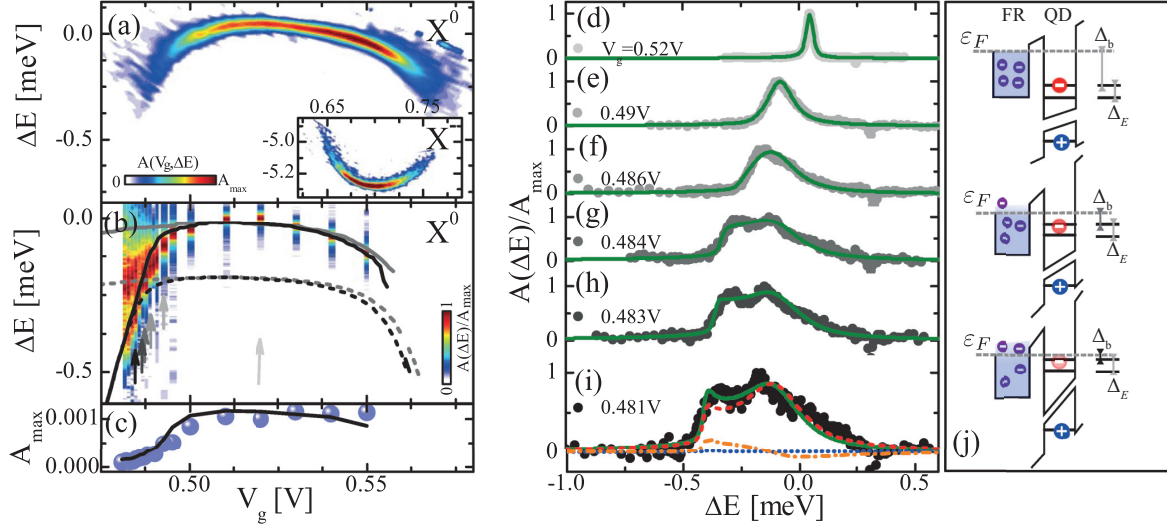
F. HAUPT *et al.*PHYSICAL REVIEW B **88**, 161304(R) (2013)

FIG. 1. (Color online) (a) Differential transmission measurements of the X^0 and the X^- (inset) QD charging states, after subtracting the dc Stark shift (Ref. 27). $\Delta E = E - E_0$ incorporates the peak absorption energy $E_0 = 1.3913$ eV at $V_g = 0.52$ V. (b) High-resolution laser absorption scans (color scale) at selected gate voltages. Solid lines show fits of the calculated lowest-energy peak position, ΔE_{peak} , either without the scattering potential ($H_S^a = 0$, solid gray), or including it ($H_S^a \neq 0$, solid black). Dashed lines show the ground state energy difference, $\hbar\omega_{\text{th}}$, between the initial and final states of the absorption process, calculated for $H_S^a = 0$ (dashed gray) or $H_S^a \neq 0$ (dashed black). The difference $\Delta E_{\text{peak}} - \hbar\omega_{\text{th}}$ is on the order of the dark-bright splitting Δ_E in the plateau center. (c) Comparison of the measured (dots) and calculated (curve) maximum absorption amplitudes (the latter scaled vertically by an overall fixed oscillator strength), shown as a function of gate voltage. (d)–(i) Measured absorption line shapes of the transition from a neutral exciton to a correlated many-body state (normalized by the experimental peak height A_{max}) at gate voltages indicated by corresponding color-coded arrows in (b). The green curves display calculated results, scaled vertically and shifted horizontally to minimize the χ^2 value of each fit (Ref. 27). The absorption components of the direct (red dashed), indirect (blue dotted), and interference (orange dash-dotted) terms are exemplarily depicted in (i). Since the tail of the X^0 state spectrally overlaps with the X^+ state, we can excite the latter, which shows up as a dip in the absorption line shapes for red detunings. (j) Schematic of the renormalized transition energies of the bright $\varepsilon_F - \Delta_b$ and dark $\varepsilon_F - \Delta_b - \Delta_E$ electron levels with respect to the Fermi energy ε_F directly after the single-photon absorption event. Δ_b indicates the energy difference between the Fermi energy and the bright state, corresponding to the line shape shown in (d) (top), in (f) (middle), and in (i) (bottom).

higher-energy peak corresponding to the X^0 transition that is tunnel broadened, and a second, lower-energy peak associated with the onset of absorption from the QD valence band directly into the FR [Fig. 1(i)]. As we argue below, this second peak carries the signatures of a many-body resonance and reveals its nonequilibrium dynamics that is the focus of our work.

Model. In order to understand the various features of the absorption line shapes depicted in Figs. 1(d)–1(i), we generalize the excitonic Anderson model (EAM), previously used to describe the optical signatures of the Kondo effect,^{5,6} by including a dynamic scattering potential:

$$H_A^a = H_{\text{QD}}^a + H_{\text{FR}} + H_S^a, \quad (1)$$

$$H_{\text{QD}}^a = \sum_{\sigma} \varepsilon_{\sigma}^a(V_g) \hat{n}_{\sigma} + U_{\text{ee}} \hat{n}_{\uparrow} \hat{n}_{\downarrow} + \delta_{a,f} \varepsilon_h(V_g), \quad (2)$$

$$H_{\text{FR}} = \sum_{k\sigma} [\varepsilon_{k\sigma} \hat{c}_{k\sigma}^{\dagger} \hat{c}_{k\sigma} + \sqrt{\Gamma/(\pi\rho)} (\hat{e}_{\sigma}^{\dagger} \hat{c}_{k\sigma} + \text{H.c.})], \quad (3)$$

$$H_S^a = \left[G_{\text{ee}} \left(\sum_{\sigma} \hat{n}_{\sigma} \right) - G_{\text{eh}} \delta_{a,f} \right] \sum_{\sigma'} \left(\hat{\Psi}_{\sigma'}^{\dagger} \hat{\Psi}_{\sigma'} - \frac{1}{2} \right). \quad (4)$$

Here, $a = i, f$ differentiates between the initial (i) Hamiltonian before absorption [Fig. 2(a)], and the final (f) Hamiltonian [Fig. 2(d)] after creation of an exciton. In the QD

Hamiltonian H_{QD}^a the electron occupancy is denoted as $\hat{n}_{\sigma=\uparrow,\downarrow} = \hat{e}_{\sigma}^{\dagger} \hat{e}_{\sigma}$. We assume a static hole spin and denote the bright state by $|\uparrow\downarrow\rangle$ and the dark state by $|\downarrow\downarrow\rangle$.³¹ The bare energy of the electronic level, measured with respect to the Fermi energy ($\varepsilon_F = 0$), is given by $\varepsilon_{\sigma}^a(V_g) = \varepsilon_0(V_g) - \delta_{a,f}(U_{\text{eh}} + \delta_{\sigma,\downarrow} \Delta_E)$, where $\delta_{a,f}$ is the Kronecker delta and Δ_E is the dark-bright splitting. Both the conduction-band electron [$\varepsilon_0(V_g) = \varepsilon_0 - |e|V_g l$] and valence-band hole [$\varepsilon_h(V_g) = -\varepsilon_{h,0} + |e|V_g l$] state energies shift linearly with the gate voltage, l being the voltage-to-energy conversion factor (lever arm). The energy of the optically excited QD states is lowered by the Coulomb attraction U_{eh} and lifted by the on-site Coulomb repulsion U_{ee} . H_{FR} describes the FR as a noninteracting conduction band with bandwidth W , symmetric around ε_F , and constant density of states $\rho = 1/W$ per spin, tunnel coupled to the QD, where $\hat{\Psi}_{\sigma} = \sum_k \hat{c}_{k\sigma}$ annihilates a FR electron at the QD position and Γ is the tunneling rate. Finally, the dynamic scattering potential H_S^a , which becomes important in the crossover between the local moment and free orbital regimes ($\varepsilon_{\sigma}^f \gtrsim 0$),²⁵ describes the contact Coulomb attraction, G_{eh} , and repulsion, G_{ee} , between FR electrons and the QD hole or QD electrons, respectively, as depicted in Fig. 2(d). Note that the effective scattering strength depends on the QD occupation and thus on the screened QD hole charge.

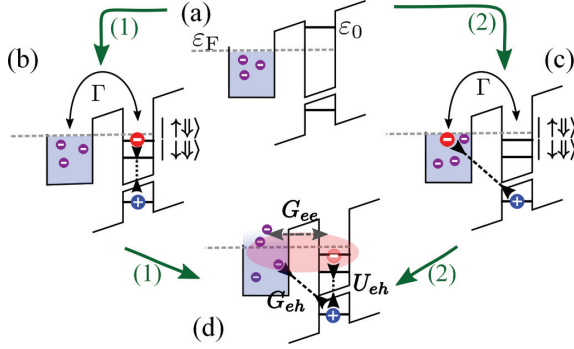


FIG. 2. (Color online) Scheme of the quantum impurity system consisting of a single QD and a nearby FR. (a) Initial quantum state where the QD with energy ε_0 above the Fermi energy ε_F is empty and the FR is unperturbed. The absorption of a single photon leads either (b) to a bound exciton on the QD or (c) to an indirect exciton. (d) The final state as $t \rightarrow \infty$ involves many-body correlations (red) between the FR and the QD. The black dashed and dotted lines depict the scattering potential between QD and FR, or the intradot Coulomb attraction, respectively.

Fano interference. Starting from a neutral QD [Fig. 2(a)], a photon absorption event can either create a QD exciton, involving \hat{e}_\uparrow^\dagger [Fig. 2(b)], or an indirect exciton, involving $\hat{\Psi}_\uparrow^\dagger$ [Fig. 2(c)]. Both of these intermediate states evolve into a common final state [Fig. 2(d)], where the QD hole scattering potential modifies the eigenstates of the FR due to the partial ionization of the QD and scattering of the FR electrons by the unscreened charge. The resulting absorption spectrum is given by

$$A(\nu) = \alpha^2 A_{\text{QD}}(\nu) + (1 - \alpha)^2 A_{\text{FR}}(\nu) + 2\alpha(1 - \alpha)\cos(\phi)A_I(\nu), \quad (5)$$

with α being the branching ratio between the two optical paths and a Fano phase $\phi = 0$ or $\phi = \pi$.²⁷ $\nu = \omega - \omega_{\text{th}}$ describes the detuning between the laser frequency ω and the ground state energy difference, $\omega_{\text{th}} = (E_G^f - E_G^i)/\hbar$, of the initial and final Hamiltonian. Using Fermi's golden rule, the direct absorption is calculated as $A_{\text{QD}}(\nu) = 2\text{Re} \int_0^\infty dt e^{i\nu t} \langle \hat{e}_\uparrow(t) \hat{e}_\uparrow^\dagger \rangle$ and the indirect Mahan absorption as $A_{\text{FR}}(\nu) = 2\text{Re} \int_0^\infty dt e^{i\nu t} \langle \hat{\Psi}_\uparrow(t) \hat{\Psi}_\uparrow^\dagger \rangle$.¹⁴ Here, we used the notation $\langle \hat{b}_2(t) \hat{b}_1^\dagger \rangle = \text{Tr}(e^{i\hat{H}t} \hat{b}_2 e^{-i\hat{H}t} \hat{b}_1^\dagger \rho)$, where \hat{b} stands for either \hat{e}_\uparrow or $\hat{\Psi}_\uparrow$, $\hat{H}^a = \hat{H}^a - E_G^a$, and ρ is the Boltzmann weight at a FR temperature T .⁶ The absorption line shape features a Fano interference, described by the term $A_I(\nu) = 2\text{Re} \int_0^\infty dt e^{i\nu t} \langle \hat{\Psi}_\uparrow(t) \hat{e}_\uparrow^\dagger \rangle$. The correspondence between the experimental $[A(\Delta E)]$ and theoretical $[A(\nu)]$ spectra follow from $\Delta E = \hbar\nu + \hbar\omega_{\text{th}} - \tilde{E}_0$; here, \tilde{E}_0 is a fit parameter.²⁷

Parameters. The recorded absorption maxima in Fig. 1(b) are fitted with the calculated absorption maxima (black curves) that we obtained from a numerical renormalization group simulation³² using Eq. (5). A simultaneous fit of the charging plateaus and the X^0 line shapes allows us to extract all experimental parameters.²⁷ The intradot electron repulsion $U_{ee} = 6.8$ meV is determined by the X^- plateau length. From the $X^0 - X^-$ energy separation, we extract $U_{eh} - U_{ee} = 6.6$ meV, neglecting correlation effects. In the center of the X^0 plateau

[Fig. 1(d)], the linewidth is determined by the FR-assisted relaxation into the dark exciton state, which in turn is determined by the gate voltage, the tunneling rate $\Gamma = 400 \mu\text{eV}$,⁵ and the dark-bright splitting $\Delta_E = 175 \mu\text{eV}$. The FR is characterized by its bandwidth $W = 2$ meV and its temperature $T = 120$ mK. The best agreement between theory and experiment is obtained for $G_{eh} = 3$ meV and $G_{ee} = 0.7G_{eh}$. For comparison, we also plot the best fit of the X^0 plateau, if Coulomb scattering is ignored, i.e., $H_S^a \equiv 0$ [Fig. 1(b), gray line]. As a result of the scattering potentials the lengths of the charging plateaus of X^- and X^0 show different extents in gate voltage [Fig. 1(b)]: This is in stark contrast to earlier experiments, which could be explained by assuming exclusively capacitive charging.²⁷ The renormalized energy of the final bright level with respect to the Fermi energy can be parametrized as $\tilde{\varepsilon}_\uparrow^f(V_g) = \varepsilon_0(V_g) - U_{eh} + \delta\varepsilon_0(V_g)$, where $\delta\varepsilon_0(V_g)$ accounts for a tunneling- and scattering-induced shift of the final bright level. Fitting model predictions to experimental data yields a lever arm of $l = 0.058$, $\varepsilon_0(0.52 \text{ V}) = 9.205$ meV and $\tilde{\varepsilon}_\uparrow^f(0.52 \text{ V}) = -4.675$ meV at $V_g = 0.52$ V.

Line shapes. The green curves in Figs. 1(d)–1(i) represent calculated absorption line shapes for the Hamiltonian [Eq. (1)] including the optical interference effect induced by the sample structure.²⁷ We highlight that we can only reproduce the experimental data using a Fano phase of $\phi = \pi$, corresponding to a constructive Fano interference between the direct and indirect transitions. α is determined by the square root of the ratio of the oscillator strengths of the direct and indirect transitions and is assumed to be independent of the exciton transition energy. In the present experiment we obtain the best agreement between experiment and theory for $\alpha = 0.85$.²⁷ Figure 1(c) compares the measured maximum absorption amplitudes (dots) versus the calculated absorption amplitudes without adjusting any parameters. The agreement, up to a sample specific proportionality constant and fluctuations of peak contrast of the order of 10% due to alignment, underlines that our model reliably predicts the gate-voltage dependence of the peak absorption. The individual absorption line shapes of the direct (dashed curve), indirect (dotted curve), and interference (dash-dotted curve) terms are exemplarily shown in Fig. 1(i). If the final neutral exciton levels are well below the Fermi energy [Fig. 1(d)], the final state of the optical transition is the dark exciton state, which leads to a homogeneous broadening of the absorption line shape. In the tunneling regime, however, the final state is a correlated many-body state, which is a superposition of the FR states and the QD bright and dark exciton states. Close to the Fermi energy [Fig. 1(i)], the final state has vanishing probability amplitude for finding the electron in the QD. In this regime the QD electron tunnels out into the FR lowering QD hole screening and thereby increasing the effective scattering potential. As a consequence, a screening cloud is formed in the FR that leads to a FES singularity. We emphasize that the absorption strength of the indirect element featuring the FES is very small ($1 - \alpha = 0.15$) and can only be detected due to a significant enhancement by the Fano interference. Due to the spectral overlap of $A_{\text{FR}}(\nu)$ and $A_{\text{QD}}(\nu)$, we cannot determine experimentally the power-law tail of the FES. However, the good agreement between our experimental data and theory indirectly demonstrates the presence of a FES.

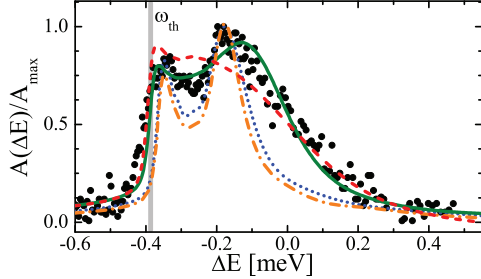
F. HAUPT *et al.*PHYSICAL REVIEW B **88**, 161304(R) (2013)

FIG. 3. (Color online) Comparison of the experimental absorption line shape at $V_g = 0.482$ V with theory assuming different scattering scenarios. For the scales, the same conventions were used as for Figs. 1(d)–1(i). The red dashed line shows the best fit for the EAM model ($H_S^a = 0$). Neglecting the electron-electron repulsion ($H_S^a \neq 0$ with $G_{ee} = 0$) the best fit yields the blue dotted curve, while the mean-field approach (H_S^a) is shown by the orange dash-dotted curve. The green solid line depicts a dynamic scattering potential.

Dynamical screening. In order to verify the role of the dynamical screening potential, we compare in Fig. 3 our experimental data with theory, for four different screening potentials. (i) The EAM model (dashed line, $H_S^a = 0$) resembles the experimental data for $\nu \gg \Gamma$, indicating the absence of a scattering potential for very short time scales. As the indirect absorption spectrum $A_{FR}(\nu)$ only probes the constant density of states in the FR, the EAM model fails to reproduce the double-peak structure dominating the low-energy part of the spectrum. (ii) Inclusion of a scattering potential leads to the pronounced low-energy peak associated with the FES. Usually, the FES singularity is described by the Mahan–Nozieres–De Dominicis Hamiltonian,^{7–9} which considers a scattering potential G_{eh} while neglecting any

Coulomb repulsion between QD and FR electrons, i.e., $G_{ee} = 0$ (dotted curve). (iii) A possible way to include the latter interaction in our description while still using, for simplicity, a time-independent scattering potential would be to use a mean QD electron occupation, $H_{(S)}^a = (G_{ee} \sum_{\sigma} \langle \hat{n}_{\sigma}(t \rightarrow \infty) \rangle) - G_{eh} \delta_{x,f} \sum_{\sigma'} (\hat{\Psi}_{\sigma'}^{\dagger} \hat{\Psi}_{\sigma'} - \frac{1}{2})$ (dash-dotted line). The models (ii) and (iii) both feature a second peak in the absorption spectrum in the long-time limit ($\nu \ll \Gamma$), but the absorption line shapes strongly deviate from the experimental data for short-time scales ($\nu \gg \Gamma$). (iv) Using the dynamical screening model of Eq. (4), we allow the QD electron occupation and thereby the screening of the QD hole potential to evolve in time. As depicted by the solid line, this dynamical screening model yields good agreement with experiment for all energy scales, showing that a scattering potential, and consequently an electron screening cloud in the FR, forms on time scales on the order of reciprocal Γ .

In contrast to prior nonresonant excitation experiments,²⁶ we directly observe a correlated many-body state formed by the direct and indirect exciton transitions and develop a model to quantify the potential scattering strength. We note that our model assumes a perfect screening potential.¹⁵ A partial screening of the scattering potential due to imperfections in the FR would lead to a stronger power-law decay of the FES,^{20,33,34} which could explain the residual difference between experiment and theory. In conclusion, we demonstrated a *dynamic* regime of Fermi-edge physics that highlights the importance of optically active quantum dots in the investigation of quantum impurity physics.

We acknowledge helpful discussions with B. Sbierski. This work was supported by an ERC Advanced Investigator Grant (F.H., S.S., W.W., J.-M.S., A.I.). J.v.D., M.H., and A.W. acknowledge DFG via NIM, SFB631, SFB-TR12, and WE4819/1-1.

*fhaupt@phys.ethz.ch; <http://www.quantumphotonics.ethz.ch>

¹P. W. Anderson, *Phys. Rev. Lett.* **18**, 1049 (1967).

²A. K. Geim, P. C. Main, N. LaScala, L. Eaves, T. J. Foster, P. H. Beton, J. W. Sakai, F. W. Sheard, M. Henini, G. Hill, and M. A. Pate, *Phys. Rev. Lett.* **72**, 2061 (1994).

³H. Frahm, C. von Zobeltitz, N. Maire, and R. J. Haug, *Phys. Rev. B* **74**, 035329 (2006).

⁴E. E. Vdovin, Y. N. Khanin, O. Makarovskiy, Y. V. Dubrovskii, A. Patane, L. Eaves, M. Henini, C. J. Mellor, K. A. Benedict, and R. Airey, *Phys. Rev. B* **75**, 115315 (2007).

⁵C. Latta, F. Haupt, M. Hanl, A. Weichselbaum, M. Claassen, W. Wuester, P. Fallahi, S. Faelt, L. Glazman, J. von Delft, H. E. Tureci, and A. Imamoglu, *Nature (London)* **474**, 627 (2011).

⁶H. E. Tureci, M. Hanl, M. Claassen, A. Weichselbaum, T. Hecht, B. Braunecker, A. Govorov, L. Glazman, A. Imamoglu, and J. von Delft, *Phys. Rev. Lett.* **106**, 107402 (2011).

⁷G. D. Mahan, *Phys. Rev.* **163**, 612 (1967).

⁸P. Nozieres and C. de Domini, *Phys. Rev.* **178**, 1097 (1969).

⁹L. N. Oliveira and J. W. Wilkins, *Phys. Rev. B* **32**, 696 (1985).

¹⁰K. Ohtaka and Y. Tanabe, *Rev. Mod. Phys.* **62**, 929 (1990).

¹¹H. Neddermeyer, *Phys. Rev. B* **13**, 2411 (1976).

¹²T. Ishii, T. Shii, Y. Sakisaka, S. Yanaguchi, T. Hanyu, and H. Ishii, *J. Phys. Soc. Jpn.* **42**, 876 (1977).

¹³T. A. Callcott, E. T. Arakawa, and D. L. Ederer, *Phys. Rev. B* **18**, 6622 (1978).

¹⁴G. D. Mahan, *Phys. Rev.* **153**, 882 (1967).

¹⁵P. Hawrylak, *Phys. Rev. B* **44**, 3821 (1991).

¹⁶C. L. Kane, K. A. Matveev, and L. I. Glazman, *Phys. Rev. B* **49**, 2253 (1994).

¹⁷U. Fano, *Phys. Rev.* **124**, 1866 (1961).

¹⁸M. S. Skolnick, J. M. Rorison, K. J. Nash, D. J. Mowbray, P. R. Tapster, S. J. Bass, and A. D. Pitt, *Phys. Rev. Lett.* **58**, 2130 (1987).

¹⁹W. Chen, M. Fritze, A. V. Nurmikko, D. Ackley, C. Colvard, and H. Lee, *Phys. Rev. Lett.* **64**, 2434 (1990).

²⁰G. Yusa, H. Shtrikman, and I. Bar-Joseph, *Phys. Rev. B* **62**, 15390 (2000).

²¹V. Huard, R. T. Cox, K. Saminadayar, A. Arnoult, and S. Tatarenko, *Phys. Rev. Lett.* **84**, 187 (2000).

²²J. M. Calleja, A. R. Goni, B. S. Dennis, J. S. Weiner, A. Pinczuk, S. Schmittrink, L. N. Pfeiffer, K. W. West, J. F. Muller, and A. E. Ruckenstein, *Solid State Commun.* **79**, 911 (1991).

NONEQUILIBRIUM DYNAMICS IN AN OPTICAL ...

PHYSICAL REVIEW B **88**, 161304(R) (2013)

- ²³M. Fritze, A. V. Nurmikko, and P. Hawrylak, *Surf. Sci.* **305**, 580 (1994).
- ²⁴P. Hawrylak, *Phys. Rev. B* **44**, 6262 (1991).
- ²⁵M. Heyl and S. Kehrein, *Phys. Rev. B* **85**, 155413 (2012).
- ²⁶N. A. J. M. Kleemans, J. van Bree, A. O. Govorov, J. G. Keizer, G. J. Hamhuis, R. Notzel, A. Y. Silov, and P. M. Koenraad, *Na. Phys.* **6**, 534 (2010).
- ²⁷See Supplemental Material at <http://link.aps.org/supplemental/10.1103/PhysRevB.88.161304> for details on experimental techniques, sample properties and theoretical model.
- ²⁸R. J. Warburton, C. Schaflein, D. Haft, F. Bickel, A. Lorke, K. Karrai, J. M. Garcia, W. Schoenfeld, and P. M. Petroff, *Nature (London)* **405**, 926 (2000).
- ²⁹A. Hogele, S. Seidl, M. Kroner, K. Karrai, R. J. Warburton, B. D. Gerardot, and P. M. Petroff, *Phys. Rev. Lett.* **93**, 217401 (2004).
- ³⁰P. A. Dalgarno, M. Ediger, B. D. Gerardot, J. M. Smith, S. Seidl, M. Kroner, K. Karrai, P. M. Petroff, A. O. Govorov, and R. J. Warburton, *Phys. Rev. Lett.* **100**, 176801 (2008).
- ³¹This assumption neglects the anisotropic exchange splitting between the bright states. In our description we fix the hole spin to be $|\downarrow\rangle$ without loss of generality (Ref. 27).
- ³²A. Weichselbaum and J. von Delft, *Phys. Rev. Lett.* **99**, 076402 (2007); A. Weichselbaum, *Phys. Rev. B* **86**, 245124 (2012).
- ³³Y. Gefen, R. Berkovits, I. V. Lerner, and B. L. Altshuler, *Phys. Rev. B* **65**, 081106 (2002).
- ³⁴D. A. Abanin and L. S. Levitov, *Phys. Rev. Lett.* **93**, 126802 (2004).

Non-equilibrium dynamics in an optical transition from a neutral quantum dot to a correlated many-body state - Supplemental Material

F. Haupt,^{1,*} S. Smolka,¹ M. Hanl,² W. Wüster,¹ J. Miguel-Sanchez,¹
A. Weichselbaum,² J. von Delft,² and A. Imamoglu¹

¹*Institute of Quantum Electronics, ETH Zürich, CH-8093 Zürich, Switzerland*

²*Arnold Sommerfeld Center for Theoretical Physics,
Ludwig-Maximilians-Universität München, D-80333 München, Germany*

(Dated: September 30, 2013)

The supplementary should provide background information to the studied effect. It is structured in two main sections. The first section deals with experimental methods and sample properties, e.g. the experimental setup and QD properties. The second section addresses the excitonic Anderson model with dynamic scattering potential in detail and states the parameterizations of the model.

S-1. EXPERIMENTAL METHODS AND SAMPLE PROPERTIES

S-1.1. Experimental setup

The experimental setup, used to conduct the experiments presented in the main text, is schematically shown in Fig. S1(a). In order to achieve cold temperatures, the sample is mounted inside a fiber-based confocal microscope embedded in a dilution refrigerator with a base temperature of $T = 20$ mK in the mixing chamber. X-Y-Z positioners on the microscope allow us to select individual QDs. The microscope objective has a numerical aperture of $N.A. = 0.55$ featuring a diffraction-limited spot size. To conduct photoluminescence measurements (PL) we use a $\lambda = 780$ nm laser diode. The emitted PL signal is collected by the confocal microscope and spectrally analyzed with a spectrometer. As a second spectroscopy method, we perform differential transmission measurements by tuning a resonant single mode laser across the QD resonances, while the laser frequency and laser intensity ($P = 0.87$ nW) is stabilized against long-term drifts. To record the differential transmission signal, we modulate the resonance of the QD transition energies by varying the gate voltage between back gate and top gate with a frequency of $f = 187$ Hz and a modulation amplitude of 150 mV. For each laser frequency we detect the absorption difference signal with a Si photo diode that is mounted underneath the sample. The signal is afterwards analyzed with a lock-in amplifier.

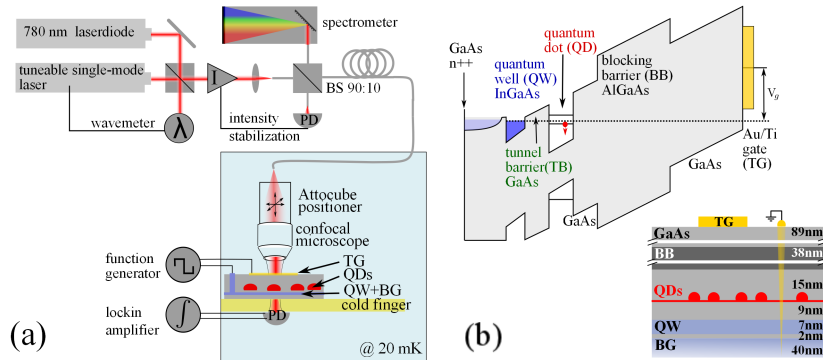


FIG. S1. (a) Scheme of the experimental setup. The He^3/He^4 dilution refrigerator (blue shaded) has a fiber-based, confocal and movable objective. A $\lambda = 780$ nm laser diode, the 90:10 beam splitter (BS), and the spectrometer are utilized for PL measurements. In differential transmission, we use a tunable laser. The sample is mounted on the cold finger of the cryostat and the resonantly scattered light of the QDs is detected by a photo diode (PD) mounted underneath the sample. (b) Schematic of the sample structure in the valence and conduction band picture (top) and growth structure (bottom). The sample consists of a n^{++} back gate (BG), quantum well (QW), tunnel barrier (TB), QDs, blocking barrier (BB) and a Ti/Au top gate (TG). GaAs spacer layers are shown in grey.

* fhaupt@phys.ethz.ch;
<http://www.quantumphotonics.ethz.ch>

S-1.2. Sample structure

The sample structure consists of self-assembled InGaAs quantum dots (QDs) embedded in a Schottky diode structure, cf. Fig. S1(b). The QDs are grown by molecular beam epitaxy. The sample design features a large tunnel coupling between the QDs and a nearby Fermi reservoir (FR). To this end, we used a modulation doped QW that defines a sharp boundary for the electron gas, consisting of a 40-nm-thick n++-doped GaAs layer and a $\text{In}_{0.08}\text{Ga}_{0.92}\text{As}$ quantum well (QW), both coupled via a 2 nm GaAs barrier. The excitonic emission wavelength of the QW is $\lambda = 840$ nm. Due to segregation of dopants and the modulation doping, the QW/doped-layer system form the back contact (BC) of the Schottky diode. From transport measurements we obtain an electron density of $n = 1.2 \times 10^{12} \text{ cm}^{-2}$. The tunnel barrier (TB) between QD and QW is designed to be 9 nm, which is in agreement with an estimate of the lever-arm, after fitting the experimental absorption line shapes, that suggests a TB of 8.5 nm. In order to prevent a current flow from the back gate to the semi-transparent 8 nm thick Ti-Au top gate, a blocking barrier (BB) of 38.5 nm $\text{Al}_{0.42}\text{Ga}_{0.58}\text{As}$ is grown 15 nm above the QDs, cf. the valence band and conduction band diagram in Fig. S1(b). Furthermore, the blocking barrier close to the QD serves to stabilize photo-excited holes in the QD [1]. Photoluminescence measurements of the QD emission as a function of gate voltage allows us to identify the different charging regimes [Fig. S2(a)]. In resonant QD spectroscopy, it is crucial to identify the saturation of an optical transition in order to prevent any power broadening [2]. In the presented experiments, we ensure that the laser power is 2.5 times smaller than the saturation power of ~ 2 nW, cf. Fig. S2(b).

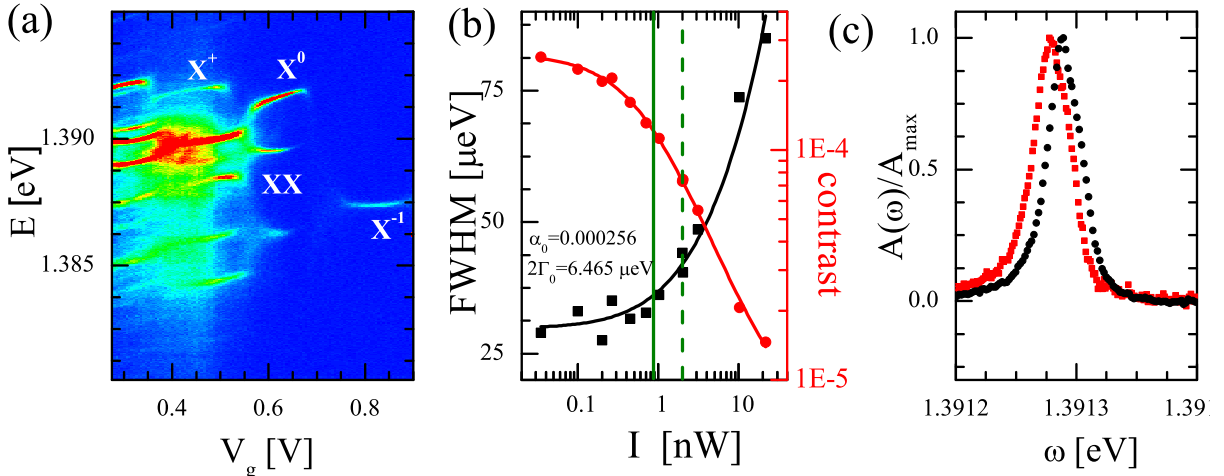


FIG. S2. (a) Photoluminescence spectrum of the QD transition energies as a function of gate voltages, allowing us to identify the different charging plateaus. (b) Saturation behavior of the X^0 transition in the plateau center ($V_g = 0.52$ V). The full width at half maximum (FWHM, black squares) and the differential transmission contrast (red squares) are measured versus laser power. The solid lines are fits according to the experimental data [2]. The green solid line depicts the laser power used in the present experiments, while the dashed line shows the saturation laser power. (c) Spectral splitting of the X^0 transition at a gate voltage of $V_g = 0.52$ V. The X^0 is split at zero magnetic field in two bright states obeying different optical selection rules. The transition that we studied throughout the paper is depicted by filled black dots, whereas the energetically higher transition (red squares) is suppressed by adjusting the laser polarization.

S-1.3. Fine structure splitting

The neutral exciton X^0 is generated by a bound electron-hole pair having as eigenstates two bright states (denoted as $|\uparrow\downarrow\rangle \pm |\downarrow\uparrow\rangle$) and two dark states ($|\downarrow\downarrow\rangle \pm |\uparrow\uparrow\rangle$), that are split by exchange splitting ($H = -\sum_{i=x,y,z} (a_i \hat{J}_{h,i} \hat{S}_{e,i} + b_i \hat{J}_{h,i}^3 \hat{S}_{e,i})$) [3] at zero magnetic field. The bright and dark manifolds are split due to electron-hole exchange coupling ($\Delta_E \gg T$, see Sec. S-2.1), whereas the bright states are split by anisotropic exchange (δ_x). After excitation of the bright exciton states, the QD electron can tunnel into the Fermi reservoir or decay into the dark state via co-tunneling events. As tunneling broadening ($\sim \Gamma$) is much larger than the anisotropic exchange splitting $\sim \delta \ll \Gamma$, the latter does not affect the absorption line shapes, when the bright states are close to or above ε_F and is therefore negligible. In the center of the X^0 plateau, where tunneling is suppressed, we observe a polarization-dependent splitting of the bright

excitons ($\delta_x = 15 \mu\text{eV}$), which is smaller than the line width, cf. Fig. S2 (c) [4, 5]. This introduces a small uncertainty in the calculated NRG center frequency with respect to the experimental data for line shapes in the plateau center. As the hole spin-flip time is much longer than any other time scale of the system, we can fix the hole spin to be $|\downarrow\rangle$ (or $|\uparrow\rangle$ with equal probability). These assumptions allow us to treat the system by NRG using only the states $|\uparrow\downarrow\rangle/|\downarrow\downarrow\rangle$ (or $|\downarrow\uparrow\rangle/|\uparrow\uparrow\rangle$).

S-1.4. Measurement of DC-Stark shift and dipole moment

The DC Stark shift in the present QD sample originating from the applied electric field can be approximated by two parameters, the permanent dipole moment p and the polarizability β :

$$\Delta E_{\text{th}} = E_{\text{off}} - pF + \beta F^2 \text{ with } F = -\delta V_g/D, \quad (\text{S1})$$

where δV_g is the change of gate voltage with respect to the reference gate voltage $V_g = 0.52 \text{ V}$. D is the distance between the ohmic back contact and the metallic top-gate. The permanent dipole moment, p , is a measure of the spatial electron-hole separation in the exciton, $r = \frac{p}{e}$. In order to extract the relevant data we proceed as follows:

- We approximate each charging plateau separately with a linear DC-Stark shift ($\tilde{E}_{\text{th}} = E_{\text{off}} - pF$) and obtain in the center of the X^0 (X^-) plateau an effective dipole moment r_{X^0} at $V_g = 0.52 \text{ V}$ (r_{X^-} at $V_g = 0.71 \text{ V}$), cf. Fig. S3 (a).
- Then we extract the quadratic overall DC-Stark shift. Here, the previously determined individual linear DC-Stark shifts at $V_g = 0.52 \text{ V}$ ($V_g = 0.71 \text{ V}$) serve as tangents with respect to the threshold value $E_{\text{off}} = 1.3913 \text{ meV}$ at $V_g = 0.52 \text{ V}$. Using the charging energy ΔE of the X^- with respect to the X^0 transition as another fit parameter in Eq. S1, we obtain the best fit with the highest confidence for $\Delta E = 5.27 \text{ meV}$, cf. Fig S3(a).

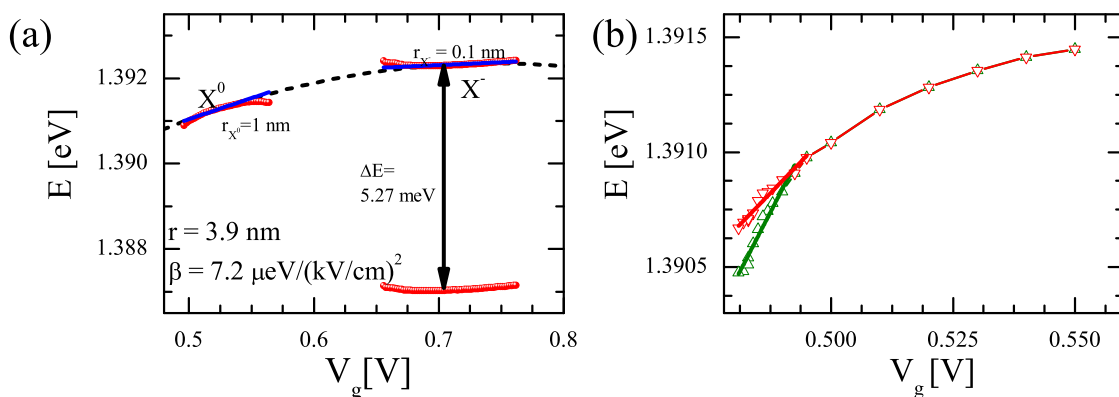


FIG. S3. (a) Quantum confined Stark shift of excitons in the QD. The experimental data (red bullets) show the maximum peak absorption positions of the X^0 and (shifted) X^- charging plateaus that are fitted by a second order approximation of the Stark shift (dashed line). The linear approximations of the individual DC stark shifts for both charging states are shown as blue solid lines. The black arrow indicates the charging energy ΔE of the X^- with respect to the X^0 transition. (b) Peak positions of the direct (red triangles) and indirect (green triangles) absorption peak maxima, plotted without subtracting the DC-Stark shift. The dipole moment of the indirect transition is larger than that of the direct transition by roughly a factor of 2.

The experimental data of the X^0 and (shifted) X^- charging plateaus show a permanent dipole of $r = 3.9 \text{ nm}$ and a polarizability of $\beta = 7.2 \mu\text{eV}/(\text{kV}/\text{cm})^2$ [6]. These values are larger than for QDs with a low tunnel coupling, possibly because the wave function of the QD charges extends into the FR. The observed two-peak structure shows a gate-voltage dependent splitting, implying different dipole momenta for the direct and indirect excitons [Fig. S3(b)].

Note, that the "bare" charging energy of the X^- in the limit of low tunnel coupling ($\Gamma = 0$) and no scattering potential $H_S = 0$ is given by $U_{\text{eh}} - U_{\text{ee}} = 6.6 \text{ meV}$ provided that we ignore the correlation effects. As the QD levels hybridize with the FR due to tunneling events and the scattering potential, this leads to an energy renormalization towards lower (higher) energies for the neutral (charged) QD transition ($\Delta E < U_{\text{eh}} - U_{\text{ee}}$). The energy renormalization difference is in the present experiment found to be $E_r = \Delta E - (U_{\text{eh}} - U_{\text{ee}}) \sim -1.33 \text{ meV}$. For details on the determination of U_{eh} and E_r see Sec. S-2.1.

S-1.5. Signatures of FES in other quantum dots

We have studied the absorption line shapes of different self-assembled QDs. For QDs with a large tunnel-coupling we find a shortening of the X^0 charging plateau as well as a double peak structure. In Fig. S4(a), the plateau lengths of the X^0 and X^- charging plateaus extracted from the PL measurements show a clear wavelength dependence. Generally, the charging regimes of QDs can be described using a capacitive charging model. If the trapping potential can be approximated by a parabolic potential, each charging plateau should have the same extent in gate voltage ($\propto U_{ee}$). However, we find that QDs at lower wavelengths have a significant shortening of the X^0 plateau length, $L(X^0)$, as compared to the X^- plateau length, $L(X^-)$, suggesting that the dynamic scattering potentials (see main text) increase in strength for QDs with lower wavelengths.

As a further hallmark of the scattering potentials, a double peak like absorption line shape arises at the X^0 plateau edge which we observed for several different QDs. Figure S4(b) shows a second QD with the X^0 at $E = 1.3757$ eV and a lower tunnel coupling Γ , which still shows the double peak structure.

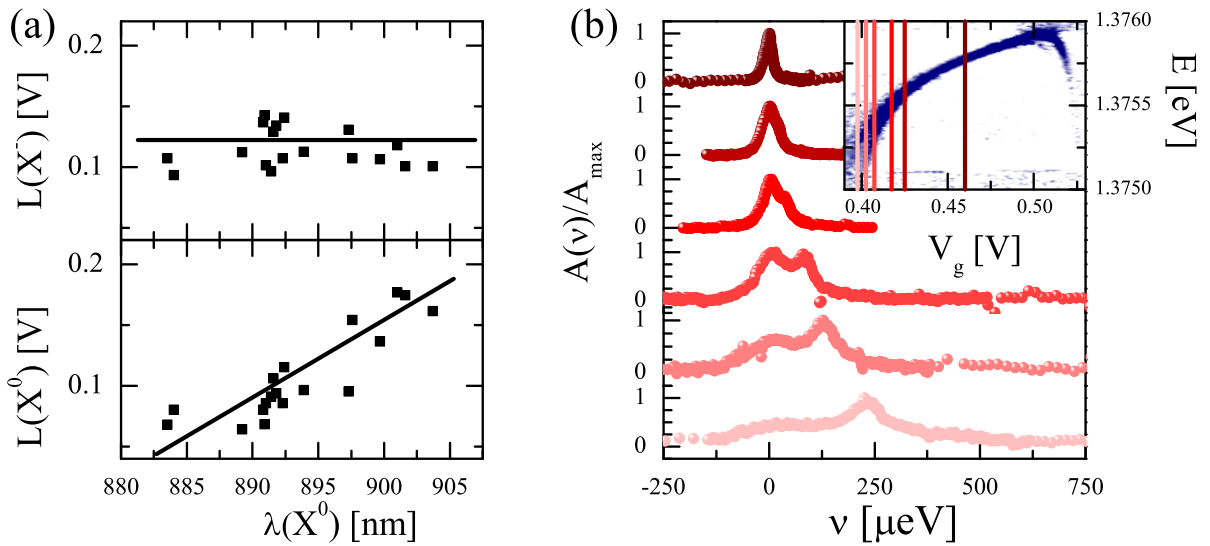


FIG. S4. (a) Gate voltage extents (lengths) of the X^- and the X^0 plateaus of all studied QDs extracted from photoluminescence measurements. The black lines are a guide to the eye. (b) An example of the double peak structure in a different dot that has smaller tunnel coupling. Inset: 2D differential transmission scan of the X^0 plateau together with the indicated positions of the measured absorption line shapes.

S-2. PARAMETERIZATIONS AND DISCUSSION OF THE MODEL

S-2.1. Parameterizations of the theoretical model

The extended Anderson model including a dynamic scattering potential, as discussed in the main text, can be parameterized with a single set of parameters by consecutive fitting of the X^0/X^- plateaus and line shapes.

$\Gamma = 400 \mu\text{eV}$, $\Delta_E = 175 \mu\text{eV}$: The charging plateaus experience a characteristic energy renormalization due to the tunnel-coupling Γ , as the QD electronic level hybridizes with the FR states and lowers the energy of the excited (ground) state of the X^0 (X^-). This results into a bending of the plateau edges towards lower (higher) energy. The line shape in the center of the X^0 plateau ($V_g = 0.52$ V) is determined by co-tunneling processes providing an irreversible decay into the dark state due to the dark-bright splitting ($T \ll \Delta_E$), which leads to homogeneous broadening. By fitting the data in the plateau center with theory, we estimate a dark-bright splitting of $\Delta_E = 175 \mu\text{eV}$, which is in agreement with prior experiments, that measured a dark-bright splitting of $200 - 500 \mu\text{eV}$ [7]. To minimize the number of variables, we have chosen $\Gamma = 400 \mu\text{eV}$ from the center of the X^0 . It is plausible that Γ for the X^- is larger. Better fits could be obtained for letting Γ vary as a function of gate voltage V_g .

$U_{ee} = 6.8 \text{ meV}$: The QD electron-electron repulsion U_{ee} is determined by the plateau length of the X^- .

$G_{ee} = 2.1 \text{ meV}$, $G_{eh} = 3.0 \text{ meV}$: As shown in the main text, the difference of the X^0 and X^- plateau length can be explained by a dynamic scattering potential. As $G_{ee} \leq G_{eh}$, the X^0 charging plateau is fitted best using $G_{eh} = G_{ee}/0.7 = 3 \text{ meV}$. The accuracy in the fits of the absorption line shapes could be improved by varying G_{eh} and G_{ee} throughout the charging plateau, which was not done here.

$W = 2.0 \text{ meV}$: The bandwidth of the Fermi reservoir was fitted from the line width of the absorption line shapes in tunnel-regime.

$U_{eh} = 13.35 \text{ meV}$: The QD electron-hole attraction U_{eh} is extracted as follows: the charging energy $\Delta E = 5.27 \text{ meV}$ between the centers of X^- and X^0 plateaus has the form $\Delta E = U_{eh} - U_{ee} + E_r$, where E_r is the shift accounting for the effects of level hybridization and the scattering potential H_S , cf. Fig. S3(a). Using the above-mentioned value for G_{eh} , G_{ee} , Γ and W , our NRG calculations yield a shift of $E_r = -1.33 \text{ meV}$ (its value is dominated by scattering, since the tunneling contribution at the plateau centers is rather small). As a result, we deduce $U_{eh} = \Delta E + U_{ee} - E_r = 13.35 \text{ meV}$. Note, we neglected any effect due to correlations, which could lead to correction of the exact value of U_{eh} and U_{ee} .

$l = 0.058$: The lever arm is $l = \tilde{D}/(D + \tilde{D})$, where $\tilde{D} = 8.5 \text{ nm}$ is the QD/FR distance and $D = 138.5 \text{ nm}$ is the QD/top gate distance indicated by both NRG calculation and the PL emission. This parameters can differ by a few Å from the predicted growth parameter ($\tilde{D} = 9 \text{ nm}$, $D = 138.5 \text{ nm}$) due to finite accuracy in the growth of the sample.

$T = 120 \text{ mK}$: The temperature T of the FR electrons is extracted by the red tail of X^- line shapes (see Sec. S-2.2).

$\alpha = 0.85$, $\phi = \pi$: The branching ratio and Fano phase can be fitted for the cases in the tunnel regime (see Sec. S-2.3).

S-2.2. Optical interference and sample temperature

In the following we discuss an optical interference effect caused by the sample structure [8] using absorption measurements of the single electron charged exciton X^- . The incident laser field on the sample E_L is Rayleigh scattered at the QD at which the scattered light can be forward and backward scattered. The backward scattered (reflected) light travels in GaAs (refractive index $n = 3.55$) a distance $D = 138.5 \text{ nm}$ to the top gate and will be again partly reflected at the top-gate (reflectivity $r = 0.75$, fitted). In first approximation the field at the transmission detector [see Fig. S1(b)] is a superposition of the transmitted light and all scattered components. Here, the back-scattered light accumulates a phase due to a different path length of $\varphi = \frac{2\pi n}{\lambda} 2D$:

$$E_{tot} = E_L e^{i\pi/2} + \chi(\lambda) E_L + r e^{i\varphi} \chi(\lambda) E_L = i E_L [1 - i\chi(\lambda)(1 + r e^{i\varphi})], \quad (\text{S2})$$

with χ being the susceptibility of the QD with absorption $\Im(\chi)$ and dispersive part $\Re(\chi)$. Due to employing a Gaussian shape on our beam, the laser field E_L acquires a Guoy phase $e^{i\pi/2}$ in the far field regime. Furthermore, in a differential transmission lock-in-method, the QD response function is modulated at a certain frequency such that the measured absorption is at this frequency:

$$A(\lambda) = \Delta I/I \sim \Re [i\chi(\lambda)(1 + r e^{i\varphi})], \quad (\text{S3})$$

where $I = E_{tot}^2$ is the intensity detected by the photo detector and we neglected terms $\sim (\chi(\lambda))^2$ as $1 \gg \chi(\lambda)$. The back-scattered light mixes the dispersive part with the absorption part of the forward-scattered light, which leads to an optical interference. The numerical renormalization group (NRG) theory used in this paper for the calculation of the absorption line shapes A_{NRG} considers $\Im(\chi_{NRG}(\lambda)) = -A_{NRG}(\lambda)$. In order to calculate the dispersive response and thereby incorporate the optical interference we convolute the calculated absorption spectra using the Kramers-Kronig relation $\Re(\chi_{NRG}(\lambda)) = -\frac{1}{\pi} \mathcal{P} \int d\lambda' \frac{\Im(\chi_{NRG}(\lambda'))}{\lambda - \lambda'}$.

The electron occupation of the fermionic reservoir (FR) is governed by a Fermi-Dirac distribution. Shake-up processes due to finite temperature modify the available states in the Fermi reservoir. For the negative charged exciton X^- of a highly tunnel-coupled QD, the absorption tails for red detunings ($\nu < -T$) are governed by the levels below the Fermi energy in the FR. The line shape thus shows an exponential tail that depends on temperature $\sim e^{-\frac{\nu}{k_B T}}$ [9]. For $\nu \ll \Gamma$, the line shape is governed by the spontaneous emission and resembles a Lorentzian tail. From fits of the red tails of X^- line shapes with NRG calculations including the optical interference effect at $V_g = 0.67 \text{ V}$ and $V_g = 0.70 \text{ V}$ [Fig. S5(a)], we extract a FR electron temperature of $T = 120 \text{ mK}$. For comparison we show in Fig. S5(a) fits for different temperatures. In Fig. S5(b), we demonstrate that without the optical interference we

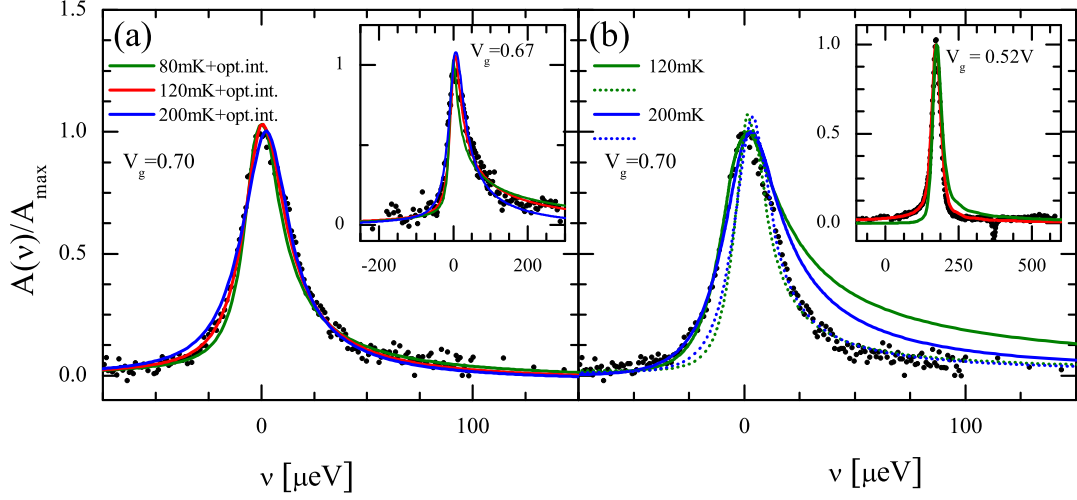


FIG. S5. (a) Fits of X^- line shapes at $V_g = 0.70$ V (inset at $V_g = 0.67$ V) for different temperatures, i.e., $T = 80$ mK (green), $T = 120$ mK (red) and $T = 200$ mK (blue) including the optical interference (without scattering potential $H_S = 0$). (b) Fits of the X^- absorption line shape ($V_g = 0.70$ V) without accounting for the optical interference. The dotted line focusses on fitting the blue tail of the experimental data, whereas the solid lines fits the red tail. The inset shows the role of optical interference for a X^0 absorption line shape at $V_g = 0.52$ V by incorporating (red curve) and neglecting (green curve) the optical interference.

cannot reproduce the full absorption line shape. Either we can fit the high energy or the low energy tail of the line shape. As the X^0 red tail is distorted by the dark-bright splitting, we determined the parameters for the optical interference and the FR temperature from the X^- line shapes to calculate the X^0 line shapes, which are in good agreement with the experiment, c.f. the inset of Fig. S5(b) (green curve shows the bare NRG calculations; red curve includes the optical interference).

S-2.3. Branching ratio α between the direct and indirect transition

The branching ratio between the direct and the indirect transition can be determined by fitting the experimental data [Fig. S6 (a)] with NRG calculations [Fig. S6 (b)]. It is defined by the wave function overlap of the QD electron and QD hole versus the FR electrons and the QD hole. This ratio is specific for every QD. Since at zero magnetic field the Hamiltonian can be chosen to be real, the Fano phase has to be $\phi = 0$ or $\phi = \pi$.

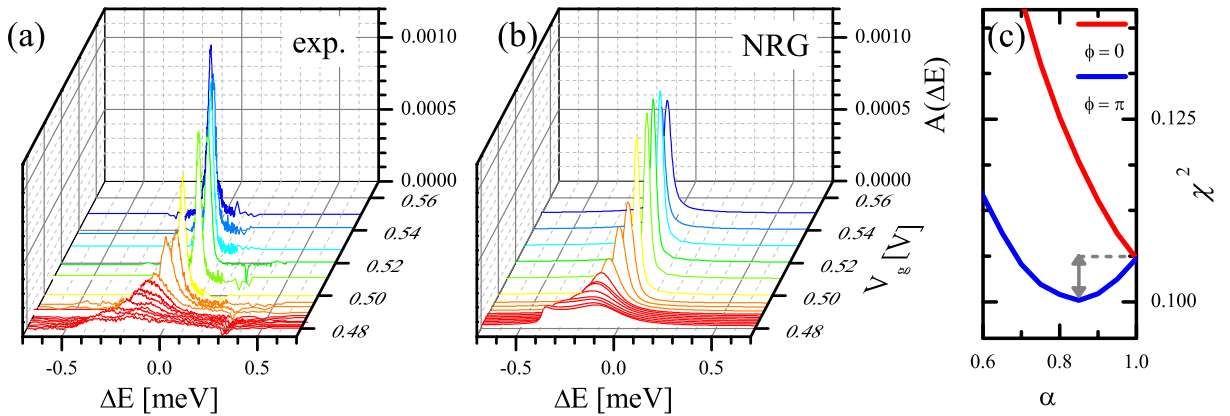


FIG. S6. Comparison of measured line shapes (a) and NRG simulations (b) in the gate voltage range of $V_g = 0.48$ V to 0.55 V (not normalized, cf. Fig. 1(c)) (c) Calculated cumulative χ^2 of all measured line shapes from $V_g = 0.481$ V to 0.55 V for destructive interference ($\phi = 0$, red) and constructive interference ($\phi = \pi$, blue) as a function of branching ratio α .

Due to variations in the peak absorption contrast stemming from the fact that the experiments were carried out on different days with uncontrolled changes in the alignment (on the order of 10%), we determined the values of the branching ratio α and the relative phase ϕ applying the following fitting procedure. This allows us to quantify and minimize the disagreement between theory and experiment as a function of α and ϕ for about 2700 data points in total:

Using the system parameters of the Hamiltonian extracted as described in Sec. S-2.1 we generate a set of initial and final eigenstates by diagonalizing the initial and final Hamiltonians using NRG. With Fermi's Golden rule we calculate the absorption spectra terms: A_{QD} , A_{FR} , and A_{I} . The theoretical line shape is then given by $A^{\text{NRG}}(\omega) = \alpha^2 A_{\text{QD}}(\omega) + (1 - \alpha)^2 A_{\text{FR}}(\omega) + 2(1 - \alpha)\alpha A_{\text{I}}(\omega) \cos(\phi)$, where $\omega = \nu + \omega_{\text{th}}$, with ν being the detuning between the laser frequency, ω , and the absorption threshold energy, $\omega_{\text{th}} = (E_{\text{G}}^{\text{f}} - E_{\text{G}}^{\text{i}})/\hbar$, that is given by the ground state energy difference between the final and initial Hamiltonian. To compare the calculated and the measured line shapes for a given gate voltage, we fit the theoretical curve $aA^{\text{NRG}}(\nu + \omega_{\text{th}} - \tilde{E}_0)$ to the normalized experimental data $A^{\text{exp}}(E - E_0)/A_{\text{max}}$, where $E_0 = 1.3913 \text{ eV}$ is the peak absorption energy at $V_{\text{g}} = 0.52 \text{ V}$. \tilde{E}_0 and a are curve-specific fit parameters, relating to the peak height and peak position. The fitting proceeds by first fixing $\{\alpha, \phi\}$ and then varying $\{a, \tilde{E}_0\}$ for each gate voltage to minimize the χ^2 . Changes in the electromagnetic environment upon optical excitation lead to random charging events of the nearby defects and/or charge accumulation at the AlGaAs/GaAs interface, which in turn modify the electric-field seen by the quantum dot at a given gate voltage. This results in variations of the experimental peak position of $\sigma(\tilde{E}_0) = 30 \mu\text{eV}$ with respect to the theoretical predictions, c.f. Fig. 1(b). a is constant for each absorption line shape and accounts for the day-to-day variations in the sample alignment which in turn leads to a modified absorption contrast (i.e. the area under the absorption line shape). For completeness, we show in Fig. 1(c) of the main text the measured experimental peak contrast together with the pure peak absorption predicted by the NRG calculation (without compensating for alignment issues). From the deviations between experiment and theory we estimate the unavoidable variations in oscillator strength to be on the order of 10%. As an objective measure of the quality of the fit we calculate the χ^2 value for each line shape as a function of the branching ratio α (for constructive, $\phi = \pi$, and destructive interference, $\phi = 0$, separately). Afterwards we estimate the cumulative χ^2 of all measured (in total 18) line shapes as a function of α . The best overall fit in the range of $V_{\text{g}} = 0.481 \text{ V} - 0.55 \text{ V}$ is obtained for $\alpha = 0.85$ and $\phi = \pi$ [Fig. S6 (c)]. The case of destructive interference ($\phi = 0$) shows an optimal branching ratio of $\alpha = 1$ for all line shapes, but the corresponding χ^2 is larger than the lowest χ^2 obtained for $\phi = \pi$.

In Fig. S7 (a), we compare the theoretical predictions for constructive and destructive interference at $V_{\text{g}} = 0.481 \text{ V}$, 0.482 V and 0.483 V . We emphasize that only the theoretical curve using a constructive interference can reproduce the low-energy peak associated with the Fermi edge singularity [Fig. S7]. Oliveira et al. [10] predicted an Anti-Fano resonance if the branching ratio α is equal to zero, which corresponds to an exclusively indirect exciton absorption. This scenario cannot be achieved in the present experiments since the QD states (direct transitions) always have a non-vanishing oscillator strength. However, in the NRG calculations, where we can decompose the individual contributions to the absorption line shape, we observe the Anti-Fano resonance (AFR) in the indirect transition [see blue curve in Fig. S7(b)].

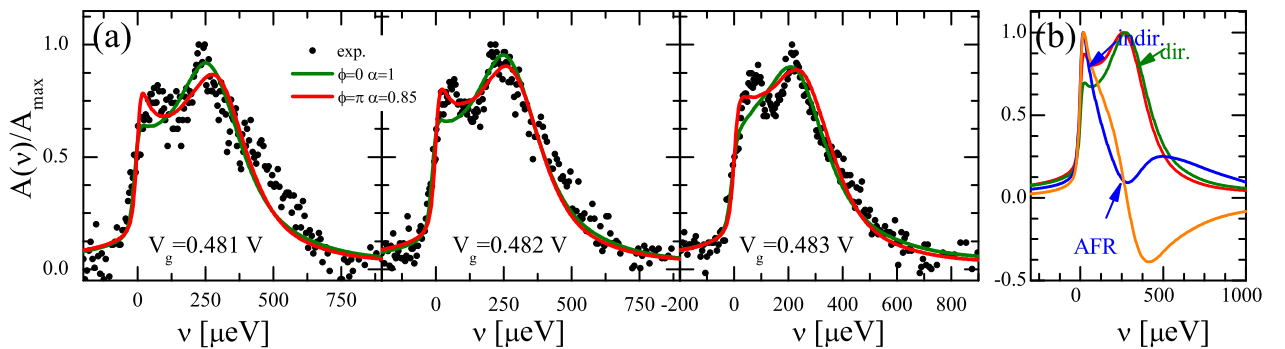


FIG. S7. (a) Comparison of line shapes for $V_{\text{g}} = 0.481 \text{ V}$, $V_{\text{g}} = 0.482 \text{ V}$ and $V_{\text{g}} = 0.483 \text{ V}$ for the best fitting values of branching ratio α for constructive ($\phi = \pi$, red) and destructive ($\phi = 0$, green) Fano interference. (b) Calculation of the decomposed normalized direct (green), indirect (blue) and interference (orange) absorption spectra for $V_{\text{g}} = 0.482 \text{ V}$. In the indirect transition an Anti-Fano resonance (AFR) can be observed.

S-2.4. Comparison of the charging plateaus with theory and estimation of electron occupations

In the following we discuss the fits of the experimentally measured charging plateaus as well as the electron occupations in the QD and the Fermi reservoir using a Numerical Renormalization Group (NRG) approach. The results are displayed in Fig. S8. While at QDs without a scattering potential the X^0 and X^- charging plateaus have equal lengths, we find a different result (experimentally and theoretically) as the scattering potential $G_{eh} \neq G_{ee}$ is turned on [Fig. S4(a)]. The X^0 plateau length is strongly modified by the scattering, whereas the X^- plateau length is unaffected, c.f. Fig. S8(a) black versus grey curve. The attractive Coulomb interaction between the QD hole and the Fermi reservoir electrons forms an indirect exciton at the QD position, lowering the ground state difference between the initial and final state of the Fermi reservoir by $\sim G_{eh}$. Equivalently, the QD electron tunnels into the Fermi reservoir for transition energies $|\varepsilon_{\uparrow}^f(V_g) - (\varepsilon_F - G_{eh})| < \Gamma$, where the calculated Fermi energy $\varepsilon_F = 0$ is at $V_0 = 0.448V$. Here, the tunnel-regime is defined for gate voltages $0.48 < V_g < 0.495$, which is confirmed by the simulations, cf. Fig. S8(c). We find furthermore that a finite scattering potential modifies the energy renormalization of the X^- plateau on its right side (of higher V_g -values, approaching the X^{2-} regime). For large detunings from the point of electron-hole symmetry (plateau center) towards the X^{-2} charging state, the model breaks down most likely because the p-shell states of the QD are not considered in the present model.

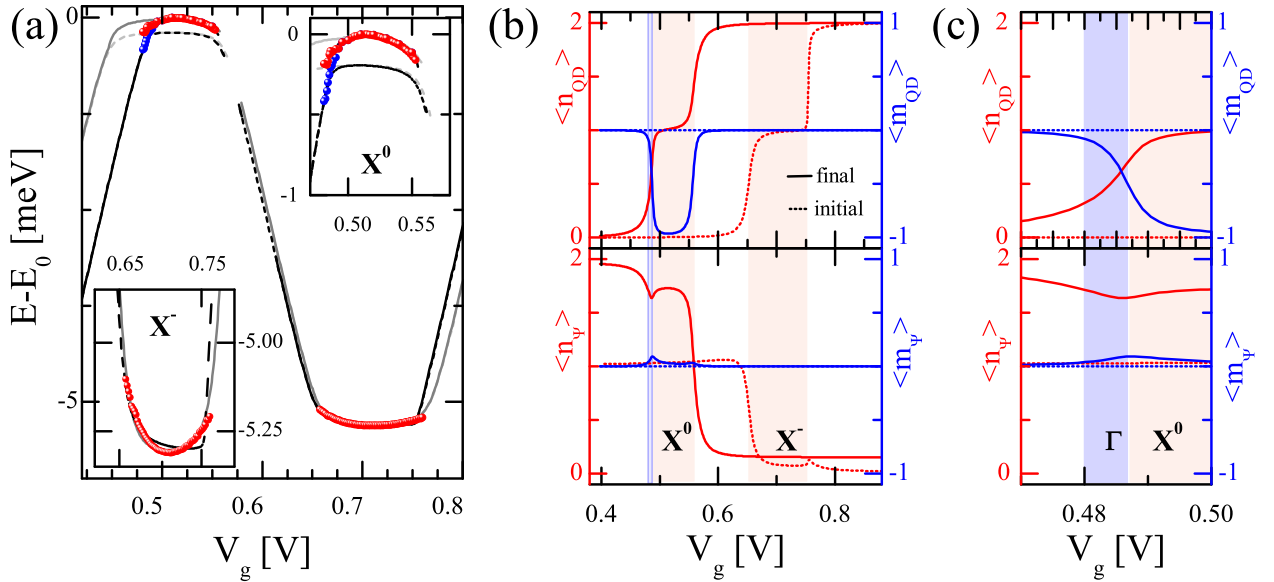


FIG. S8. (a) Fits of the measured charging plateaus using NRG calculations together with a zoom-in of the X^0 (inset upper right) and X^- (inset lower left) using the extracted parameter stated in the paper for the $H_S^g = 0$ (grey) and $H_S^g \neq 0$ (black). The solid lines depict the maximum absorption strength and the dashed lines are the ground state energy differences of the initial and final states of the system. (b) Occupation ($\langle n_x \rangle = \langle n_{\uparrow,x} \rangle + \langle n_{\downarrow,x} \rangle$, red) and population inversion of the $|\uparrow\rangle$ and $|\downarrow\rangle$ state ($\langle m_x \rangle = \langle n_{\uparrow,x} \rangle - \langle n_{\downarrow,x} \rangle$, blue) of the QD ($x = \text{QD}$) and of the FR at the position of the QD ($x = \Psi$) for the initial (dotted lines) and the final state (solid lines) including the dynamic scattering potential. (c) Zoom-in of the tunneling regime of (b).

NRG simulations allow us to calculate the QD electron occupation and the electron occupation of the FR at the QD position. Note, that the hole ($|\downarrow\rangle$) is traced out in the final Hamiltonian. The electron occupation of the QD ($\langle \hat{n}_{\text{QD}} \rangle = \sum_{\sigma} \langle \hat{n}_{\sigma} \rangle$) shows nicely the charging regimes of the X^0 and X^- while the population inversion of the $|\uparrow\rangle$ and $|\downarrow\rangle$ state of the QD ($\langle m_{\text{QD}} \rangle = \langle \hat{n}_{\uparrow} \rangle - \langle \hat{n}_{\downarrow} \rangle$) displays the decay of the bright exciton into the dark exciton in the final state and is a measure for the dark state population, provided the hole spin state ($|\downarrow\rangle$) remains preserved. Therefore we have a negative population inversion in the X^0 , whereas in the X^- both spin states are degenerate and we have an equal occupation in the final state (zero population inversion). The occupation and the population inversion of the $|\uparrow\rangle$ and $|\downarrow\rangle$ state of the FR at the position of the QD is depicted by $\langle n_{\Psi} \rangle = \sum_{\sigma} \langle n_{\Psi,\sigma} \rangle$ and $\langle m_{\Psi} \rangle = \langle n_{\Psi,\uparrow} \rangle - \langle n_{\Psi,\downarrow} \rangle$, respectively. The FR is in the initial state (no scattering potential) half filled for each spin, resulting in an expectation value of $\langle n_{\Psi} \rangle = 1$. If the scattering potential is switched on, the scattering potential G_{ee} depletes at the X^- charging state the FR at QD-position in the initial state. After absorption, the hole and the electrons in the QD lead to an attractive (repulsive) potential in the X^0 (X^-) which induces a charge surplus (deficit) of the FR at the position of the QD in contrast to the initial state. In Fig. S8(c) we highlight the tunneling regime, where a Fermi edge singularity

arises. For the line shapes with $V_g = 0.481\text{-}0.483\text{ V}$, the occupation decreased already significantly to a QD occupation of $\langle n_{\text{QD}} \rangle = 0.20\text{-}0.5$. The population inversion also decreases, as the dark state becomes close to the Fermi edge; it is in this regime that the final state of the absorption process is the correlated many-body state.

-
- [1] M. Ediger, G. Bester, A. Badolato, P. M. Petroff, K. Karrai, A. Zunger, and R. J. Warburton, *Nature Physics* **3**, 774 (2007).
 - [2] M. Kroner, S. Remi, A. Hoegele, S. Seidl, A. W. Holleitner, R. J. Warburton, B. D. Gerardot, P. M. Petroff, and K. Karrai, *Phys. E* **40**, 1994 (2008).
 - [3] *Single Quantum Dots: Fundamentals, Applications, and New Concepts* edited by P. Michler, Topics in Applied Physics (Springer, Berlin, 2003).
 - [4] D. Gammon, E. S. Snow, B. V. Shanabrook, D. S. Katzer, and D. Park, *Phys. Rev. Letters* **76**, 3005 (1996).
 - [5] W. Langbein, P. Borri, U. Woggon, V. Stavarache, D. Reuter, and A. D. Wieck, *Phys. Rev. B* **69**, 161301 (2004).
 - [6] R. J. Warburton, C. Schulhauser, D. Haft, C. Schaflein, K. Karrai, J. M. Garcia, W. Schoenfeld, and P. M. Petroff, *Phys. Rev. B* **65**, 113303 (2002).
 - [7] J. M. Smith, P. A. Dalgarno, R. J. Warburton, A. O. Govorov, K. Karrai, B. D. Gerardot, and P. M. Petroff, *Phys. Rev. Lett.* **94**, 197402 (2005).
 - [8] R. J. Warburton, C. Schaflein, D. Haft, F. Bickel, A. Lorke, K. Karrai, J. M. Garcia, W. Schoenfeld, and P. M. Petroff, *Nature* **405**, 926 (2000).
 - [9] C. Latta, F. Haupt, M. Hanl, A. Weichselbaum, M. Claassen, W. Wuester, P. Fallahi, S. Faelt, L. Glazman, J. von Delft, H. E. Tuercci, and A. Imamoglu, *Nature* **474**, 627 (2011).
 - [10] L. Oliveira and J. Wilkins, *Phys. Rev. B* **32**, 696 (1985).

6. Transport for impurity models

6.1. Kondo effect in an InAs nanowire quantum dot

Since its discovery, the Kondo effect has been realized in a range of systems: magnetic impurities in bulk metals, single molecules coupled to Fermionic reservoirs, and different kinds of quantum dots. The following section shows a detailed study of the Kondo effect for a QD made of an InAs nanowire. Whenever possible, theory is compared to experiment and it shows good agreement, apart from a stronger sensitivity of the conductance on magnetic field in the experiment. The following paper can be seen as a reference for the future study of properties related to the Kondo effect at InAs nanowire QDs.

PHYSICAL REVIEW B **84**, 245316 (2011)

Spin- $\frac{1}{2}$ Kondo effect in an InAs nanowire quantum dot: Unitary limit, conductance scaling, and Zeeman splitting

Andrey V. Kretinin,^{1,*} Hadas Shtrikman,¹ David Goldhaber-Gordon,^{2,1} Markus Hanl,³ Andreas Weichselbaum,³ Jan von Delft,³ Theo Costi,⁴ and Diana Mahalu¹

¹*Braun Center for Submicron Research, Condensed Matter Physics Department, Weizmann Institute of Science, Rehovot, Israel*

²*Physics Department, Stanford University, Stanford, California, USA*

³*Physics Department, Arnold Sommerfeld Center for Theoretical Physics, and Center for NanoScience, Ludwig-Maximilians-Universität, Theresienstraße 37, DE-80333 München, Germany*

⁴*Peter Grünberg Institut and Institute for Advanced Simulation, Research Centre Jülich, DE-52425 Jülich, Germany*

(Received 9 August 2011; revised manuscript received 1 December 2011; published 19 December 2011)

We report on a comprehensive study of spin- $\frac{1}{2}$ Kondo effect in a strongly coupled quantum dot realized in a high-quality InAs nanowire. The nanowire quantum dot is relatively symmetrically coupled to its two leads, so the Kondo effect reaches the unitary limit. The measured Kondo conductance demonstrates scaling with temperature, Zeeman magnetic field, and out-of-equilibrium bias. The suppression of the Kondo conductance with magnetic field is much stronger than would be expected based on a g -factor extracted from Zeeman splitting of the Kondo peak. This may be related to strong spin-orbit coupling in InAs.

DOI: 10.1103/PhysRevB.84.245316

PACS number(s): 72.15.Qm, 75.20.Hr, 73.23.Hk, 73.21.La

I. INTRODUCTION

The Kondo effect¹ is one of the most vivid manifestations of many-body physics in condensed matter. First observed in 1930s in bulk metals through an anomalous increase in resistivity at low temperatures, it was later associated with the presence of a small amount of magnetic impurities.² The modern theoretical understanding is that the single unpaired spin of the magnetic impurity forms a many-body state with conduction electrons of the host metal. This many-body state is characterized by a binding energy expressed as a Kondo temperature (T_K). When the temperature is decreased below T_K , the conduction electrons screen the magnetic impurity's unpaired spin, and the screening cloud increases the scattering cross-section of the impurity. More recently, advances in microfabrication opened a new class of experimental objects—semiconductor quantum dots—in which a few electrons are localized between two closely spaced tunneling barriers.³ At the same time, it had been theoretically predicted that an electron with unpaired spin localized in a quantum dot could be seen as an artificial magnetic impurity and, in combination with the electrons of the leads, would display the Kondo effect.^{4,5} The first observation of Kondo effect in quantum dots was made in GaAs-based two-dimensional structures.^{6–10} Initially thought to be very difficult to observe in such experiments, the Kondo effect has now been seen in quantum dots based on a wide variety of nanomaterials such as carbon nanotubes,^{11,12} C₆₀ molecules,^{13,14} organic molecules,^{15–18} and semiconductor nanowires,^{19–22} and has also been invoked to explain behavior of quantum point contacts.²³

In this paper, we present a comprehensive study of the Kondo effect in a nanosystem of emerging interest, namely, InAs nanowires grown by the vapor-liquid-solid (VLS) method.²⁴ Building on initial reports of Kondo effect in InAs nanowires,^{19,20} we report Kondo valleys with conductance near $2e^2/h$ in multiple devices and cooldowns. This high conductance, combined with temperature far below the Kondo temperature, allows quantitative measurements of conductance scaling as a function of temperature, bias, and magnetic field,

which we compare to theoretical predictions independent of materials system. The high g -factor and small device area, characteristic of InAs nanowires, allows measurement of the splitting of the zero-bias anomaly over a broad range of magnetic field, and we find that splitting is pronounced at lower magnetic field than predicted theoretically.

II. EXPERIMENT

The quantum dot from which data are presented in this paper is based on a 50-nm-diameter InAs nanowire suspended over a predefined groove in a p^+ -Si/SiO₂ substrate and held in place by two Ni/Au (5nm/100nm) leads deposited on top of the nanowire. The leads' 450-nm separation defines the length of the quantum dot. The p^+ -Si substrate works as a backgate. The InAs nanowire was extracted from a forest of nanowires grown by molecular beam epitaxy on a (011) InAs substrate using Au-catalyst droplets. Wires from this ensemble were found to have a pure wurtzite structure, with at most one stacking fault per wire, generally located within 1 μ m from the tip. We therefore formed devices from sections of nanowire farther from the wires' end, with a reasonable presumption that the active area of each device is free of stacking faults. Schottky barriers, and screening of the electric field from the gate electrode by the source and drain electrodes, together create potential barriers next to the metal contacts. Thus electrons must tunnel to the central part of the nanowire (the quantum dot) and the contacts, giving rise to Coulomb blockade (CB). An SEM image of a typical device is shown in Fig. 1(a). More details on growth, fabrication, and charging effects have been published previously.²²

Transport experiments were carried out in a dilution refrigerator with a base temperature $T_{\text{base}} \sim 10$ mK. All experimental wiring was heavily filtered and thermally anchored to achieve electron temperature close to cryostat base temperature, as verified in shot noise measurements.²⁵ Conductance measurements used standard lock-in techniques with a home-built ultra-low-noise transimpedance preamplifier operated at

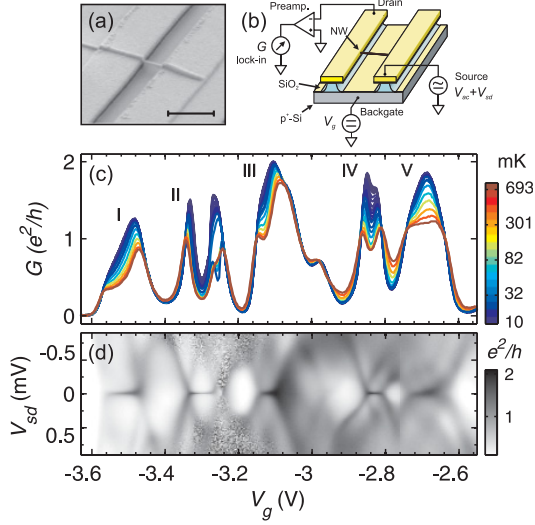


FIG. 1. (Color online) (a) SEM image of a typical suspended nanowire-based quantum dot device used in the experiment. The scale bar corresponds to $1 \mu\text{m}$. (b) Schematic representation of the nanowire-based quantum dot device and its experimental setup. (c) The temperature dependence of the nanowire-based quantum dot conductance measured over a wide range of the backgate voltage V_g . Five Kondo valleys are labeled I through V here. This identification of valleys will be used throughout the paper. Discontinuities in the temperature dependence in valley II are caused by device instability at this particular range of V_g . (d) The gray-scale conductance plot in the V_g - V_{sd} plane measured in the same range of V_g as in (c) at temperature $T_{\text{base}} = 10 \text{ mK}$. Panels (a) and (b) are adapted with permission from A. V. Kretinin *et al.*, *Nano Lett.* **10**, 3439 (2010). Copyright © 2011 American Chemical Society.

frequencies of $\sim 2 \text{ kHz}$. Depending on the temperature T , the ac excitation bias was set in the range of 1 – $10 \mu\text{V}_{\text{rms}}$ to keep it equal to or smaller than $k_B T$ (k_B is the Boltzmann constant). The magnetic field was applied perpendicular to both the substrate and the axis of the nanowire. A schematic representation of the nanowire-based device together with the experimental setup is shown in Fig. 1(b).

III. RESULTS AND DISCUSSION

First, we would like to outline the main features associated with the Kondo effect, which were studied in our experiment. The conductance of a quantum dot weakly coupled to leads is dominated by CB, seen as nearly periodic peaks in the conductance as a function of gate voltage, with the conductance strongly suppressed between peaks. Each peak signals a change in the dot occupancy by one electron. In contrast, a dot strongly coupled to the leads can show the Kondo effect, with the following signatures:^{6,8,26} (1) the Kondo effect enhances conductance between alternate pairs of Coulomb blockade peaks (that is, for odd dot occupancy). These ranges of enhanced conductance are conventionally termed “Kondo valleys.” (2) Conductance in Kondo valleys is suppressed by increasing temperature. (3) Conductance in Kondo valleys is suppressed by applied source-drain bias (V_{sd}), giving rise to a zero-bias anomaly (ZBA). The full width at half maximum

(FWHM) of the zero-bias peak is of the order of $4k_B T_K/e$ (e is the elementary charge). (4) In contrast to the conductance in the CB regime whose upper limit is e^2/h ,²⁷ the Kondo valley conductance can reach $2e^2/h$, equivalent to the conductance of a spin-degenerate 1D wire.²⁸ In this limit, “valley” is a misnomer, as the valley is higher than the surrounding peaks! (5) The Kondo ZBA splits in magnetic field (B) with the distance between the peaks in bias being twice the Zeeman energy. (6) The dependence of the Kondo conductance on an external parameter A such as temperature, bias, or magnetic field can be calculated in the low- and high-energy limits.²⁹ In the low-energy limit, $k_B T_K \gg A = \{k_B T, eV_{sd}, |g|\mu_B B\}$, the conductance has a characteristic quadratic Fermi-liquid behavior:^{14,30–32}

$$G(A) = G_0 \left[1 - c_A \left(\frac{A}{k_B T_K} \right)^2 \right], \quad (1)$$

where $G_0 \equiv G(A=0)$ and c_A is a coefficient of order unity. Its numerical value is different for each parameter A , and depends on the definition of T_K . In the present paper, we use a convention⁷ used in many experimental papers and define T_K by the relation

$$G(T = T_K) = 0.5G_0. \quad (2)$$

In the opposite limit of high energy, when $k_B T_K \ll A$, the conductance shows a logarithmic dependence. For example, as a function of temperature:¹⁵

$$G(T) \propto G_0 / \ln^2 \left(\frac{T}{T_K} \right). \quad (3)$$

There is no analytical expression for the intermediate regime, where the parameter $A \approx k_B T_K$, but numerical renormalization group (NRG) calculations³³ show that the connection between one limit and the other is smooth and monotonic, without any sharp feature at $A = k_B T_K$.

Before detailed consideration and discussion of the results, we give a broad overview of the experimental data used in this study. It will be followed by three subsections focusing on the observed unitary limit of the Kondo effect (Sec. III A), conductance scaling with different external parameters (Sec. III B), and some peculiarities observed in the Zeeman splitting (Sec. III C).

Figure 1(c) presents the linear conductance G as a function of the backgate voltage V_g . Different color corresponds to different temperature, ranging from 10 to 693 mK. The Kondo effect modifies the CB peaks so strongly that the separate peaks are no longer recognizable and the simplest way to identify Kondo valleys is to look at the the gray-scale plot of differential conductance as a function of both V_g and V_{sd} (“diamond plot”), Fig. 1(d). Every Kondo valley is marked by a ZBA seen as a short horizontal line at $V_{sd} = 0$. Different widths of ZBAs on the gray-scale plot reflect differences in the Kondo temperature. In these same Kondo valleys, conductance decreases with increasing temperature [see Fig. 1(c)]. Note that Kondo valleys alternate with valleys having opposite temperature dependence or almost no temperature dependence, corresponding to even occupancy of the quantum dot. A small unnumbered peak at about $V_g = -2.95 \text{ V}$ departs from the general pattern of conductance observed in the experiment.

Most likely, this feature, which occurs for even occupancy, is associated with transition to a triplet ground state, and thus emergence of spin-1 and singlet-triplet Kondo effect.^{34–36} However, it is difficult to conclusively identify the nature of this anomaly since its temperature and bias dependencies are weak.

All conductance peaks shown in Fig. 1(c) exceed e^2/h , reflecting Kondo-enhanced conductance and relatively symmetric coupling to the two leads. In particular, conductance around $V_g = -3.1$ V in valley III reaches the unitary limit of $2e^2/h$, to within our experimental accuracy.

A. Kondo effect in the unitary limit

To realize maximum conductance in resonant tunneling, the quantum dot should be symmetrically coupled to the leads. In the conventional case of CB, electrostatic charging allows only one spin at a time to tunnel, limiting the maximum conductance through the dot to e^2/h .²⁷ The Kondo effect dramatically changes the situation by forming a spin-degenerate many-body singlet state, enabling both spins to participate in transport in parallel so that Kondo conductance can reach its unitary limit at $2e^2/h$.^{4,5} Experimentally, the unitary limit, first observed by van der Wiel *et al.*²⁸ in a GaAs-based gate-defined quantum dot, remains the exception rather than the rule, because it requires being far below the Kondo temperature, having symmetric tunnel coupling to the two leads, and having precisely integer dot occupancy.

Figure 2 presents a zoomed-in view of valley III from Fig. 1(c), showing the Kondo effect in the unitary limit. Note how the conductance maximum gradually approaches $2e^2/h$ with decreasing temperature. Here, the limit is reached only at some particular V_g , showing a peak instead of an extended plateau as reported by van der Wiel *et al.*²⁸ Since tunneling is so strong that level widths are almost as large as the Coulomb interaction on the dot, the dot occupancy n_d is not well quantized but rather changes monotonically, passing

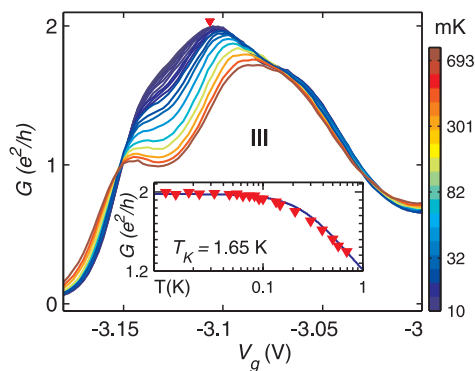


FIG. 2. (Color online) The Kondo effect in its unitary limit. The main plot shows the linear conductance G in valley III, as a function of backgate voltage V_g at different temperatures. The dark blue curve corresponds to the lowest temperature of 10 mK. Inset: the red triangles correspond to the temperature dependence of the conductance at a fixed $V_g = -3.107$ V (marked by the red triangle in the main graph). The blue curve represents the result of approximation with Eq. (4) where $G_0 = 1.98e^2/h$ and $T_K = 1.65$ K.

through $n_d = 1$ ($n_\uparrow = n_\downarrow = 1/2$) at $V_g \approx -3.1$ V, where the unitary limit is observed. In accordance with the Friedel sum rule, the conductance of the dot is predicted to depend on the dot occupancy $n_{\uparrow,\downarrow}$ as $G(\uparrow, \downarrow) = (e^2/h) \sin^2(\pi n_{\uparrow,\downarrow})$. So the sum of the conductances is $2e^2/h$ when $n_d = 1$. Note that the Kondo conductance shown in Fig. 1(c) always exceeds $1.3 e^2/h$ for different dot occupancies, showing that the wave-function overlap with the two leads is rather equal: the two couplings are within a factor of four of each other over this whole range, suggesting that disorder along the nanowire and especially at the tunnel barriers is quite weak. To extract the Kondo temperature, we apply a widely used phenomenological expression⁶ for the conductance G as a function of temperature:

$$G(T) = G_0[1 + (T/T'_K)^2]^{-s}, \quad (4)$$

where G_0 is the zero-temperature conductance, $T'_K = T_K/(2^{1/s} - 1)^{1/2}$, and the parameter $s = 0.22$ was found to give the best approximation to NRG calculations for a spin-1/2 Kondo system.³³ Here, the definition of T_K is such that $G(T_K) = G_0/2$. The inset of Fig. 2 shows the conductance for different temperatures at $V_g = -3.107$ V (marked by the red triangle in the main figure). The blue curve in the inset represents the result of the data approximation using Eq. (4) where the fitting parameters G_0 and T_K are $(1.98 \pm 0.02)e^2/h$ and 1.65 ± 0.03 K,³⁷ respectively, showing that the system is in the “zero-temperature” limit at base temperature, $T_K/T_{\text{base}} \approx 165$.

B. Conductance scaling with temperature, magnetic field, and bias

As noted above, the Kondo conductance as a function of temperature, bias or magnetic field should be describable by three universal functions common for any system exhibiting the Kondo effect. Before discussing expectations for universal scaling we describe in detail how temperature, magnetic field, and bias affect the Kondo conductance in our experimental system.

1. Kondo conductance and Kondo temperature at zero magnetic field

For a more detailed look at the spin-1/2 Kondo effect at $B = 0$, we select the two Kondo valleys IV and V [see Fig. 1(c)]. The zoomed-in plot of these two valleys is shown in Figs. 3(a) and 3(b). The coupling to the leads, and hence the Kondo temperature, is much larger in valley V than in valley IV. Valley IV shows a typical example of how two wide Coulomb blockade peaks merge into one Kondo valley as the temperature decreases below T_K .^{7,8,28} Valley V, in contrast, does not evolve into separate CB peaks even at our highest measurement temperature of 620 mK. Also, as seen from Fig. 3(b), the width of the ZBA, which is proportional to T_K , is larger for valley V. To illustrate this, in Figs. 4(a) and 4(b), we plot the conductance as a function of V_{sd} at different temperatures for two values of V_g [marked by red triangles in Fig. 3(a)] corresponding to the two valleys. In addition to the ZBA of valley IV being significantly narrower than that of valley V, at the highest temperatures, the ZBA of valley IV is completely absent, while the ZBA of valley V is still visible, pointing to a significant difference in T_K . To quantify this

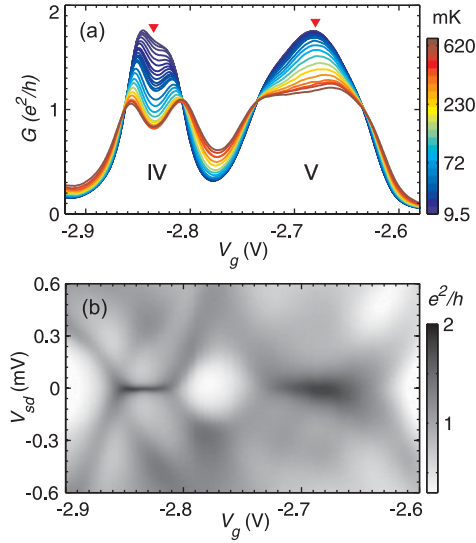


FIG. 3. (Color online) (a) The detailed measurement of the conductance temperature dependence shown in Fig. 1(c), valleys IV and V. The red triangles mark two values of $V_g = -2.835$ and -2.680 V for which the conductance as a function of V_{sd} is plotted in Figs. 4(a) and 4(b), respectively. (b) The gray-scale conductance plot in the V_g - V_{sd} plane was measured in the same range of V_g as in (a), at temperature $T = 10$ mK.

observation, we found T_K as a function of V_g for both valleys by fitting the temperature-dependent conductance using Eq. (4). The result of this fit is presented in Figs. 4(c) and 4(d). T_K shows a parabolic evolution across each valley, with T_K ranging from 0.3 to 1 K for valley IV and from 1.3 to 3 K for valley V. This significant difference in T_K correlates with the difference in the ZBA width shown in Figs. 4(a) and 4(b). However, the relation between the FWHM of the ZBA peak and T_K is more ambiguous due to out-of-equilibrium physics.³⁸

To understand the dependence of T_K on V_g and to extract some relevant parameters of the system, we use an analytic prediction for the dependence of the Kondo temperature based on the microscopic parameters in the Kondo regime of the single-impurity Anderson model.³⁹

$$T_K = \eta_{\text{NRG}} \frac{\sqrt{\Gamma U}}{2} \exp \left[\frac{\pi \varepsilon_0 (\varepsilon_0 + U)}{\Gamma U} \right]. \quad (5)$$

Here, Γ is the width of the resonant tunneling peak, $U = e^2/C_{\text{tot}}$ is the charging energy (C_{tot} is the total capacitance of the dot), and ε_0 is the energy of the resonant level relative to the Fermi level. As T_K is derived from the conductance [c.f. text following Eq. (4)], the prefactor η_{NRG} in Eq. (5) of order unity was calibrated using the NRG. To this end, we calculated the conductance $G(T)$ for the single-impurity Anderson model at $\varepsilon_0 = -U/2$, for fixed $U/\Gamma \simeq 4.5$. The requirement that $G(T = T_K)/G(0) = G_0/2$ fixes the prefactor in T_K to $\eta_{\text{NRG}} \simeq 1.10$, which we took constant throughout. η_{NRG} does vary as a function of U/Γ within a few tens of percent, due to the exponential sensitivity of Eq. (5), however, since U and Γ are already pretty well constrained in our case, this results in negligible variations in our fitted U , ε_0 , or Γ .

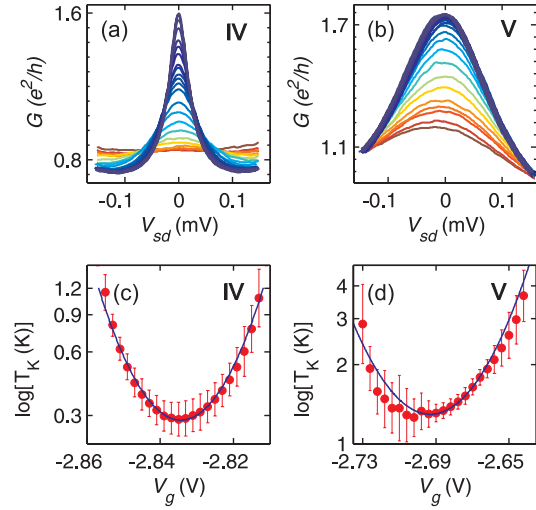


FIG. 4. (Color online) Nonlinear conductance as a function of V_{sd} around zero bias for different temperatures at $V_g = -2.835$ V (a) and $V_g = -2.680$ V (b), near the centers of Kondo valleys IV and V. The color scale is as in Fig. 3(a). (c) and (d) The Kondo temperature T_K , plotted on a semi-log scale, as a function of V_g for these same valleys. Panel (c) corresponds to valley IV and panel (d) to valley V. Blue curves in both panels show fits of Eq. (5) to data, with $\Gamma_{IV} \approx 176$ μeV for valley IV and $\Gamma_V \approx 435$ μeV for valley V.

To determine the parameters U , ε_0 , and Γ , we proceed as follows. The value of $U \approx 400$ μeV was found from Fig. 3(b) for valley IV (we assume the value is equal for valley V, though it may be slightly lower, given the stronger tunnel coupling there). To relate ε_0 and V_g , we used a simple linear relation $V_g - V_{g0} = \alpha \varepsilon_0$ with the lever arm $\alpha = C_{\text{tot}}/C_g$, where V_{g0} is the position of the Coulomb peak and C_g is the gate capacitance. Here, $C_{\text{tot}} = e^2/U$ and $C_g = e/\Delta V_g$ where ΔV_g is the CB period. Γ was determined by fitting the curvature of $\ln T_K$ with respect to gate voltage in Figs. 4(c) and 4(d), yielding $\Gamma_{IV} \approx 176$ μeV and $\Gamma_V \approx 435$ μeV for valleys IV and V, respectively.

As noted above, the predicted dependence of T_K in Eq. (5) is based on the Anderson model in the Kondo regime ($\varepsilon_0/\Gamma < -1/2$).³⁹ The fitting of the data with Eq. (5), however, gave $\varepsilon_0/\Gamma_{IV} \sim -1.1$ and $\varepsilon_0/\Gamma_V \sim -0.5$ in the centers of valleys IV and V, respectively. So the Kondo regime $\{|\varepsilon_0|, |\varepsilon_0 + U|\} > \Gamma/2$ is reached only near the center of valley IV and only at the very center of valley V. The rest of the gate voltage range in these valleys is the mixed valence regime, where charge fluctuations are important and Kondo scaling should not be quantitatively accurate.⁴⁰ Note that our NRG calculations show that the deviations from universal scaling up to $\varepsilon_0 \sim -\Gamma/2$ should be small for $T < T_K$. In any case, we have not attempted to take into account multiple levels in our calculations, which could quantitatively but not qualitatively modify the predicted behaviors.

2. Kondo conductance at nonzero magnetic field

The Kondo effect in quantum dots at nonzero magnetic field is predicted and observed to exhibit a Zeeman splitting of the ZBA by an energy $\Delta = 2|g|\mu_B B$ ^{6,8} (g is the g -factor

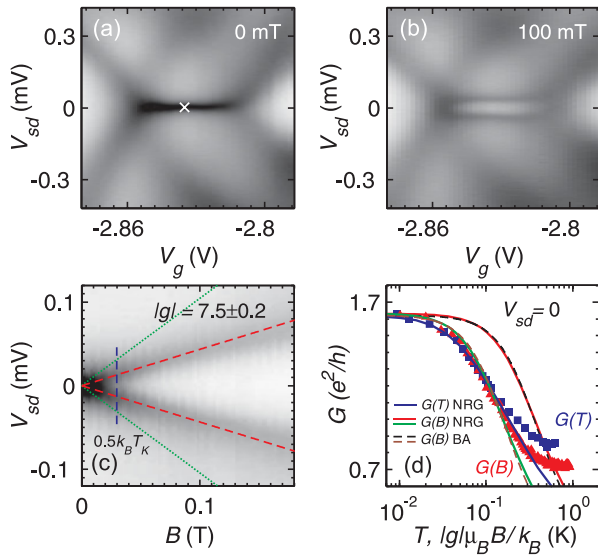


FIG. 5. (Color online) The Zeeman splitting of the Kondo ZBA measured at $T = 10$ mK. (a) The gray-scale conductance plot of Kondo valley IV [see Fig. 3(a)] measured at $B = 0$. (b) The same as in (a) but at $B = 100$ mT. (c) Gray-scale conductance plot in the V_{sd} - B plane measured at fixed $V_g = -2.835$ V denoted by the cross in panel (a). The red dashed lines represent the result of the fitting with expression $V_{sd} = \pm |g| \mu_B B / e$, where $|g| = 7.5 \pm 0.2$. Vertical blue dashed line marks magnetic field value $0.5k_B T_K / |g| \mu_B$ as a reference for the onset of Zeeman splitting (here $T_K = 300$ mK). While $|g| = 7.5$ gives the best match to linear Zeeman splitting, $|g| = 18$ (green dotted lines) could account for the fact that Zeeman splitting is resolved at very low field. (d) Conductance at $V_{sd} = 0$ as a function of T (blue squares) and as a function of the effective temperature $T_B \equiv |g| \mu_B B / k_B$ (red triangles). The solid blue curve shows $G(T)$ from NRG, the solid red curve $G(B)$ from NRG, and the dashed black curve $G(B)$ from exact Bethe ansatz (BA) calculations for the Kondo model.^{44,45} These assume $|g| = 7.5$. For NRG and BA calculations of magnetic field dependence, additional curves (solid green and dashed brown) are plotted for $|g| = 18$, showing better match to linear conductance data—though not to the differential conductance in (c) above.

and μ_B is the Bohr magneton), which is a direct consequence of the (now broken) spin-degeneracy of the many-body Kondo singlet.^{41,42}

To analyze the Zeeman splitting in our nanowire-based quantum dot, we focus on Kondo valley IV. The Kondo ZBA at zero field, seen in a zoom-in in Fig. 5(a), is suppressed at $B = 100$ mT, but recovers once a bias of ~ 40 μ V is applied [Fig. 5(b)]. Contrary to earlier observations in InAs nanowires,²⁰ we find that the g -factor at a given field is independent of V_g as illustrated by the parallel slitlike shape of the Zeeman splitting [see Fig. 5(b)]. (The g -factor measured for valley III at $V_g = -3.12$ V is $|g| = 7.5 \pm 0.2$. Unfortunately, it was problematic to extract the g -factor reliably for valley V due to large Γ_V and it was hence assumed to be the same as for valley IV. The g -factor for valley I measured at $V_g = -3.5$ V [see Fig. 1(c)] turns out to be somewhat larger $|g| = 8.7 \pm 0.2$.) The gray-scale conductance plot in Fig. 5(c) presents the evolution of the Zeeman splitting with

magnetic field at fixed $V_g = -2.835$ V, marked by the cross in Fig. 5(a) [for the associated ZBA measured at $B = 0$ refer to Fig. 4(a)]. The plot shows the splitting in bias Δ/e to be almost linear in magnetic field, which allows us to deduce the value of the g -factor by fitting the data with a linear dependence $V_{sd} = \pm |g| \mu_B B / e$ for 30 mT $< B < 100$ mT. Two red lines in Fig. 5(c) show the result of fitting with $|g| = 7.5 \pm 0.2$ (the meaning of the dotted green lines will be discussed below). This number is smaller by a factor of two than the InAs bulk value of $|g| = 15$, possibly due to the reduced dimensionality of the nanowire device,⁴³ and it is consistent with previous measurements.¹⁹

We now compare the dependence of the Kondo conductance on the temperature and magnetic field, respectively. In order to do so, we plot on the same graph $G(T, B = 0)$ and $G(T = T_{\text{base}}, B)$ both taken in equilibrium at $V_g = -2.835$ V [see Fig. 5(d)]. In order to quantitatively compare the effect of magnetic field to that of temperature, we associate each magnetic field value with an effective temperature $T_B(B) \equiv |g| \mu_B B / k_B$, where $|g| = 7.5$ is extracted from the linear Zeeman splitting of peaks in differential conductance. The comparison of the linear conductance data is presented in Fig. 5(d), where $G(T)$ is shown by the blue squares, $G(B)$ by the red triangles. In this same plot, theoretical predictions are shown as curves: blue for $G(T)$ and red for $G(B)$. Note that for $|g| = 7.5$ (this value extracted from the splitting of the differential conductance peaks), the blue and red curves differ substantially for essentially all nonzero values of their arguments, with magnetic field having a much weaker predicted effect than temperature. Surprisingly, in light of this theoretical prediction, the two sets of experimental data lie almost on top of one another up to about 200 mK $\approx T_K$. The NRG results for $G(T = 0, B)$ ^{42,44} have been checked against exact Bethe ansatz calculations^{42,45} for $G(T = 0, B)$ [dashed black curve in Fig. 5(d)] and are seen to be in excellent agreement, so the disagreement between theory and experiment is not related to a particular calculational framework. Were we to assume $|g| = 18$, we could explain the experimental magnetic field dependence of linear conductance $G(T = 0, B)$, as shown by alternative curves (solid green and dashed brown) plotted in Fig. 5(d). This value of g is within the realm of possibility for InAs nanowires.²⁰ However, we are inclined to rely on the g value of 7.5 extracted from the splitting of the peaks in the differential conductance. With $|g| = 18$ we would have the puzzling result that the splitting of peaks in differential conductance would be less than half the expected $2|g| \mu_B B$ [see dotted green lines in Fig. 5(c)], which would be hard to explain. Regardless, the mismatch between the strength of magnetic field effects on linear and differential conductance is a conundrum. We hope this work will stimulate further theory and experiment to address this issue.

3. Universal conductance scaling

In testing universal conductance scaling, we concentrate first on the scaling of the linear conductance with T and B . In the case of temperature dependence, the universal scaling function has the form of Eq. (4). This expression has been applied to a wide variety of experimental Kondo systems^{7,11,14,19} and after expansion in the low-energy limit

ANDREY V. KRETININ *et al.*PHYSICAL REVIEW B **84**, 245316 (2011)

($T/T_K \ll 1$) it becomes Eq. (1) describing the quadratic dependence on temperature:³²

$$G \approx G_0[1 - c_T(T/T_K)^2], \quad (6)$$

where $c_T = c_A = s(2^{1/s} - 1) = 4.92$ and $s = 0.22$ is taken from Eq. (4). Note that this coefficient c_T is about 10% smaller than the more reliable value $c_T = 5.38$ ^{30,33,46,47} found from the NRG calculations on which the phenomenological form of Eq. (4) is based. (This slight disagreement stems from the fact that the phenomenological expression given by Eq. (4) was designed for the intermediate range of temperatures and does not necessarily describe the dependence accurately at asymptotically low $T \ll T_K$ or asymptotically high $T \gg T_K$ temperatures. Hereafter, for the low-temperature analysis, we use the theoretically predicted value $c_T = 5.38$, see Table I) Since Eq. (4) is independent of the particular system, it can be used as the universal scaling function $G/G_0 = f(T/T_K)$. Figures 6(a) and 6(b) show the equilibrium Kondo conductance ($1 - G/G_0$) of valleys IV and V [see Fig. 3(a)] plotted as a function of T/T_K , taken at different V_g . Here, the values of G_0 and T_K are found by fitting the data with Eq. (4) for $T \leq 200$ mK (for higher temperatures the conductance starts to deviate from the expected dependence due to additional high-temperature transport mechanisms). As seen in Figs. 6(a) and 6(b), all the data collapse onto the same theoretical curve (dashed) regardless of the values of V_g or T_K . In the low-energy limit $T/T_K < 0.1$, the conductance follows a quadratic dependence set by Eq. (1) with coefficient $c_A = c_T = 5.38$ as shown by the dotted line. As noted above, in the low-energy limit, the phenomenological expression Eq. (4) is less accurate and shows a quadratic dependence with $c_T = 4.92$. This explains why the dashed and dotted curves in Figs. 6(a) and 6(b) do not coincide at $T/T_K < 0.1$.

It should also be possible to scale $G(B)$ as a function of a single parameter T_B/T_K . As an example, we present in Fig. 6(a) scaled $G(B)$ data from Fig. 5(d). At low fields, the measured conductance is found to depend on B according to Eq. (1), with the coefficient $c_A = c_B \approx c_T$. This equality has also been independently checked by fitting the $G(B)$ and $G(T)$ data for $T/T_K, T_B/T_K < 0.1$ with Eq. (1). The ratio between the two fit coefficients, c_B/c_T , is approximately 1 ($c_B/c_T = 0.95 \pm 0.2$), strongly counter to the theoretical expectations where $c_B = 0.55$ and $c_B/c_T = 0.101$, see Table I. To illustrate this discrepancy, we plot Eq. (1) with $c_A = c_B = 0.55$ in Fig. 6(a) (dash-dot line). The reason for such a dramatic difference in $G(B)$ dependence between theory and experiment for both low- and intermediate-field range is unclear. We speculate that the spin-orbit interaction, previously observed in InAs nanowire-based quantum dots,⁴⁸ may play a role.

It is important to note that in order for the universal scaling $G(B)$ to be valid, the coefficient G_0 in Eqs. (1) and (3) should be independent of B . In the case of GaAs quantum dots^{7,8,26,49} with $|g_{\text{GaAs}}| = 0.44$, the magnetic field required to resolve the Zeeman splitting is high and the orbital effects of that field contribute significantly, resulting in a B -dependent G_0 , even for a field parallel to the plane of the heterostructure. In contrast, in our InAs nanowire-based quantum dot, with large g -factor and small dot area $S = 50 \text{ nm} \times 450 \text{ nm}$, Kondo resonances are suppressed (split to finite bias) at fields smaller

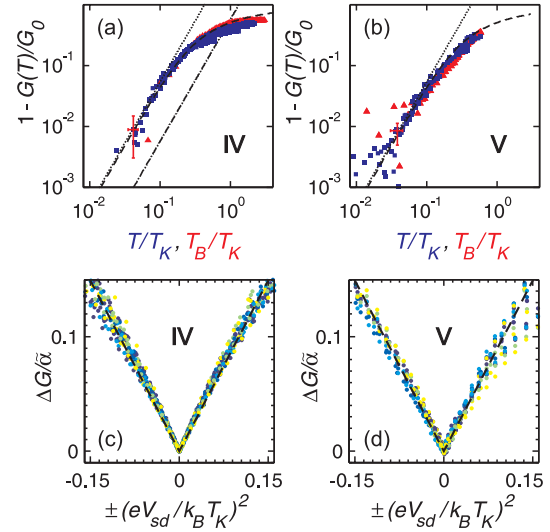


FIG. 6. (Color online) (a) and (b) The equilibrium conductance of Kondo valleys IV (a) and V (b) at different V_g , scaled as a function of a single argument T/T_K (blue squares) and T_B/T_K (red triangles), where $T_B \equiv |g|\mu_B B/k_B$. The dashed curve shows the universal function described by Eq. (4). The dotted line represents the low-energy limit of Eq. (1) with $c_A = c_T = 5.38$. The dash-dotted line shows the theoretically predicted low-field scaling of $G(B)$ with $c_B = 0.55$. The values of G_0 and T_K were found by fitting the data with Eq. (4), see Sec. III B 1. For values of V_g refer to Figs. 4(c), 4(d), and 5(d). (c) and (d) The scaled conductance $\Delta G/\bar{\alpha} = [1 - G(T, V_{sd})/G(T, 0)]/\bar{\alpha}$, where $\bar{\alpha} = c_T \alpha / [1 + c_T(\gamma/\alpha - 1)](T/T_K)^2$, versus $(eV_{sd}/k_B T_K)^2$ taken at several V_g along Kondo valleys IV (c) and V (d). For valley IV, the backgate voltage was chosen from the range $V_g = -2.82$ to -2.85 V with 5 mV step and for valley V from the range $V_g = -2.68$ to -2.72 V with 20 mV step. Different colors of the data points represent different temperatures (9.5, 12.9, 22.4, 32.6, 46.1, and 54.2 mK). The dashed line shows the corresponding scaling function given by Eq. (7) with $\alpha = 0.18$ and $\gamma = 1.65$.

than that required to thread one magnetic flux quantum $B < (h/e)/S \approx 180$ mT, thus making the orbital effects negligible and G_0 magnetic field independent.

Now that the scaling of the linear conductance has been established, including the stronger-than-expected effect of magnetic field, we examine how the out-of-equilibrium conductance scales as a function of bias and temperature $G/G_0 = f(T/T_K, eV_{sd}/k_B T_K)$. The function used to test the universal scaling in a GaAs quantum dot,³² and in a single-molecule device,¹⁴ originates from the low-bias expansion of the Kondo local density of states⁵⁰ and has the following form:

$$G(T, V_{sd}) = G(T, 0) \left[1 - \frac{c_T \alpha}{1 + c_T \left(\frac{\gamma}{\alpha} - 1\right) \left(\frac{T}{T_K}\right)^2} \left(\frac{eV_{sd}}{k_B T_K}\right)^2 \right]. \quad (7)$$

The coefficients α and γ relate to the zero-temperature width and the temperature-broadening of the Kondo ZBA, respectively. The zero-bias conductance $G(T, 0)$ is defined by Eq. (6). The coefficients α and γ are independent of the

definition of the Kondo temperature and in the low-energy limit Eq. (7) reduces to the theoretically predicted expression for nonequilibrium Kondo conductance:³¹

$$\frac{G(T, V_{sd}) - G(T, 0)}{c_T G_0} \approx \alpha \left(\frac{eV_{sd}}{k_B T_K} \right)^2 - c_T \gamma \left(\frac{T}{T_K} \right)^2 \left(\frac{eV_{sd}}{k_B T_K} \right)^2. \quad (8)$$

The independence of α and γ on the definition of Kondo temperature is important; though we have chosen an explicit definition for T_K , consistent with the choice used for most quantum dot experiments and NRG calculations, other definitions may differ by a constant multiplicative factor.

Figures 6(c) and 6(d) show the scaled finite-bias conductance $[1 - G(T, V_{sd})/G(T, 0)]/\tilde{\alpha}$, where $\tilde{\alpha} = c_T \alpha/[1 + c_T(\gamma/\alpha - 1)](T/T_K)^2$, versus $(eV_{sd}/k_B T_K)^2$, measured at different temperatures and a few values of V_g . The conductance data are fit with Eq. (7) using a procedure described by M. Grobis *et al.*³² with two fitting parameters α and γ . The range of temperatures and biases used for the fitting procedure was chosen to be close to the low-energy limit, namely, $T/T_K < 0.2$ and $eV_{sd}/k_B T_K \lesssim 0.2$, which is comparable to the ranges used in Ref. 32. Averaging over different points in V_g gives $\alpha = 0.18 \pm 0.015$ and $\gamma = 1.65 \pm 0.2$ for valley IV. Despite valley V being in the mixed-valence regime, the parameters α and γ are close to those found for valley IV. The scaled conductance in both cases collapses onto the same curve, shown by the dashed line, for $\pm(eV_{sd}/k_B T_K)^2 \leq 0.1$, though the data from valley V deviate more from the predicted scaling. This is not surprising because the valley V data are in the mixed-valence regime, beside that the bias can cause additional conduction mechanisms due to proximity of the Coulomb blockade peaks.

Overall, the value of α obtained in our experiment is larger than previously observed in a GaAs dot^{32,51} ($\alpha = 0.1$) and single molecule¹⁴ ($\alpha = 0.05$). The exact reason for this discrepancy is unknown, but the smaller ratio T_{base}/T_K may play a role.

There is a large number of theoretical works devoted to the universal behavior of finite-bias Kondo conductance based on both the Anderson^{33,47,52–59} and Kondo^{29,31,60–63} models. Early predictions based on an exactly solvable point of the anisotropic nonequilibrium Kondo model^{31,60,61} yielded a value $\alpha = c_V/c_T = 3/\pi^2 \approx 0.304$. This turned out to be in disagreement with experiment, which is not surprising, since this coefficient is not universal and hence will not be the same for the isotropic Kondo models. A number of subsequent papers that used a Fermi-liquid approach to treat the strong-coupling fixed point of the Kondo model^{29,64,65} or studied the $U \rightarrow \infty$ limit of the symmetric Anderson model,^{52–57} all found $\alpha = 3/(2\pi^2) \approx 0.152$. Our measured value of $\alpha = 0.18$ is in a good agreement with this prediction. A Bethe-Ansatz treatment of the nonequilibrium Anderson model⁴⁷ yielded a different result, $\alpha = 4/\pi^2$, but this was obtained using some approximations and was not claimed to be exact. Some of the more recent theoretical papers have studied the α_V coefficients for the nonequilibrium Anderson model under less restrictive conditions, i.e., allow for a left-right asymmetry and a noninfinite U , in an attempt to

explain the experimental results of Refs. 14,32. J. Rincón and coauthors^{53–55} found that by setting U to be finite the expected value of α is decreased from 0.152 to 0.1, but γ remains ≈ 0.5 . Later, P. Roura-Bas⁵⁶ came to a similar conclusion considering the Anderson model in the strong-coupling limit in both the Kondo and the mixed-valence regimes. It was shown⁵⁶ that α reduces from 0.16 to 0.11 if some charge fluctuation is allowed by shifting from the Kondo to the mixed-valence regime, and the parameter γ is not necessarily temperature independent. In an attempt to explain the small α observed in molecular devices¹⁴ Sela and Malecki⁵⁷ evaluated a model for the Anderson impurity asymmetrically coupled to the leads. They concluded that deep in the Kondo regime α takes the value of $3/(2\pi^2) \approx 0.152$ independent of coupling asymmetry. However, if U is made finite or, in other words, some charge fluctuations are included, the parameter can vary within the range $3/(4\pi^2) \leq \alpha \leq 3/\pi^2$ ($0.075 \leq \alpha \leq 0.3$) depending on the asymmetry of the tunneling barriers. Despite the fact that our system is far from the strong coupling limit ($U \sim \Gamma$, instead of $U \gg \Gamma$, see Sec. III B 1), the observed value of $\alpha = 0.18$ is a good match to the strong-coupling prediction.

From temperature, magnetic field, and bias scaling of the measured conductance, we are able to define a complete set of coefficients c_A to be used in Eq. (1) in order to describe the Kondo effect in the low-energy limit:

$$\begin{aligned} G(T) &= G_0[1 - c_T(T/T_K)^2], \\ G(B) &= G_0[1 - c_B(|g|\mu_B B/k_B T_K)^2], \\ G(V_{sd}) &= G_0[1 - c_V(eV_{sd}/k_B T_K)^2], \end{aligned}$$

where G_0 is the conductance at zero temperature, magnetic field, and bias, $c_T \approx 5.6 \pm 1.2$, $c_B \approx 5.1 \pm 1.1$, and $c_V = c_T \alpha \approx 1.01 \pm 0.27$. The substantial uncertainties originate from the small number of experimental points satisfying the requirement of low temperature, field, and bias used during fitting with Eq. (1). Table I summarizes the experimental value of these three parameters and compares to their theoretical predictions. (The parameter α discussed above is denoted by α_V in the table.)

C. Zeeman splitting

At nonzero magnetic field, the spin degeneracy of the Kondo singlet is lifted and the linear conductance through the dot is suppressed.⁴¹ To recover strong transport through the dot, a bias of $\pm \frac{1}{2} \Delta/e = \pm |g|\mu_B B/e$ should be applied in order to compensate for the spin-flip energy. As a result, in experiments, the ZBA is split into two peaks separated by $e\Delta = 2|g|\mu_B B/e$,^{6,8} providing information on the effective g -factor. This is why the splitting of the Kondo conductance feature has become a popular tool for evaluating the value and behavior of the g -factor in quantum dots made of different materials.^{12,16,17,19,20,26,72} In this section, we discuss two unexpected features related to the Zeeman splitting. First, the minimal value of field needed to resolve the Zeeman splitting is lower than expected. Second, the splitting is weakly sublinear with magnetic field at larger fields.

Some attention has been previously paid to the value of the critical field B_c at which the splitting of the Kondo ZBA occurs. The theory developed by one of the present

TABLE I. Summary of theoretically predicted parameters c_T , c_V , c_B , and B_c and their experimental values. The second column lists the values of the parameters c'_A appearing in $G(A) = G_0[1 - c'_A(A/k_B T_0)^2]$, using a definition for the Kondo scale that is widespread in theoretical papers, namely, $T_0 = 1/(4\chi_0)$, where χ_0 is the static impurity spin susceptibility at $T = 0$. This definition of the Kondo temperature differs from the T_K used in this paper, i.e., $G(T_K) = G(0)/2$, by the factor $T_K/T_0 = 0.94$.⁶⁶ Thus the coefficients c_A defined in our Eq. (1) and listed in the fourth column are related to those in the second by $c_A/c'_A = (T_K/T_0)^2$. We cite only references that are relevant for the symmetric Anderson model in the large- U limit, where the local occupancy is one; generalizations for the asymmetric Anderson model may be found in Refs. 53–55, 57, 58, 63. The last row lists values for the critical magnetic field B_c beyond which the Kondo ZBA splits and it is expressed in units of T_K defined by Eq. (2) (Theory: column 2; Experiment: column 5).

Parameter	Predicted c'_A	$\alpha_A = c'_A/c'_T$	$c_A = c'_A(T_K/T_0)^2$	Experimental value
c_T	$\pi^4/16 \approx 6.088^a$	1	5.38	5.6 ± 1.2^b
c_V	$3\pi^2/32 \approx 0.925^c$	$3/(2\pi^2) \approx 0.152$	0.82	$1.01 \pm 0.27,^b 0.670,^d 0.304^e$
c_B	$\pi^2/16 \approx 0.617^f$	$1/\pi^2 \approx 0.101$	0.55	5.1 ± 1.1^b
$ g \mu_B B_c/k_B T_K$	$1.06,^g 1.04,^h 1.1^i$			$<0.5,^b 0.5,^j 1,^k 1.5^l$

^aReferences 29,30,33,46,47,64,65,67–69.

^bPresent experiment.

^cReferences 29,52–57,63–65.

^dReferences 32,51.

^eReference 14.

^fReferences 29,47,64,65.

^gReference 42.

^hReference 70.

ⁱReference 71.

^jReference 72.

^kReference 49.

^lReference 12.

authors⁴² predicts the value of the critical field at $T/T_K < 0.25$ to be $B_c = 1.06k_B T_K/|g|\mu_B$, with similar values being found by other authors.^{70,71,73} Treating nonequilibrium more realistically gives a slightly larger value.⁷¹ Recent work by the authors, using density matrix approaches,^{74,75} suggests that a precise determination of the critical field is a numerically difficult task, which will require further work in order to establish this beyond any doubt. There are also somewhat conflicting experimental data on this issue. The value of B_c predicted by Costi⁴² and Hewson *et al.*⁷⁰ seems to agree with the experimental findings for GaAs dots,⁴⁹ however, in gold break junctions⁷² the onset of the splitting was measured at $0.5k_B T_K/|g|\mu_B$ and in the case of carbon nanotubes¹² at about $1.5k_B T_K/|g|\mu_B$. In our case, $T_K = 300$ mK [see Fig. 4(c)], thus the predicted B_c ^{42,70,71,73} is expected to be ~ 60 mT (for $|g| = 7.5$), more than twice as large as that observed experimentally: as seen in Figs. 7(a) and 5(c), the splitting is already well resolved at $B = 30$ mT, which corresponds to $\sim 0.5k_B T_K/|g|\mu_B$, the same as the result for gold break junctions.⁷² Such a wide deviation of B_c found for various Kondo systems (see Table I) may be associated with a different width of ZBA (relative to T_K) in the various experiments. Since the conductance peak discussed here [see Fig. 4(a)] is rather narrow, most likely due to the relatively low temperature $T/T_K \approx 1/30$, it is possible to resolve the splitting onset at lower magnetic field. The analysis of the nonequilibrium scaling parameters, described in Sec. III B 3, confirms the above assumption.

Finally, we discuss the evolution of the splitting Δ with magnetic field. Theory predicts that the peaks in the spectral function for spin-up and spin-down electrons should cling closer to zero energy at relatively low magnetic fields than

might naively be expected, so that Δ should be suppressed by up to $\approx 1/3$ in the low-field limit.^{46,76–80} One recent experimental report corroborates this predicted trend of suppressed splitting at low field.¹² But the variety of deviations from linear splitting in experiments—especially near the onset of splitting—is large.^{12,49} To make small variations in Δ more visible, we plotted the normalized value $\delta(B) \equiv \Delta/(2|g|\mu_B B)$ in Fig. 7(b). The value of Δ was deduced from a simple peak maximum search (blue squares) and by fitting the data with the sum of two asymmetric peak shapes and some background (red triangles). To fit G as a function of V_{sd} we used a combination of two Fano-shape asymmetric peaks on a cubic background:

$$G(V_{sd}) = A_1 \frac{\left(-\frac{V_{sd}+V_1}{\Gamma_1} + q_1\right)^2}{1 + \left(-\frac{V_{sd}+V_1}{\Gamma_1}\right)^2} + A_2 \frac{\left(\frac{V_{sd}+V_2}{\Gamma_2} + q_2\right)^2}{1 + \left(\frac{V_{sd}+V_2}{\Gamma_2}\right)^2} + B|V_{sd}|^3 + C. \quad (9)$$

Here, A_1 and A_2 are the amplitudes, Γ_1 and Γ_2 are the widths, q_1 and q_2 are the asymmetry parameters of the two Fano resonances positioned at dc bias V_1 and V_2 , respectively. Parameters B and C characterize the cubic conductance background. Without the cubic background, the positions of the conductance peaks, which correspond to Fano resonances at V_1 and V_2 would be $V_{p1} = V_1 + \Gamma_1/q_1$ and $V_{p2} = V_2 + \Gamma_2/q_2$. The peak separation is deduced from the fit according to the equation $\Delta/e = V_{p2} - V_{p1}$. The quality of this fit is shown in Fig. 7(a) by red solid curves. It is clear that at $B > 100$ mT, the splitting is sublinear in magnetic field. Coincidence of the splitting data extracted by two different methods [blue triangles and red squares in Fig. 7(b)] makes us believe that this effect is genuine and not an artifact due to weakly bias-dependent

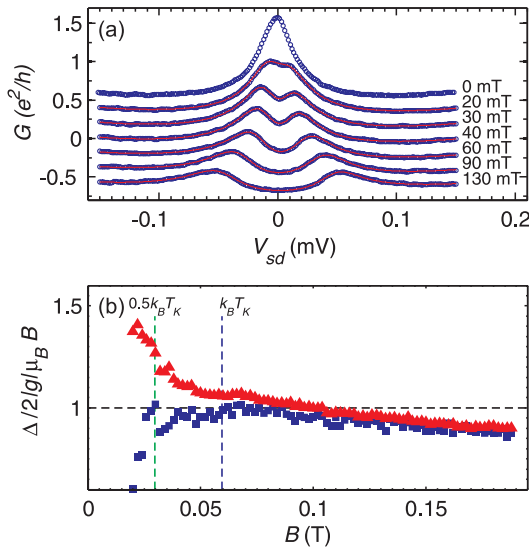


FIG. 7. (Color online) (a) The nonequilibrium Kondo conductance as a function of V_{sd} for several values of B (open blue squares). The solid red curves represent the approximation of the data made with the sum of two Fano-shaped peaks and a cubic background. (b) The normalized Zeeman splitting $\Delta/[2|g|\mu_B B]$ as a function of B data acquired from the peak maximum search (blue squares) and after fitting with two asymmetric peak shapes (red triangles). The vertical blue and green dashed lines denote magnetic field of $0.5k_B T_K/|g|\mu_B$ and $k_B T_K/|g|\mu_B$ correspondingly (here $|g| = 7.5$ and $T_K = 300$ mK).

background conductance. In contrast, splitting extracted from our data at low fields $B < k_B T_K/|g|\mu_B$ is dependent on the extraction method used, so we do not wish to make quantitative claims for the magnitude of splitting in that field range. Our results differ from previous observations mainly in that a sublinear field splitting occurs also at higher fields and not only at the onset of the splitting.^{12,49} We are unaware of any theoretical predictions which would explain such sublinear splitting or effective reduction in the g -factor at higher fields.

Previous theoretical works on the Kondo model predicted a suppressed splitting $\delta(B) = \Delta/[2|g|\mu_B B]$ increasing monotonically toward one for $g\mu_B B \gg k_B T_K$ with logarithmic corrections.^{76,80,81} For the Anderson model, similar results have been found with $\delta(B)$ rising monotonically with increasing B .^{77,82,83} However, in some works^{71,77,82} $\delta(B \gg k_B T_K)$ is found to exceed one, whereas in other works,^{46,83} $\delta(B \gg k_B T_K)$ remains below one. This discrepancy between different approaches is likely due to different approximations and the extent to which universal aspects as opposed to nonuniversal aspects are being addressed and remains to be clarified. For example, it is known that extracting peak positions in equilibrium spectral functions within NRG is problematic.^{71,83,84} Extracting a Zeeman splitting from experimental dI/dV_{sd} at finite bias and large magnetic fields is also complicated by the increasing importance of higher levels and nonequilibrium charge fluctuations.⁸⁵ Nevertheless, our results for $\delta(B \gg k_B T_K)$ in Fig. 7(b) exhibit a monotonically decreasing $\delta(B)$ in the high-field limit for $B > 1.5k_B T_K/|g|\mu_B$. This contrasts to current theoretical predictions. As we cannot exclude the

contribution of orbital effects at higher B , the magnetic fields used to determine the g -factor were chosen to be smaller than 100 mT (flux through dot $\leq 0.6\Phi_0$).

IV. CONCLUSION

In conclusion, we have performed a comprehensive study of the spin-1/2 Kondo effect in an InAs nanowire-based quantum dot. This experimental realization of a quantum dot allowed us to observe and thoroughly examine the main features of the Kondo effect including the unitary limit of conductance and dependence of the Kondo temperature on the parameters of the quantum dot. Also the Kondo temperature's quantitative relation to the Kondo ZBA shape, Zeeman splitting of the ZBA, and scaling rules for equilibrium and nonequilibrium Kondo transport were studied. A previously undetected dependence of the g -factor on magnetic field was observed. The nonequilibrium conductance matches the previously introduced universal function of two parameters with expansion coefficients, $\alpha = 0.18$ and $\gamma = 1.65$, in quantitative agreement with predictions for the infinite- U Anderson model, and consistent with the allowed range for the finite- U asymmetric Anderson model. We conclude that InAs nanowires are promising new objects to be used in future mesoscopic transport experiments, including highly quantitative studies.

There is one experimental observation, however, that is strikingly at odds with theoretical expectations: the conductance $G(B)$ at low temperatures shows a much stronger magnetic field dependence than expected from theoretical calculations for the single-impurity Anderson model [see Fig. 5(d)]. As possible cause for this unexpected behavior, we suggest spin-orbit interactions, which are known to be strong in InAs nanowires.⁴⁸ The occurrence of a Kondo effect is compatible with the presence of spin-orbit interactions, since they do not break time-reversal symmetry. However, they will, in general, modify the nature of the spin states that participate in the Kondo effect.^{86–89} In the present geometry, where spin-orbit interactions are present in the nanowire (but not in the leads), there will be a preferred quantization direction (say \vec{n}_{so}) for the doublet of local states. In general, \vec{n}_{so} is not collinear with the direction of the applied magnetic field, \vec{B} . The local doublet will be degenerate for $\vec{B} = 0$, allowing a full-fledged Kondo effect to develop as usual in the absence of an applied magnetic field. However, the energy splitting of this doublet with increasing field will, in general, be a nonlinear function of $|\vec{B}|$, whose precise form depends on the relative directions of \vec{B} and \vec{n}_{so} . According to this scenario, the magnetoconductance curves measured in the present work would not be universal, but would change if the direction of the applied field were varied. A detailed experimental and theoretical investigation of such effects is beyond the scope of the present paper, but would be a fruitful subject for future studies.

ACKNOWLEDGMENTS

The authors would like to thank Moty Heiblum for making this work possible and for suggestions and critical remarks made during the work. We also acknowledge Yuval Oreg, Mike

Grobis, Nancy Sandler, Sergio Ulloa, and Jens Paaske for fruitful discussions, Ronit Popovitz-Biro for the TEM analysis of nanowires, and Michael Fourmansky for technical assistance. We thank David Logan and Martin Galpin for reading an earlier version of our manuscript and pointing out that the dependence of linear conductance (but not differential conductance) on magnetic field could be understood quantitatively by taking a higher value for g -factor. A.V.K. is grateful to Yunchul

Chang for his design ideas and expertise in electronics. This work was partially supported by the EU FP6 Program Grant 506095, by the Israeli Science Foundation Grant 530-08 and Israeli Ministry of Science Grant 3-66799. D.G.-G. acknowledges NSF contract DMR-0906062 and US-Israel BSF grant No. 2008149. T.A.C. acknowledges supercomputer support from the John von Neumann Institute for Computing (Jülich).

*andrey.kretinin@weizmann.ac.il

- ¹J. Kondo, *Prog. Theor. Phys.* **32**, 37 (1964).
- ²M. P. Sarachik, E. Corenzwit, and L. D. Longinotti, *Phys. Rev.* **135**, A1041 (1964).
- ³M. A. Reed, J. N. Randall, R. J. Aggarwal, R. J. Matyi, T. M. Moore, and A. E. Wetzel, *Phys. Rev. Lett.* **60**, 535 (1988).
- ⁴L. I. Glazman and M. E. Raikh, *JETP Lett.* **47**, 452 (1988).
- ⁵T. K. Ng and P. A. Lee, *Phys. Rev. Lett.* **61**, 1768 (1988).
- ⁶D. Goldhaber-Gordon, H. Shtrikman, D. Mahalu, D. Abusch-Magder, U. Meirav, and M. Kastner, *Nature (London)* **391**, 156 (1998).
- ⁷D. Goldhaber-Gordon, J. Göres, M. A. Kastner, H. Shtrikman, D. Mahalu, and U. Meirav, *Phys. Rev. Lett.* **81**, 5225 (1998).
- ⁸S. M. Cronenwett, T. H. Oosterkamp, and L. P. Kouwenhoven, *Science* **281**, 540 (1998).
- ⁹J. Schmid, J. Weis, K. Eberl, and K. von Klitzing, *Physica B* **256**, 182 (1998).
- ¹⁰F. Simmel, R. H. Blick, J. P. Kotthaus, W. Wegscheider, and M. Bichler, *Phys. Rev. Lett.* **83**, 804 (1999).
- ¹¹J. Nygard, D. Cobden, and P. Lindelof, *Nature (London)* **408**, 342 (2000).
- ¹²C. H. L. Quay, J. Cumings, S. J. Gamble, R. dePicciotto, H. Kataura, and D. Goldhaber-Gordon, *Phys. Rev. B* **76**, 245311 (2007).
- ¹³L. H. Yu and D. Natelson, *Nano Lett.* **4**, 79 (2004).
- ¹⁴G. D. Scott, Z. K. Keane, J. W. Ciszek, J. M. Tour, and D. Natelson, *Phys. Rev. B* **79**, 165413 (2009).
- ¹⁵J. Li, W.-D. Schneider, R. Berndt, and B. Delley, *Phys. Rev. Lett.* **80**, 2893 (1998).
- ¹⁶W. Liang, M. Shores, M. Bockrath, J. Long, and H. Park, *Nature (London)* **417**, 725 (2002).
- ¹⁷J. Park, A. Pasupathy, J. Goldsmith, C. Chang, Y. Yaish, J. Petta, M. Rinkoski, J. Sethna, H. Abruna, P. McEuen, and D. Ralph, *Nature (London)* **417**, 722 (2002).
- ¹⁸L. H. Yu, Z. K. Keane, J. W. Ciszek, L. Cheng, J. M. Tour, T. Baruah, M. R. Pederson, and D. Natelson, *Phys. Rev. Lett.* **95**, 256803 (2005).
- ¹⁹T. S. Jespersen, M. Aagesen, C. Sorensen, P. E. Lindelof, and J. Nygard, *Phys. Rev. B* **74**, 233304 (2006).
- ²⁰S. Csonka, L. Hofstetter, F. Freitag, S. Oberholzer, C. Schoenberger, T. S. Jespersen, M. Aagesen, and J. Nygard, *Nano Lett.* **8**, 3932 (2008).
- ²¹H. A. Nilsson, P. Caroff, C. Thelander, M. Larsson, J. B. Wagner, L.-E. Wennerström, L. Samuelson, and H. Q. Xu, *Nano Lett.* **9**, 3151 (2009).
- ²²A. V. Kretinin, R. Popovitz-Biro, D. Mahalu, and H. Shtrikman, *Nano Lett.* **10**, 3439 (2010).
- ²³S. M. Cronenwett, H. J. Lynch, D. Goldhaber-Gordon, L. P. Kouwenhoven, C. M. Marcus, K. Hirose, N. S. Wingreen, and V. Umansky, *Phys. Rev. Lett.* **88**, 226805 (2002).
- ²⁴J. Salfi, S. Roddaro, D. Ercolani, L. Sorba, I. Savelyev, M. Blumin, H. E. Ruda, and F. Beltram, *Semicond. Sci. Technol.* **25**, 024007 (2010).
- ²⁵A. Bid, N. Ofek, H. Inoue, M. Heiblum, C. L. Kane, V. Umansky, and D. Mahalu, *Nature (London)* **466**, 585 (2010).
- ²⁶A. Kogan, S. Amasha, D. Goldhaber-Gordon, G. Granger, M. A. Kastner, and H. Shtrikman, *Phys. Rev. Lett.* **93**, 166602 (2004).
- ²⁷*Single Charge Tunneling: Coulomb Blockade Phenomena in Nanostructures*, edited by H. Grabert and M. H. Devoret, NATO Advanced Studies Institute, Series B: Physics (Plenum Press, New York, 1992), Vol. 294, p. 167.
- ²⁸W. van der Wiel, S. De Franceschi, T. Fujisawa, J. Elzerman, S. Tarucha, and L. Kouwenhoven, *Science* **289**, 2105 (2000).
- ²⁹M. Pustilnik and L. Glazman, *J. Phys. Condens. Matter* **16**, R513 (2004).
- ³⁰P. Nozières, *J. Low Temp. Phys.* **17**, 31 (1974).
- ³¹A. Schiller and S. Hershfield, *Phys. Rev. B* **51**, 12896 (1995).
- ³²M. Grobis, I. G. Rau, R. M. Potok, H. Shtrikman, and D. Goldhaber-Gordon, *Phys. Rev. Lett.* **100**, 246601 (2008).
- ³³T. A. Costi, A. C. Hewson, and V. Zlatić, *J. Phys. Condens. Matter* **6**, 2519 (1994).
- ³⁴A. Kogan, G. Granger, M. A. Kastner, D. Goldhaber-Gordon, and H. Shtrikman, *Phys. Rev. B* **67**, 113309 (2003).
- ³⁵G. Granger, M. A. Kastner, I. Radu, M. P. Hanson, and A. C. Gossard, *Phys. Rev. B* **72**, 165309 (2005).
- ³⁶N. Roch, S. Florens, V. Bouchiat, W. Wernsdorfer, and F. Balestro, *Nature (London)* **453**, 633 (2008).
- ³⁷Here and throughout the text, the errors and error bars represent the 68% confidence interval. The systematic errors caused by the uncertainty in conductance and temperature measurements are believed to be less than 3%.
- ³⁸F. B. Anders, *Phys. Rev. Lett.* **101**, 066804 (2008).
- ³⁹F. D. M. Haldane, *Phys. Rev. Lett.* **40**, 416 (1978).
- ⁴⁰A. Makarovski, J. Liu, and G. Finkelstein, *Phys. Rev. Lett.* **99**, 066801 (2007).
- ⁴¹Y. Meir, N. S. Wingreen, and P. A. Lee, *Phys. Rev. Lett.* **70**, 2601 (1993).
- ⁴²T. A. Costi, *Phys. Rev. Lett.* **85**, 1504 (2000).
- ⁴³M. T. Björk, A. Fuhrer, A. E. Hansen, M. W. Larsson, L. E. Fröberg, and L. Samuelson, *Phys. Rev. B* **72**, 201307 (2005).
- ⁴⁴T. A. Costi, *Phys. Rev. B* **64**, 241310 (2001).
- ⁴⁵N. Andrei, *Phys. Lett. A* **87**, 299 (1982).
- ⁴⁶R. M. Konik, H. Saleur, and A. W. Ludwig, *Phys. Rev. Lett.* **87**, 236801 (2001).

- ⁴⁷R. M. Konik, H. Saleur, and A. Ludwig, *Phys. Rev. B* **66**, 125304 (2002).
- ⁴⁸C. Fasth, A. Fuhrer, L. Samuelson, V. N. Golovach, and D. Loss, *Phys. Rev. Lett.* **98**, 266801 (2007).
- ⁴⁹S. Amasha, I. J. Gelfand, M. A. Kastner, and A. Kogan, *Phys. Rev. B* **72**, 045308 (2005).
- ⁵⁰K. Nagaoka, T. Jamneala, M. Grobis, and M. F. Crommie, *Phys. Rev. Lett.* **88**, 077205 (2002).
- ⁵¹Y. Yamauchi, K. Sekiguchi, K. Chida, T. Arakawa, S. Nakamura, K. Kobayashi, T. Ono, T. Fujii, and R. Sakano, *Phys. Rev. Lett.* **106**, 176601 (2011).
- ⁵²A. Oguri, *J. Phys. Soc. Jpn.* **74**, 110 (2005).
- ⁵³J. Rincón, A. A. Aligia, and K. Hallberg, *Phys. Rev. B* **79**, 121301 (2009).
- ⁵⁴J. Rincón, A. A. Aligia, and K. Hallberg, *Phys. Rev. B* **80**, 079902(E) (2009).
- ⁵⁵J. Rincón, A. A. Aligia, and K. Hallberg, *Phys. Rev. B* **81**, 039901(E) (2010).
- ⁵⁶P. Roura-Bas, *Phys. Rev. B* **81**, 155327 (2010).
- ⁵⁷E. Sela and J. Malecki, *Phys. Rev. B* **80**, 233103 (2009).
- ⁵⁸E. Muñoz, C. J. Bolech, and S. Kirchner, e-print [arXiv:1111.4076](https://arxiv.org/abs/1111.4076) (unpublished).
- ⁵⁹A. A. Aligia, *J. Phys.: Condens. Matter* **24**, 015306 (2012).
- ⁶⁰A. Schiller and S. Hershfield, *Phys. Rev. B* **58**, 14978 (1998).
- ⁶¹K. Majumdar, A. Schiller, and S. Hershfield, *Phys. Rev. B* **57**, 2991 (1998).
- ⁶²B. Doyon and N. Andrei, *Phys. Rev. B* **73**, 245326 (2006).
- ⁶³C. Mora, P. Vitushinsky, X. Leyronas, A. A. Clerk, and K. Le Hur, *Phys. Rev. B* **80**, 155322 (2009).
- ⁶⁴L. Glazman and M. Pustilnik, in *New Directions in Mesoscopic Physics (Towards Nanoscience)*, edited by R. Fazio, V. Gantmakher, and Y. Imry (Kluwer, Dordrecht, 2003).
- ⁶⁵L. Glazman and M. Pustilnik, in *Nanophysics: Coherence and Transport*, edited by H. Bouchiat *et al.* (Elsevier, Amsterdam, 2005), pp. 427–478.
- ⁶⁶T. Micklitz, A. Altland, T. A. Costi, and A. Rosch, *Phys. Rev. Lett.* **96**, 226601 (2006).
- ⁶⁷K. Yamada, *Prog. Theor. Phys.* **53**, 970 (1975).
- ⁶⁸K. Yosida and K. Yamada, *Prog. Theor. Phys.* **53**, 1286 (1975).
- ⁶⁹K. Yamada, *Prog. Theor. Phys.* **54**, 316 (1975).
- ⁷⁰A. C. Hewson, J. Bauer, and A. Oguri, *J. Phys. Condens. Matter* **17**, 5413 (2005).
- ⁷¹C. J. Wright, M. R. Galpin, and D. E. Logan, *Phys. Rev. B* **84**, 115308 (2011).
- ⁷²A. A. Houck, J. Labaziewicz, E. K. Chan, J. A. Folk, and I. L. Chuang, *Nano Lett.* **5**, 1685 (2005).
- ⁷³R. Žitko, R. Peters, and T. Pruschke, *New J. Phys.* **11**, 053003 (2009).
- ⁷⁴W. Hofstetter, *Phys. Rev. Lett.* **85**, 1508 (2000).
- ⁷⁵A. Weichselbaum and J. von Delft, *Phys. Rev. Lett.* **99**, 076402 (2007).
- ⁷⁶J. E. Moore and X.-G. Wen, *Phys. Rev. Lett.* **85**, 1722 (2000).
- ⁷⁷D. E. Logan and N. L. Dickens, *J. Phys. Condens. Matter* **13**, 9713 (2001).
- ⁷⁸T. Costi, in *Concepts in Electron Correlation*, NATO Science Series II: Mathematics Physics and Chemistry, edited by A. C. Hewson and V. Zlatić (NATO, 2003), Vol. 110, pp. 247–256.
- ⁷⁹M. Garst, P. Wölfle, L. Borda, J. von Delft, and L. Glazman, *Phys. Rev. B* **72**, 205125 (2005).
- ⁸⁰A. Weichselbaum, F. Verstraete, U. Schollwöck, J. I. Cirac, and J. von Delft, *Phys. Rev. B* **80**, 165117 (2009).
- ⁸¹A. Rosch, T. A. Costi, J. Paaske, and P. Wölfle, *Phys. Rev. B* **68**, 014430 (2003).
- ⁸²H. Zhang, X. C. Xie, and Q.-f. Sun, *Phys. Rev. B* **82**, 075111 (2010).
- ⁸³R. Žitko, *Phys. Rev. B* **84**, 085142 (2011).
- ⁸⁴S. Schmitt and F. B. Anders, *Phys. Rev. B* **83**, 197101 (2011).
- ⁸⁵S. Schmitt and F. B. Anders, *Phys. Rev. Lett.* **107**, 056801 (2011).
- ⁸⁶Q.-f. Sun, J. Wang, and H. Guo, *Phys. Rev. B* **71**, 165310 (2005).
- ⁸⁷E. Vernek, N. Sandler, and S. E. Ulloa, *Phys. Rev. B* **80**, 041302 (2009).
- ⁸⁸J. Paaske, A. Andersen, and K. Flensberg, *Phys. Rev. B* **82**, 081309 (2010).
- ⁸⁹M. Pletyukhov and D. Schuricht, *Phys. Rev. B* **84**, 041309 (2011).

6.2. Transport at gold and silver with iron impurities

The Kondo effect, while not known at that time, was first observed in noble metals like gold and silver [12, 94], contaminated with iron impurities. In the following section, we will compare experimental measurements of the resistivity for both finite magnetic field and finite temperature to numerical calculations for different models which represent possible candidates for the correct microscopic description of the experimental systems. We thus extend a previous study [95] by showing improved numerical data, explaining the details of the numerical calculations, and showing also numerical data for the magnetoresistivity, which was not possible before. Part of the calculations, especially those with three channels and finite magnetic field are numerically very expensive and are feasible only by making heavy use of the symmetries of the system, both abelian and non-abelian. In contrast to calculations of previous studies [96, 97] for the single-channel Kondo model, which could only fit different quantities by using different Kondo temperatures, for one of the models under consideration, we find excellent agreement between theory and experiment for all quantities, using a single Kondo scale.

Iron impurities in gold and silver: Comparison of transport measurements to numerical renormalization group calculations exploiting non-Abelian symmetries

M. Hanl,¹ A. Weichselbaum,¹ T. A. Costi,² F. Mallet,³ L. Saminadayar,^{3,4} C. Bäuerle,³ and J. von Delft¹

¹*Physics Department, Arnold Sommerfeld Center for Theoretical Physics and Center for NanoScience, Ludwig-Maximilians-Universität München, 80333 München, Germany*

²*Peter Grünberg Institut and Institute for Advanced Simulation, Research Centre Jülich, 52425 Jülich, Germany*

³*Institut Néel-CNRS and Université Joseph Fourier, 38042 Grenoble, France*

⁴*Institut Universitaire de France, 103 boulevard Saint-Michel, 75005 Paris, France*

(Received 18 May 2013; revised manuscript received 1 August 2013; published 30 August 2013)

We consider iron impurities in the noble metals gold and silver and compare experimental data for the resistivity and decoherence rate to numerical renormalization group results. By exploiting non-Abelian symmetries, we show improved numerical data for both quantities as compared to previous calculations [Costi *et al.*, *Phys. Rev. Lett.* **102**, 056802 (2009).], using the discarded weight as criterion to reliably judge the quality of convergence of the numerical data. In addition, we also carry out finite-temperature calculations for the magnetoresistivity of fully screened Kondo models with $S = \frac{1}{2}$, 1, and $\frac{3}{2}$, and compare the results with available measurements for iron in silver, finding excellent agreement between theory and experiment for the spin- $\frac{3}{2}$ three-channel Kondo model. This lends additional support to the conclusion of Costi *et al.* that the latter model provides a good effective description of the Kondo physics of iron impurities in gold and silver.

DOI: 10.1103/PhysRevB.88.075146

PACS number(s): 73.23.-b, 72.70.+m, 75.20.Hr

I. INTRODUCTION

The magnetic alloys for which the Kondo effect was first observed, in the 1930s, were iron impurities in gold and silver.^{1,2} They showed an anomalous rise in the resistivity with decreasing temperature, which Kondo explained in 1964 as being due to an antiferromagnetic exchange coupling between the localized magnetic impurity spins and the spins of the delocalized conduction electrons.³ For his work, Kondo used a spin- $\frac{1}{2}$, one-band model, which undoubtedly captures the essential physics correctly in a qualitative way.

However, detailed comparisons between theory and experiment have since shown that this model does not yield a *quantitatively* correct description of the Kondo physics of dilute Fe impurities in Au or Ag. Such a description must meet the challenge of quantitatively reproducing, using the Kondo temperature T_K as only fitting parameter, several independent sets of experimental measurements: the contributions by magnetic impurities (indicated by a subscript m) to the temperature and field dependencies of the resistivity, $\rho_m(T, B)$, and to the temperature dependence of the decoherence rate, $\gamma_m(T)$, extracted from weak (anti)localization measurements. The spin- $\frac{1}{2}$, 1-band Kondo model does not meet this challenge: when comparing its predictions, obtained by the numerical renormalization group (NRG),⁴⁻⁶ to transport measurements on dilute Fe impurities in Ag wires, different Kondo scales were required for fitting the resistivity and decoherence rates.^{7,8}

In a recent publication (Ref. 9, involving most of the present authors, henceforth referred to as paper I), it was argued that the proper effective low-energy Kondo model for Fe in Au or Ag is, in fact, a fully screened, spin- $\frac{3}{2}$ three-channel Kondo model. Paper I arrived at this conclusion by the following chain of arguments. Previous transport experiments^{7,8} had indicated that these systems are described by a fully screened Kondo model,¹⁰⁻¹⁴ i.e., a Kondo model in which the local spin S is related to the number of conduction bands n by $S = n/2$. As mentioned above, the choice $n = 1$ had already been ruled

out in earlier work.^{7,8} Density-functional theory calculations for Fe in Au and Ag, presented in paper I, showed that in these host metals Fe preferentially acts as a substitutional defect with cubic symmetry, leading to a substantial crystal field splitting (≥ 0.15 eV) between a higher-lying e_g doublet and a lower-lying t_{2g} triplet. Moreover, the local spin moment was predicted to be 3 Bohr magnetons, with an almost fully quenched orbital angular momentum. This suggested a fully screened Kondo model with $n = 3$ as the most likely candidate, while leaving some scope for the possibility of $n = 2$ (but none for $n = 4$ or 5). To discriminate between the options $n = 2$ and 3, $\rho_m(T, 0)$ and $\gamma_m(T)$ were then calculated using NRG, for $n = 1$ (as reference), 2 and 3. Next, for both material systems (Fe in Au and Ag), the $\rho_m(T, 0)$ curves were fitted to experimental data to obtain a Kondo temperature, $T_K^{(n)}$, for each of the three models. Finally, using these $T_K^{(n)}$ values, the $\gamma_m(T)$ curves, which constituted parameter-free predictions of the decoherence rate, were compared to corresponding measurements, with the conclusion that the choice $n = 3$ worked distinctly better than $n = 2$.

The goal of the present paper is twofold. First, we describe technical details of the numerical calculations performed in paper I that could not be presented there for lack of space. Second and more important, we extend the analysis of paper I to the case of finite magnetic fields. Indeed, though experimental data for $\rho_m(T, B \neq 0)$ had been available for Fe in Ag even at the time of writing of paper I, it had not been possible then to compare them to theoretical predictions for $n = 3$. The reason is that multichannel calculations present an enormous challenge for the NRG, as the numerical complexity grows exponentially with the number of channels. In paper I, only Abelian symmetries (charge conservation in each channel and total spin S_z) were exploited. For the purposes of paper I, this turned out to be sufficient, but for the aforementioned three-channel Kondo model, the calculations were numerically extremely costly, and even at $B = 0$ just barely within the

limits of feasibility. When the present authors attempted, in subsequent work (unpublished), to treat the more general case of a finite magnetic field using the same approach, the latter turned out to be inadequate, plagued by numerical convergence issues. Therefore further progress required enhancing the numerical efficiency by exploiting non-Abelian symmetries.

Now, the effective fully screened symmetric three-channel Kondo model mentioned above has several *non*-Abelian symmetries, including, in particular, an SU(3) channel symmetry. This implies that the eigenspectrum of the Hamiltonian can be organized into degenerate symmetry multiplets, and great gains in numerical efficiency can be made by exploiting this multiplet structure at every step of the NRG procedure. We took this observation as incentive to implement non-Abelian symmetries in our code on a completely generic footing for tensor networks such as the NRG.¹⁵ Although the exploitation of symmetries, Abelian as well as non-Abelian, together with their respective strong gain in numerical efficiency is well known in the literature, the treatment of non-Abelian symmetries in NRG has been largely restricted to the symmetry of SU(2).^{4,5,16,17} The non-Abelian symmetry SU(2), however, is simpler than the general case, since for $n \geq 3$ the SU(n) representation theory involves complications due to the presence of inner and outer multiplicities. A generic numerical framework for treating arbitrary non-Abelian symmetries thus had been missing, and became available only very recently.^{15,18,19}

More specifically, the model Hamiltonians studied here possess SU(2) particle-hole symmetry, SU(n) channel symmetry, and SU(2) spin symmetry for $B = 0$ or Abelian S_z symmetry for $B \neq 0$. By exploiting the non-Abelian symmetries, we were able to drastically reduce the computational effort and generate fully converged numerical data, even for the highly challenging case of three channels. With a significantly more powerful NRG at our hands then, the following analysis serves two purposes. First, we present a thorough reanalysis of paper I with improved NRG data. In particular, we give a detailed discussion of NRG truncation and convergence issues, which are under much better control with the new non-Abelian scheme. The new numerical results show discernible quantitative differences w.r.t. paper I, leading to changes in the deduced Kondo temperatures that are quite substantial for $n = 3$ (the relative change in T_K is 31% for Fe in Au and 53% for Fe in Ag). Second, we present a detailed analysis of the new numerical magnetoresistivity data and compare these to experimental results for Fe in Ag. The results of both analyses fully confirm the main conclusion of paper I: the effective microscopic model for dilute iron impurities in the noble metals gold and silver is given by a fully screened three-channel Kondo model.

The remainder of this paper is organized as follows: Sec. II describes the model, Sec. III describes NRG-related details, and Sec. IV provides a comparison of experimental and numerical magnetoresistance data, followed by a summary in Sec. V.

II. MODEL

In paper I, we found it numerically convenient for our NRG calculations to start not from a pure Kondo model but from an effective Anderson-type model, because it is then possible

to obtain an improved spectral function by using the so-called “self-energy trick,”²⁰ which involves calculating the impurity-level self-energy. It has recently been shown²¹ that a similar strategy can be used for Kondo-type models, but this fact was brought to our attention only after completion of the present study.²² We here adhere to the strategy of paper I and adopt the following Anderson-type model,

$$\hat{H} = \sum_{\alpha=1}^n \sum_{k\sigma} [t(\hat{d}_{\alpha\sigma}^\dagger \hat{c}_{k\alpha\sigma} + \text{H.c.}) + \varepsilon_k \hat{c}_{k\alpha\sigma}^\dagger \hat{c}_{k\alpha\sigma}] - J_H^{(n)} \hat{S}_{\text{imp}}^2 + g\mu_B B \hat{S}_{\text{imp}}^z, \quad (1)$$

which reduces to a Kondo-type model at low energies.^{23,24} The index α labels n degenerate local levels as well as n independent channels of conduction electrons, each forming a flat band of half-bandwidth $D = 1$ with constant density of states $\nu_0 = 1/2D$ per spin and channel. (In the remainder of the paper, all energies are specified in units of half-bandwidth, unless indicated otherwise.) $\hat{d}_{\alpha\sigma}$ is the annihilation operator of an impurity electron with spin σ in level α , whereas $\hat{c}_{k\alpha\sigma}$ annihilates a reservoir electron in channel α with wave number k and energy ε_k . Levels and channels are tunnel-coupled diagonally in spin and channel indices, resulting in a width $\Gamma = \pi\nu_0 t^2$ for each level, t being the hopping matrix element between impurity and reservoir. The third term in \hat{H} describes a Hund-type exchange interaction with $J_H^{(n)} > 0$, added to favor a local spin of $S = n/2$, where $\hat{S}_{\text{imp}} = \sum_{\alpha=1}^n \hat{S}_\alpha$ is the total impurity spin operator, $\hat{S}_\alpha = \frac{1}{2} \sum_{\sigma\sigma'} \hat{d}_{\alpha\sigma}^\dagger \vec{\tau}_{\sigma\sigma'} \hat{d}_{\alpha\sigma}$ is the spin operator for an electron in level α , and $\vec{\tau} = (\tau_x, \tau_y, \tau_z)$ are Pauli spin matrices. The last term in \hat{H} describes the effect of an applied local magnetic field, with $g = 2$. To ensure particle-hole symmetry (which renders the numerics more efficient), we take $\varepsilon_{\alpha\sigma} = 0$ for the local level positions and do not include any further charging energy.

The energies of the free orbital (FO) states are given by roughly $J_H^{(n)} S(S+1)$ and the energy difference between two FO states that differ by spin $\frac{1}{2}$ is therefore given by $\Delta E^{(n)} \approx J_H^{(n)} [S(S+1) - (S - \frac{1}{2})(S + \frac{1}{2})] = J_H^{(n)} (S + \frac{1}{4})$. To focus on the local moment regime of the Anderson model, we choose $J_H^{(n)}$ such that $\Delta E^{(n)}$ is significantly larger than Γ and $g\mu_B B$, ensuring a well-defined local spin of $S = n/2$, and an average total occupancy of the local level of $\sum_{\alpha\sigma} \langle \hat{d}_{\alpha\sigma}^\dagger \hat{d}_{\alpha\sigma} \rangle = n$. Moreover, the ratios $J_H^{(n)}/\Gamma$ are chosen such that the resulting Kondo temperatures have comparable magnitudes. In paper I, we had implemented this strategy using the same $\Delta E^{(n)}$ for all three n values, with $\Gamma = 0.01$ and $J_H^{(1)} = 0.053$, $J_H^{(2)} = 0.032$, $J_H^{(3)} = 0.023$. We have since realized that much better NRG convergence properties can be obtained by choosing much larger values of $J_H^{(n)}$, to ensure that the energy differences of the FO states truly lie well above the bandwidth ($\Delta E^{(n)} \gtrsim 100$). This is the numerical counterpart to the Schrieffer-Wolff transformation:^{15,25} it shifts the numerically most expensive, yet irrelevant, FO regime to an energy range that lies outside the range whose energies are finely resolved during the NRG diagonalization, thus reducing the numerical costs needed for treating the Anderson model to a level comparable to that of the Kondo model. For the numerical calculations presented

here, we set the level width to $\Gamma = 25$ and choose $J_H^{(n)}$ such that the resulting spectral functions have the same half-width at half maximum ($= 2 \times 10^{-4}$) for all three cases, $n \in \{1, 2, 3\}$, thus ensuring that the Kondo temperatures are equal. This is achieved by choosing the Hund couplings as $J_H^{(1)} = 358.9$, $J_H^{(2)} = 112.8$, and $J_H^{(3)} = 57.14$.

For the model in Eq. (1), the resistivity and decoherence rate due to magnetic impurities (relevant for weak localization) can be calculated as follows:^{26,27}

$$\rho_m^{\text{NRG}}(T, B) = \frac{\rho_m^0}{2n} \int d\omega f'(\omega) \sum_{\alpha\sigma} \text{Im}(\Gamma G_{\alpha\sigma}^R(\omega)), \quad (2)$$

$$\gamma_m^{\text{NRG}}(T) = \left[\int d\omega (-f'(\omega)) \sqrt{\gamma_m(\omega, T)} \right]^2, \quad (3)$$

$$\gamma_m(\omega, T) = -\frac{\gamma_m^0}{2n} \sum_{\alpha\sigma} [\text{Im}(\Gamma G_{\alpha\sigma}^R(\omega)) + |\Gamma G_{\alpha\sigma}^R(\omega)|^2]. \quad (4)$$

Here, $G_{\alpha\sigma}^R(\omega)$ is the fully interacting retarded impurity Green's function, $f'(\omega)$ is the derivative of the Fermi function, $\rho_m(0) = \rho_m^0 = 2\tau\bar{\rho}/\pi\hbar v_0$ and $\gamma_m^0 = 2/\pi\hbar v_0$, where $\bar{\rho}$ is the resistivity due to static disorder and τ the corresponding elastic scattering time. For *real* materials with complex Fermi surfaces, both prefactors ρ_m^0 and γ_m^0 contain material-dependent (hence unknown) factors arising from integrals involving the true band structure of the conduction electrons.

III. NRG DETAILS

A. Wilson chain and spectral function

Within the NRG, the noninteracting bath in Eq. (1) is coarse grained using the dimensionless discretization parameter $\Lambda > 1$, followed by the mapping onto the so-called Wilson chain in terms of the fermionic Wilson sites⁴⁻⁶ $\hat{f}_{i'\alpha\sigma}$ with $i' \in \{0, 1, \dots\}$. Therefore $\hat{H} \cong \lim_{N \rightarrow \infty} \hat{H}_N$, where

$$\hat{H}_N \cong \hat{H}_{\text{loc}} + \sum_{i'=0}^{N-1} t_{i'} \sum_{\alpha=1}^n \sum_{\sigma} (\hat{f}_{i',\alpha\sigma}^\dagger \hat{f}_{i'+1,\alpha\sigma} + \text{H.c.}) \quad (5a)$$

$$\hat{H}_{\text{loc}} \cong \hat{H}_J + \sum_{\alpha=1}^n \sum_{\sigma} \sqrt{\frac{2\Gamma}{\pi}} (\hat{d}_{\alpha\sigma}^\dagger \hat{f}_{0\alpha\sigma} + \text{H.c.}), \quad (5b)$$

where

$$\hat{H}_J = -J_H^{(n)} \hat{S}_{\text{imp}}^2 + g\mu_B B \hat{S}_{\text{imp}}^z, \quad (5c)$$

The impurity spin is coupled to a semi-infinite tight-binding chain with the exponentially decaying couplings $t_{i'} \propto \Lambda^{-i'/2}$. For large enough $\Lambda \gtrsim 2$, this ensures energy scale separation, and thus justifies the iterative diagonalization of the Hamiltonian in the representation of the Wilson chain.⁴⁻⁶ In particular, the energies of the Hamiltonian \hat{H}_i at intermediate iterations that include all terms $i' < i$, are rescaled in units of ω_i , where

$$\omega_i \equiv a\Lambda^{-i/2}. \quad (6)$$

Here, the constant a is chosen such that $\lim_{i \rightarrow \infty} t_i/\omega_i = 1$. An analytic expression for a in the presence of z shifts is given in Ref. 28.

To obtain the Green's function $G_{\alpha\sigma}^R(\omega)$, which determines $\rho_m^{\text{NRG}}(T, B)$ and $\gamma_m^{\text{NRG}}(T)$, we calculate the spectral function

$A_{\alpha\sigma}(\omega) = -\frac{1}{\pi} \text{Im}(G_{\alpha\sigma}^R(\omega))$ using its Lehmann representation:

$$A_{\alpha\sigma}(\omega) = \sum_{a,b} \frac{e^{-\beta E_a} + e^{-\beta E_b}}{Z} |\langle a | \hat{d}_{\alpha\sigma} | b \rangle|^2 \delta(\omega - E_{ab}), \quad (7)$$

where $E_{ab} = E_b - E_a$, with E_a , E_b and $|a\rangle$, $|b\rangle$ being the eigenenergies and many-body eigenstates obtained by NRG in the full density matrix (FDM) approach.²⁹⁻³² Note that due to the $SU(n)$ symmetry of the Hamiltonian, the spectral function $A_{\alpha\sigma}(\omega)$ does not depend on the index α . Thus when exploiting non-Abelian symmetries, in practice, one calculates the channel-independent symmetrized spectral function $A_\sigma(\omega) \equiv \frac{1}{n} \sum_{\alpha=1}^n A_{\alpha\sigma}(\omega)$, which corresponds to the normalized scalar contraction $\hat{d}_\sigma^\dagger \cdot \hat{d}_\sigma \equiv \sum_{\alpha} \hat{d}_{\alpha\sigma}^\dagger \cdot \hat{d}_{\alpha\sigma}$ of the spinors \hat{d}_σ .¹⁵

For the calculation of $\gamma_m(T)$, the knowledge of both the real and the imaginary part of $G_{\alpha\sigma}^R(\omega) \equiv G_\sigma^R(\omega)$ is necessary. The real part can be determined via the Kramers-Kronig relations from $A_\sigma(\omega)$ after smoothing the discrete data. $\rho_m^{\text{NRG}}(T, B)$, on the other hand, requires only the imaginary part of the Green's function. This makes the application of the Kramers-Kronig relations and with it the broadening of the discrete data unnecessary and $\rho_m^{\text{NRG}}(T, B)$ can therefore be directly calculated from the discrete data,²⁹ thus avoiding possible broadening errors. Furthermore, due to particle-hole symmetry, it is sufficient to calculate $A_\sigma(\omega)$ only for one spin σ , since the spectral functions for opposite spins σ and $\bar{\sigma}$ are symmetric with respect to each other: $A_\sigma(\omega) = A_{\bar{\sigma}}(-\omega)$.

B. Convergence criteria and discarded weight

As mentioned in the introduction, when using Abelian symmetries the calculations described above are standard for $n = 1$ and $n = 2$, but a real challenge for $n = 3$. The reason is that the number of degenerate eigenstates in a typical symmetry multiplet increases strongly with the rank of the symmetry group. For example, for the present model with $n = 3$, the typical degeneracy quickly becomes of order 10^2 to 10^3 even for low-lying energy multiplets (this is illustrated by the presence of long "plateaux" in the excitation spectra shown in Fig. 1). This implies that the number of kept states needs to increase dramatically, too. Moreover a crucial prerequisite for well-converged results is that the multiplet structure should be respected during NRG truncation. No multiplet should be kept only partially, i.e., cut in two; instead, each multiplet should be kept or discarded as a whole. In the present paper, cutting multiplets is avoided by implementing non-Abelian symmetries explicitly and keeping all multiplets below a specified truncation energy, as described further below. In paper I, which implemented only Abelian symmetries, we had used the more conventional NRG truncation scheme of specifying the total maximum number of states to typically be kept. However, we had adjusted this number as needed to ensure that the lowest-lying discarded states were not degenerate with the highest-lying kept states. Moreover, the energy of the highest kept multiplet turned out to lie just below a wide gap in the energy spectrum [see Fig. 1(a)]. In our subsequent work, we have found that the presence of this wide gap considerably stabilizes the results; when we keep some more multiplets such that the highest ones lie just

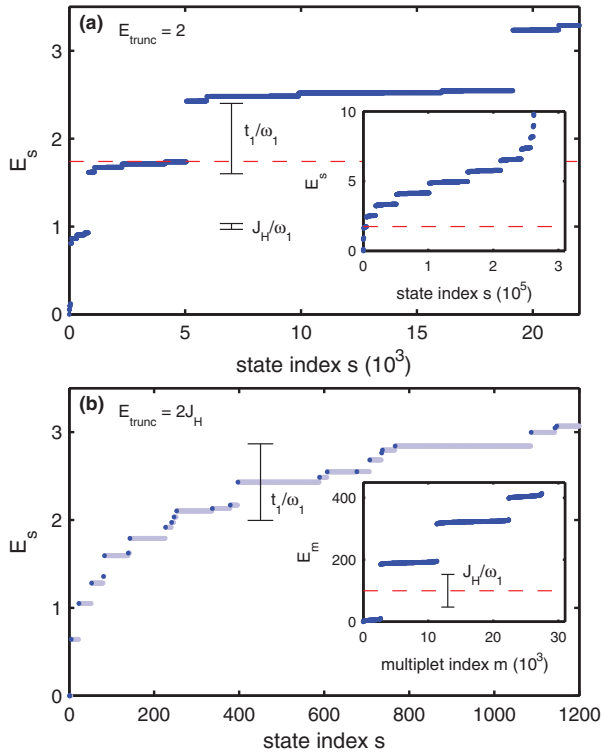


FIG. 1. (Color online) Eigenenergies of the $n = 3$ calculations from (a) paper I and (b) this work, for the lowest eigenstates (blue circles) and truncation energy (dashed red line) of NRG iteration $i = 1$. This iteration includes the impurity and the first two Wilson sites \hat{f}_0 and \hat{f}_1 , which by Eq. (5a) corresponds to \hat{H}_1 ; it is the first iteration where truncation occurred. All energies E_s are given in units of ω_1 [cf. Eq. (6)]. In (a), each dark blue dot marks an eigenstate; in (b), each dark blue dot marks a multiplet, whose degeneracy is indicated by the length of the adjacent light blue lines. Dashed red lines indicate the truncation energy E_{trunc} . In paper I, the number of kept states at iteration $i = 1$ was 4840 which was 216 states short of truncating into the wider energy gap starting at $E_s = 5056$. For the present paper, we chose the truncation energy to lie well within a wide spectral gap and kept 16 384 out of 262 144 states [only a small subset of which are shown in the main panel of (b)]. This large number was achievable by grouping the kept states into 2688 symmetry multiplets with internal degeneracy. The insets of (a) and (b) show, respectively, the full spectrum of states or multiplets at iteration $i = 1$. (The fine structure seen in the main panel in (b) is not resolved in the inset, since the latter uses a much coarser energy resolution on the vertical axis.) The spectra in (a) and (b) have different fine structure, because the model parameters were chosen differently in paper I and the present work, respectively: the former used $J_H^{(3)} = 0.0229$, $\Gamma = 0.01$, the latter $J_H^{(3)} = 57.14$, $\Gamma = 25$. As a result, the energy separation between degenerate multiplets at the truncation energy is different, namely $\mathcal{O}(t_1/\omega_1)$ in (a) versus $\mathcal{O}(J_H^{(n)}/\omega_1)$ in (b), where t_1 is the hopping matrix element between the first two sites of the Wilson chain [cf. Eq. (5a)]. The different values of J_H and t_1 used in (a) and (b) are indicated by black lines in the plots.

above the wide gap, the results deteriorate considerably, as judged by the criterion discussed next. The criterion used in paper I to judge the quality of convergence was based on

the Friedel sum rule,³³ which for the present model implies that the Kondo peak of the zero-temperature spectral function should satisfy $\pi\Gamma \cdot A_{\alpha\sigma}(\omega = 0) = 1$. For paper I, this check was satisfied to within 2% for spectral functions calculated using the self-energy trick, which we had taken as indication that the data could be trusted. When calculated *without* the self-energy trick, though, the Kondo peak height was off by 1%, 16%, and 32% for $n = 1, 2$, and 3, respectively, which, in retrospect, indicates lack of full convergence for the latter two cases. Indeed, this became apparent *a posteriori* in the course of the present study when we reanalyzed the NRG data of paper I using a more reliable tool for checking NRG convergence that had been developed in 2011,²⁸ based on monitoring the discarded weight. In essence, the discarded weight measures the relevance of the highest-lying kept states for obtaining an accurate description of the ground state space a few iterations later. More concretely, it is calculated as follows: construct a reduced density matrix for a chain of length i from the mixed density matrix of the ground state space of a chain of length $i + i_0$ by tracing out the last i_0 sites (typically $i_0 \gtrsim 4$ to ensure that all eigenvalues of the reduced density matrix are nonzero); find the eigenvalues and eigenstates of this reduced density matrix, say $\rho_r^{[i:i_0]}$ and $|r_{i:i_0}\rangle$, and sort them according to their energy expectation values, $E_r^{[i:i_0]} = \langle r_{i:i_0} | \hat{H}_i | r_{i:i_0} \rangle$. The weight $\varepsilon_{5\%,i}^D \cong \sum_r^{\text{top } 5\%} \rho_r^{[i:i_0]}$ contributed by the highest-lying 5% of states in this energy-sorted list then provides an estimate for the discarded weight at iteration i . It provides a quantitative measure for the importance of the discarded states had they been included in the description of the ground state space of iteration $i + i_0$ by keeping a larger number of states. Repeating this analysis for different sites i , the largest $\varepsilon_{5\%,i}^D$ value is taken to define the “discarded weight” of the entire Wilson chain, $\varepsilon_{5\%}^D = \max_i(\varepsilon_{5\%,i}^D)$. The entire analysis concerns the kept space only, hence it is fast relative to the actual NRG calculation itself. Well-converged physical quantities are obtained when the discarded weight satisfies $\varepsilon_{5\%}^D \lesssim 10^{-10}$. For the NRG data used in paper I, the discarded weight calculated *a posteriori* turned out to be 2.8×10^{-13} , 2.9×10^{-9} , and 8.3×10^{-7} for $n = 1, 2$, and 3, respectively. This indicates lack of proper convergence for $n = 2$, and especially for $n = 3$.

C. Truncation scheme for non-Abelian symmetries

For the calculations presented here, we therefore use an improved code, which also exploits non-Abelian symmetries.¹⁵ Here, the idea is to make use of the fact that degenerate states can be gathered into symmetry multiplets. By the Wigner-Eckart theorem, matrix elements including states from the same multiplet are then related via Clebsch Gordan coefficients. Thus it is sufficient to keep track not of all individual states inside each multiplet, but only of entire multiplets, and to store only one reduced matrix element for each multiplet. This drastically reduces the size of the matrix that has to be diagonalized at an NRG iteration, with corresponding reductions in calculation times and memory requirements.

Our model possesses the following non-Abelian symmetries: SU(2) particle-hole, SU(2) spin (in the absence of magnetic field), and SU(n) channel symmetry. For many of our calculations, we need $B \neq 0$, in which case the SU(2) spin symmetry is reduced to an Abelian symmetry using

S_z . Moreover, particle-hole and channel symmetries do not commute in general, yet their combination generates the larger symplectic symmetry $\text{Sp}(2n)$ (see Ref. 15). This symmetry, which encompasses both particle-hole and channel symmetry, fully exhausts the model's symmetry; consequently, no degeneracies remain between different $\text{Sp}(2n)$ multiplets (a typical multiplet contains several hundreds up to several thousands of states). For the calculations presented in this work, using $\text{SU}(n)$ [rather than $\text{Sp}(2n)$] turned out to be sufficient. Here, we use $\text{SU}(n)$ channel symmetry together with total charge for $n \in \{2, 3\}$ and particle-hole symmetry for $n = 1$. The gain in numerical efficiency due to these symmetries is huge. For example, for $n = 3$, the largest $\text{SU}(n)$ multiplets kept in our NRG calculations already reach dimensions of above 100. By exploiting these symmetries, calculation times as well as memory requirements are reduced by more than two orders of magnitude compared to those of paper I. As a consequence, the calculations presented here can be simply performed within a few hours on standard workstations.

We used an NRG discretization parameter of $\Lambda = 4$, and perform z averaging³⁴ with $N_z = 2$ (and $z \in \{0, 0.5\}$) to minimize discretization artifacts.³⁵ For $n = 3$, the computationally most challenging case, we used the following truncation scheme. For the diagonalization of $H_0 \equiv \hat{H}_{\text{loc}}$, all states were kept. For iteration $i = 1$, we used a truncation energy [given in rescaled units of $\omega_{i=1}$, cf. Eq. (6)] of $E_{\text{trunc}} = 2J_H/D > 7$. Figure 1(b) shows a subset of the corresponding kept eigenenergies and multiplet degeneracies, while Fig. 1(a) shows corresponding information for the calculations from paper I. The inset of Fig. 1(b) shows that *all* Kondo-like states of the Anderson model have been retained. For iterations $i \geq 2$, we used $E_{\text{trunc}} = 7$, except for $z = 0.5$ at iteration $i = 2$, where we used $E_{\text{trunc}} = 6$ to reduce computational costs due to the extraordinary large density of states at that iteration; this choice of parameters corresponds to keeping $\lesssim 10\,000$ multiplets ($\lesssim 77\,000$ states). Using this scheme, a single NRG run for $n = 3$ required about 40 GB of RAM and took on the order of 10 hours of calculation time on an 8-core processor. The subsequent calculation of the spectral function required a similar amount of time and 55 GB memory. The large number of kept multiplets then resulted in high numerical accuracy. In particular, the spectral functions calculated with and without using the improved self-energy, already agreed very well with each other, which clearly demonstrates fully converged numerical data. Having established this for a few representative cases, we proceeded to calculate the data presented below without using the self-energy trick.

D. Resistivity obtained by non-Abelian NRG

To compare the results obtained with our new approach with those of paper I, Fig. 2(a) shows the temperature dependence of the zero-field resistivity for $n = 1, 2$, and 3, computed using both Abelian NRG with self-energy trick as in paper I (dashed lines) and using our new non-Abelian NRG approach (solid lines), which produced truly well-converged results. We define the Kondo temperature $T_K^{(n)}$ associated with a given numerical resistivity curve $\rho_m^{\text{NRG}}(T, 0)$ by the condition

$$\rho_m^{\text{NRG}}(T_K^{(n)}, 0) = \frac{1}{2} \rho_m^{\text{NRG}}(0, 0). \quad (8)$$

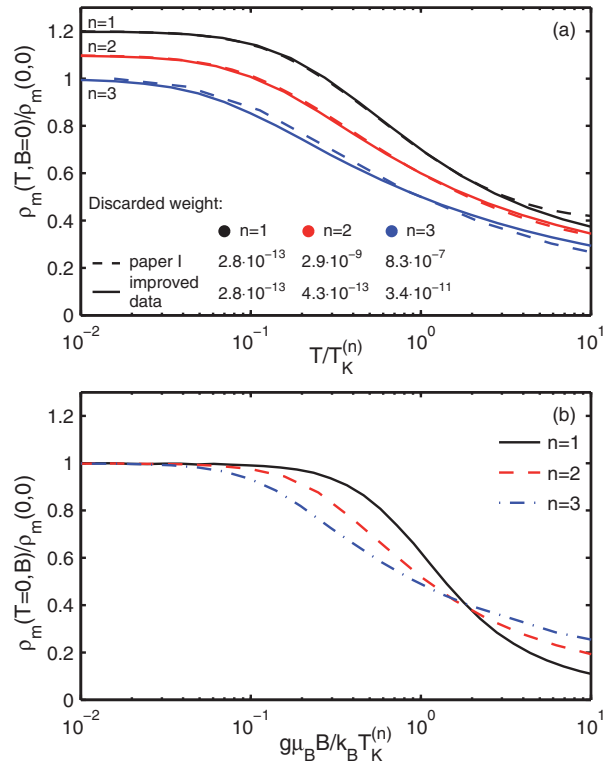


FIG. 2. (Color online) (a) Temperature dependence of the zero-field resistivity for $n = 1, 2$, and 3, computed using both Abelian NRG with self-energy trick as in paper I (dashed lines) and our new non-Abelian NRG approach (solid lines). For clarity, successive curves have been vertically shifted by 0.1. (b) The magnetic-field dependence of the zero-temperature resistivity for $n = 1, 2$, and 3, calculated using non-Abelian NRG.

Then $\rho_m^{\text{NRG}}(T, 0)/\rho_m^{\text{NRG}}(0, 0)$ versus T/T_K should be a universal curve for given n . For $n = 1$ and 2, the solid and dashed lines in Fig. 2(a) agree well (except at large temperatures for $n = 1$, where the dashed curve is affected by free-orbital states, implying that in paper I, $T_K^{(1)}$ had not been chosen sufficiently small with respect to the FO excitation energy). For $n = 3$, however, the shapes of the dashed and solid curves actually differ quite noticeably. The reason for the difference is the lack of full convergence of the Abelian NRG data. This becomes clearly evident by comparing the discarded weights, listed in the legend of Fig. 2(a), of the non-Abelian and Abelian calculations: for $n = 3$, the respective discarded weights of 3.4×10^{-11} and 8.3×10^{-7} indicate that the former calculations, but not the latter, are well converged. This comparison thus highlights both the benefits of exploiting non-Abelian symmetries in order to reduce convergence problems, and the importance of checking the latter in a reliable fashion by monitoring the discarded weight.

The fact that the resistivity curve for $n = 3$ shows a more gradual decrease with increasing temperature for the new non-Abelian results than for the old Abelian ones, implies that fits to experiment will yield a larger Kondo temperature for the former, as we indeed find below.

M. HANL *et al.*PHYSICAL REVIEW B **88**, 075146 (2013)

TABLE I. Values of parameters determined from fitting the experimental measurement. The values for $T_K^{(n)}$ and $\delta^{(n)}$ are extracted using the fitting procedure whose results are shown in Fig. 3. $\Delta\rho^{\text{exp}}(0,0)$ is the measured value for the resistivity at zero magnetic field and the lowest temperature available. For the sake of completeness, we also show $\rho_m^{\text{uni.}(n)}(0,0) = \Delta\rho^{\text{exp}}(0,0) - \delta^{(n)}$, which, according to Eq. (10), corresponds to the unitary Kondo resistivity.

	n	AuFe3	AgFe2	AgFe3
$T_K^{(n)}$ (K)	1	0.6 ± 0.1	2.5 ± 0.2	2.8 ± 0.2
	2	1.0 ± 0.1	4.3 ± 0.3	4.7 ± 0.3
	3	1.7 ± 0.1	7.4 ± 0.5	8.2 ± 0.5
$\delta^{(n)}$ (n Ω cm/ppm)	1	-0.002	0.003	0.001
	2	-0.045	-0.005	-0.007
	3	-0.090	-0.013	-0.016
$\Delta\rho^{\text{exp}}(0,0)$ (n Ω cm/ppm)		0.211	0.041	0.041
$\rho_m^{\text{uni.}(n)}(0,0)$ (n Ω cm/ppm)	1	0.213	0.038	0.040
	2	0.256	0.046	0.048
	3	0.301	0.054	0.057

Figure 2(b) shows the zero-temperature magnetoresistivity curves for $n = 1, 2$, and 3, calculated by non-Abelian NRG. The curves are scaled by the same $T_K^{(n)}$ as derived from the temperature-dependent data where the latter, by construction, cross at $T = T_K^{(n)}$ [cf. Eq. (8)]. Interestingly, the magnetic-field dependent curves here also approximately cross a common point at a magnetic field of about $g\mu_B B \sim 1.8 k_B T_K^{(n)}$ having $\rho_m(T = 0, B)/\rho_m(0,0) \simeq 0.4$. The general trend of the curves in Fig. 2(b) is similar to that seen in Fig. 2(a): the larger n the more gradual the decrease in resistivity with increasing temperature or field. This indicates that the larger the local spin $S = n/2$, the larger the energy range (in units of $T_K^{(n)}$) within which its spin-flip-scattering effects are felt strongly by conduction electrons. In absolute energy units, this tendency is even stronger, since the fits to experiment performed below yield $T_K^{(1)} < T_K^{(2)} < T_K^{(3)}$ (cf. Table I). Interestingly, the n -dependent differences in curve shapes are more pronounced for the field dependence than for the temperature dependence;³⁶ in Fig. 2(b), the decrease of the resistivity for a given n sets in at a higher energy and then is steeper than in Fig. 2(a). Thus the comparison between experiment and theory for the magnetoresistivity performed below constitutes a stringent test of which choice of n is most appropriate, independent of and complementary to the tests performed in paper I.

IV. COMPARISON WITH EXPERIMENT

To identify the microscopic model that describes the system of iron impurities in gold and silver correctly, we compare NRG calculations for the resistivity $\rho_m^{\text{NRG}}(T, B)$ and the decoherence rate $\gamma_m^{\text{NRG}}(T)$ to experimental data, $\rho_m^{\text{exp}}(T, B)$ and γ_m^{exp} . [In the following, when referring to both NRG and experiment, we omit the upper index and write $\rho_m(T, B)$ and $\gamma_m(T)$.] The data to be analyzed stem from a detailed experimental study⁷ performed in 2006 on quasi-one-dimensional wires. One AuFe sample and two AgFe samples were studied, to be denoted by AuFe3, AgFe2, and AgFe3, with impurity concentrations of 7 ± 0.7 , 27 ± 3 , and

67.5 ± 7 ppm, respectively. These concentrations are so small that multi-impurity effects can be ignored. Low-field measurements of the temperature-dependence of the resistivity, performed at $B = 0.1$ T to suppress weak localization, are available for all three samples. We will denote this data by $\rho_m^{\text{exp}}(T, 0)$ [rather than $\rho_m^{\text{exp}}(T, 0.1\text{T})$], and compare it to numerical results for $\rho_m^{\text{NRG}}(T, 0)$ computed at $B = 0$, since $1 - \rho_m^{\text{NRG}}(T, 0.1\text{T})/\rho_m^{\text{NRG}}(T, 0) < 0.5\%$ for all three cases $n \in \{1, 2, 3\}$. Moreover, experimental data are available for $\gamma_m^{\text{exp}}(T)$ from AgFe2 and AuFe3, and for $\rho_m^{\text{exp}}(T, B)$ from AgFe2.

The comparison between experiment and theory proceeds in three steps. (i) First, we compare measured data and NRG predictions for the resistivity at zero magnetic field $\rho_m(T, B = 0)$ to determine two fit parameters, $T_K^{(n)}$ and $\delta^{(n)}$, for each of the samples and each of the three models $n \in \{1, 2, 3\}$. After the fit parameters have been determined, we use $T_K^{(n)}$ and $\delta^{(n)}$ to make parameter-free predictions for (ii) the decoherence rate $\gamma_m(T)$ and (iii) the temperature-dependent magnetoresistivity $\rho_m(T, B)$, and compare these to experiment for those samples for which corresponding data is available. Here, (i) and (ii) represent a thorough reanalysis of the experimental data of paper I using our new, improved numerical data, while (iii) involves experimental data not published previously, and new numerical data.

A. Determination of fit parameters

The experimental resistivity data to be discussed below (shown in Fig. 3) have several contributions of different physical origin:

$$\Delta\rho^{\text{exp}}(T, B) = \rho_m^{\text{exp}}(T, B) + \rho_{\text{ph}}(T) + \delta. \quad (9)$$

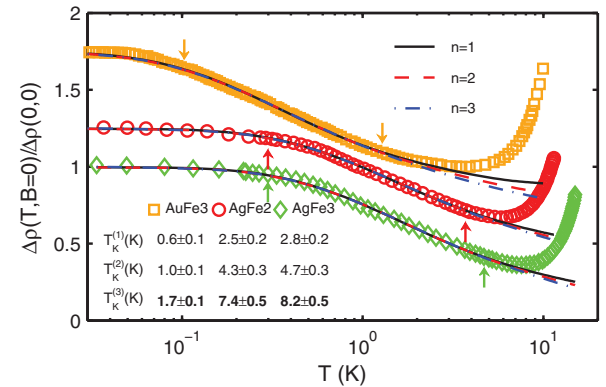


FIG. 3. (Color online) Similar figure as Fig. 3 of paper I, but using substantially improved numerical data. The figure shows low-field experimental data for the temperature dependence of the resistivity, denoted by $\Delta\rho^{\text{exp}}(T, 0)$ but taken in a small field of 0.1 T to suppress weak localization (see text), and NRG calculations for $n \in \{1, 2, 3\}$, performed at $B = 0$. The NRG curves were fitted to the experimental data, using $T_K^{(n)}$ and $\delta^{(n)}$ as fitting parameters [see Eq. (10)] with the fitting range being indicated by arrows. For temperatures below the fitting range, the data are less reliable due to a long equilibration time, whereas for temperatures above the fitting range the phonon contribution to $\Delta\rho^{\text{exp}}(T, B = 0)$ becomes relevant. For clarity, the curves for AgFe2 and AuFe3 have been shifted vertically by 0.25 and 0.75, respectively.

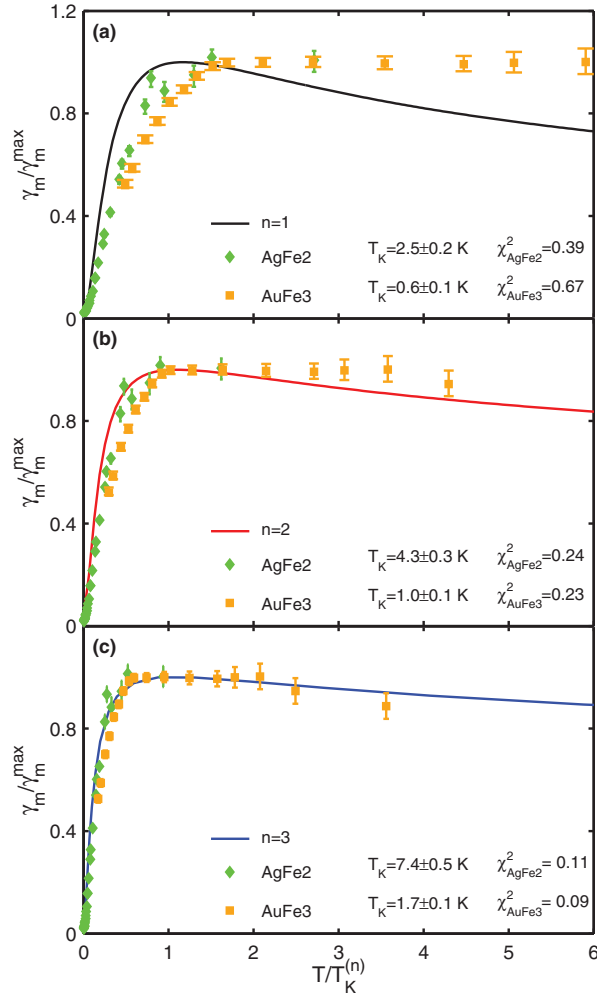


FIG. 4. (Color online) Similar figure as Fig. 4 of paper I, but using clearly improved numerical data. Panels (a), (b), and (c) show the normalized decoherence rate $\gamma_m(T)/\gamma_m^{\max}$ vs. $T/T_K^{(n)}$ for $n \in \{1, 2, 3\}$, respectively. The Kondo temperatures are determined from the fits of $\rho_m^{\text{NRG}}(T, B=0)$ to the experimental data according to Eq. (10). The χ^2 values indicated in the legends were obtained as the sum of the least squares between the experimental data and the linearly interpolated NRG curves.

Here, $\rho_m^{\text{exp}}(T, B)$ is the resistivity due to magnetic impurities, $\rho_{\text{ph}}(T)$ is the resistivity due to phonon scattering, and δ is an unknown offset which does not depend on temperature or magnetic field. There are two further contributions to the resistivity: a classical contribution,⁸ which scales as B^2 , and a contribution due to electron-electron interactions,^{37,38} which scales as $1/\sqrt{T}$. These have already been subtracted from the measured resistivity data shown in Figs. 3 and 5 using procedures described in Refs. 39,40, and hence are not displayed in Eq. (9).

For the fitting process at $B=0$, the normalized NRG data $\rho_m^{\text{NRG}}(T, 0)/\rho_m^{\text{NRG}}(0, 0)$ are approximated by a fitting function $g_n(T/T_K^{(n)})$ constructed from higher-order polynomials, where $g_n(0) = 1$ and $T_K^{(n)}$ is fixed by scaling the temperature axis such

that $g_n(1) = \frac{1}{2}$ [cf. Eq. (8)]. We then fit the experimental data to the form

$$\Delta\rho^{\text{exp}}(T, 0) \approx \delta^{(n)} + (\Delta\rho^{\text{exp}}(0, 0) - \delta^{(n)})g_n(T/T_K^{(n)}), \quad (10)$$

using a χ^2 minimization with $T_K^{(n)}$ and $\delta^{(n)}$ as fit parameters. While a similar analysis was performed in paper I, the numerical data in the present paper are of improved quality, in that we can report fully converged data also for the numerically extremely challenging case of $n=3$. The newly extracted values of $T_K^{(n)}$ for the three samples are given in Table I. For $n \in \{1, 2\}$, they are slightly different from the ones of paper I, yet within the given error bars (14 % and 0 % for AuFe3, 9 % and 5 % for AgFe, respectively) due to the fact that we used different fitting ranges to minimize the error arising from the phonon-contribution for larger T and because we use higher-order polynomials to approximate the NRG data, which may be considered more accurate than the analytical expression used in paper I. The difference in T_K is more substantial for $n=3$ (31 % for AuFe3 and 53 % for AgFe) reflecting larger differences between the previous and our new, improved NRG results for $n=3$. Experimental and fitted NRG data are shown in Fig. 3.

B. Decoherence rate and magnetoresistivity

With the $T_K^{(n)}$ for AgFe2 and AuFe3 determined above we are now in a position to make a parameter-free theoretical prediction of the decoherence rate. As shown in Fig. 4 for AgFe2 and AuFe3, the agreement is clearly best for $n=3$ and becomes worse with decreasing n , both for low and high temperatures. A quantitative measure for the agreement is given by the χ^2 values for $n \in \{1, 2, 3\}$, which are displayed in each of the panels in Fig. 4. This conclusion is in accordance with paper I, where the $n=3$ case also agreed best with the experimental data, although T_K and $\gamma_m(T)$ for $n=3$ were significantly less accurate then.

Next we turn to the magnetoresistivity. The above-mentioned implementation of non-Abelian symmetries in our NRG code,¹⁵ which drastically reduces computation time and memory requirements, allows us to extend the analysis of $\rho_m(T)$ of paper I to the whole two-dimensional parameter space of T and B . Since the fitting procedure of $\rho_m(T, B=0)$ described above leaves no further free parameters, this comparison is an additional strong check of the validity of the $n=3$ model. The experimental data of $\rho_m(T, B)$ for the sample AgFe2 are shown together with the numerical data for $n \in \{1, 2, 3\}$ in Fig. 5. [The values of $\rho_m(T, B=0)$ differ for $n \in \{1, 2, 3\}$ in Fig. 5. [The values of $\rho_m(T, B=0)$ differ from Eq. (10).] Again, the three-channel model reproduces the measured results best. Even though there are still slight deviations between theory and experiment at high magnetic field for the $n=3$ curves at 0.1 and 0.85 K, which might originate from very small temperature drifts, the overall agreement, combined with that for $\gamma_m(T)$ (see Fig. 4) and $\rho_m(T, 0)$ (see Fig. 3), is rather impressive. Thus we conclude that the $n=3$ model consistently reproduces all the transport data discussed above.

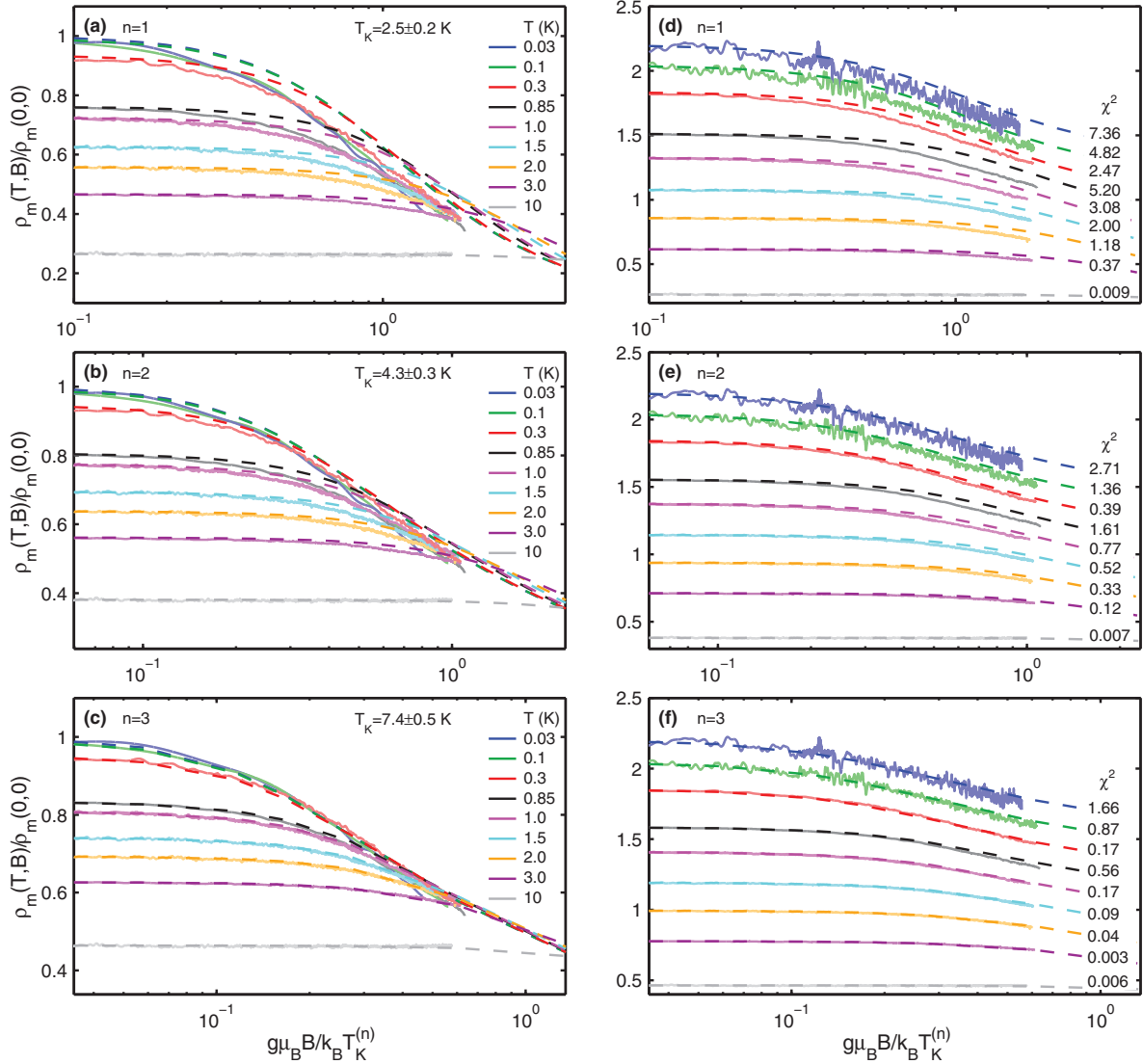


FIG. 5. (Color online) Experimental and theoretical results for $\rho_m(T, B)$, shown using solid or dashed curves, respectively. Left column: (a), (b), and (c) compare the experimental data for AgFe2 to NRG-calculations for $n \in \{1, 2, 3\}$, respectively. Right column: (d), (e), and (f) show the same data as in the left column, except that for clarity the curves for successive temperatures are shifted vertically by 0.15 to avoid them from overlapping, thus enabling a better comparison between experiment and theory for each temperature. $T_K^{(n)}$ and $\delta^{(n)}$ are already determined by the fitting procedure of Eq. (10), which allows a parameter-free theoretical prediction for $\rho_m(T, B)$. The χ^2 values indicated in (d)–(f) were calculated using a set of 1000 uniformly spaced field values in the range $B \in [0.07349, 3.05000]$ T. The experimental data clearly show best agreement with theory for $n = 3$, which supports the conclusion from the examination of γ_m . For $T = 0.030$ and 0.10 K, the signal to noise ratio is much lower than for the other curves since the measurement current had to be reduced to stay in thermal equilibrium; therefore in the left panels, the experimental data for these two temperatures have been smoothed for better visibility. For the largest temperature, $T = 10$ K, the phonon contribution has been subtracted from the experimental data for comparison to theory. For the purpose of this subtraction, the phonon contribution was assumed to be B -independent and taken to correspond to the difference of $\Delta\rho(T = 10\text{ K}, B = 0)/\Delta\rho(0, 0)$ between experiment and theory (see Fig. 3).

C. Channel anisotropy

To conclude this section, let us briefly discuss the possibility that the true effective Kondo model for Fe in Au and Ag could include some channel anisotropy. Channel anisotropy, if present at all, will be weak for the present system due to a symmetry argument. As mentioned in Introduction, Fe acts

as substitutional defect in Au or Ag; it hence finds itself in an environment with cubic symmetry. This cubic symmetry protects the equivalence of the three local t_{2g} levels and of the three bands involved in the effective low-energy Kondo model. In particular, this cubic symmetry offers a rather strong protection against any splitting of the t_{2g} levels. A significant

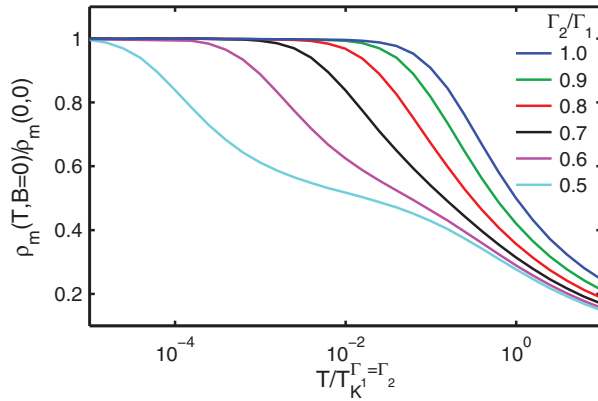


FIG. 6. (Color online) Temperature dependence of the resistivity for a channel-anisotropic Kondo model with $S = 1$, $n = 2$, for several different choices of Γ_2/Γ_1 .

spin-orbit coupling, which could result in a splitting of the t_{2g} levels, was ruled out by density functional theory calculations in paper I.

With this in mind, let us nevertheless briefly discuss the possible effects of channel anisotropy, that could arise if some perturbation breaks the cubic symmetry. In general, such a perturbation could result in a small splitting in the n impurity d levels that yield the spin $n/2$, or in slightly different band widths or density of states for the n conduction-band channels, or in slightly different coupling strengths between local and band states in each channel. All of these will have similar effects on the low-energy Kondo physics.

For concreteness, we consider here only the latter case, implemented in our model by setting $t \rightarrow t_\alpha$ in Eq. (1), leading to channel-dependent level widths $\Gamma_\alpha = \pi v_0 t_\alpha$. For a spin $n/2$, n -channel Kondo model, the presence of channel anisotropy quickly leads to a multistage Kondo effect,^{10,14} characterized by n different Kondo temperatures $T_{K\alpha}$ in which channels of decreasing Γ_α successively screen the bare spin $n/2$ first to spin $(n-1)/2$, then to $(n-2)/2$, etc., down to 0. Since the corresponding Kondo temperatures $T_{K\alpha}$ depend exponentially on Γ_α , even a small amount of channel anisotropy changes the shape of the resistivity curve $\rho_m(T, B=0)$ drastically. In particular, it spoils the purely logarithmic temperature dependence of the resistivity for $T \simeq T_K$, which is characteristic of the channel-isotropic Kondo effect: though each screening

stage separately produces a logarithmic contribution to the resistivity, the sum of these contributions no longer behaves purely logarithmically, as illustrated in Fig. 6 for $n = 2$. Our experimental data, however, do not show signatures of such multistage Kondo physics. This implies that any channel anisotropy, if present, is weak. Therefore the differences between the various $T_{K\alpha}$ -values associated with the successive stages of screening are, first, too small to be discernible in the data, and second, not at all required for the interpretation of the experimental data. We conclude that a fully channel-symmetric model suffices.

V. CONCLUSION

We have considered iron impurities in gold and silver and compared experimental data for the resistivity and decoherence rate to NRG results for a fully screened n channel, spin- $\frac{n}{2}$ Kondo model. Compared to previous work on this subject,⁹ we showed improved numerical data for both quantities at finite temperature. In particular, we offered a detailed discussion of NRG convergence and truncation issues, using the discarded weight as a criterion for reliably judging the quality of convergence. Our most important new result is the analysis of the resistivity at finite magnetic field, where we compare the numerical calculations with as yet unpublished experimental data. In contrast to previous attempts to explain the experimental results with models with less channels which were inconsistent or yielded several different values for the Kondo temperature, depending on which set of measurements was used to extract T_K ,⁸ we showed that all examined quantities can be described consistently with a single value of T_K . The excellent agreement between experiment and theory for $n = 3$ shows that both systems are well described by a spin-3/2 three-channel Kondo model.

ACKNOWLEDGMENTS

We thank Norman Birge for helpful comments on the manuscript. We gratefully acknowledge financial support from ANR PNANO ‘‘QuSPIN’’ for L.S. and C.B., from the John von Neumann Institute for Computing (Jülich) for T.C., from WE4819/1-1 for A.W., and from SFB-TR12, SFB-631 and the Cluster of Excellence Nanosystems Initiative Munich for J.v.D., M.H., and A.W.

¹W. J. de Haas, J. de Boer, and G. J. van den Berg, *Physica* **1**, 1115 (1934).

²W. J. de Haas and G. J. van den Berg, *Physica* **3**, 440 (1936).

³J. Kondo, *Prog. Theor. Phys.* **32**, 37 (1964).

⁴K. G. Wilson, *Rev. Mod. Phys.* **47**, 773 (1975).

⁵H. R. Krishna-murthy, J. W. Wilkins, and K. G. Wilson, *Phys. Rev. B* **21**, 1003 (1980).

⁶R. Bulla, T. A. Costi, and T. Pruschke, *Rev. Mod. Phys.* **80**, 395 (2008).

⁷F. Mallet, J. Ericsson, D. Maily, S. Ünlübayir, D. Reuter, A. Melnikov, A. D. Wieck, T. Micklitz, A. Rosch, T. A. Costi, L. Saminadayar, and C. Bäuerle, *Phys. Rev. Lett.* **97**, 226804 (2006).

⁸G. M. Alzoubi and N. O. Birge, *Phys. Rev. Lett.* **97**, 226803 (2006).

⁹T. A. Costi, L. Bergqvist, A. Weichselbaum, J. von Delft, T. Micklitz, A. Rosch, P. Mavropoulos, P. H. Dederichs, F. Mallet, L. Saminadayar, and C. Bäuerle, *Phys. Rev. Lett.* **102**, 056802 (2009).

¹⁰P. Nozières and P. Blandin, *J. Phys.* **41**, 193 (1980).

¹¹N. Andrei and C. Destri, *Phys. Rev. Lett.* **52**, 364 (1984).

- ¹²A. M. Tsvelik and P. B. Wiegmann, *J. Stat. Phys.* **38**, 125 (1985).
- ¹³I. Affleck, *Nucl. Phys. B* **336**, 517 (1990).
- ¹⁴I. Affleck, A. W. W. Ludwig, H.-B. Pang, and D. L. Cox, *Phys. Rev. B* **45**, 7918 (1992).
- ¹⁵A. Weichselbaum, *Ann. Phys.* **327**, 2972 (2012).
- ¹⁶A. I. Tóth and G. Zaránd, *Phys. Rev. B* **78**, 165130 (2008).
- ¹⁷A. I. Tóth, C. P. Moca, O. Legeza, and G. Zaránd, *Phys. Rev. B* **78**, 245109 (2008).
- ¹⁸A. Alex, M. Kalus, A. Huckleberry, and J. von Delft, *J. Math. Phys.* **52**, 023507 (2011).
- ¹⁹C. P. Moca, A. Alex, J. von Delft, and G. Zaránd, *Phys. Rev. B* **86**, 195128 (2012).
- ²⁰R. Bulla, A. C. Hewson, and T. Pruschke, *J. Phys.: Condens. Matter* **10**, 8365 (1998).
- ²¹A. K. Mitchell, D. E. Logan, and H. R. Krishnamurthy, *Phys. Rev. B* **84**, 035119 (2011).
- ²²We thank a referee for pointing out Ref. 21.
- ²³B. Mühlischlegel, *Zeitschrift für Physik* **208**, 94 (1968).
- ²⁴Y. Nishikawa and A. C. Hewson, *Phys. Rev. B* **86**, 245131 (2012).
- ²⁵J. R. Schrieffer and P. A. Wolff, *Phys. Rev.* **149**, 491 (1966).
- ²⁶T. Micklitz, A. Altland, T. A. Costi, and A. Rosch, *Phys. Rev. Lett.* **96**, 226601 (2006).
- ²⁷G. Zarand, L. Borda, J. von Delft, and N. Andrei, *Phys. Rev. Lett.* **93**, 107204 (2004).
- ²⁸A. Weichselbaum, *Phys. Rev. B* **84**, 125130 (2011).
- ²⁹A. Weichselbaum and J. von Delft, *Phys. Rev. Lett.* **99**, 076402 (2007).
- ³⁰F. B. Anders and A. Schiller, *Phys. Rev. Lett.* **95**, 196801 (2005).
- ³¹R. Peters, T. Pruschke, and F. B. Anders, *Phys. Rev. B* **74**, 245114 (2006).
- ³²A. Weichselbaum, *Phys. Rev. B* **86**, 245124 (2012).
- ³³D. C. Langreth, *Phys. Rev.* **150**, 516 (1966).
- ³⁴M. Yoshida, M. A. Whitaker, and L. N. Oliveira, *Phys. Rev. B* **41**, 9403 (1990).
- ³⁵L. Merker, S. Kirchner, E. Muñoz, and T. A. Costi, *Phys. Rev. B* **87**, 165132 (2013).
- ³⁶The n -dependent differences in the shapes of the resistivity curve can be characterized in terms of analytic expressions for their asymptotic behavior at large and small ratios of $T/T_K^{(n)}$ and $g\mu_B B/k_B T_K^{(n)}$. Such an analysis would go beyond the scope of the present paper and will be published elsewhere.
- ³⁷B. L. Altshuler and A. G. Aronov, in *Electron-Electron Interactions in Disordered Systems*, edited by A. L. Efros and M. Pollak (Elsevier, Amsterdam, 1985).
- ³⁸E. Akkermans and G. Montambaux, *Mesoscopic Physics of Electrons and Photons* (Cambridge University Press, Cambridge, UK, 2007).
- ³⁹C. Bäuerle, F. Mallet, F. Schopfer, D. Mailly, G. Eska, and L. Saminadayar, *Phys. Rev. Lett.* **95**, 266805 (2005).
- ⁴⁰L. Saminadayar, P. Mohanty, R. A. Webb, P. Degiovanni, and C. Bäuerle, *Physica E* **40**, 12 (2007).

6.3. Local susceptibility and Kondo scaling with finite bandwidth

Since in the universal Kondo regime, the Kondo temperature T_K is the only relevant energy scale of the system, energy-dependent quantities can be scaled on top of each other for different model parameters, if energies are rescaled with T_K . With the definition of the Kondo temperature via the inverse local susceptibility, as is common in numerical calculations, scaling is only provided in the limit of infinite bandwidth. We propose two altered definitions of T_K via two different susceptibilities χ^{FS} and χ^{sc} , depending on whether one considers the ground state of the system with perturbations that change the Hamiltonian or if one considers perturbative excitations of a Hamiltonian that is left unchanged, as it is the case for finite temperature or for dynamical quantities. The following paper is also a necessary prerequisite for section 6.4, where the correct determination of T_K in the presence of finite bandwidth is crucial for consistency with theory.

Local susceptibility and Kondo scaling in the presence of finite bandwidth

Markus Hanl and Andreas Weichselbaum

Physics Department, Arnold Sommerfeld Center for Theoretical Physics, and Center for NanoScience, Ludwig-Maximilians-Universität, 80333 Munich, Germany

(Received 16 October 2013; revised manuscript received 27 December 2013; published 21 February 2014)

The Kondo scale T_K for impurity systems is expected to guarantee universal scaling of physical quantities. However, in practice, not every definition of T_K necessarily supports this notion away from the strict scaling limit. Specifically, this paper addresses the role of finite bandwidth D in the strongly correlated Kondo regime. For this, various theoretical definitions of T_K are analyzed based on the inverse magnetic impurity susceptibility at zero temperature. While conventional definitions in that respect quickly fail to ensure universal Kondo scaling for a large range of D , this paper proposes an altered definition of T_K^{sc} that allows universal scaling of dynamical or thermal quantities for a given fixed Hamiltonian. If the scaling is performed with respect to an external parameter that directly enters the Hamiltonian, such as magnetic field, the corresponding $T_K^{\text{sc,B}}$ for universal scaling differs, yet becomes equivalent to T_K^{sc} in the scaling limit. The only requirement for universal scaling in the full Kondo parameter regime with a residual error of less than 1% is a well-defined isolated Kondo feature with $T_K \lesssim 0.01 D$ irrespective of specific other impurity parameter settings. By varying D over a wide range relative to the bare energies of the impurity, for example, this allows a smooth transition from the Anderson to the Kondo model.

DOI: [10.1103/PhysRevB.89.075130](https://doi.org/10.1103/PhysRevB.89.075130)

PACS number(s): 02.70.-c, 05.10.Cc, 75.20.Hr, 72.15.Qm

I. INTRODUCTION

The Kondo scale represents a dynamically generated low-energy scale, which arises when an unpaired spin, to be referred to as the impurity, is screened by a metallic host. Prototypical examples include actual dilute magnetic impurities in metals [1–4], but also highly controllable quantum dot settings which are characterized through transport measurements [5,6]. The precise definition of the Kondo scale, however, is usually subject to conventions. Nevertheless, whatever the definition of the Kondo scale T_K , clean isolated Kondo features are expected to be universal: that is after proper scaling with respect to T_K , the resulting data is expected to fully collapse onto a single universal curve. Therefore whatever the specific definition of the Kondo scale, e.g., up to an irrelevant definition-dependent prefactor of order one, this represents an important stringent requirement: T_K must allow for accurate scaling of Kondo related features. A prototypical application that requires such scaling, for example, is the analysis of the prefactors in Fermi-liquid scaling of interacting impurity models [7–10], which strongly depends on the precise definition of T_K . As a matter of fact, the present work emerged and thus was motivated from preliminary work in exactly this direction for multiband models [4,11], with the results on the related Fermi liquid coefficients to be published elsewhere.

With T_K typically described by an exponential expression [12], the terms in the exponent usually do not depend on the full bandwidth D of a given model. The prefactor in the definition of T_K , however, may depend on D with the consequence that certain definitions of T_K can spoil universal Kondo scaling even if $T_K \ll D$. Consider, for example, the standard single impurity Anderson model (SIAM, see model Hamiltonian further below) with the impurity onsite interaction U . For $U \ll D$, the full bandwidth D becomes irrelevant for the impurity related physics. This turns out to be the safe regime for impurity related quantities. For the case $U \gtrsim D$, however, the bandwidth D becomes relevant for Kondo related quantities. Importantly, this regime is (i) experimentally relevant, in that

the experiment is never truly in the Kondo scaling limit. Moreover, through Schrieffer-Wolff transformation in the limit $U \rightarrow \infty$ of the particle-hole symmetric SIAM, (ii) this leads to the Kondo model, a widely used model itself. With its Kondo temperature given by $T_K \simeq D\sqrt{2\nu J}e^{-1/(2\nu J)}$ [1,12,13], with J the Kondo coupling and ν the density of states at the Fermi edge, this model is *intrinsically and strongly* affected by finite bandwidth. Therefore, in particular, the present discussion is of clear relevance also for the Kondo model.

Proper Kondo scaling is already built-in by construction in the experiment-like approach of using (full-width-) half-maximum type measures of T_K [5,6], which strictly focuses on the low-energy features of the measured quantities, typically assuming $T_K \ll D$. However, this requires to measure or calculate an entire curve while possibly subtracting a broader background still [4]. In contrast, for the theoretical analysis it appears more desirable to have a single measurable quantity, instead, which uniquely defines T_K up to a convention-dependent constant prefactor of order one. To be specific, this requires a definition of T_K at zero temperature in the absence of magnetic field in a static context, i.e., $T = B = \omega = 0$ (using $k_B = g\mu_B = \hbar = 1$ throughout, for convenience). This T_K is measured through a weak perturbation of the system, and hence can be computed within linear response. Considering that the Kondo state is sensitive to an external magnetic field, the quantity of interest discussed in this paper is the magnetic susceptibility of the impurity. The following discussion, however, can be generalized to other local susceptibilities.

A standard definition for the Kondo temperature for the one-channel Kondo model is given by [12,14]

$$T_K \equiv \frac{1}{4\chi_0}, \quad (1)$$

with $\chi_0 \equiv \lim_{T \rightarrow 0} \chi(T)$ the static magnetic susceptibility of the impurity in the limit of zero temperature. The constant prefactor of 1/4 is part of the definition, which may be chosen differently, for example, for multichannel models [12]. The immanent question, however, that arises with Eq. (1) is how

does one precisely define the impurity contribution χ_0 to the magnetic susceptibility? The predominant conventions to be found in the literature are [12, 14–16]

$$\chi^{(d)}(T) \equiv \langle \hat{S}_z^d \parallel \hat{S}_z^d \rangle_T, \quad (2a)$$

$$\chi^{\text{tot}}(T) \equiv \langle \hat{S}_z^{\text{tot}} \parallel \hat{S}_z^{\text{tot}} \rangle_T - \langle \hat{S}_z^{\text{tot}} \parallel \hat{S}_z^{\text{tot}} \rangle_T^{(0)}, \quad (2b)$$

where $\langle \hat{S}^\alpha \parallel \hat{S}^\beta \rangle \equiv \frac{d}{dB} \langle \hat{S}^\beta \rangle|_{B=0}$ describes the static linear spin susceptibility of $\langle \hat{S}^\beta \rangle$ in response to the perturbation $\hat{H}' = -B\hat{S}^\alpha$ with B an external magnetic field (the minus sign in \hat{H}' ensures $\chi \geq 0$ if $\hat{S}^\alpha = \hat{S}^\beta$). Here \hat{S}_z^d (\hat{S}_z^{tot}) stands for the total spin of the impurity (the entire system), respectively. Since, in general, the spin of the impurity \hat{S}_z^d is not conserved and hence does not commute with the Hamiltonian, Eq. (2a) is equivalent to the evaluation of a dynamical correlation function [14]. It is a somewhat abstract quantity since from an experimental point of view it is difficult to just apply a magnetic field at the impurity itself. The second definition of the impurity susceptibility in Eq. (2b), on the other hand, is typically considered closer to an experimental realization, in that the impurity contribution to the total susceptibility is evaluated by taking the difference of the total susceptibility with $[\langle \cdot \rangle_T]$ and without $[\langle \cdot \rangle_T^{(0)}]$ the impurity, where the latter acts as a reference system. Equation (2b) includes the total spin \hat{S}_z^{tot} of the system, which is assumed to be conserved and hence is simply proportional to the overall spin fluctuations, $\langle \hat{S}_z^{\text{tot}} \parallel \hat{S}_z^{\text{tot}} \rangle_T = \beta[(\langle \hat{S}_z^{\text{tot}} \rangle^2) - \langle \hat{S}_z^{\text{tot}} \rangle^2]$ where $\beta = 1/T$. Hence, in principle, it is easier to evaluate. However, from a computational point of view, it has the disadvantage that one essentially needs two calculations, one with and one without the impurity, followed by the subtraction of two extensive macroscopic and thus large values in order to obtain an intrinsic impurity-related finite quantity. While one may expect that both definitions in Eq. (2) give comparable results, they are not strictly equivalent. In particular, neither definition in Eq. (2) necessarily guarantees proper scaling of Kondo related features at finite bandwidth.

Scaling onto a universal curve requires an appropriate and consistent set of parameters. For the Kondo physics analyzed in this paper, these are simply a particle-hole symmetric setting (or a similarly consistent asymmetric setting, e.g., $U/\varepsilon_d = \text{const}$ for the SIAM below), together with the bare requirement of a well-defined isolated low-energy feature with $T_K \lesssim 0.01 D$, e.g., the Kondo peak in the spectral function, which allows to observe Kondo physics to start with. Here universal scaling is understood in the usual way. Given a set of individual curves $y(x; \{p\})$, when plotted versus x , these depend on a set $\{p\}$ of external model parameters. Here, x represents an energy, e.g., $x \in \{\omega, T, B, \dots\}$. Therefore universal scaling of x by an appropriately chosen Kondo scale $T_K^{\text{sc},x}$, i.e., $\tilde{x} \equiv x/T_K^{\text{sc},x}$, implies that the curves $y(T_K^{\text{sc},x}\tilde{x}; \{p\})/y_0 =: \tilde{y}(\tilde{x})$ collapse onto a single universal curve $\tilde{y}(\tilde{x})$ independent of $\{p\}$. Note that away from the Kondo scaling limit, this Kondo scale $T_K^{\text{sc},x}$ can depend on the specific $x \in \{\omega, T, B, \dots\}$ chosen. Moreover, the vertical normalization y_0 of the curves is not necessarily related to $T_K^{\text{sc},x}$. Rather, it depends on the measured quantity, which may not even have units of energy. Typically, the specific choice for y_0 emerges out of context in a straightforward way, and as such is specified with each application below.

The main result of this paper is the proposition of the altered definition of the impurity susceptibility,

$$\chi^{\text{sc}}(T) \equiv \langle \hat{S}_z^{\text{tot}} \parallel \hat{S}_z^{\text{tot}} \rangle_T - \langle \hat{S}_z^{\text{bath}} \parallel \hat{S}_z^{\text{bath}} \rangle_T \quad (3a)$$

$$= 2\langle \hat{S}_z^d \parallel \hat{S}_z^{\text{tot}} \rangle_T - \langle \hat{S}_z^d \parallel \hat{S}_z^d \rangle_T, \quad (3b)$$

used for the scaling of dynamical or thermal quantities, i.e., $x \in \{\omega, T\}$. Here, $\hat{S}_z^{\text{bath}} \equiv \hat{S}_z^{\text{tot}} - \hat{S}_z^d$ and $\langle \hat{S}^\alpha \parallel \hat{S}^\beta \rangle$ as defined with Eq. (2). As will be demonstrated numerically, the definition of the susceptibility in Eq. (3) provides a sensitive Kondo scale through Eq. (1), i.e., $T_K^{\text{sc}} \equiv \lim_{T \rightarrow 0} [1/4\chi^{\text{sc}}(T)] \equiv 1/(4\chi_0^{\text{sc}})$, which allows for proper scaling (sc) of frequency or temperature dependent curves onto a single universal curve in a wide range of impurity parameters with bare energies from much smaller to much larger than the bandwidth D , provided that one has a well-defined Kondo regime, i.e., $T_K \ll D$. For notational simplicity, x will not be specified with T_K here, i.e., $T_K^{\text{sc}} \equiv T_K^{\text{sc},\omega} \equiv T_K^{\text{sc},T}$. A motivation of Eq. (3) in terms of the noninteracting system is given in the Appendix A. More generally, as pointed out with Appendix A2, the above scale-preserving susceptibility may be understood in terms of the scaling of frequency by the quasiparticle weight z [17].

In contrast, the earlier definitions in Eq. (2) can be reliably used for scaling in certain parameter regimes only (e.g. the scaling limit when the bandwidth is the largest energy scale by far). The major differences of the impurity susceptibility in Eq. (3) to the definitions in Eq. (2) are apparent. As compared to Eq. (2b), the last term in Eq. (3a) is calculated *in the presence* of the impurity. This comes with the benefit that, similar to Eq. (2a), Eq. (3b) can be computed entirely through the *nonextensive* quantities since the extensive leading term in Eq. (3a) cancels. Therefore, in contrast to Eq. (2b), the impurity susceptibility in Eq. (3) can be computed for a given system without having to resort to a reference system without the impurity. Compared to Eq. (2a), on the other hand, Eq. (3) acquires the relevant correction $\langle \hat{S}_z^d \parallel \hat{S}_z^d \rangle_T \rightarrow \langle \hat{S}_z^d \parallel \hat{S}_z^d \rangle_T - 2[\langle \hat{S}_z^d \parallel \hat{S}_z^d \rangle_T - \langle \hat{S}_z^d \parallel \hat{S}_z^{\text{tot}} \rangle_T]$.

For the T_K^{sc} derived from Eq. (3), the emphasis is on a given fixed Hamiltonian with infinitesimal perturbations whose (many-body) excitations are explored either dynamically or thermally. For this, the Kondo scale derived from χ_0^{sc} *mimics* the scaling limit, even if the parameters that enter the Hamiltonian do not strictly adhere to the scaling limit. In contrast, as will be shown below, *if the Hamiltonian itself* is altered through an external parameter $x \in \{B, \dots\}$ via $\hat{H}' = -x\hat{X}$, universal scaling vs. a finite range in x analyzed at zero temperature is generally governed by a slightly different Kondo scale, $T_K^{\text{sc},x}$, based on a variant of the impurity susceptibility (henceforth, the notation $T_K^{\text{sc},x}$ will be reserved for this context only).

In the scaling limit where bandwidth is the largest energy scale by far, it is found that $\langle \hat{S}_z^d \parallel \hat{S}_z^{\text{tot}} \rangle_T \simeq \langle \hat{S}_z^d \parallel \hat{S}_z^d \rangle_T$ (for a proof of this in the noninteracting case, see Appendix A2). Only in this regime, the static magnetic susceptibility can be computed equivalently in various ways including Eq. (2), i.e., $\chi^{\text{sc}}(T) \simeq \chi^d(T) \simeq \chi^{\text{FS}}(T)$. Here, in particular, the more conventional magnetic susceptibility $\chi^d(T)$ may be replaced by $\chi^{\text{FS}}(T)$, which is much simpler and cheaper to evaluate.

The definitions for proper scale-preserving Kondo temperatures at finite bandwidth as proposed in this paper are

TABLE I. Proposed corrections to the Kondo temperature based on the commonly used zero-temperature impurity susceptibility χ_0^d away from the strict scaling limit of infinite bandwidth, yet in the Kondo regime having $T_K \lesssim 10^{-2}D$. In the scaling limit, all corrections vanish, i.e., $\chi_0^{\text{FS}} = \chi_0^d$.

dependence on	universal Kondo scale $T_K = \frac{1}{4\chi_0}$	correction to χ_0^d	see also
ω or T	T_K^{sc} where $\chi_0^{\text{sc}} = 2\chi_0^{\text{FS}} - \chi_0^d$	$2 \times (\chi_0^{\text{FS}} - \chi_0^d)$	Eq. (3)
B	$T_K^{\text{sc},B}$ where $\chi_0^{\text{sc},B} = \chi_0^{\text{FS}}$	$1 \times (\chi_0^{\text{FS}} - \chi_0^d)$	Eq. (4)

summarized in Table I. This includes the Kondo temperature T_K^{sc} for fixed Hamiltonian for scaling of dynamical or thermal quantities, as well as the Kondo temperature $T_K^{\text{sc},B}$ for scaling versus an external parameter that alter the Hamiltonian at $T = \omega = 0$, here for the specific case of magnetic field B . The derivation of the latter (see Sec. IIC) may also serve as a general guide for scaling versus other external physical parameters that directly enter the Hamiltonian.

The remainder of the paper then is organized as follows. The rest of the introduction discusses the role of the new susceptibility $\langle \hat{S}_z^d \parallel \hat{S}_z^{\text{tot}} \rangle_T$ introduced with Eq. (3) in terms of the Friedel sum rule (Sec. IA). Furthermore, Sec. I still provides general computational aspects on the static linear susceptibility (Sec. IB), followed by model conventions and methods (Sec. IC). Section II presents the results and discussion on the scaling of dynamical impurity spin susceptibility (versus frequency), as well as the scaling of the linear conductance (versus temperature and magnetic field). Following summary and outlook, the appendices provide detailed technical discussions. It includes (Appendix A) a motivation for the scale-preserving susceptibility, which is mainly based on the noninteracting system, (Appendix B) a technical discussion of finite-size effects of the dynamical impurity susceptibility, and (Appendix C) technicalities on the evaluation of the mixed susceptibility $\chi^{\text{FS}}(T)$ within the fdm-NRG framework. The latter also contains a short discussion on the evaluation of the impurity specific heat which, in a wider sense, also resembles the structure of an impurity susceptibility. Finally, Appendix D comments on the conventional extraction of phase shifts from the many-body fixed-point spectra of the NRG, while also providing a detailed analysis of discretization, i.e., finite size, effects.

A. Magnetic susceptibility and Friedel sum rule

The definition of the impurity susceptibility in Eq. (3) introduces the additional impurity susceptibility,

$$\chi^{\text{FS}}(T) \equiv \langle \hat{S}_z^d \parallel \hat{S}_z^{\text{tot}} \rangle_T = \beta \langle \hat{S}_z^{\text{tot}} \hat{S}_z^d \rangle_T, \quad (4)$$

where $\beta \equiv 1/T$, and ‘‘FS’’ stands for Friedel sum rule as motivated shortly. It will also be referred to as *mixed* susceptibility, as it combines the impurity spin with the total spin. Assuming $B = 0$, the last equality in Eq. (4) used $\langle \hat{S}_z^{\text{tot}} \rangle_T = \langle \hat{S}_z^d \rangle_T = 0$. Given that \hat{S}_z^{tot} commutes with the Hamiltonian, this reduces to the simple thermal expectation value as indicated, which can be evaluated efficiently (see Appendix C for details). Consequently, for $T = 0^+$, this corresponds to a *strict* low-energy quantity that does not explore the dynamics at intermediated frequency $\omega \gtrsim T_K$

[which is the case, for example, for the definition of the impurity susceptibility in Eq. (2a)].

The susceptibility in Eq. (4) can be interpreted twofold: (i) as the local contribution to the total magnetization due to a global external field, or equivalently (ii) as the response in the total magnetization of the system due to a local magnetic field at the impurity only. The first can be seen as (yet another) intuitive and qualitative description of the local spin susceptibility. The latter interpretation, on the other hand, allows a direct link to the Friedel-sum rule (FS) [hence the label in Eq. (4)]: given an (infinitesimal) local change of the Hamiltonian, FS relates the low-energy phase shifts φ_σ of the entire system to the *total* change in local charge that flows to or from infinity (note that this change in local charge includes the displaced charge of both, the impurity itself as well as the close vicinity of the impurity, which in total may simply be interpreted as displaced ‘‘local’’ charge [18]).

The dependence of the low-energy phase shifts φ_σ of the bath electrons on an external magnetic field at the impurity can be used to define a Kondo scale T_K^φ [7],

$$\lim_{B \rightarrow 0} \frac{d}{dB} \varphi_\sigma \equiv \sigma \frac{\pi}{4T_K^\varphi}, \quad (5)$$

evaluated at $T = 0$, where $\sigma \in \{\uparrow, \downarrow\} \equiv \pm 1$. As a direct consequence of the Friedel-sum rule then, it follows

$$T_K^\varphi = T_K^{\text{FS}} \quad (T = 0), \quad (6)$$

since $\langle \hat{S}_z^{\text{tot}} \rangle = \frac{1}{2}(\Delta N_\uparrow - \Delta N_\downarrow) \stackrel{\text{FS}}{=} \frac{1}{2\pi}(\varphi_\uparrow - \varphi_\downarrow)$, with ΔN_σ the change in total number of particles with spin σ relative to $B = 0$. Consequently, $\chi^{\text{FS}} \equiv \frac{d}{dB_{\text{imp}}} \langle \hat{S}_z^{\text{tot}} \rangle = 1/(4T_K^\varphi)$, which coincides with the definition of T_K^{FS} , and hence proves Eq. (6). The identity in Eq. (6) has also been verified numerically to within 1% accuracy (using NRG with $\Lambda = 2$ as defined below; for a more detailed discussion on the explicit extraction of phase shifts within the NRG, see Appendix D).

While, intuitively, one may have expected that the dependence of the low-energy phase shifts on the magnetic field yields a universal Kondo scale, this is true only in the specific case that data is scaled versus magnetic field at $T = \omega = 0$, i.e., having $x = B$ (see Sec. IIC further below). However, this alters the Hamiltonian. For dynamical or thermal quantities for a given fixed Hamiltonian, having Eq. (3b), T_K^{FS} does not guarantee universal scaling. The reason for this may be seen as follows: while, in fact, the phase shifts themselves are not necessarily affected by finite bandwidth at $B = 0^+$, i.e., at the low-energy fixed point (cf. the discussion of χ_0^{FS} for the noninteracting case in Appendix A2), when investigating an entire universal curve with respect to frequency or temperature, this necessarily also explores states at intermediate energies.

By exploring a range of energies, however, this becomes susceptible to finite bandwidth. Hence T_K^φ fails to provide proper scaling onto a universal curve for dynamical or thermal data.

B. Static linear susceptibility

Consider the general static linear susceptibility for obtaining a response in the measured operator $\langle \hat{Y} \rangle$ by applying the infinitesimal external perturbation $\hat{H}'(\lambda) = -\lambda \hat{X}$ to a given Hamiltonian,

$$\langle \hat{X} \parallel \hat{Y} \rangle_T \equiv \lim_{\lambda \rightarrow 0} \frac{d}{d\lambda} \langle \hat{Y} \rangle_{T,\lambda} = \int_0^\beta d\tau \cdot \langle \delta \hat{X}(\tau) \cdot \delta \hat{Y} \rangle_T, \quad (7)$$

with $\beta \equiv 1/T$, $\delta \hat{X} \equiv \hat{X} - \langle \hat{X} \rangle_T$, similarly for $\delta \hat{Y}$, and $\hat{X}(\tau) \equiv e^{\tau \hat{H}} \hat{X} e^{-\tau \hat{H}}$ evaluated at $\lambda = 0$. By definition, the operators \hat{X} and \hat{Y} are assumed Hermitian. The last equality in Eq. (7), i.e., the imaginary-time Matsubara susceptibility, represents an *exact* mathematical relation [27], which satisfies the properties of a scalar product for Hermitian operators, i.e., $\langle \hat{X} \parallel \hat{Y} \rangle_T \equiv \langle \hat{Y} \parallel \hat{X} \rangle_T^*$ with $\langle \hat{X} \parallel \hat{X} \rangle_T \geq 0$ (cf. Bogoliubov-Kubo-Mori scalar product [27]). If \hat{X} and \hat{Y} do not commute with the Hamiltonian and $\langle \hat{X} \rangle_T = \langle \hat{Y} \rangle_T = 0$, then Eq. (7) is equivalent to the Kubo formula for linear response in the thermodynamic limit,

$$\langle \hat{X} \parallel \hat{Y} \rangle_T \simeq \langle \hat{X} \parallel \hat{Y} \rangle_T^{(R)} \equiv - \lim_{\omega \rightarrow 0} \chi_{XY}^R(\omega) \quad (8)$$

with $\chi_{XY}^R(\omega)$ the Fourier transformed dynamical retarded (R) correlation function $\chi_{XY}^R(t) \equiv -i \vartheta(t) \langle [\hat{X}(t), \hat{Y}] \rangle_T$ [the sign with the last term in Eq. (8) originates in the sign of the definition of \hat{H}' with Eq. (7), which ensures a positive susceptibility for $\hat{X} = \hat{Y}$]. The Kubo formula, as in Eq. (8), however, assumes that the system has no long-time memory of the applied operators \hat{X} or \hat{Y} . Importantly, for exactly this reason, for discretized, i.e., effectively finite-size systems, only Eq. (7) represents a reliable working definition, whereas corrections can apply to Eq. (8) (e.g., see Appendix B). Most notably, if the Hamiltonian preserves total spin (which will be assumed throughout this paper), then with $\hat{X} = \hat{Y} = \hat{S}_z^{\text{tot}}$, the resulting dynamical correlation function $\text{Im} \chi(\omega) \propto \delta(\omega)$ is pathological. In contrast, Eq. (7) yields the correct result $\langle \hat{S}_z^{\text{tot}} \parallel \hat{S}_z^{\text{tot}} \rangle_T = \beta \langle (\hat{S}_z^{\text{tot}})^2 \rangle_T - \langle \hat{S}_z^{\text{tot}} \rangle_T^2 \equiv \beta \cdot \Delta^2 S_z^{\text{tot}}$, i.e., the thermal fluctuations in the total spin of the system, using the grand-canonical ensemble in the evaluation of the thermal average $\langle \cdot \rangle_T$.

C. Models and method

A prototypical quantum impurity model is the single impurity Anderson model (SIAM) [19,20]. It consists of the local Hamiltonian, $\hat{H}_0^{\text{SIAM}} \equiv \hat{H}_{\text{imp}} + \hat{H}_{\text{cpl}}$, with

$$\hat{H}_{\text{imp}} = \sum_{\sigma} \varepsilon_{d\sigma} \hat{n}_{d\sigma} + U \hat{n}_{d\uparrow} \hat{n}_{d\downarrow}, \quad (9a)$$

$$\hat{H}_{\text{cpl}} = \sum_{k\sigma} (V_{k\sigma} \hat{d}_{\sigma}^{\dagger} \hat{c}_{k\sigma} + \text{H.c.}) \equiv \sqrt{\frac{2D\Gamma}{\pi}} \sum_{\sigma} (\hat{d}_{\sigma}^{\dagger} \hat{f}_{0\sigma} + \text{H.c.}). \quad (9b)$$

It describes a single interacting fermionic (d) level, i.e., the impurity (imp), with level-position $\varepsilon_{d\sigma}$ and onsite interaction U , which is coupled (cpl) through hybridization to a non-interacting macroscopic Fermi sea $\hat{H}_{\text{bath}} \equiv \sum_{k\sigma} \varepsilon_{k\sigma} \hat{n}_{k\sigma}$ with $\varepsilon_{k\sigma} \in [-D, D]$ of half bandwidth $D := 1$ (all energies taken in units of D , unless specified otherwise). Here, $\hat{d}_{\sigma}^{\dagger}$ ($\hat{c}_{k\sigma}^{\dagger}$) creates an electron with spin $\sigma \in \{\uparrow, \downarrow\}$ at the d level (in the bath at momentum k), respectively, with $\hat{n}_{d\sigma} \equiv \hat{d}_{\sigma}^{\dagger} \hat{d}_{\sigma}$, and $\hat{n}_{k\sigma} \equiv \hat{c}_{k\sigma}^{\dagger} \hat{c}_{k\sigma}$. If a magnetic field is applied at the impurity (in the bath), then $\varepsilon_{d\sigma} = \varepsilon_d - \frac{\sigma}{2} B$ ($\varepsilon_{k\sigma} = \varepsilon_k - \frac{\sigma}{2} B$), respectively. The sign has been chosen such that for $B > 0$, a positive magnetization $\langle \hat{S}_z \rangle$ arises. With ν the density of states, $\Gamma_{\sigma}(\varepsilon) \equiv \pi \nu V_{\sigma}^2(\varepsilon) = \Gamma \theta(D - |\omega|)$ is the hybridization strength. It is taken constant and the same for each spin σ , for simplicity.

In the limit of large U , the SIAM reduces to the Kondo model with a singly occupied impurity (a fluctuating spin), which couples to the electrons in the bath through the spin-spin interaction [1,12]

$$\hat{H}_0^{\text{Kondo}} = 2J \hat{S}_d \cdot \hat{S}_0 \quad (10)$$

with $J > 0$ the antiferromagnetic Heisenberg coupling (using constant density of states $\nu = 1/2D$ of the bath, for simplicity) [12], \hat{S}_d the spin operator of the impurity and $\hat{S}_0^x \equiv \frac{1}{2} \sum_{\sigma\sigma'} \hat{f}_{0\sigma}^{\dagger} \tau_{\sigma\sigma'}^x \hat{f}_{0\sigma'}$, the normalized spin operator of the bath site $\hat{f}_{0\sigma}$ at the location of the impurity with τ^x the Pauli spin matrices ($x \rightarrow \{x, y, z\}$).

The generic interacting impurity setting above involves the solution of a strongly correlated quantum many-body system, which can be simulated efficiently using the quasi-exact numerical renormalization group (NRG) [14,21]. In order to deal with arbitrary temperatures in an accurate manner, the fdm-NRG is employed [22–24], which is based on complete basis sets [25]. While not explained in detail here (for this see Refs. [14,21,24]), the essential NRG related computational parameters indicated with the figures below are the dimensionless logarithmic discretization parameter $\Lambda \gtrsim 2$, the truncation energy E_{tr} in rescaled units (as defined in Ref. [24]), the number N_z of z -shifts for z -averaging [26], and the log-Gaussian broadening parameter σ for smooth spectral data.

II. RESULTS AND DISCUSSION

A. Scaling of dynamical susceptibility

The dynamical magnetic susceptibility of the impurity is analyzed in Fig. 1 for both the SIAM (upper panels) as well as the Kondo model (lower panels) for a wide range of parameters, resulting in a dense set of curves. For the left panels, the horizontal frequency axis is scaled by $T_K^d \equiv 1/(4\chi_0^d)$, which clearly fails to reproduce a single universal curve. The universal scaling is provided only by the scaling of frequency using the altered T_K^{sc} (right panels). The residual tiny deviations stem from the data with largest T_K , i.e. with $T_K \gtrsim 10^{-3} D$.

By analyzing the universal scaling at an accuracy of $\lesssim 1\%$, this required at the very minimum a parameter setting in the strongly correlated Kondo regime. Hence the Kondo temperature was kept clearly smaller than the bandwidth, i.e., $T_K < 10^{-2}$. For the SIAM, this allowed a wide range for the interaction strength from significantly smaller to significantly

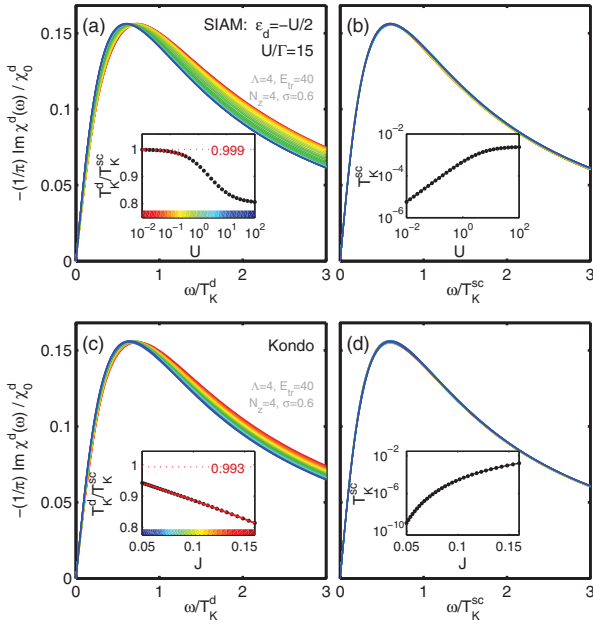


FIG. 1. (Color online) Scaling of the frequency of the dynamical spin susceptibility $\chi^d(\omega)/\chi_0^d$ by the conventional impurity susceptibility $T_K^d \equiv 1/(4\chi_0^d)$ (left) vs. the scale-preserving definition of Kondo temperature $T_K^{\text{sc}} \equiv 1/(4\chi_0^{\text{sc}})$ (right): all the densely lying curves of the left panels collapse onto a single universal curve in the right panels, respectively. (a) and (b) analyze the SIAM. The inset to (a) demonstrates the dependence of T_K^d/T_K^{sc} vs. the onsite interaction U , while keeping the ratios $U/\Gamma = 15$ and $\varepsilon_d = -U/2$ fixed. The color bar at the bottom of the inset relates the color of the lines in the main panel to the specific values of U ranging from $U \ll 1$ to $U \gg 1$ (with $D \equiv 1$ the bandwidth). The limit $\lim_{U \rightarrow 0} [T_K^d/T_K^{\text{sc}}]$ has been fitted, resulting in the value of 1, with excellent accuracy (actual value indicated together with the horizontal dotted line). The inset to (b) shows the dependence of T_K^{sc} vs. U , which stretches over several orders of magnitude. In complete analogy, (c) and (d) analyze the Kondo model. In particular, the fitted limit $\lim_{J \rightarrow 0} T_K^d/T_K^{\text{sc}} \simeq 1$ in the inset of (c) is the same as for the SIAM [cf. (a)] within the numerical error of significantly less than 1% [for comparison, the same calculation yet with the cheaper and less accurate setting of $\Lambda = 2$ and $E_{\text{ir}} = 12$ (not shown) already resulted in $T_K^d/T_K^{\text{sc}} \simeq 0.98$, while $\Lambda = 4$ and $E_{\text{ir}} = 20$ (not shown) already agreed well with the above results. In this sense, the above results for $\Lambda = 4$ and $E_{\text{ir}} = 40$ are considered fully converged].

larger than the bandwidth [28], nevertheless, while keeping $\Gamma/U = \frac{1}{15}$ and $\varepsilon_d/U = -\frac{1}{2}$ constant [cf. Fig. 1(a); similarly, the scaling was also tested away from the particle-hole symmetric point at $\varepsilon_d/U = -\frac{1}{3}$, resulting in equally excellent scaling of the data (not shown). The scaling also was tested for the noninteracting case ($U = \varepsilon_d = 0$ yet finite Γ ; not shown), where Γ takes the role of T_K . As a consequence, in complete analogy to above, for $\Gamma < 10^{-2}$ this allowed for similar excellent scaling of the data, yet, of course, to a different universal curve].

The different definitions of the Kondo temperature, T_K^d versus T_K^{sc} , are analyzed in the insets of the left panels, showing clear deviations of T_K^{sc} from T_K^d of up to 20%,

with T_K^d consistently smaller than T_K^{sc} . The deviations are more pronounced for the Kondo model, remembering that this essentially reflects the large- U limit of the Anderson model, which implies $U \gg D$ (even for Kondo temperatures as small as $T_K \simeq 10^{-10}$, the difference between T_K^d and T_K^{sc} is still about 6% (see inset in lower panels). In the limit $T_K \rightarrow 0$, both, the SIAM ($U \rightarrow 0$ with appropriately adjusted Γ and ε_d) as well as the Kondo model ($J \rightarrow 0$) result in the same ratio $T_K^d/T_K^{\text{sc}} = 1$ within the accuracy of the fitted extrapolations in the insets (using third-order polynomials with the fitting range indicated with the fit in red on top of the data; see caption on the convergence of T_K^d/T_K^{sc} with varying NRG parameters).

B. Scaling of static susceptibility and linear conductance versus temperature ($B = 0$)

The scaling of the static magnetic susceptibility and the linear conductance of the SIAM and Kondo model vs. temperature is analyzed in Fig. 2. The left panels analyze the SIAM in a wide range of the onsite interaction U . The center panels analyze the SIAM still, yet in the large- U limit while varying Γ , thus transitioning to the Kondo model. The right panels, finally, analyze the Kondo model itself. In all cases, the parameters were chosen such that $T_K \lesssim 10^{-2}$ with T_K plotted in the insets with the lower panels (the T_K for the largest Γ in the center panels exceeded 10^{-2} hence was excluded from the scaling analysis as indicated by the gray cross in the insets for the center panels).

The quantity $T \cdot \chi(T)$ as plotted in the upper panels of Fig. 2 for the spin susceptibility, reflects spin fluctuations at the impurity. The high-temperature limit for the Anderson (Kondo) impurity is given by $1/8$ ($1/4$), respectively, indicated by the horizontal dashed lines. Clearly, once T exceeds U for the SIAM (or D for the Kondo model), the large temperature limit is rapidly and accurately approached for either definition of the impurity susceptibility. For the SIAM, for $U \gg D$, an intermediate regime $D < T < U$ emerges that represents a free spin, consistent with $T \cdot \chi(T) \rightarrow \frac{1}{4}$ [see Figs. 2(a) and 2(b)]. For the Kondo model [Fig. 2(c)], this regime is represented by $T > D$.

In the regime $U \ll D$ for the SIAM, the effective bandwidth relevant for the impurity is given by U , such that the actual full bandwidth D of the Fermi sea becomes irrelevant in the description of the impurity [see $U = 10^{-2}$ data (dark blue) in Fig. 2(a)]. As a consequence, here the impurity susceptibility is rather insensitive to its precise definition, i.e., $\chi^d(T) \simeq \chi^{\text{FS}}(T) \simeq \chi^{\text{sc}}(T)$ [see $U = 10^{-2}$ data in inset of Fig. 2(a)], which thus is considered a safe regime for local susceptibility calculations and subsequent Kondo scaling. The differences between the three definitions of the impurity susceptibility, however, become strongly visible as U increases and surpasses the bandwidth [e.g., see $U = 10^2$ data (red curves) in Fig. 2(a)]. This behavior is precisely also reflected in the zero-temperature ratios T_K^d/T_K^{sc} as shown in the inset to Fig. 2(a), which strongly deviate from ≈ 1 as U increases.

For fixed large $U \gg D$, T_K can be strongly varied by tuning the hybridization Γ . The resulting data for the magnetic susceptibility is shown in Fig. 2(b). By plotting temperature in units of T_K^{sc} , the data for $\chi^{\text{sc}}(T)$ nicely collapse onto a universal curve for $T < D$, a feat which, in particular,

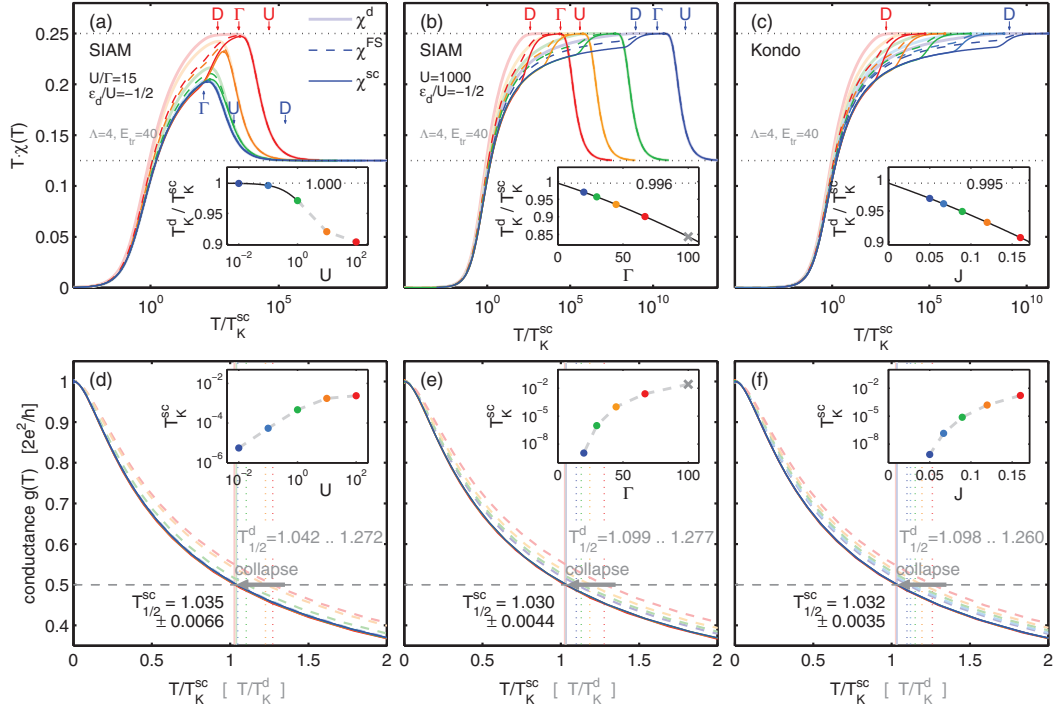


FIG. 2. (Color online) Temperature dependent scaling of the static spin susceptibility $\chi(T)$ (top) and the linear conductance $g(T)$ (in units of $2e^2/h$; bottom) for the SIAM (left and middle), as well as for the Kondo model (right). The color of the lines in the main panels matches the colors of the symbols in the inset, hence this indicates the respective parameter setting. The upper panels compare various definitions of the static spin susceptibility (χ^d , χ^{FS} , χ^{sc} in faint, dashed and solid, respectively). In the upper main panels, for clarity, the actual value of the relevant parameters $\{D, \Gamma, U\}$ for (a) and (b) and D for (c) are indicated in units of T_K^{sc} for the largest and smallest T_K only. Similar to Fig. 1, the insets to the upper panels analyze the relation between T_K^{d} and T_K^{sc} as function of the parameters. Their ratio is fitted towards $T_K \rightarrow 0$, resulting in a comparable value of 1 to very good accuracy as indicated for all three cases (a)–(c). The actual exponential range of T_K^{sc} is shown in the insets to the lower panels. The lower panels show the static linear conductance $g(T)$ vs. T/T_K^{d} (nonuniversal; dashed faint lines, but color match with symbols of inset otherwise) and vs. T/T_K^{sc} (solid lines), which show proper scaling behavior, in that all lines collapse onto a single universal curve. With $T_{1/2}$ the temperature where $g(T)$ passes through 1/2, in units of T_K^{d} , this ranges from $T_{1/2}^{\text{d}} \equiv T_{1/2}/T_K^{\text{d}} = 1.25$ down to 1.03 [indicated by the vertical dotted lines with the range of $T_{1/2}^{\text{d}}$ specified with each panel (gray text at center right in each panel)]. In units of T_K^{sc} , this range collapses to the fixed value of $T_{1/2}^{\text{sc}} \equiv T_{1/2}/T_K^{\text{sc}} \simeq 1.03$ to within residual relative variations of clearly less than 1% for all three cases [panels d-f; indicated by vertical solid light lines with their range specified by $T_{1/2}^{\text{sc}}$ (black text)]. Using $\Lambda = 4$ and $E_{\text{tr}} = 40$ as indicated, the value of $T_{1/2}^{\text{sc}} \simeq 1.03$ above is considered well converged [for comparison, for $\Lambda = 2$ and $E_{\text{tr}} = 8$ a similar calculation (not shown) resulted in $T_{1/2}^{\text{sc}} \simeq 0.99$, while $\Lambda = 2$ and $E_{\text{tr}} = 12$ resulted in $T_{1/2}^{\text{sc}} \simeq 1.01$; while good overall scaling can already be observed for $E_{\text{tr}} \lesssim 10$, the minor variations for smaller E_{tr} can be mostly eliminated by normalizing $g(T)$ by the numerical value $g(0) \approx 1$, which was not included here].

cannot be achieved for $\chi^d(T)$ in a similarly accurate manner. Furthermore, having $U \gg D$, the data in Fig. 2(b) for $T < U$ clearly resembles the Kondo model, as can be seen by direct comparison to the data of the actual Kondo model in Fig. 2(c).

The lower panels of Fig. 2 analyze the scaling of the linear conductance as measured in transport through a quantum dot, which represents a prototypical *quantum impurity* setting [5,6]. It is computed by folding the impurity spectral function $A_\sigma(\omega; T) \equiv \int \frac{dt}{2\pi} \langle \{\hat{d}_\sigma(t), \hat{d}_\sigma^\dagger\} \rangle_T$ with the derivative of the Fermi distribution function, i.e., $g(T) = \frac{\pi\Gamma}{2} \sum_\sigma \int d\omega A_\sigma(\omega; T) (-\frac{df}{d\omega})$ in units of $2e^2/h$. When scaling the temperature by T_K^{d} , the resulting data is plotted in light dashed lines, which show a clear nonuniversal spread akin to the earlier analysis in Fig. 1(a). In particular, the temperature $T_{1/2}^{\text{d}}$ where $g(T)$ passes through 1/2 changes from 1.25 down to 1.03 in units of T_K^{d} , with the large- U regime for the SIAM

[Fig. 2(e)] and in particular also the Kondo model itself [Fig. 2(f)] most strongly affected. In contrast, when scaling the temperature by T_K^{sc} , again an excellent scaling collapse is observed (solid lines in lower panels of Fig. 2). Note, furthermore, that the resulting $T_{1/2}^{\text{sc}} \equiv T_{1/2}/T_K^{\text{sc}} = 1.032 \pm 0.005$ nicely agrees across all panels from the SIAM [Figs. 2(a) and 2(b)] to the Kondo model [Fig. 2(c)], despite the broad parameter range analyzed. Given $\Lambda = 4$ together with $E_{\text{tr}} = 40$, these results are considered well converged (see figure caption on the convergence of $T_{1/2}/T_K^{\text{sc}}$ with NRG parameters). Finally, note that the value for $T_{1/2}/T_K^{\text{sc}}$ above also agrees well with the one cited by Merker *et al.* [10], which in the wide-band limit suggests $T_{1/2}/T_K^{\text{sc}} \simeq 1.04$. Overall, with $T_{1/2}/T_K^{\text{sc}}$ being constant, this is fully consistent with the fact that $T_{1/2}$ itself may serve and is frequently used as a universal definition of T_K , with a minor constant proportionality factor of 1.03 to the T_K^{sc} used here.

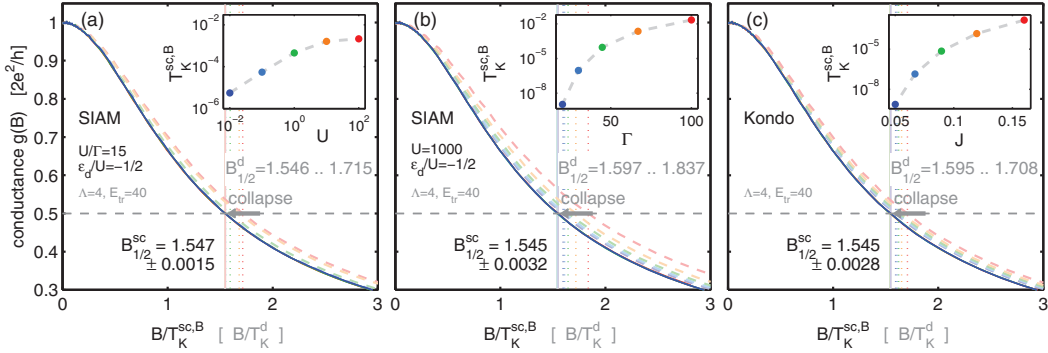


FIG. 3. (Color online) Linear conductance vs. magnetic field at $T = 0$ for the SIAM (left and center panel), as well as for the Kondo model (right panel). Again the insets indicate the respective parameter setting of the lines in the main panels. Analogous to the analysis in Figs. 2(d)–2(f), here, the main panels show the static linear conductance $g(B)$ vs. B/T_K^d (nonuniversal; dashed faint lines, but color match with symbols of inset otherwise) and vs. $B/T_K^{\text{sc},B}$ (solid lines), which demonstrate universal scaling. With $B_{1/2}$ the magnetic field where $g(B)$ passes through $1/2$, in units of T_K^d , changes from $B_{1/2}^d \equiv B_{1/2}/T_K^d = 1.84$ down to 1.55 for given data [indicated by the vertical dotted lines with their individual range specified with each panel (gray text at center right in each panel)]. In units of $T_K^{\text{sc},B}$, this range collapses to the value $B_{1/2}^{\text{sc}} \equiv B_{1/2}/T_K^{\text{sc}} = 1.55$ to within relative uncertainties of clearly less than 1% for all three cases [panels d–f; indicated by vertical solid light lines with the range T_K^{sc} specified by the black text]. Using $\Lambda = 4$ and $E_{\text{tr}} = 40$ as indicated, the data is considered fully converged (regarding minor variations for significantly lower $E_{\text{tr}} \lesssim 10$ and thus much faster calculations, see caption to Fig. 2).

The above results have direct implications on the Fermi liquid coefficients derived from the conductance $g(T)$. For example, with the Fermi liquid coefficient c_T defined by $g(T) \simeq 1 - c_T(T/T_K)^2$ for $T \ll T_K$ [7–10], this strongly depends on the precise definition of T_K . Note that even though T_K is apparently well defined through the magnetic susceptibility, depending on the precise definition of the latter, nevertheless, variations of up to 10% are seen in the ratio T_K^d/T_K^{sc} within a well-defined Kondo regime [cf. insets to upper panels of Fig. 2]. Therefore, when using T_K^d , this systematically underestimates c_T by up to 20%. It follows from the present analysis that the correct choice for T_K in the definition of c_T is T_K^{sc} , as it reflects the scaling limit, despite using parameters that do not strictly represent the scaling limit itself. Note, however, that the strict scaling limit is given by the regime $T_K^d/T_K^{\text{sc}} \simeq 1$, which for the Kondo model through the inset to Fig. 2(c) implies $J \lesssim 0.01$, resulting in the extremely small and rather impractical $T_K \lesssim 10^{-45}$.

C. Scaling of linear conductance versus magnetic field ($T = 0$)

The linear conductance at finite magnetic field yet zero temperature is a strict low-energy quantity, in that $g(B) = \frac{\pi\Gamma}{2} \sum_{\sigma} A_{\sigma}(\omega = 0; B, T = 0)$ requires the spectral function evaluated at $\omega = 0$ only. As a consequence, its sensitivity on finite bandwidth is minimal (cf. Appendix A). This already suggests that in a given case where the Hamiltonian is altered by a finite external parameter, universal scaling is not governed by the same T_K^{sc} as introduced in Eq. (3). Instead, through the Landauer formula, which in a given case implies $\pi\Gamma \cdot A_{\sigma}(\omega = 0; B, T = 0) = \sin^2(\varphi_{\sigma}(B))$, the conductance can be directly linked to the spin-dependent low-energy phase shifts φ_{σ} of the entire system. For a given particle-hole symmetric case, these can be written as $\varphi_{\sigma}(B) = \frac{\pi}{2} + \delta_{\sigma}(B)$, where for $|B| \ll T_K^{\text{FS}}$, $\delta_{\sigma}(B) \equiv \sigma\pi B/(4T_K^{\text{FS}})$

[cf. Eq. (5)] with $\sigma \in \{\uparrow, \downarrow\} \equiv \pm 1$. This directly identifies T_K^{FS} as defined in Eq. (4) as the relevant Kondo temperature for universal scaling. Specifically, one obtains

$$g(B) = \frac{1}{2} \sum_{\sigma} \sin^2(\varphi_{\sigma}) \simeq \frac{1}{2} \sum_{\sigma} \left(1 - \frac{1}{2} \delta_{\sigma}^2\right)^2 \simeq 1 - \left(\frac{\pi B}{4T_K^{\text{FS}}}\right)^2 \equiv 1 - c_T \left(\frac{B}{\pi T_K^{\text{FS}}}\right)^2 \quad (11)$$

with $c_T \equiv \frac{\pi^4}{16}$ the well-known Fermi-liquid coefficient with respect to temperature for Kondo impurities [7–10].

The scaling of the linear conductance $g(B)$ with T_K^{FS} is demonstrated in Fig. 3 for values of B that stretch well beyond the quadratic regime in Eq. (11). The analysis in Fig. 3 is completely analogous to Figs. 2(d)–2(f), except that here the dependence is on magnetic field B . Consistent with the earlier analysis, the data for the SIAM with smallest $U = 0.01$ in Fig. 3(a) already closely resembles the scaling limit. In contrast, the curves for the Kondo model in Fig. 3(c) even for the smallest coupling J with its extremely small T_K still do not strictly represent the scaling limit.

The above scaling analysis for $g(B)$ has major consequences for the extraction of the Fermi-liquid coefficient c_B , defined by $g(B) \simeq 1 - c_B(B/T_K)^2$ for $B \ll T_K$ at $T = 0$ [7–10]. The above analysis suggests that the Kondo scale, which needs to be considered for an accurate evaluation of c_B in a practical setting, is T_K^{FS} . This then again resembles the scaling limit while, nevertheless, it allows to use finite or narrow bandwidth in ones analysis provided that $T_K \lesssim 10^{-2}$ (in units of D as always).

III. SUMMARY AND OUTLOOK

In summary, an adapted scheme for the calculation of the local susceptibility has been introduced that at zero

temperature, allows to define a proper universal Kondo scale T_K^{sc} . The latter fully respects scaling of measured low-energy properties such as Kondo related features. A distinction needs to be made between dynamical or temperature dependent quantities that are described by the same fixed Hamiltonian (T_K^{sc}), as compared to dependence on external parameters that directly enter the Hamiltonian, such as magnetic field ($T_K^{\text{sc,B}}$). The corrections to the commonly used T_K based on the local susceptibility χ_0^{d} have been summarized in Table I. For the parameter sets analyzed in this paper, these corrections range from about 0% to 10% (which become about twice as large still for Fermi liquid coefficients), yet vanish in the scaling limit.

The effect of finite bandwidth on the Kondo scale was discussed while assuming a featureless hybridization otherwise. Proper scaling was demonstrated for the SIAM in a broad parameter regime, with the interaction U ranging from much smaller to much larger than the bandwidth D . The latter large- U limit then also was shown to smoothly connect the SIAM to the Kondo model. Essentially, this is the numerical equivalent of the Schrieffer-Wolff transformation without actually making any approximation [23]. By construction, the effects of finite bandwidth are clearly most prominent in the large- U limit ($U \gg D$), and as a consequence also affect most strongly the Kondo model itself. The discussion of a universal low-energy scale for specific model parameters away from the abstract true Kondo scaling limit with the bandwidth by far the largest energy is important in the experimental context, but also in the numerical context by choosing a parameter regime where simulations can be performed more efficiently (e.g., Kondo model versus SIAM). The explicit analysis and discussion of the universal Kondo scale applied to Fermi-liquid coefficients is beyond the scope of this paper, and will be published elsewhere.

Finally, it is pointed out that the impurity contribution to the specific heat, $c_V(T)$, essentially also has the structure of a susceptibility, namely, the response in energy at the impurity due to an increase in the external parameter T , i.e., the temperature. The analogies remain vague, since temperature is special as compared to other external parameters such as the magnetic field as it enters in the Boltzmann distribution for thermal statistics. Moreover, it is also unclear *a priori* whether and to what extent to associate the coupling term \hat{H}_{cpl} with the impurity or the bath. Nevertheless, an approximate expression for the impurity contribution to the specific heat can be evaluated by computing $c_V(T) \simeq \frac{d}{dT} \langle \hat{H}_{\text{imp}} + \frac{1}{2} \hat{H}_{\text{cpl}} \rangle_T$ [29]. In contrast to Ref. [29], however, which computes $c_V(T)$ by the explicit numerical derivative with respect to temperature, the latter can be fully circumvented along the lines of the mixed susceptibility χ^{FS} discussed above by directly computing the plain thermal expectation value $\beta \langle \hat{H}_{\text{imp}} + \frac{1}{2} \hat{H}_{\text{cpl}} \parallel \hat{H}_{\text{tot}} \rangle_T = \beta^2 \langle (\hat{H}_{\text{imp}} + \frac{1}{2} \hat{H}_{\text{cpl}}) \hat{H}_{\text{tot}} \rangle_T$ within the fdm-NRG framework (see Appendix C2 for details).

ACKNOWLEDGMENTS

We want to thank Oleg Yevtushenko, Herbert Wagner, and Jan von Delft for fruitful discussions, and also Theo Costi and Mikhail Pletyukhov for their comments on the manuscript.

This work has received support from DFG (TR-12, SFB631, NIM, and WE4819/1-1).

APPENDIX A: MOTIVATION FOR SCALE PRESERVING SUSCEPTIBILITY AT $T = 0$

The definition of the magnetic susceptibility $\chi^{\text{d}}(T)$ in Eq. (1) is typically computed through its spectral function $\chi''(\omega) \equiv -\frac{1}{\pi} \text{Im} \chi^{\text{R}}(\omega)$, having $\chi(\omega) \equiv \chi'(\omega) - i\pi \chi''(\omega)$ [for simplicity, the following discussion only refers to the static local impurity susceptibility $\chi^{\text{d}}(T)$, hence the superscript d will be skipped for readability]. This spectral function is given by

$$\begin{aligned} \chi''(\omega) &= \int \frac{dt}{2\pi} e^{i\omega t} \chi(t) \\ &= \sum_{a,b} (\rho_a - \rho_b) |\hat{S}_z^{\text{d}}|_{ab}^2 \delta(\omega - E_{ab}), \end{aligned} \quad (\text{A1})$$

with $\chi(t) \equiv \langle [\hat{S}_z(t), \hat{S}_z]_T \rangle \equiv \chi^>(t) - \chi^<(t)$, corresponding to the two terms of the commutator, respectively. The last line in Eq. (A1) provides the Lehmann representation of $\chi''(\omega)$, with a and b complete many-body eigenbasis sets, having $\rho_a = \frac{1}{Z} e^{-\beta E_a}$ and $E_{ab} \equiv E_b - E_a$. Hence with $\chi(\omega) = \chi'(\omega) - i\pi \chi''(\omega)$, the static spin susceptibility $\chi(T)$ is obtained through Kramers-Kronig relations (Hilbert transform),

$$\chi(T) = \lim_{\omega \rightarrow 0} \text{P} \int \frac{\chi''(\omega')}{\omega - \omega'} d\omega' = -\text{P} \int \frac{\chi''(\omega')}{\omega'} d\omega', \quad (\text{A2})$$

with P indicating principal value integral [for finite discrete systems, this skips all energetically degenerate terms in Eq. (A1) with $E_a = E_b$; the implications of the terms $E_a = E_b$ for finite-size systems or for preserved operators are discussed in Appendix B]. Note that even though $\chi_0 \equiv \lim_{T \rightarrow 0} \chi(T)$ describes a low-energy property, through Eq. (A2), it requires dynamical information from all frequencies. In contrast, the mixed impurity susceptibility in Eq. (4) results in the plain expectation value $\chi^{\text{FS}}(T) = \beta \langle \hat{S}_z^{\text{tot}} \hat{S}_z^{\text{d}} \rangle_T$. At $T = 0$, this corresponds to a ground-state expectation value. Consequently, this quantity is static and does not explore the dynamics of the system, and hence strictly focuses on the low-energy sector. For this reason, as pointed out in the main text, this quantity exactly reflects, for example, the phase-shifts experienced by the electrons of the bath in the low-energy fixed point spectrum.

Nevertheless, this mixed impurity susceptibility is still insufficient for the evaluation of a proper scale-preserving susceptibility. In order to proceed, while still insufficient, it is instructive to consider the effects of spectral moments (next section). This will be followed by the actual motivation of the scale-preserving susceptibility based on the plain noninteracting resonant level model.

1. Effects of spectral moments

The Kramers-Kronig or Hilbert transform in Eq. (A2), in a sense, corresponds to the spectral moment with $n = -1$ [by using the spectral weight $(\omega')^n$ within the integral]. This clearly weights small frequencies more strongly. Hence this emphasizes the low-energy sector while, nevertheless, it weakly reaches out towards large energies. This becomes more pronounced still for $n = 0$, which simply corresponds to the

spectral sum rule,

$$I \equiv \int \chi^>(\omega') d\omega' = \int (1 - f(\omega')) \chi''(\omega') d\omega' = \langle (\hat{S}_z^d)^2 \rangle_T \lesssim \frac{1}{4}, \quad (\text{A3})$$

with $f(\omega)$ the Fermi function. For $T = 0$, this exactly describes the area underneath the spin-spin correlation function $\chi''(\omega)$ for positive or, up to a sign, for negative frequencies [cf. Fig. 1; the integral over the entire $\chi^d(\omega)$ for all frequencies yields zero by the antisymmetry of $\chi^d(\omega)$].

For the SIAM in the local-moment (Kondo) regime, the value of the integral in Eq. (A3) at $T = 0$ is close to its upper bound, $I_0^{\text{SIAM}} \lesssim 0.25$, with minor variations of $\lesssim 10\%$ depending on the specific model parameters. For the Kondo model (which represents the large- U limit of the SIAM, i.e., $U \gg D$), by construction, the sum-rule in Eq. (A3) exactly yields the upper bound $I_0^{\text{Kondo}} = 1/4$.

At $T = 0$, the scaling of the spectral data $\chi''(\omega)$ by $\chi_0 = \lim_{T \rightarrow 0} \chi(T)$ ensures that the height of $\chi''(\omega)$ is properly normalized [e.g., see Fig. 1, all panels]. Since the area underneath $\chi''(\omega)$ is (roughly) conserved, scaling of the frequency ω by χ_0^{-1} leads to approximate scaling (left panels of Fig. 1). Specifically, since for the Kondo model the area is exactly preserved (see above), the remaining horizontal variations in Fig. 1(c) *must be due to finite bandwidth*. In conclusion, the sum-rule in Eq. (A3) is not particularly useful for a proper scale-preserving local susceptibility. This is not surprising, considering that it represents the spectral moment $n = 0$, and hence is strongly susceptible to effects of finite bandwidth (for the Kondo model this means that, while the area in Eq. (A3) is preserved, there can be a shift of spectral weight from the band edge to low-energy Kondo regime and vice versa, hence spoiling the scaling of the low-energy Kondo features). Higher spectral moments will make things even worse. Hence this route appears ill-suited for the search of a scale-preserving local susceptibility at $T = 0$.

2. Motivation through the noninteracting SIAM

The scale-preserving susceptibility proposed in the main text was also tested successfully for the asymmetric SIAM, as well as in the limit $U \rightarrow 0$ at finite Γ , i.e., the plain noninteracting resonant level model. Even there, the proposed χ_0^{sc} still nicely allowed for the scaling of low-energy features, such as the impurity spectral function $A(\omega) \equiv -\frac{1}{\pi} \text{Im} G_d(\omega)$, as long as the low-energy scale (here Γ) is clearly smaller than the bandwidth, i.e., $\Gamma \lesssim 10^{-2}$. The reason for this will be explained in what follows. Considering that the general impurity Green's function for an interacting system can be written as $G_d(\omega) = [\omega - \varepsilon_d - \Delta(\omega) - \Sigma(\omega)]^{-1}$, with $\Sigma(\omega)$ the impurity self-energy, the discussion of the effects of finite bandwidth on the hybridization function $\Delta(\omega)$ below may serve as a more general motivation, indeed, for the definition of a scale preserving susceptibility. In particular, as it is demonstrated in the main paper, the result can also be nicely applied to interacting systems.

For the noninteracting case, with $\sigma \in \{\uparrow, \downarrow\} \equiv \{\pm 1\}$, the spin susceptibility reduces to the impurity charge-susceptibility for the spinless model. With $\langle \hat{S}_z^d \rangle_T = 0$,

one has

$$\begin{aligned} \chi^d(T) &= \frac{1}{4} \sum_{\sigma, \sigma'} \sigma \sigma' \langle \hat{n}_\sigma \parallel \hat{n}_{\sigma'} \rangle_0 = \frac{1}{2} \langle \hat{n}_{(\sigma)} \parallel \hat{n}_{(\sigma)} \rangle_0 \\ &\equiv -\frac{1}{2} \lim_{\omega \rightarrow 0} \chi^c(\omega), \end{aligned} \quad (\text{A4a})$$

[regarding the sign in the last line, see Eq. (A2)], with the charge susceptibility given by

$$\chi^c(\omega) \equiv \text{FT}\{-i\vartheta(t)\langle [\hat{n}(t), \hat{n}] \rangle_T\}, \quad (\text{A4b})$$

with $\hat{n} \equiv \hat{d}^\dagger \hat{d}$, and $\text{FT}(\cdot)$ indicating Fourier transform. In the noninteracting case, this results in the impurity susceptibility

$$\chi^d(T) = -\frac{\partial}{\partial \varepsilon_d} \langle \hat{n} \rangle_T = \text{Im} \int \frac{d\omega}{2\pi} [G_d(\omega)]^2 f(\omega), \quad (\text{A5})$$

with $G_d(\omega)$ the impurity Green's function and $f(\omega)$ the Fermi function. This results in the correct large temperature limit, $\lim_{T \rightarrow \infty} T \chi_0(T) = \frac{1}{8}$ for arbitrary $G_d(\omega)$. The low-temperature limit is model dependent. Considering the noninteracting case, the impurity Green's function is given by $G_d(\omega) = [\omega - \varepsilon_d - \Delta(\omega)]^{-1}$, with $\Delta(\omega^+) \equiv \sum_k \frac{V_k^2}{\omega^+ - \varepsilon_k} \equiv E(\omega) - i\Gamma(\omega)$ the hybridization function. In the wide-band limit for constant $\Gamma(\omega) = \theta(D - |\omega|)\Gamma$, it follows that $E(\omega) \rightarrow 0$. The effects of finite bandwidth D manifest themselves at small frequencies ω through

$$\varepsilon_d \rightarrow \varepsilon_d + E(\omega) \simeq \tilde{\varepsilon}_d - a\omega, \quad (\text{A6a})$$

with $\tilde{\varepsilon}_d \equiv \varepsilon_d + E(0)$ and $a \equiv -\frac{d}{d\omega} E(\omega)|_{\omega=0} \sim \Gamma/D \ll 1$ some dimensionless small constant (note that for the particle-hole symmetric resonant level model with constant Γ , one has $a \geq 0$). This leads to the scaling

$$\omega \rightarrow \tilde{\omega} \equiv (1 - a)\omega \quad (\text{A6b})$$

of the frequency in $G_d(\omega)$ in Eq. (A5) (interestingly, this may be interpreted more generally in an interacting context as the scaling of frequency by the quasiparticle weight z [17]). Therefore far away from the bandwidth, $|\omega| \ll D$, the impurity spectral function appears slightly *stretched* along the frequency axis while preserving its height. Overall, however, the line shape for small frequencies *remains unaltered* up to proper scaling factors.

With respect to frequency, Eq. (A6b) suggests the *increased* energy scale $T_K^{\text{sc}} = T_K^\infty / (1 - a)$ relative to T_K^∞ which, to lowest order in a , represents the energy scale in the wide-band limit. Remembering that $\chi_0 \propto T_K^{-1}$ represents an inverse energy scale, one obtains

$$\chi_0^{\text{sc}}(D) = (1 - a)\chi_0^\infty, \quad (\text{A6c})$$

with $\chi_0^{\text{sc}}(D)$ the scale-preserving local susceptibility at given finite bandwidth, and $\chi_0^\infty \equiv 1/(4T_K^\infty)$.

On the other hand, at $T = 0$, the Fermi function in Eq. (A5) is unaffected by the scaling $\omega \rightarrow \tilde{\omega}$, such that the overall integral in Eq. (A5) may be rewritten in terms of $\tilde{\omega}$, resulting in

$$\chi_0^d(D) \simeq \frac{1}{1 - a} \chi_0^\infty \stackrel{(\text{A6c})}{=} \left(\frac{1}{1 - a} \right)^2 \chi_0^{\text{sc}}(D). \quad (\text{A7})$$

With $a > 0$, this shows that $\chi_0^d(D)$ overestimates the scale-preserving susceptibility $\chi^{\text{sc}}(D)$ for given finite bandwidth D .

The mixed susceptibility now allows to determine and subsequently eliminate the scale factors $(1-a)$. With

$$\begin{aligned}\chi^{\text{FS}}(T) &= \int_0^\beta d\tau \langle \hat{S}_z^{\text{d}}(\tau) \hat{S}_z^{\text{tot}} \rangle = \beta \langle \hat{S}_z^{\text{d}} \hat{S}_z^{\text{tot}} \rangle \\ &= \frac{\beta}{2} (\langle \hat{n} \hat{N} \rangle - \langle \hat{n} \rangle \langle \hat{N} \rangle),\end{aligned}\quad (\text{A8a})$$

the last line again already refers to a spinless model, with $\hat{n} \equiv \hat{d}^\dagger \hat{d}$ the number of particles at the impurity and \hat{N} the total number of particles in the system. In the noninteracting case with $A(\omega) \equiv -\frac{1}{\pi} \text{Im} G_a(\omega)$ the impurity spectral function, this becomes

$$\chi^{\text{FS}}(T) = \frac{1}{2} \int d\omega A(\omega) [-f'(\omega)]. \quad (\text{A8b})$$

In the limit $T \rightarrow 0$, this yields $\chi_0^{\text{FS}} = A(0)/2$. While $A(\omega)$ depends on the rescaled frequency $\omega \rightarrow (1-a)\omega$, as discussed above, this is irrelevant here since $A(\omega)$ is evaluated at $\omega = 0$. In the wide-band limit of a featureless bath, i.e., constant hybridization Γ , Eq. (A5) exactly agrees with Eq. (A8b). Together with the fact that χ_0^{FS} does not explicitly depend neither on the bandwidth nor dynamically on finite frequency, this allows to identify $\chi_0^{\text{FS}} = \chi_0^\infty$ even at finite D .

Using Eq. (A7), the effects of finite bandwidth on $\chi_0^{\text{sc}}(D)$ to lowest-order in a are thus summarized by

$$\chi_0^{\text{sc}}(D) = (1-a)^2 \chi_0^{\text{d}}(D) \simeq (1-2a) \chi_0^{\text{d}}(D). \quad (\text{A9})$$

The first reduction of $\chi_0^{\text{d}}(D)$ by the factor $(1-a)$ leads to χ_0^{FS} . Another reduction by the same factor leads to the desired $\chi_0^{\text{sc}}(D)$. With $a \ll 1$, this implies that the difference between $\chi_0^{\text{sc}}(D)$ and χ_0^{FS} , as well as the difference between χ_0^{FS} and $\chi_0^{\text{sc}}(D)$ are the same to lowest order in a , and are given by the first equality in Eq. (A7), $a \chi_0^{\text{d}}(D) \simeq \chi_0^{\text{d}}(D) - \chi_0^{\text{FS}}$. Together with the last term in Eq. (A9) then, one obtains the final expression for the scale-preserving local susceptibility,

$$\chi_0^{\text{sc}}(D) = 2\chi_0^{\text{FS}} - \chi_0^{\text{d}}(D), \quad (\text{A10})$$

in agreement with Eq. (3b) in the main text.

APPENDIX B: IMPURITY SUSCEPTIBILITY AND FINITE SIZE EFFECTS

Consider the Lehmann representation of the generic impurity susceptibility given by the last term in Eq. (7):

$$\begin{aligned}\langle \hat{X} \parallel \hat{Y} \rangle_T &= \sum_{a,b} \frac{e^{-\beta E_a}}{Z} (\delta X)_{ab} (\delta Y)_{ba} \frac{1 - e^{-\beta E_{ab}^+}}{E_{ab}^+} \\ &= \underbrace{\sum_{a \neq b} \frac{e^{-\beta E_a} - e^{-\beta E_b}}{Z} \frac{X_{ab} Y_{ba}}{E_{ab}^+}}_{\equiv \langle \hat{X} \parallel \hat{Y} \rangle_T^{(R)}} + \beta \underbrace{\sum_a \frac{e^{-\beta E_a}}{Z} (\delta X)_{aa} (\delta Y)_{aa}}_{\equiv \langle \hat{X} \parallel \hat{Y} \rangle_T^{(S)}}.\end{aligned}\quad (\text{B1a})$$

Here, a and b represent complete many-body eigenbasis sets, i.e., $\hat{H}|a\rangle = E_a|a\rangle$ with $E_{ab} \equiv E_b - E_a$, and the Boltzmann distribution $\rho_a = e^{-\beta E_a}/Z$ [note that $(\delta X)_{aa} = X_{aa} - \langle \hat{X} \rangle_T \neq 0$ in general]. In the first line, the positive

infinitesimal, $E_{ab}^+ \equiv E_{ab} + i0^+$, was added for convenience to correctly deal with the case $E_a = E_b$ (the sign of the infinitesimal imaginary part is initially actually irrelevant here). By splitting off the terms $a = b$ of the sum in Eq. (B1a) into the correction $\langle \hat{X} \parallel \hat{Y} \rangle_T^{(S)}$, the first term in Eq. (B1b) then translates into the Kubo formula for linear response $\langle \hat{X} \parallel \hat{Y} \rangle_T^{(R)}$ based on the retarded response function. By the way the specific infinitesimals are chosen, actually, all degenerate terms $E_a = E_b$ drop out of the first term (principal value integral in the continuum's limit), which therefore ignores accidental degeneracies, i.e., degeneracies beyond strict internal multiplet degeneracies due to symmetries that are included with the second term. As a consequence, the sum in the first term can be relaxed back to all a, b including $a = b$. Furthermore, the correction $\langle \hat{X} \parallel \hat{Y} \rangle_T^{(S)}$ in Eq. (B1b) is relevant only if the spin states of the states a are sufficiently long-lived. In the extreme case $\hat{X} = \hat{Y} = \hat{S}_z^{\text{tot}}$, the first term $\langle \hat{X} \parallel \hat{Y} \rangle_T^{(R)}$ in Eq. (B1) is strictly zero, and therefore the entire susceptibility is carried by the second term. In contrast, for the case that the Hamiltonian does not commute with, say, \hat{X} , in the thermodynamic limit one expects that $X_{aa} \rightarrow 0$ and the second term in Eq. (B1) vanishes. In this case, linear response using either Kubo formula or the imaginary-time Matsubara susceptibility is safe. However, in the presence of discretized finite-size systems, $X_{aa} \neq 0$ can become a significant contribution nevertheless! In this case, both contributions in Eq. (B1) must be included.

1. Limit of large temperature for finite system

For a finite system in the limit $\beta|E_{ab}| \ll 1$, Eq. (B1a) becomes

$$\begin{aligned}\lim_{T \rightarrow \infty} \langle \hat{X} \parallel \hat{Y} \rangle_T &\simeq \sum_{a,b} \frac{e^{-\beta E_a}}{Z} (\delta X)_{ab} (\delta Y)_{ba} \underbrace{\frac{1 - (1 - \beta E_{ab}^+)}{E_{ab}^+}}_{=\beta} \\ &= \beta \lim_{T \rightarrow \infty} \langle \delta \hat{X} \cdot \delta \hat{Y} \rangle_T \\ &= \beta \lim_{T \rightarrow \infty} [\langle \hat{X} \hat{Y} \rangle_T - \langle \hat{X} \rangle_T \langle \hat{Y} \rangle_T],\end{aligned}\quad (\text{B2})$$

which is equivalent to the situation where either operator \hat{X} or \hat{Y} actually commutes with the Hamiltonian! This again serves to emphasize the importance of both terms in the evaluation of the impurity susceptibility in Eq. (B1) in any numerical setting for a finite system, even if both, \hat{X} and \hat{Y} , do not commute with the Hamiltonian. While in the case of small T the last term in Eq. (B1b) may be negligible, it gains relative importance with increasing temperature, to the extent that for a finite system with $T \rightarrow \infty$, comparable weight is carried by both terms in Eq. (B1b) [note that for large T , $\langle \hat{X} \parallel \hat{Y} \rangle_T^{(R)} \propto 1/T$, while the $1/T$ behavior of the correction $\langle \hat{X} \parallel \hat{Y} \rangle_T^{(S)}$ is caused by the leading β ; cf. explicit NRG analysis in Fig. 4].

2. Impurity susceptibility at large temperatures

In the limit $T \rightarrow \infty$, the thermal density matrix is fully mixed and hence independent of the eigenbasis of the actual Hamiltonian. The thermal average therefore can be reduced to

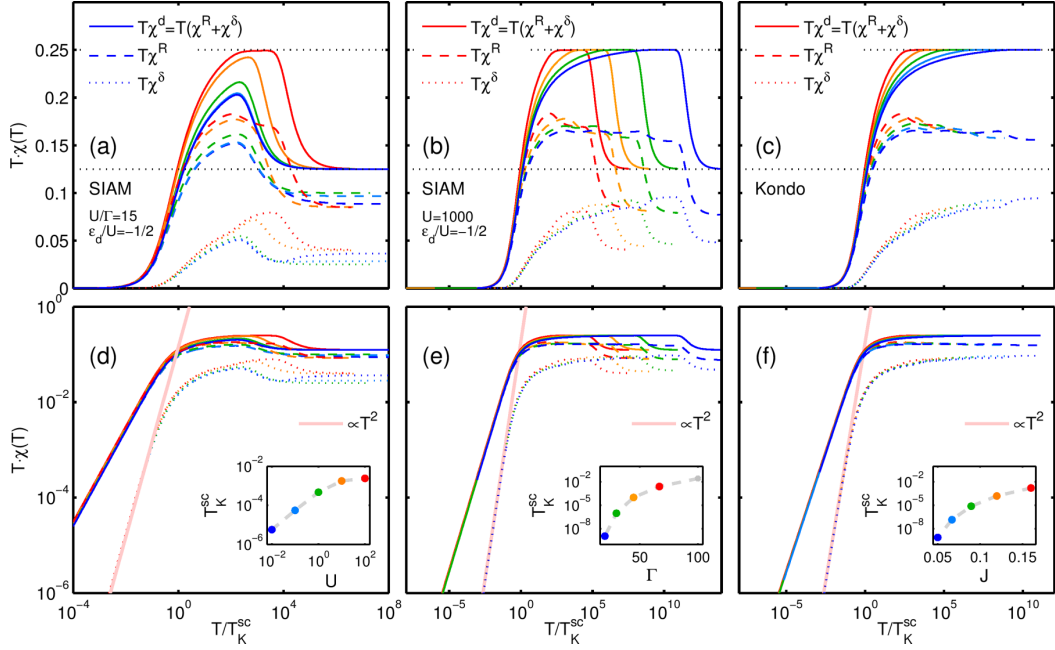


FIG. 4. (Color online) Contributions to the impurity susceptibility χ^d as in Eq. (B1) for the data in Fig. 2 in the main text [(a)–(c) have exactly the same parameter setting as Figs. 2(a)–2(c)]. The lower panels replicate the same data as in the upper panel, yet switch to a logarithmic scale also on the vertical axis. The thick light solid line corresponds to a plain power-law fit, suggesting that the correction $T\chi^\delta$ decays like $1/T^2$, hence becomes irrelevant in the limit $T \rightarrow 0$. The insets in the lower panels have been replicated from Fig. 2 to indicate the parameter setting.

the thermal average within the impurity space alone. Therefore with $\hat{S}_z^{\text{tot}} \equiv \sum_n \hat{S}_z^{(n)}$ summed over all (Wilson) sites n including the impurity, having $\langle \hat{S}_z^d \rangle_T = 0$, Eqs. (2)–(4) reduce to the same asymptotic form

$$\begin{aligned} (T\chi)_\infty &\equiv \lim_{T \rightarrow \infty} T\chi^{\text{sc}}(T) \simeq \lim_{T \rightarrow \infty} \langle \hat{S}_z^d \parallel \hat{S}_z^d \rangle_T \\ &= \frac{1}{d_i} \sum_{\sigma_i} (S_{z,\sigma_i})^2, \end{aligned} \quad (\text{B3})$$

where the impurity is described by the state space σ_i of dimension d_i that also diagonalizes \hat{S}_z^d . For a Kondo impurity, or also for an Anderson impurity in the case $T_K \ll D \ll T \ll U$, this implies $\chi_\infty = \frac{1}{4T}$ [this also may be taken as a motivation for the definition of the Kondo temperature $T_K = \frac{1}{4\chi_0}$ in Eq. (1) in the opposite limit of $T \rightarrow 0$; more generally still, for an impurity of spin S one obtains $(T\chi)_\infty = \frac{S(S+1)}{3}$]. On the other hand, for an Anderson impurity with $T \gg U$, one obtains $\chi_\infty = \frac{1}{8T}$ due to the enlarged accessible local state space [30] [see also Figs. 2(a)–2(b)].

3. Implications for the NRG

The above considerations are clearly relevant for numerical simulations such as the NRG. There the effective length of the Wilson chain becomes ever shorter for calculations with increasing temperature (automatically so in case of fdm-NRG) [22,24]. In case of NRG, the interplay between finite-size effects and large temperatures can therefore be considered enhanced.

The two contributions to the static susceptibility in Eq. (B1) are analyzed in detail in Fig. 4 for the data in Fig. 2 of the main text. From the log-log plots in the lower panels, it is clearly seen that the correction χ^δ behaves like $T \cdot \chi^\delta \propto 1/T^2$ for $T \ll T_K$ [in contrast to $T \cdot \chi^R \propto 1/T$], and hence becomes negligible in the limit $T \rightarrow 0$. Nevertheless, once T increases and becomes comparable to T_K , the correction $T \cdot \chi^R(T)$ becomes sizable. While the two contributions to the static susceptibility in Eq. (B1b) show rather irregular behavior individually, as seen in Fig. 4, their sum yields a smooth physically meaningful curve.

In practice, when computing the first term in Eq. (B1b) as standard susceptibility within linear response (Kubo formula), the second term shows up in a disguised manner as $\delta(0)$ contribution with opposite sign for $\omega = 0^\pm$. This may be collected in the smallest frequency bin for positive and negative frequencies, respectively, when collecting the discrete data. While these $\delta(0)$ contributions drop out of the principal value summation in the Kramers-Kronig transformation, nevertheless, they represent and thus can be simply used to subsequently evaluate the correction given by the last term in Eq. (B1b).

APPENDIX C: CALCULATION OF THE MIXED SUSCEPTIBILITY $\chi^{\text{FS}}(T)$ WITHIN FDM-NRG

Given that the total spin operator \hat{S}_z^{tot} commutes with the Hamiltonian, the mixed susceptibility $\chi^{\text{FS}}(T) \equiv \langle \hat{S}_z^d \parallel \hat{S}_z^{\text{tot}} \rangle_T$ in Eq. (4) can be evaluated in a simple and cheap manner, as it reduces to the plain set of expectation values, $T\chi^{\text{FS}}(T) = \langle \hat{S}_z^{\text{tot}} \hat{S}_z^d \rangle_T - \langle \hat{S}_z^{\text{tot}} \rangle_T \langle \hat{S}_z^d \rangle_T$. This includes one local operator \hat{S}_z^d

and one global operator, the total spin operator $\hat{S}_z^{\text{tot}} \equiv \sum_n \hat{S}_z^{(n)}$ which is given by the sum of local spins $\hat{S}_z^{(n)}$ associated with site n along the Wilson chain including the impurity, say, at $n = -1$. Being interested in the magnetic susceptibility at zero magnetic field, it follows $\langle \hat{S}_z^{\text{tot}} \rangle_T = \langle \hat{S}_z^{\text{d}} \rangle_T = 0$. The remaining quantity,

$$T \cdot \chi^{\text{FS}}(T) = \langle \hat{S}_z^{\text{tot}} \hat{S}_z^{\text{d}} \rangle_T = \text{tr}[\hat{\rho}(T) \cdot \hat{S}_z^{\text{tot}} \hat{S}_z^{\text{d}}], \quad (\text{C1})$$

then is a simple intrinsic quantity linked to the impurity. In given case, only a single sum over a complete many-body eigenbasis a suffices, with the Lehmann representation of Eq. (C1) given by

$$T \cdot \chi^{\text{FS}}(T) = \sum_a \frac{e^{-\beta E_a}}{Z} S_{z,a}^{\text{tot}} (\hat{S}_z^{\text{d}})_{aa}, \quad (\text{C2})$$

where $\hat{H}|a\rangle \equiv E_a|a\rangle$. By construction, the full thermal density matrix as well as the total spin operator S_z^{tot} are strictly diagonal, with the matrix elements given by $[S_z^{\text{tot}}]_{aa'} = \delta_{aa'} S_{z,a}^{\text{tot}}$ and $[\hat{\rho}(T)]_{aa'} = \delta_{aa'} e^{-\beta E_a}/Z$, respectively, with $Z(T) \equiv \sum_a e^{-\beta E_a}$ the grand-canonical partition function.

In what follows, the complete basis set a is given by the iteratively discarded state spaces generated by the NRG [25], i.e., $|a\rangle \rightarrow |se\rangle_n^D \equiv |s\rangle_n^D \otimes |e\rangle_n$ with $s_n \in D$ a discarded state at iteration n and e_n the environment with respect to iteration n , i.e., the full state space for the remainder of the Wilson chain $n < n' \leq N$ with N the final length of the Wilson chain considered. The resulting full thermal density matrix (fdm) is given by [22,24]

$$\hat{\rho}(T) = \sum_n w_n(T) \hat{\rho}_n^D(T), \quad (\text{C3})$$

where $w_n(T)$ is a well-defined temperature-dependent weight distribution along the Wilson chain that is peaked near the energy scale of temperature. The operators $\hat{\rho}_n^D$ are normalized thermal density matrices within the discarded state space of iteration n (the sum over the environment of the remaining iterations, resulting in the degeneracy factor d^{N-n} with d the dimension of the local state space of a single Wilson site, has been already properly included in the weight distribution w_n) [22,24]. With the full thermal density matrix a scalar operator, all entries in Eq. (C3) are block-diagonal. In particular, being initialized within the discarded (eigen-) state space at iteration n itself, all $\hat{\rho}_n^D$ are strictly diagonal.

Now, assuming that also \hat{S}_z^{tot} commutes with the Hamiltonian, it is also block diagonal. Using the complete basis set $|se\rangle_n^D \equiv |s\rangle_n^D \otimes |e\rangle_n$, in the expectation value in Eq. (C2) for the mixed susceptibility, the environment is traced over. Specifically with

$$\hat{S}_z^{\text{tot}} \equiv \sum_n \hat{S}_z^{(n)} = \underbrace{\sum_{n' \leq n} \hat{S}_z^{(n')}}_{\equiv \hat{S}_z^{n,\text{tot}}} + \underbrace{\sum_{n' > n} \hat{S}_z^{(n')}}_{\equiv \hat{S}_z^{e,\text{tot}}},$$

the total spin of the entire Wilson chain splits into two parts with respect to a given iteration n , the total spin up to and including site n , and the total spin for the remainder of the chain. The corresponding matrix elements are given by (note that the degeneracy factor d^{N-n} has been already included

with the weight distribution w_n and is thus compensated in the following expression)

$$\begin{aligned} & \frac{1}{d^{N-n}} \sum_{e_n} \langle se | \hat{S}_z^{\text{tot}} | s' e \rangle_n \\ &= \delta_{ss'} S_{z,s}^{n,\text{tot}} + \delta_{ss'} \sum_{n' > n} \frac{1}{d} \sum_{\sigma_{n'}} \underbrace{\langle \sigma_{n'} | \hat{S}_z^{(n')} | \sigma_{n'} \rangle}_{= (\hat{S}_z^{(n')})_{\infty=0}}, \end{aligned}$$

where $\sigma_{n'}$ spans the d -dimensional local Hilbert space of Wilson site n' . The last term represents the fully mixed average of the local spin for a given site n' , i.e., corresponding to an effective $T = \infty$, and thus vanishes identically by symmetry. Overall, this implies that at iteration n , only the total spin $\hat{S}_z^{n,\text{tot}}$ up to and including iteration n needs to be considered. Therefore the mixed susceptibility in Eq. (C1) can be evaluated in the NRG context as follows:

$$T \cdot \chi^{\text{FS}}(T) = \sum_n w_n(T) \text{tr} \left[\underbrace{\rho_n^D(T)}_{= \sum_{s \in D_n} \rho_{n,s}(T)} S_z^{n,\text{tot}} S_z^{\text{d}} \right], \quad (\text{C4})$$

where the trace runs over the discarded state space of iteration n as indicated. Here, the notation of the operators without hats indicates that they already correspond to the matrix representations in the basis $s \in D_n$, i.e., the discarded states at iteration n . The computationally most expensive part for the result Eq. (C4) is the evaluation of the matrix elements of \hat{S}_z^{d} in the discarded state space of iteration n . From these, however, only the diagonals are required. Once computed, the calculation of $\chi^{\text{FS}}(T)$ becomes extremely fast for an arbitrary set of temperatures. It is important, though, that for the physically correct impurity susceptibility thermal averaging at $T = 0^+$ is required. Hence the Wilson chain has to be chosen long enough such that the weight distribution $w_n(T)$ clearly fits within the Wilson chain, i.e., $T \gg \omega_N$, with N the length of the Wilson chain considered (in practice, $w_N(T) \lesssim 10^{-2}$; in contrast, if $T \ll \omega_N$, then $T \chi^{\text{FS}}(T) \rightarrow \langle 0 | \hat{S}_z^{\text{tot}} \hat{S}_z^{\text{d}} | 0 \rangle = 0$).

1. Evaluation in the presence of non-Abelian symmetries

In the above discussion, the external magnetic field was applied in the z direction. However, if the magnetic susceptibility at $B = 0$ is computed, the Hamiltonian typically possesses SU(2) spin symmetry. This can be taken advantage of when evaluating the mixed susceptibility above as follows. Clearly, the evaluation of the mixed susceptibility Eq. (C1) can be symmetrized with respect to x , y , and z components [23],

$$T \chi^{\text{FS}}(T) = \langle \hat{S}_z^{\text{tot}} \hat{S}_z^{\text{d}} \rangle_T = \frac{1}{3} \langle \hat{S}^{\text{tot}} \cdot \hat{S}^{\text{d}} \rangle_T,$$

where $\hat{S} \equiv [\frac{-1}{\sqrt{2}} \hat{S}_+, \hat{S}_z, \frac{+1}{\sqrt{2}} \hat{S}_-]^T \equiv \{\hat{S}_\mu\}$ with $\mu \in \{+1, 0, -1\}$ represents the irreducible three-dimensional spinor for the spin operator which transforms according to a spin $J = 1$ multiplet. Now every component in the spinor \hat{S}^{tot} commutes with the Hamiltonian such that \hat{S}_\pm^{tot} only raises or lowers the state index within the *same* multiplet, but never leaves a given multiplet. As a consequence, \hat{S}^{tot} is still a strictly diagonal operator in multiplet space, while the nondiagonal matrix elements within the same multiplet factorize as Clebsch-Gordan coefficients (cf. Wigner Eckart theorem). To be specific, in the presence

of symmetries, the state space at each iteration n is organized using the composite index labels [23] $|s\rangle_n \rightarrow |Js; M\rangle_n$ where $s_{(J)}$ now labels a specific multiplet within symmetry sector J , and $M_{(J)}$ represents the S_z labels, i.e. sequences the internal state space of multiplet J . With this, the matrix elements of the total spin operators are given by

$$\begin{aligned} \langle J'n'; M' | \hat{S}_\mu^{n,\text{tot}} | Jn; M \rangle \\ = \delta_{JJ'} \delta_{nn'} \underbrace{\sqrt{J(J+1)}}_{\equiv \|S_J^{n,\text{tot}}\|_{nn'}} \cdot (JM' | 1\mu; JM), \end{aligned}$$

with $(\cdot | \cdot; \cdot)$ indicating the Clebsch-Gordan coefficients. The prefactor represents the reduced matrix elements $\|S_J^{n,\text{tot}}\|$ for symmetry sector J . It guarantees that one obtains the familiar Casimir operator,

$$\langle Jn; M' | (\hat{S}^{n,\text{tot}})^\dagger \cdot \hat{S}^{n,\text{tot}} | Jn; M \rangle = J(J+1) \delta_{MM'}. \quad (\text{C5})$$

Consequently, in the presence of SU(2) spin symmetry, within the NRG the mixed susceptibility in Eq. (C4) can be rewritten as follows:

$$T\chi^{\text{FS}}(T) = \frac{1}{3} \sum_n w_n \text{tr}[\rho_n^D (S^d \cdot S^{n,\text{tot}})]. \quad (\text{C6})$$

The apparent overhead in terms of the extra summation over the μ components of the spinors in $S^d \cdot S^{n,\text{tot}}$ is completely negligible when compared to the gain by the reduced dimensionality on the reduced matrix element, i.e., the multiplet level. First of all, it only affects Clebsch-Gordan coefficient spaces. Moreover, by inspecting the block-diagonal structure of Eq. (C6), for the specific contribution of any symmetry sector within the trace *exactly the same* Clebsch-Gordan coefficient space appears twice, in both $S_\mu^{n,\text{tot}}$ as well as S_μ^d . Hence, by performing the trace for the Clebsch-Gordan coefficient space similar to Eq. (C5), this only adds a factor $(2J+1)$, i.e., the $3j$ -symbol, which is simply equal to the dimensionality of multiplet J . Hence the explicit contraction of the Clebsch-Gordan coefficients can be fully circumvented. In summary, the effect of non-Abelian symmetries on the evaluation of the mixed susceptibility in Eq. (C6) is that (i) S^d can be reduced to its block-diagonal components due to the block-diagonal structure of all the remaining participants. (ii) The traced-over Clebsch-Gordan spaces together with the definition of $S^{n,\text{tot}}$ results in the combined factor $\frac{1}{3}\sqrt{J(J+1)}(2J+1)$ for symmetry sector J that can be directly multiplied onto the reduced matrix elements of S^d . Finally, with the Clebsch-Gordan coefficients taken care of, (iii) the remaining trace is carried out over the reduced multiplet space only.

2. Evaluation of the approximate impurity specific heat

$(\hat{H}_{\text{imp}} + \frac{1}{2}\hat{H}_{\text{cpl}})\hat{H}_{\text{tot}})_T$ within fdm-NRG

The impurity specific heat has a similar mathematical structure when compared to the general discussion of susceptibility above. However, since it would be a susceptibility that refers to the temperature itself as the variable physical parameter, in the presence of thermal averages, these similarities necessarily remain vague and the impurity specific heat is special. Nevertheless, as it turns out [29], the impurity specific heat can

also be computed through the following *local* approximation:

$$c_V(T) \simeq \frac{\partial}{\partial T_{(\text{tot})}} \langle \hat{H}_{\text{ipc}} \rangle_T = \frac{\partial}{\partial T_{\text{ipc}}} \langle \hat{H}_{\text{tot}} \rangle_T, \quad (\text{C7})$$

where $\hat{H}_{\text{ipc}} \equiv \hat{H}_{\text{imp}} + \frac{1}{2}\hat{H}_{\text{cpl}}$, with \hat{H}_{imp} and \hat{H}_{cpl} the impurity Hamiltonian and its coupling to the bath, respectively [e.g., see Eq. (9)]; here *ipc* stands for impurity plus part of the coupling to the bath]. The first expression, $\frac{\partial}{\partial T_{(\text{tot})}} \langle \hat{H}_{\text{ipc}} \rangle$, has the intuitive physical interpretation that it represents the change in energy at the impurity due to a change in the overall total temperature, where the contribution of the hybridization is shared *in equal parts* with the bath [29]. Mathematically, this is equivalent to the second expression in Eq. (C7), $\frac{\partial}{\partial T_{\text{ipc}}} \langle \hat{H}_{\text{tot}} \rangle$, which represents the change in total energy due to a change in local temperature, i.e., with $\beta \equiv 1/T_{(\text{tot})}$ and $\hat{H}_{(\text{tot})} \equiv \hat{H}_{\text{ipc}} + \hat{H}_{\text{bpc}}$ (where *bpc* stands for bath plus remaining contribution from the coupling to the impurity),

$$\begin{aligned} e^{-\beta\hat{H}} &\equiv \exp\left[-\frac{1}{T_{(\text{tot})}}(\hat{H}_{\text{ipc}} + \hat{H}_{\text{bpc}})\right] \\ &\rightarrow \exp\left(-\frac{1}{T_{\text{ipc}}}\hat{H}_{\text{ipc}} - \frac{1}{T_{\text{bpc}}}\hat{H}_{\text{bpc}}\right), \end{aligned} \quad (\text{C8})$$

evaluated at $T_{\text{ipc}} = T_{\text{bpc}} = T_{(\text{tot})}$ after taking the derivative for $c_V(T)$, as indicated by the trailing subscript T in the last term of Eq. (C7).

While in Ref. [29] the derivative in Eq. (C7) was computed numerically by first computing the expectation values $\langle \hat{H}_{\text{ipc}} \rangle_T$, the derivative in Eq. (C7) can be easily expressed analytically,

$$c_V(T) = \beta^2 (\langle \hat{H}_{\text{ipc}} \hat{H}_{\text{tot}} \rangle_T - \langle \hat{H}_{\text{ipc}} \rangle_T \langle \hat{H}_{\text{tot}} \rangle_T), \quad (\text{C9})$$

which still can be directly evaluated numerically within the NRG using complete basis sets [22,24,25]. The term $\langle \hat{H}_{\text{ipc}} \rangle_T$ corresponds to a simple thermal average of a local quantity [24]. The total energy, on the other hand, is given by

$$\begin{aligned} \langle \hat{H}_{\text{tot}} \rangle_T &= \sum_{n,s \in D} \underbrace{\sum_e \frac{e^{-\beta E_s^n}}{Z}}_{=w_n(T) \frac{e^{-\beta E_s^n}}{Z_n} \equiv w_n \rho_s^n} (\omega_n \tilde{E}_s^n + \delta_n) \end{aligned} \quad (\text{C10a})$$

with the eigenenergies $E_s^n \equiv \omega_n \tilde{E}_s^n + \delta_n$ as is customary, the NRG eigenenergies \tilde{E}_s^n are given in rescaled units, with ω_n the energy scale at iteration n and δ_n here the *cumulative* subtracted energy offset with respect to the ground state at iteration n . While a global energy reference drops out of the entire definition of the impurity specific heat Eq. (C9), of course, the individual energy references δ_n for Wilson shell n do not cancel and hence must be properly included. Therefore $E_s^n \equiv \omega_n \tilde{E}_s^n + \delta_n$ represent the eigenenergies in nonrescaled physical units with respect to a single common energy reference, e.g., the ground-state energy of the entire Wilson chain. In this case, the offsets δ_n , when computed starting from the low-energy side (i.e., large n) scale like $\delta_n \propto \omega_n$. In Eq. (C10a), finally, again a single sum over the complete discarded (D) basis set $(s, e, n)^D$ suffices, since, obviously, \hat{H}_{tot} commutes with itself, i.e., with the Hamiltonian used in the evaluation of the overall thermodynamic average.

With the remaining term in Eq. (C9) given by

$$\langle \hat{H}_{\text{ipc}} \hat{H}_{\text{tot}} \rangle_T = \sum_{n,s \in D} w_n \rho_s^n (\omega_n \tilde{E}_s^n + \delta_n) \langle s_n | \hat{H}_{\text{ipc}} | s_n \rangle, \quad (\text{C10b})$$

the resulting impurity specific heat can be expressed as follows:

$$\begin{aligned} c_V(T) &= \beta^2 \sum_{n,s \in D} w_n \omega_n \rho_s^n \tilde{E}_s^n (\langle s_n | \hat{H}_{\text{ipc}} | s_n \rangle - \langle \hat{H}_{\text{ipc}} \rangle_T) \\ &\quad + \beta^2 \sum_{n,s \in D} w_n \delta_n \rho_s^n (\langle s_n | \hat{H}_{\text{ipc}} | s_n \rangle - \langle \hat{H}_{\text{ipc}} \rangle_T) \\ &\equiv \sum_n w_n \left[\frac{1}{\omega_n} \tilde{c}_V^{(D,n)}(T) + \frac{\delta_n}{T^2} (\langle \hat{H}_{\text{ipc}} \rangle_n^D - \langle \hat{H}_{\text{ipc}} \rangle_T) \right], \end{aligned} \quad (\text{C11})$$

where $\tilde{c}_V^{(D,n)}(T)$ stands for the specific heat computed within the discarded states space of Wilson shell n in *rescaled* units, i.e., using \tilde{E}_s^n and $T \rightarrow \tilde{T}_n \equiv T/\omega_n$. While $\tilde{c}_V^{(D,n)}(T)$ is clearly independent of the energy references δ_n for each individual Wilson shell n , these δ_n do lead to a *finite* contribution through the very last term in Eq. (C11). The reason is that, in general, the thermal expectation value $\langle \hat{H}_{\text{ipc}} \rangle_n^D$ in the discarded state space of iteration n is unequal to the full thermal average $\langle \hat{H}_{\text{ipc}} \rangle_T$ for the entire system. Only for very late Wilson shells in the low-energy fixed point, i.e., $T \rightarrow 0$, it follows $\langle s_n | \hat{H}_{\text{ipc}} | s_n' \rangle \simeq \langle \hat{H}_{\text{ipc}} \rangle_0 \cdot \delta_{ss'}$. This leads to cancellation of the last term, which is required for $\lim_{T \rightarrow 0} c_V(T) = 0$.

APPENDIX D: ON THE EXTRACTION OF PHASE SHIFTS WITHIN THE NRG

The Kondo scale T_K^{FS} derived from the mixed susceptibility [see Eq. (4)] is identical to the Kondo scale T_K^φ obtained from the phase shifts [see Eq. (5)], i.e., $T_K^{\text{FS}} = T_K^\varphi$, as discussed with Eq. (6) in the main text. For a Fermi liquid in the thermodynamic limit, the one-particle level spacing can be considered equally spaced around the Fermi energy yet different for each electronic flavor such as spin σ ,

$$\tilde{\epsilon}_{k\sigma} = \epsilon_{1\sigma} + k \epsilon_{2\sigma}, \quad (\text{D1})$$

with $k \in \{\dots, -2, -1, 0, 1, 2, \dots\}$ and $\epsilon_{1\sigma} \in [0, \epsilon_{2\sigma}[$, given that $\epsilon_{1\sigma}$ is essentially defined up to modulo $\epsilon_{2\sigma}$. Here the tilde on $\tilde{\epsilon}_{k\sigma}$ indicates that the original decoupled fixed bath modes may already have been (phase-) shifted by the presence of a coupled impurity. If the baths are identical for each flavor σ including their discretization, $\epsilon_{2\sigma}$ is independent of σ . This is typically the case for NRG where $\epsilon_{2\sigma} \propto \omega_N \propto \Lambda^{-N/2}$, with ω_N the energy scale at large but finite length N of the Wilson chain. Hence $\epsilon_{1\sigma}/\omega_N$ and $\epsilon_{2\sigma}/\omega_N$ are both of order 1. For the ground state, all levels with $\tilde{\epsilon}_{k\sigma} < 0$ are occupied. If $\epsilon_{1\sigma} = 0$, the many-body ground state is degenerate. For a Fermi liquid, the phase shift φ_σ can be extracted independently for each σ . In the thermodynamic limit, it is given by the ratio

$$\frac{\varphi_\sigma}{\pi} = \frac{\epsilon_{1\sigma}}{\epsilon_{2\sigma}} \quad (\text{D2})$$

[this can be simply motivated by using the connection of phase shifts to the change in (local) occupation through the Friedel sum rule, while taking a proper continuum limit starting from a finite yet large system, i.e., a discrete model].

Within the NRG, the one-particle level position in energy can be determined from the many-body eigenspectrum of the energy flow diagram, i.e., the finite-size fixed-point spectra at $T = 0^+$. This allows to extract φ_σ through Eq. (D2). Note, however, that due to the intrinsic even-odd alternations with the actual shell of the Wilson chain, the resulting phases φ_σ differ by the constant offset of $\pi/2$ between even and odd shells; nevertheless, since only differences in the phases due to the presence of the impurity, i.e., phase *shifts*, are considered, for an arbitrary but fixed energy shell this offset is irrelevant. The problem with Eq. (D2), however, is that it is based on an equally spaced one-particle level spectrum around the Fermi energy, which is not quite the case within NRG at all! Even though NRG does allow to *directly* access the thermodynamic limit in the numerical simulation due to the underlying logarithmic discretization in Λ [21,31], for a given length N of the Wilson chain and a necessarily rather coarse discretization with $\Lambda \gtrsim 2$, the approximately uniform level spacing around the Fermi energy quickly transforms into exponentially separated energy levels further away from the Fermi energy [32], as shown in Fig. 5.

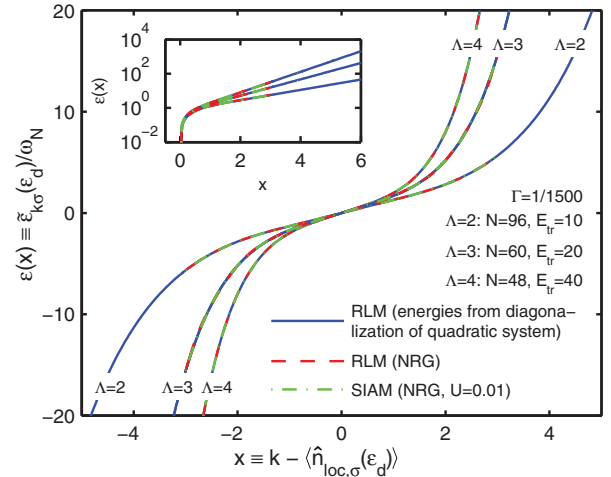


FIG. 5. (Color online) Dependence of single-particle energy level spectra $\tilde{\epsilon}_{k\sigma}(\epsilon_d)$ on local occupation $\langle \hat{n}_{\text{loc},\sigma}(\epsilon_d) \rangle$ and level index k for the SIAM [NRG (green dot-dashed)] as well as the RLM [quadratic solution (blue) and NRG (red dashed)] using a long even Wilson chain of length N as specified. The local occupation $\langle \hat{n}_{\text{loc},\sigma}(\epsilon_d) \rangle$ and thus the phase shift is changed by varying the position of the impurity energy level $\epsilon_{d(\sigma)}$. While this level is swept from $+\infty$ to $-\infty$, $\langle \hat{n}_{\text{loc},\sigma}(\epsilon_d) \rangle$ changes smoothly from 0 to 1. Combining all energies in units of the energy scale ω_n vs. $x \equiv k - \langle \hat{n}_{\text{loc},\sigma}(\epsilon_d) \rangle$, this results in a single continuous antisymmetric curve $\epsilon(x)$ that is linear for small $|x|$, yet is quickly dominated by exponential behavior for larger $|x| \gtrsim 2$ (see inset and text). The discrete levels $\tilde{\epsilon}_{k\sigma}(\epsilon_d) < 0$ (i.e., within the range $x < 0$) correspond to single-particle levels below the Fermi energy and are thus occupied in the ground state. The data for the blue curve were obtained by numerical diagonalization of the quadratic Hamiltonian (RLM), hence all single-particle energies are easily obtained. In particular, their energies are not restricted to the energy range below the truncation energy, as is the case for the NRG-method (dashed and dot-dashed lines).

Figure 5 analyzes the single-particle level spectra for the interacting as well as the noninteracting SIAM [the latter also referred to as the resonant level model (RLM)] as defined in Eq. (9) for an arbitrary late but fixed even Wilson shell N [i.e., H_0 such as in Eq. (9) plus some larger even number of further Wilson sites; for an odd length of the Wilson chain, all curves in Fig. 5 would be trivially offset horizontally by $1/2$, which can be ignored]. With $\varepsilon_d \equiv \{\varepsilon_{d\sigma}\}$ the (magnetic field dependent) level positions of the impurity, $\tilde{\varepsilon}_{k\sigma}(\varepsilon_d)$ is the one-particle level spectrum of the entire system. The shift of the discrete single-particle spectrum due to an arbitrary but fixed ε_d is directly related to phase shifts via Friedel sum rule. Thus when plotted versus the *continuous* variable $x \equiv k - \langle \hat{n}_{\text{loc},\sigma}(\varepsilon_d) \rangle$ having $\varepsilon_{d(\sigma)} \in [-\infty, \infty]$ and hence $\langle \hat{n}_{\text{loc},\sigma}(\varepsilon_d) \rangle \in [0, 1]$ with $\langle \hat{n}_{\text{loc},\sigma}(\varepsilon_d) \rangle$ the change in local charge at and close to the impurity [18] depending on the impurity setting, this allows to collect all one-particle level spectra $\tilde{\varepsilon}_{k\sigma}(\varepsilon_d)$ after rescaling by the approximate one-particle level spacing ω_N into a *single continuous curve* $\varepsilon(x)$, as demonstrated in Fig. 5. In a sense, with the Wilson chain in mind, the presence of the impurity allows to alter the boundary condition for the bath electrons, thus resulting in an impurity-dependent phase shift, which sets the horizontal offset $\langle \hat{n}_{\text{loc},\sigma}(\varepsilon_d) \rangle$ of the discrete energy levels in Fig. 5.

The resulting curve $\varepsilon(x)$, which describes the *macroscopic* bath, is universal in the sense that it only depends on the bath discretization (i.e., Λ), but is independent of the specifics of the *microscopic* impurity as long as the low-energy behavior represents an effective Fermi liquid. For example, as demonstrated in Fig. 5, the resulting curve $\varepsilon(x)$ is exactly the same independent of whether the impurity is interacting (SIAM) or not (RLM, with or without NRG). Using the same bath discretization for all flavors σ , as is customary within the NRG, this curve $\varepsilon(x)$ is also independent of σ , as already indicated by its notation.

As a consequence, for a given bath discretization, the curve $\varepsilon(x)$ can simply be computed for the noninteracting case (spinless RLM) by repeated diagonalization of the underlying

quadratic Hamiltonian while sweeping $\varepsilon_d \in [-\infty, \infty]$ (e.g., see solid line in Fig. 5). With the NRG bath discretization being particle-hole symmetric, the resulting curve $\varepsilon(x)$ is antisymmetric in x , i.e., $\varepsilon(-x) = -\varepsilon(x)$. Then given the reference curve $\varepsilon(x)$ together with the requirement of its antisymmetry, the single-particle spectrum for any other impurity setting can be fitted (provided Fermi liquid behavior), which allows to extract the horizontal offset $\langle \hat{n}_{\text{loc},\sigma}(\varepsilon_d) \rangle$ and hence the phase shift φ_σ independently for each flavor σ , *even if* the single-particle spectrum is not exactly uniformly spaced around the Fermi energy.

The range of linearity of $\varepsilon(x)$ around $x = 0$ indicates the regime of equally spaced single-particle levels closest to the Fermi energy, given an exponentially large but finite system size, as represented by the length N of the Wilson chain. For $\Lambda = 2$, linearity is given to a good approximation (within about 0.8%) for $x \in [-0.5, 0.5]$, i.e., for the lowest single-particle and single-hole excitation in the particle-hole symmetric case, and hence justifies using Eq. (D2) [this method was used for extracting T_K^φ and verifying Eq. (6) to within 1% accuracy in the main text]. In contrast, for $\Lambda = 4$, the linearity of $\varepsilon(x)$ even within this minimal regime is already clearly compromised (about 3%). Here usage of Eq. (D2) already leads to clear systematic errors due to the strongly increased coarseness of the underlying logarithmic discretization, leading to about a 7% error in Eq. (6). Therefore the extraction of phase shifts for larger Λ from the single-particle spectra requires a more careful analysis such as the aforementioned fitting to the curve $\varepsilon(x)$. Given a logarithmic discretization, it follows that $\varepsilon_k \sim \text{sgn}(k) \omega_N \Lambda^{|k|}$ for larger $|k|$ for a fixed length N of the Wilson chain. From the semilog- y representation in the inset of Fig. 5 it can be seen, that for $|x| \gtrsim 2$, $\varepsilon(x)$ is already described by a plain exponential behavior to within 0.1%. Thus rather than fitting the data for $|x| \lesssim 1$, alternatively, one may simply concentrate on the exponential behavior for larger $|x|$, which, however, requires to extract the single-particle spectrum at least up to the third single-particle level.

-
- [1] J. Kondo, *Prog. Theor. Phys.* **32**, 37 (1964).
[2] C. Bäuerle, F. Mallet, F. Schopfer, D. Mailly, G. Eska, and L. Saminadayar, *Phys. Rev. Lett.* **95**, 266805 (2005).
[3] F. Mallet, J. Ericsson, D. Mailly, S. Ünlübayir, D. Reuter, A. Melnikov, A. D. Wieck, T. Micklitz, A. Rosch, T. A. Costi *et al.*, *Phys. Rev. Lett.* **97**, 226804 (2006).
[4] T. A. Costi, L. Bergqvist, A. Weichselbaum, J. von Delft, T. Micklitz, A. Rosch, P. Mavropoulos, P. H. Dederichs, F. Mallet, L. Saminadayar *et al.*, *Phys. Rev. Lett.* **102**, 056802 (2009).
[5] D. Goldhaber-Gordon, H. Shtrikman, D. Mahalu, D. Abusch-Magder, U. Meirav, and M. A. Kastner, *Nature (London)* **391**, 156 (1998); W. G. van der Wiel, S. De Franceschi, T. Fujisawa, J. M. Elzerman, S. Tarucha, and L. P. Kouwenhoven, *Science* **289**, 2105 (2000).
[6] A. V. Kretinin, H. Shtrikman, D. Goldhaber-Gordon, M. Hanl, A. Weichselbaum, J. von Delft, T. Costi, and D. Mahalu, *Phys. Rev. B* **84**, 245316 (2011).
[7] P. Nozières, *J. Low Temp. Phys.* **17**, 31 (1974).
[8] M. Grobis, I. G. Rau, R. M. Potok, H. Shtrikman, and D. Goldhaber-Gordon, *Phys. Rev. Lett.* **100**, 246601 (2008).
[9] M. Pletyukhov and H. Schoeller, *Phys. Rev. Lett.* **108**, 260601 (2012).
[10] L. Merker, S. Kirchner, E. Muñoz, and T. A. Costi, *Phys. Rev. B* **87**, 165132 (2013).
[11] M. Hanl, A. Weichselbaum, T. A. Costi, F. Mallet, L. Saminadayar, C. Bäuerle, and J. von Delft, *Phys. Rev. B* **88**, 075146 (2013).
[12] A. Hewson, *The Kondo Problem to Heavy Fermions* (Cambridge University Press, New York, 1993).
[13] T. A. Costi, *Phys. Rev. Lett.* **85**, 1504 (2000).
[14] R. Bulla, T. Costi, and T. Pruschke, *Rev. Mod. Phys.* **80**, 395 (2008).
[15] A. Dirks, S. Schmitt, J. E. Han, F. Anders, P. Werner, and T. Pruschke, *Europhys. Lett.* **102**, 37011 (2013).
[16] M. Höck and J. Schnack, *Phys. Rev. B* **87**, 184408 (2013).
[17] B. S. Shastry, E. Perepelitsky, and A. C. Hewson, [arXiv:1307.3492](https://arxiv.org/abs/1307.3492) [cond-mat.str-el].

MARKUS HANL AND ANDREAS WEICHELBAUM

PHYSICAL REVIEW B **89**, 075130 (2014)

- [18] W. Mnder, A. Weichselbaum, M. Goldstein, Y. Gefen, and J. von Delft, *Phys. Rev. B* **85**, 235104 (2012).
- [19] J. Friedel, *Adv. Phys.* **3**, 446 (1954).
- [20] P. W. Anderson, *Phys. Rev. Lett.* **18**, 1049 (1967).
- [21] K. G. Wilson, *Rev. Mod. Phys.* **47**, 773 (1975).
- [22] A. Weichselbaum and J. von Delft, *Phys. Rev. Lett.* **99**, 076402 (2007).
- [23] A. Weichselbaum, *Annal. Phys.* **327**, 2972 (2012).
- [24] A. Weichselbaum, *Phys. Rev. B* **86**, 245124 (2012).
- [25] F. B. Anders and A. Schiller, *Phys. Rev. Lett.* **95**, 196801 (2005).
- [26] L. N. Oliveira, V. L. Libero, H. O. Frota, and M. Yoshida, *Physica B* **171**, 61 (1991).
- [27] M. Le Bellac, F. Mortessagne, and G. G. Batrouni, *Equilibrium and Non-Equilibrium Statistical Thermodynamics* (Cambridge University Press, Cambridge, 2004).
- [28] W. Hofstetter and S. Kehrein, *Phys. Rev. B* **59**, R12732 (1999).
- [29] L. Merker and T. A. Costi, *Phys. Rev. B* **86**, 075150 (2012).
- [30] L. Merker, A. Weichselbaum, and T. A. Costi, *Phys. Rev. B* **86**, 075153 (2012).
- [31] A. Weichselbaum, W. Mnder, and J. von Delft, *Phys. Rev. B* **84**, 075137 (2011).
- [32] H. R. Krishna-murthy, J. W. Wilkins, and K. G. Wilson, *Phys. Rev. B* **21**, 1003 (1980).

6.4. Equilibrium Fermi Liquid coefficients for fully screened Kondo models

For an analytical treatment, it is a great simplification if a system can be described with Fermi liquid theory since it is an effective single particle theory. In the Fermi liquid regime, which is valid for low energies, the impurity density of states and related quantities typically show quadratic behavior with respect to parameters like temperature or magnetic field, and can be characterized by the so called Fermi liquid coefficients. In the following paper we calculate the Fermi liquid coefficients of the resistivity with respect to magnetic field and temperature, $\rho(B)$ and $\rho(T)$, and of the impurity spectral function $A(\omega)$ (to be denoted $A(\epsilon)$ in this section), for a fully screened Kondo model with different numbers of channels. We use both analytics and NRG for the calculations, where the numerical results agree with the analytical values within a relative error of $\lesssim 5\%$.

PHYSICAL REVIEW B **89**, 195131 (2014)**Equilibrium Fermi-liquid coefficients for the fully screened N -channel Kondo model**M. Hanl,¹ A. Weichselbaum,¹ J. von Delft,¹ and M. Kiselev²¹*Physics Department, Arnold Sommerfeld Center for Theoretical Physics and Center for NanoScience, Ludwig-Maximilians-Universität München, 80333 München, Germany*²*The Abdus Salam International Centre for Theoretical Physics, Strada Costiera 11, I-34151 Trieste, Italy*

(Received 3 March 2014; published 23 May 2014)

We analytically and numerically compute three equilibrium Fermi-liquid coefficients of the fully screened N -channel Kondo model, namely c_B , c_T , and c_ε , characterizing the magnetic field and temperature dependence of the resistivity, and the curvature of the equilibrium Kondo resonance, respectively. We present a compact, unified derivation of the N dependence of these coefficients, combining elements from various previous treatments of this model. We numerically compute these coefficients using the numerical renormalization group, with non-Abelian symmetries implemented explicitly, finding agreement with Fermi-liquid predictions on the order of 5% or better.

DOI: [10.1103/PhysRevB.89.195131](https://doi.org/10.1103/PhysRevB.89.195131)

PACS number(s): 05.10.Cc, 71.10.Ay, 73.63.Kv, 72.15.Qm

I. INTRODUCTION

The Kondo effect was first observed, in the 1930s, for iron impurities in gold and silver [1,2], as an anomalous rise in the resistivity with decreasing temperature. Kondo [3] showed that this effect is caused by an antiferromagnetic exchange coupling between the localized magnetic impurity spins and the spins of the delocalized conduction electrons [3], and based his arguments on a spin- $\frac{1}{2}$, one-band model. While this model undoubtedly captures the essential physics correctly in a qualitative way, it has recently been shown [4,5] that a quantitatively correct description of the Kondo physics of dilute Fe impurities in Au or Ag requires a fully screened Kondo model involving three channels and a spin- $\frac{3}{2}$ impurity. This conclusion was based on a comparison of temperature and magnetic field dependent transport measurements [4–6] to theoretical predictions for fully screened Kondo models with channel number N and local spin S related by $N = 2S$, with $N = 3$ yielding much better agreement than $N = 1$ or 2.

The theoretical results in Ref. [5] were obtained using the numerical renormalization group (NRG) [7–10], and for $N = 3$ various non-Abelian symmetries [5,11], such as $SU(2) \times U(1) \times SU(N)$, had to be exploited to achieve reliable results at finite magnetic field. The technology for implementing non-Abelian symmetries with $N > 2$ in NRG calculations has been developed only recently [11,12]. Given the complexity of such calculations, it is desirable to benchmark their quality by comparing their predictions to exact results. The motivation for the present paper was to perform such a comparison for the low-energy Fermi-liquid behavior of fully screened Kondo models, as elaborated upon below.

All fully screened Kondo models feature a ground state in which the impurity spin is screened by the conduction electrons into a spin singlet. The low-energy behavior of these models can be described by a phenomenological Fermi-liquid theory (FLT) formulated in terms of the phase shift experienced by conduction electrons that scatter elastically off the screened singlet. Such a description was first devised for the simplest case of $N = 1$ by Nozières [13,14] in 1974, and generalized to the case of arbitrary N by Nozières and Blandin (NB) [15] in 1980. Their results were confirmed and elaborated by various authors and methods, including NRG [7,8,16–20], field-theoretic calculations [21,22], the

Bethe ansatz [23,24], conformal field theory (CFT) [25,26], renormalized perturbation theory [27], and reformulations [28–30] and generalizations [31–33] of Nozières' approach in the context of Kondo quantum dots.

In the present paper, we focus on three particular Fermi-liquid coefficients, c_B , c_T , and c_ε , characterizing the leading dependence of the resistivity on magnetic field (B) and temperature (T), and the curvature of the equilibrium Kondo resonance as a function of excitation energy (ε), respectively. Explicit formulas for all three of these coefficients are available in the literature for $N = 1$, but for general N only for the case of c_T . Given the wealth of previous studies of fully screened Kondo models, the lack of corresponding formulas for c_B and c_ε was somewhat unexpected. Thus, we offer here a unified derivation of all three Fermi-liquid coefficients, c_T , c_B , and c_ε . We follow the strategy which Affleck and Ludwig (AL) [26] have used to reproduce Nozières' results [13] for $N = 1$, namely doing perturbation theory in the leading irrelevant operator, and generalize it to the case of arbitrary N . Our formulation of this strategy follows that used by Pustilnik and Glazman (PG) [29] for their discussion of Kondo quantum dots. While all pertinent ideas used here can be found in the literature, we hope that our rather compact way of combining them will be found useful.

For our numerical work, we faced two challenges: First, the complexity of the numerical calculations increases rapidly with increasing N ; this was dealt with by exploiting non-Abelian symmetries. Second, numerical calculations do not achieve the scaling limit that is implicitly presumed in analytical calculations; its absence was compensated by using suitable definitions of the Kondo temperature, following Ref. [34].

The paper is organized as follows. In Sec. II we define the model and summarize our key results for the Fermi-liquid coefficients c_B , c_T , and c_ε . Section III compactly summarizes relevant elements of FLT and uses them to calculate these coefficients. Section IV describes our numerical work and results. Section V summarizes our conclusions.

II. MODEL AND MAIN RESULTS

The fully-screened Kondo model for N conduction bands coupled to a single magnetic impurity at the origin is defined

6.4 Equilibrium Fermi Liquid coefficients for fully screened Kondo models 159

M. HANL, A. WEICHELBAUM, J. VON DELFT, AND M. KISELEV

PHYSICAL REVIEW B **89**, 195131 (2014)

by the Hamiltonian $H = H_0 + H_{\text{loc}}$, with

$$H_0 = \sum_{km\sigma} \xi_k c_{km\sigma}^\dagger c_{km\sigma}, \quad (1a)$$

$$H_{\text{loc}} = J_K \sum_{kk'm\sigma\sigma'} c_{km\sigma}^\dagger \frac{\vec{\tau}_{\sigma\sigma'}}{2} c_{k'm\sigma'} \vec{S} - BS_z. \quad (1b)$$

Here H_0 describes N channels of free conduction electrons, with spin index $\sigma = (+, -) = (\uparrow, \downarrow)$ and channel index $m = 1, \dots, N$. We take the dispersion $\xi_k = \varepsilon_k - \varepsilon_F$ to be linear and symmetric around the Fermi energy, $\xi_k = k\hbar v_F$. Each channel has exchange coupling J_K to a local SU(2) spin of size $S = N/2$ with spin operators \vec{S} , and B describes a local Zeeman field in the z direction (we use units $g\mu_B = 1$). The overall symmetry of the model [19] is SU(2) \times Sp(2N) for $B = 0$, and U(1) \times Sp(2N) for $B \neq 0$ (see Sec. IV A for details). The model is characterized by a low-energy scale, the Kondo temperature, $T_K \sim \tilde{D} \exp[-1/(\nu J_K)]$, where ν is the density of states per channel and spin species and \tilde{D} is of the order of the conduction electron bandwidth.

For a disordered metal containing a dilute concentration of magnetic impurities, the magnetic-impurity contribution to the resistivity has the form [5,35]

$$\rho(T, B) \propto \int d\varepsilon [-\partial_\varepsilon f(\varepsilon, T)] \sum_{m\sigma} A_{m\sigma}(\varepsilon, T, B). \quad (2)$$

Here $f(\varepsilon, T)$ is the Fermi function, and the impurity spectral function $A_{m\sigma}(\varepsilon) = -\frac{1}{\pi} \text{Im} \mathcal{T}_{m\sigma}(\varepsilon)$ is the imaginary part of the T matrix $\mathcal{T}_{m\sigma}(\varepsilon)$ describing scattering off a magnetic impurity. The latter is defined through [37,38]

$$\mathcal{G}_{m\sigma, \mathbf{k}, \mathbf{k}'}^c(\varepsilon) = \mathcal{G}_{m\sigma, \mathbf{k}}^0(\varepsilon) \delta(\mathbf{k} - \mathbf{k}') + \mathcal{G}_{m\sigma, \mathbf{k}}^0(\varepsilon) \mathcal{T}_{m\sigma}(\varepsilon) \mathcal{G}_{m\sigma, \mathbf{k}'}^0(\varepsilon), \quad (3)$$

with $\mathcal{G}_{m\sigma, \mathbf{k}, \mathbf{k}'}^c$ and $\mathcal{G}_{m\sigma, \mathbf{k}}^0$ the full and bare conduction electron Green's functions, respectively. [For a Kondo quantum dot tuned such that the low-energy physics is described by Eq. (1), the conductance G through the dot has a form similar to Eq. (2), with ρ replaced by G [29]].

As mentioned in the Introduction, the ground state of the fully screened Kondo model is a spin singlet, and the regime of low-energy excitations below T_K shows Fermi-liquid behavior [13,15]. One characteristic Fermi-liquid property is that the leading dependence of the T matrix on its arguments, when they are small relative to T_K , is quadratic,

$$\frac{A_{m\sigma}(\varepsilon, T, B)}{A_{m\sigma}(0, 0, 0)} = 1 - \frac{c_\varepsilon \varepsilon^2 + c'_T T^2 + c_B B^2}{T_K^2}. \quad (4)$$

(Particle-hole and spin symmetries forbid terms linear in ε or B .) This implies the same for the resistivity,

$$\frac{\rho(T, B)}{\rho(0, 0)} = 1 - \frac{c_T T^2 + c_B B^2}{T_K^2}, \quad (5)$$

with $c_T = (\pi^2/3)c_\varepsilon + c'_T$. The so-called Fermi-liquid coefficients c_ε , c_T , and c_B are universal, N -dependent numbers, characteristic of the fully screened Fermi-liquid fixed point. For $N = 1$, the coefficients c_T and c_B have recently been measured experimentally in transport studies through quantum

dots and compared to theoretical predictions [39]. The coefficient c_ε is, in principle, also measurable via the nonlinear conductance of a Kondo dot coupled strongly to one lead and very weakly to another [29]. (The latter condition corresponds to the limit of a weak tunneling probe; it ensures that the nonlinear conductance probes the *equilibrium* shape of the Kondo resonance, and hence the equilibrium Fermi-liquid coefficient c_ε .)

The goal of this paper is twofold: first, to analytically establish the N dependence of c_ε , c_T , and c_B using Fermi-liquid theory similar to NB; and second, to numerically calculate them using an NRG code that exploits non-Abelian symmetries, in order to establish a benchmark for the quality of the latter. Our main results are as follows: First, if the Kondo temperature is defined by

$$T_K = \frac{N(N+2)}{3\pi\chi^{\text{imp}}} = \frac{4S(S+1)}{3\pi\chi^{\text{imp}}}, \quad (6)$$

where χ^{imp} is the static impurity susceptibility at zero temperature, the Fermi-liquid coefficients are given by

$$c_B = \frac{(N+2)^2}{9}, \quad c_T = \pi^2 \frac{4N+5}{9}, \quad c_\varepsilon = \frac{2N+7}{6}. \quad (7)$$

For general N , the formula for c_T has first been found by Yoshimori [21], while those for c_B and c_ε are new (though not difficult to obtain). Second, our numerical results for $N = 1, 2$, and 3 are found to agree with the predictions of Eq. (7) to within 5%.

III. FERMI-LIQUID THEORY

In this section, we analytically calculate the Fermi-liquid coefficients c_B , c_T , and c_ε for general N . With the benefit of hindsight, we selectively combine various elements of the work on FLT of Nozières [13], NB [15], AL [26], and PG [29]. Detailed justifications for the underlying assumptions are given by these authors in their original publications and hence will not be repeated here. Instead, our goal is to assemble their ideas in such a way that the route to the desired results is short and sweet.

We begin by summarizing Nozières' ideas for expressing the T matrix in terms of scattering phase shifts and expanding the latter in terms of phenomenological Fermi-liquid parameters. Next, we recount AL's insight that this expansion can be reproduced systematically by doing perturbation theory in the leading irrelevant operator of the model's zero-temperature fixed point. Then we adopt PG's strategy of performing the expansion in a quasiparticle basis in which the constant part of the phase shift has already been taken into account, which considerably simplifies the calculation. Our own calculation is presented using notation analogous to that of PG, while taking care to highlight the extra terms that arise for $N > 1$. It turns out that their extra contributions can be found with very little extra effort.

A. Phase shift and T matrix

Since the ground state of the fully screened Kondo model is a spin singlet, a low-energy quasiparticle scattering off the impurity experiences strong elastic scattering as if the impurity

were nonmagnetic. Moreover, it also experiences a weak local interaction if some energy ($\ll T_K$) is available to weakly excite the singlet, causing some inelastic scattering. Since the singlet binding energy is T_K , the strength of this local interaction is proportional to $1/T_K$.

Nozières [13] realized that this combination of strong elastic scattering and a weak local interaction can naturally be treated in terms of scattering phase shifts. The phase shift of a quasiparticle with quantum numbers $m\sigma$ and excitation energy ε relative to the Fermi energy can be written as

$$\delta_{m\sigma}(\varepsilon) = \delta_{m\sigma}^0 + \tilde{\delta}_{m\sigma}(\varepsilon), \quad \delta_{m\sigma}^0 = \pi/2. \quad (8)$$

Here $\delta_{m\sigma}^0$ is the phase shift for $\varepsilon = B = T = 0$; it has the maximum possible value for scattering off a nonmagnetic impurity, namely $\pi/2$. Finite-energy corrections arising from weak excitations of the singlet are described by $\tilde{\delta}_{m\sigma}(\varepsilon)$, which is proportional to $1/T_K$.

If inelastic scattering is weak, unitarity of the S matrix can be exploited [13] to write the T matrix in the following form (we use the notation PG [29]; for a detailed analysis, see AL's discussion [26] of the terms arising from their Figs. 6 and 7):

$$1 - 2\pi v i \mathcal{T}_{m\sigma}(\varepsilon) = e^{2i\delta_{m\sigma}(\varepsilon)} [1 - 2\pi v i \tilde{\mathcal{T}}_{m\sigma}^{\text{in}}(\varepsilon)]. \quad (9)$$

Here $\tilde{\mathcal{T}}^{\text{in}}$ accounts for weak inelastic two-body scattering processes, and is proportional to $1/T_K^2$. It is to be calculated in a basis of quasiparticle states in which the phase shift $\delta_{m\sigma}^0$ has already been accounted for. (Here and below, tildes will be used on quantities defined with respect to the new basis if they differ from corresponding ones in the original basis.)

Expanding Eq. (9) in the small (real) number $\tilde{\delta}_{m\sigma}(\varepsilon)$ and recalling that $e^{2i\delta_{m\sigma}^0} = -1$, one finds that the imaginary part of the T matrix, which determines the spectral function, can be expressed as

$$-\pi v \text{Im} \mathcal{T}_{m\sigma}(\varepsilon) = 1 - [\tilde{\delta}_{m\sigma}^2(\varepsilon) - \pi v \text{Im} \tilde{\mathcal{T}}_{m\sigma}^{\text{in}}(\varepsilon)], \quad (10)$$

to order $1/T_K^2$. Comparing this to Eq. (4), we conclude that knowing $\tilde{\delta}$ to order $1/T_K$ and $\tilde{\mathcal{T}}^{\text{in}}$ to order $1/T_K^2$ suffices to fully determine the Fermi-liquid coefficients c_B , c_T , and c_ε .

Now, a systematic calculation of $\tilde{\delta}$ and $\tilde{\mathcal{T}}^{\text{in}}$ requires a detailed theory for the strong-coupling fixed point, which became available only with the work of AL in the early 1990s. Nevertheless, Nozières succeeded in treating the case $N = 1$ already in 1974 [13], using a phenomenological expansion of $\tilde{\delta}_{m\sigma}(\varepsilon)$ in powers of $(\varepsilon - \varepsilon_\sigma^Z)/T_K$ [ε_σ^Z represents the Zeeman energy of quasiparticles in a magnetic field; see Eq. (14) below] and $\delta\tilde{n}_{m'\sigma'} = n_{m'\sigma'} - n_{m'\sigma'}^0$, the deviation of the total quasiparticle number $n_{m'\sigma'}$ from its ground-state value. The prefactors in this expansion have the status of phenomenological Fermi-liquid parameters. Using various ingenious heuristic arguments, he was able to show that all these parameters, and also $\tilde{\mathcal{T}}^{\text{in}}$, are related to each other and can be expressed in terms of a single energy scale, namely the Kondo temperature. Moreover, by choosing the prefactor of ε in this expansion to be $1/T_K$, he suggested a definition of the Kondo temperature that also fixes its numerical prefactor. (Our paper adopts this definition, too.) In 1980, NB generalized this strategy [15] to general N , finding an expansion of

the form

$$\tilde{\delta}_{m\sigma}(\varepsilon) = \alpha(\varepsilon - \varepsilon_\sigma^Z) - 3\psi\delta\tilde{n}_{m,-\sigma} + \psi \sum_{m' \neq m} (\delta\tilde{n}_{m'\sigma} - \delta\tilde{n}_{m',-\sigma}), \quad (11)$$

where α and ψ are phenomenological Fermi-liquid parameters related by $\alpha = 3\psi v = 1/T_K$. [NB's initial version of Eq. (11), their Eq. (34), does not contain the Zeeman contribution ε_σ^Z , but the latter is implicit in their subsequent treatment of the Zeeman field before their Eq. (37).]

In the following subsections, we show how NB's expansion for $\tilde{\delta}$ can be derived systematically. AL [26] and PG [29] have shown how to do this for $N = 1$; we will generalize their discussion to arbitrary N .

B. Leading irrelevant operator

AL showed [26] that NB's heuristic results can be derived in a systematic fashion by doing perturbation theory in the leading irrelevant operator of the model's zero-temperature fixed point. As perturbation, they took the operator with the lowest scaling dimension satisfying the requirements of being (i) local, (ii) independent of the impurity spin operator \vec{S} , since the latter is fully screened, (iii) SU(2)-spin invariant, (iv) and independent of the local charge density, just as the Kondo interaction. The operator satisfying these criteria has the form [25]

$$H_\lambda = -\lambda : \vec{J}(0) \cdot \vec{J}(0) : , \quad (12)$$

where $\vec{J}(0)$ is the quasiparticle spin density at the impurity site, and $: \dots :$ denotes the point-splitting regularization procedure (see Appendix). In Appendix D of Ref. [26], AL showed in great detail how NB's phase shifts can be computed using Eq. (12), for the single-channel case of $N = 1$. They did not devote as much attention to the case of general N , though the needed generalizations are clearly implied in their work. We here present the corresponding calculation in some detail, following the notational conventions of PG, which differ from those of AL in some regards (see Appendix). The main difference is that PG formulate the perturbation expansion in a new basis of quasiparticle states, in which the phase shift $\delta_{m\sigma}^0$ has already been accounted for, which somewhat simplifies the discussion. (We remark that PG chose $\delta_{m\sigma}^0 = \sigma\pi/2$ rather than $\pi/2$ as used by NB and us, but the extra σ has no consequences for the ensuing arguments.)

The quasiparticle Hamiltonian describing the vicinity of the strong-coupling fixed point (fp) has the form

$$H_{\text{fp}} = H_{\text{fp},0} + H_\lambda, \quad (13)$$

where

$$H_{\text{fp},0} = \sum_{m\sigma k} (\xi_k + \varepsilon_\sigma^Z) : \psi_{km\sigma}^\dagger \psi_{km\sigma} : , \quad \varepsilon_\sigma^Z = -\frac{\sigma B}{2} \quad (14)$$

describes free quasiparticles in a magnetic field B , with Zeeman energy ε_σ^Z . Note that although the Zeeman term in the bare Hamiltonian (1) is local, it is global in Eq. (14), because the effective quasiparticle Hamiltonian H_{fp} contains no local spin. Using standard point-splitting techniques, which we review in pedagogical detail in the Appendix, the leading

6.4 Equilibrium Fermi Liquid coefficients for fully screened Kondo models 161

M. HANL, A. WEICHELBAUM, J. VON DELFT, AND M. KISELEV

PHYSICAL REVIEW B **89**, 195131 (2014)

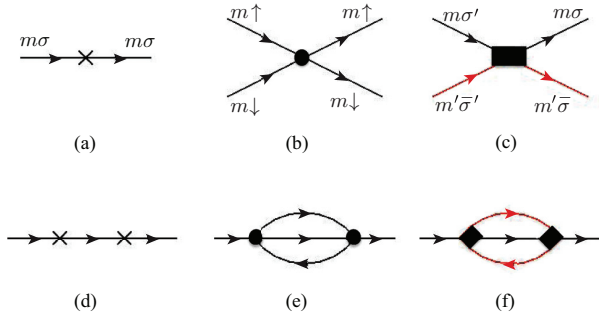


FIG. 1. (Color online) (a)–(c) Vertices associated with H_1 , H_2 , and H_3 , respectively. (d)–(f) Nonzero second-order contributions to the quasiparticle self-energy, $\tilde{\Sigma}_{m\sigma}^R$, involving H_1^2 , H_2^2 , and H_3^2 , respectively. The contributions involving $H_1 H_2$, $H_1 H_3$, and $H_2 H_3$ all vanish, the former two due to the odd power of energy in the two-leg vertex.

irrelevant operator (12) can be written as $H_\lambda = H_1 + H_2 + H_3$, with

$$H_1 = -\frac{1}{2\pi v T_K} \sum_{m\sigma k k'} (\xi_k + \xi_{k'}) : \psi_{km\sigma}^\dagger \psi_{k'm\sigma} : , \quad (15a)$$

$$H_2 = \frac{1}{\pi v^2 T_K} \sum_m : \rho_{m\uparrow} \rho_{m\downarrow} : , \quad (15b)$$

$$H_3 = -\frac{2}{3\pi v^2 T_K} \sum_{m \neq m'} : \vec{j}_m \cdot \vec{j}_{m'} : , \quad (15c)$$

where

$$\rho_{m\sigma} = \sum_{kk'} \psi_{km\sigma}^\dagger \psi_{k'm\sigma} , \quad (16a)$$

$$\vec{j}_m = \frac{1}{2} \sum_{kk'\sigma\sigma'} \psi_{km\sigma}^\dagger \vec{v}_{\sigma\sigma'} \psi_{k'm\sigma'} . \quad (16b)$$

Here we have expressed the coupling constant λ in terms of the inverse Kondo temperature using [cf. Eq. (A11)]

$$\lambda = \frac{8\pi(\hbar v_F)^2}{3T_K} , \quad (17)$$

with the numerical proportionality factor chosen such that T_K agrees with the definition of the Kondo temperature used by NB and PG, as discussed below. Importantly, the point-splitting procedure fixes the relative prefactors arising in H_1 , H_2 , and H_3 (whereas NB's approach requires heuristic arguments to fix them). Our notation for H_1 and H_2 coincides with that used by PG. H_3 contains all new contributions that enter additionally for $N > 1$. Figure 1 gives a diagrammatic depiction of all three terms.

C. First-order terms

Our first goal is to recover NB's expansion of the phase shift $\tilde{\delta}$ to leading order in $\varepsilon - \varepsilon_\sigma^Z$ and $\delta\bar{n}$. Following PG, this can be done by calculating $\tilde{\delta}$ perturbatively to first order in $1/T_K$, in the new basis of quasiparticle states that already incorporate the phase shift δ^0 . To order $1/T_K$, no inelastic scattering occurs,

and $\tilde{\delta}$ is related to the elastic T matrix by

$$e^{2i\tilde{\delta}_{m\sigma}(\varepsilon)} = 1 - 2\pi v i \tilde{T}_{m\sigma}^{\text{el}}(\varepsilon) . \quad (18)$$

The elastic T matrix, in turn, equals the real part of the quasiparticle self-energy, $\tilde{T}_{m\sigma}^{\text{el}}(\varepsilon) = \text{Re} \tilde{\Sigma}_{m\sigma}^R(\varepsilon)$. (Actually, to order $1/T_K$, the self-energy is purely real.) By expanding Eq. (18) for small $\tilde{\delta}$, the phase shift is thus seen to be given by the real part of the self-energy:

$$\tilde{\delta}_{m\sigma}(\varepsilon) \simeq -\pi v \text{Re} \tilde{\Sigma}_{m\sigma}^R(\varepsilon) . \quad (19)$$

Now, as pointed out already by Nozières in 1974 [13], a first-order perturbation calculation of the self-energy is equivalent to treating interaction terms in the mean-field (MF) approximation. They then take the form

$$H_2^{\text{MF}} = \frac{1}{\pi v^2 T_K} \sum_{m\sigma} : \rho_{m\sigma} : \delta\bar{n}_{m,-\sigma} , \quad (20a)$$

$$H_3^{\text{MF}} = -\frac{1}{3\pi v^2 T_K} \sum_{\sigma} \sum_{m \neq m'} : \rho_{m\sigma} : (\delta\bar{n}_{m'\sigma} - \delta\bar{n}_{m',-\sigma}) , \quad (20b)$$

where $\delta\bar{n}_{m\sigma} = (: \rho_{m\sigma} :)$, the quasiparticle number relative to the $B = 0$ ground state, is given by

$$\delta\bar{n}_{m\sigma} = -v \varepsilon_\sigma^Z = \sigma v B/2 . \quad (21)$$

The mean-field version of the leading irrelevant operator thus has the form

$$H_\lambda^{\text{MF}} = \sum_{m\sigma k k'} h_{m\sigma}(\xi_k, \xi_{k'}) : \psi_{km\sigma}^\dagger \psi_{k'm\sigma} : , \quad (22)$$

$$h_{m\sigma}(\xi_k, \xi_{k'}) = \frac{1}{\pi v T_K} \left[-\frac{1}{2}(\xi_k + \xi_{k'}) + \frac{\delta\bar{n}_{m,-\sigma}}{v} - \sum_{m' \neq m} \frac{\delta\bar{n}_{m'\sigma} - \delta\bar{n}_{m',-\sigma}}{3v} \right] . \quad (23)$$

For such a single-particle perturbation, the self-energy can be directly read off from $h_{m\sigma}$ using

$$\tilde{\Sigma}_{m\sigma}^R(\varepsilon) = h_{m\sigma}(\varepsilon - \varepsilon_\sigma^Z, \varepsilon - \varepsilon_\sigma^Z) , \quad (24)$$

because k sums of the type $\sum_k 1/(\varepsilon - \xi_k - \varepsilon_\sigma^Z + i0^+)$ yield residues involving $\xi_k = \varepsilon - \varepsilon_\sigma^Z$. Using Eq. (24) in Eq. (19) for the phase shift, we find

$$\tilde{\delta}_{m\sigma}(\varepsilon) = \frac{1}{T_K} \left[\varepsilon - \varepsilon_\sigma^Z - \frac{\delta\bar{n}_{m,-\sigma}}{v} + \sum_{m' \neq m} \frac{\delta\bar{n}_{m'\sigma} - \delta\bar{n}_{m',-\sigma}}{3v} \right] . \quad (25)$$

This fully agrees with the expansion (11) of NB if we make the identification $1/T_K = \alpha = 3\psi v$, thus confirming the validity of NB's heuristic arguments. Note that the coefficient of $\varepsilon - \varepsilon_\sigma^Z$ in Eq. (25) comes out as $1/T_K$, in agreement with the conventions of NB and PG, as intended by our choice of numerical prefactor in Eq. (17).

As consistency check, let us review how NB used Eq. (25) to calculate the Wilson ratio. First, Eq. (25) implies an impurity-induced change in the density of states per spin and channel of $v_{m\sigma}^{\text{imp}}(\varepsilon) = \frac{1}{\pi} \partial_\varepsilon \tilde{\delta}_{m\sigma}(\varepsilon)$. This yields a corresponding impurity-induced change in the specific heat, C^{imp} . At zero field (where

EQUILIBRIUM FERMI-LIQUID COEFFICIENTS FOR THE ...

PHYSICAL REVIEW B **89**, 195131 (2014)

ε_σ^Z and $\delta\bar{n}_{m\sigma}$ vanish), the change relative to the bulk is given by

$$\frac{C^{\text{imp}}}{C} = \frac{2N\nu_{m\sigma}^{\text{imp}}(0)}{2N\nu} = \frac{1}{\pi\nu T_K}. \quad (26)$$

Second, the Friedel sum rule for the impurity-induced change in local charge in channel m for spin σ at $T = 0$ gives

$$N_{m\sigma}^{\text{imp}} = \frac{1}{\pi} \delta_{m\sigma}(0) = \frac{1}{2} + \frac{1}{\pi} \tilde{\delta}_{m\sigma}(0), \quad (27)$$

and Eq. (25), together with Eq. (21) for $\delta\bar{n}_{m\sigma}$, leads to

$$\tilde{\delta}_{m\sigma}(0) = \frac{\sigma B}{T_K} \left[\frac{1}{2} + \frac{1}{2} + \frac{N-1}{3} \right] = \frac{\sigma B(N+2)}{3T_K}. \quad (28)$$

The linear response of the impurity-induced magnetization, $M^{\text{imp}} = \frac{1}{2} \sum_m (N_{m\uparrow}^{\text{imp}} - N_{m\downarrow}^{\text{imp}})$, then gives the impurity contribution to the spin susceptibility as

$$\chi^{\text{imp}} = \frac{M^{\text{imp}}}{B} = \frac{N(N+2)}{3\pi T_K} = \frac{4S(S+1)}{3\pi T_K}. \quad (29)$$

(For all expressions involving χ^{imp} here and below, the limit $B \rightarrow 0$ is implied.) The corresponding bulk contribution is $\chi = \nu N/2$. Thus, the Wilson ratio is found to be

$$R = \frac{\chi^{\text{imp}}/\chi}{C^{\text{imp}}/C} = \frac{2(N+2)}{3} = \frac{4(S+1)}{3}, \quad (30)$$

in agreement with more elaborate calculations by Yoshimori [21] and by Mihály and Zawadowski [22].

Note that Eq. (29) relates Nozières' definition of the Kondo temperature to an observable quantity, χ^{imp} , that can be calculated numerically. We used this as a precise way of defining T_K in our numerical work. (Subtleties involved in calculating χ^{imp} are discussed in Sec. IV B.) Note that up to a prefactor, Eq. (29) for χ^{imp} has the form $\chi^{\text{free}}(T_K)$, where $\chi^{\text{free}}(T) = S(S+1)/(3T)$ is the static susceptibility of a free spin S at temperature T .

We are now in a position to extract our first Fermi-liquid coefficient, c_B . For this, it suffices to know the spectral function A in Eq. (4) to quadratic order in B , at $\varepsilon = T = 0$, where $\tilde{\mathcal{T}}^{\text{in}} = 0$. Inserting the corresponding expression (28) for $\tilde{\delta}_{m\sigma}(0)$ into Eq. (10) for $\text{Im}\mathcal{T}$, we find

$$A_{m\sigma}(0,0,B) = \frac{1}{\nu\pi^2} \left[1 - \frac{(N+2)^2 B^2}{9 T_K^2} \right]. \quad (31)$$

Comparing this to Eq. (4), we read off $c_B = (N+2)^2/9$.

Note that if the definition (29) of T_K in terms of χ^{imp} is taken as given, c_B can actually be derived on the back of an envelope: for a fully screened Kondo model, the impurity-induced spin susceptibility gets equal contributions from all N channels, $\chi^{\text{imp}} = N\chi_m^{\text{imp}}$, and the Friedel sum rule relates the contribution from each channel to phase shifts, $\chi_m^{\text{imp}} = M_m^{\text{imp}}/B = [\tilde{\delta}_{m\uparrow}(0) - \tilde{\delta}_{m\downarrow}(0)]/(2\pi B)$, implying $\tilde{\delta}_{m\sigma}(0) = \sigma(\pi\chi^{\text{imp}}/N)B$. Using this in Eq. (10) yields

$$A_{m\sigma}(0,0,B) = \frac{1}{\nu\pi^2} [1 - (\pi\chi^{\text{imp}}/N)^2 B^2], \quad (32)$$

which is equivalent to Eq. (31) if Eq. (29) holds.

D. Second-order terms

We next discuss inelastic scattering for $B = 0$, but at finite temperature. To order $1/T_K^2$, inelastic scattering is described by the imaginary part of the quasiparticle self-energy arising from the second-order contributions of H_1 , H_2 , and H_3 , shown in diagrams (d)–(f) of Fig. 1, respectively. These diagrams give

$$\text{Im}\tilde{\Sigma}_{m\sigma}^{R,1}(\varepsilon) = -\frac{\varepsilon^2}{\pi\nu T_K^2}, \quad (33a)$$

$$\text{Im}\tilde{\Sigma}_{m\sigma}^{R,2}(\varepsilon) = -\frac{\varepsilon^2 + \pi^2 T^2}{2\pi\nu T_K^2}, \quad (33b)$$

$$\text{Im}\tilde{\Sigma}_{m\sigma}^{R,3}(\varepsilon) = \frac{2}{3}(N-1)\text{Im}\tilde{\Sigma}_{m\sigma}^{R,2}(\varepsilon). \quad (33c)$$

The first two can also be found in the discussion of PG, whose strategy we follow here. (They also appear, in slightly different guise, in the discussion of AL [26].) The third is proportional to the second, and the factor $2/3$ originates from $(2/3)^2 2s(s+1)$ with $s = 1/2$, since the relative prefactor between H_3 and H_2 brings in two powers of $2/3$, and the algebra of Pauli matrices yields a factor $2s(s+1)$.

Now, the term called $\tilde{\mathcal{T}}^{\text{in}}$ in Eq. (9) by definition describes the contribution of the *two-body* terms H_2 and H_3 to inelastic scattering:

$$\text{Im}\tilde{\mathcal{T}}_{m\sigma}^{\text{in}}(\varepsilon) = \text{Im}[\tilde{\Sigma}_{m\sigma}^{R,2}(\varepsilon) + \tilde{\Sigma}_{m\sigma}^{R,3}(\varepsilon)]. \quad (34)$$

The contribution $\text{Im}\tilde{\Sigma}^{R,1}$ from H_1 is *not* included in $\text{Im}\tilde{\mathcal{T}}^{\text{in}}$ here, since it actually equals $-\delta^2/\pi\nu$, and hence is already contained in the factor $e^{2i\delta}$ in Eq. (9). Indeed, in Eq. (10) for the imaginary part of the T matrix in the original basis, the δ^2 term equals $-\pi\nu\text{Im}\tilde{\Sigma}^{R,1}$. Collecting all ingredients, Eq. (10) gives

$$\begin{aligned} A_{m\sigma}(\varepsilon, T, 0) &= \frac{1}{\nu\pi^2} \left[1 - \frac{\varepsilon^2}{T_K^2} - \frac{\varepsilon^2 + \pi^2 T^2}{2T_K^2} \left(1 + \frac{2}{3}(N-1) \right) \right] \\ &= \frac{1}{\nu\pi^2} \left[1 - \frac{(2N+7)\varepsilon^2 + (2N+1)\pi^2 T^2}{6T_K^2} \right]. \end{aligned} \quad (35)$$

For $N = 1$, the second term reduces to the familiar form $-(3\varepsilon^2 + \pi^2 T^2)/(2T_K^2)$ found by AL [26] and GP [29]. Comparing Eqs. (35) and (4) and (5) we read off $c_\varepsilon = (2N+7)/6$ and $c'_T = \pi^2(2N+1)/6$, implying $c_T = \pi^2(4N+5)/9$.

IV. NRG RESULTS

In this section, we describe our NRG work. We had set ourselves the goal of achieving an accuracy of better than 5% for the Fermi-liquid coefficients. To achieve this, two ingredients were essential: first, exploiting non-Abelian symmetries; and second, defining the Kondo temperature with due care. The latter is a matter of some subtlety [34] because the wide-band limit assumed in analytical work does not apply in numerical calculations.

We begin below by giving the Lehmann representation for the desired spectral function. We then discuss the non-Abelian symmetries used in our NRG calculations and explain how the Kondo temperature was extracted numerically. Finally, we present our numerical results.

6.4 Equilibrium Fermi Liquid coefficients for fully screened Kondo models 163

M. HANL, A. WEICHELBAUM, J. VON DELFT, AND M. KISELEV

PHYSICAL REVIEW B **89**, 195131 (2014)

A. NRG details

To numerically calculate the \mathcal{T} matrix of Eq. (3), we use equations of motion [37,38] to express it as

$$\mathcal{T}_{m\sigma}(\varepsilon) = J_K \langle S_z \rangle + \langle \langle O_{m\sigma}; O_{m\sigma}^\dagger \rangle \rangle, \quad (36a)$$

$$O_{m\sigma} \equiv [\Psi_{m\sigma}(0), H_{\text{loc}}] = J_K \sum_{\sigma'} \vec{S} \cdot \frac{\vec{\tau}_{\sigma\sigma'}}{2} \Psi_{m\sigma'}(0). \quad (36b)$$

Here $\langle \langle \cdot; \cdot \rangle \rangle$ denotes a retarded correlation function, and $\Psi_{m\sigma}(0) = \frac{1}{\sqrt{N_{\text{disc}}}} \sum_k c_{km\sigma}$, where N_{disc} is the number of discrete levels in the band (and hence proportional to the system size). The spectral function is then calculated in its Lehmann-representation,

$$A_{m\sigma}(\varepsilon, T, B) = \sum_{a,b} \frac{e^{-\beta E_a} + e^{-\beta E_b}}{Z} |(a|O_{m\sigma}|b)|^2 \delta(\varepsilon - E_{ab}), \quad (37)$$

with $E_{ab} = E_b - E_a$, using the full density matrix (FDM) approach of NRG [9,40–42].

For our numerical work, we take the conduction-band energies to lie within the interval $\xi_k \in [-D, D]$, with Fermi energy at 0 and half bandwidth $D = 1$, and take the density of states per spin, channel, and unit length to be constant, as $1/2D$. (It is related to the extensive density of states used in Sec. III by $\nu = N_{\text{disc}}/2D$.) For the calculations used to determine the Fermi-liquid parameters, we use exchange coupling $\nu J_K = 0.1$, so that the Kondo temperature $T_K/D \propto \exp[-1/(\nu J_K)]$ has the same order of magnitude for $N = 1, 2$, and 3, namely $\lesssim 10^{-4}$. Following standard NRG protocol [7,8,10], the conduction band is discretized logarithmically with discretization parameter Λ , mapped onto a Wilson chain, and diagonalized iteratively. NRG truncation at each iteration step is controlled by either specifying the number of kept states per shell, N_K , or the truncation energy E_{tr} (in rescaled units, as defined in Ref. [43]), corresponding to the highest kept energy per shell. Spectral data are averaged over N_z different, interleaving logarithmic discretization meshes [44]. The values for NRG-specific parameters used here are given in legends in the figures below.

For the fully screened N -channel Kondo model, the dimension of the local Hilbert space of each supersite of the Wilson chain is 4^N . Since this increases exponentially with the number of channels, it is essential, specifically so for $N = 3$, to reduce computational costs by exploiting non-Abelian symmetries [11] to combine degenerate states into multiplets. Several large symmetries are available [19]: For $B = 0$, the model has $\text{SU}(2) \times \text{U}(1) \times \text{SU}(N)$ spin-charge-channel symmetry. If the bands described by H_0 are particle-hole symmetric, as assumed here, the model also has a $\text{SU}(2) \times [\text{SU}(2)]^N$ spin(charge) N symmetry, involving $\text{SU}(2)$ mixing of particles and holes in each of the N channels. The $\text{U}(1) \times \text{SU}(N)$ and $[\text{SU}(2)]^N$ symmetries are not mutually compatible (their generators do not all commute), however, implying that both are subgroups of a larger symmetry group, the symplectic $\text{Sp}(2N)$. Thus the full symmetry of the model for $B = 0$ is $\text{SU}(2) \times \text{Sp}(2N)$. For $B \neq 0$ it is $\text{U}(1) \times \text{Sp}(2N)$, since a finite magnetic field breaks the $\text{SU}(2)$ spin symmetry to the Abelian $\text{U}(1)$ S_z symmetry. When the model's *full* symmetry is exploited, the multiplet

spaces encountered in NRG calculations exhibit *no* more degeneracies in energy at all.

Using only Abelian symmetries turned out to be clearly insufficient to obtain well converged numerical data for $N = 3$, despite having a relatively large Λ . This, however, is required for accurate Fermi-liquid coefficients with errors below a few percent. For numerically converged data, therefore, it was essential to use non-Abelian symmetries. For our $B = 0$ calculations, it turned out to be sufficient to use $\text{SU}(2) \times \text{U}(1) \times \text{SU}(N)$ symmetry for calculating c_T , but the full $\text{SU}(2) \times \text{Sp}(2N)$ symmetry was needed for calculating c_ε . Likewise, for our $B \neq 0$ calculations of c_B , we needed to use the full $\text{U}(1) \times \text{Sp}(2N)$ symmetry. Doing so led to an enormous reduction in memory requirements, the more so the larger the rank of the symmetry group [$\text{Sp}(2N)$ has rank N , and $\text{SU}(N)$ has rank $N - 1$]. For $N = 3$, for example, we kept $\lesssim 13\,500$ multiplets for $\text{SU}(2) \times \text{U}(1) \times \text{SU}(3)$ or $\lesssim 3\,357$ multiplets for $\text{SU}(2) \times \text{Sp}(6)$ during NRG truncation, which, in effect, amounts to keeping $\lesssim 980\,000$ individual states [11].

B. Definition of T_K

The Fermi-liquid theory of Sec. III implicitly assumes that the model is considered in the so-called scaling limit, in which the ratio of Kondo temperature to bandwidth vanishes, $T_K/D \rightarrow 0$. In this limit, physical quantities such as $\rho(T, B)/\rho(0, 0)$ are universal scaling functions, which depend on their arguments only in the combinations B/T_K and T/T_K . Since the shape of such a scaling function, say $\rho(0, B)/\rho(0, 0)$ plotted versus B/T_K , is universal, i.e., independent of the bare parameters (coupling J_K and bandwidth D) used to calculate it, curves generated by different combinations of bare parameters can all be made to collapse onto each other by suitably adjusting the parameter T_K for each. In the same sense the Fermi-liquid parameters c_B , c_T , and c_ε , being Taylor coefficients of universal curves, are universal, too.

One common way to achieve a scaling collapse, popular particularly in experimental studies, is to identify the Kondo temperature with the field $B_{1/2}$ or temperature $T_{1/2}$ at which the impurity contribution to the resistivity has decreased to half its unitary value,

$$\rho(0, B_{1/2}) = \rho(0, 0)/2, \quad \rho(T_{1/2}, 0) = \rho(0, 0)/2. \quad (38)$$

However, this approach is not suitable for the purpose of extracting Fermi-liquid coefficients, for which T_K has to be defined in terms of (analytically accessible) low-energy properties characteristic of the strong-coupling fixed point. In Sec. III we have therefore adopted Nozières' definition of T_K in terms of the leading energy dependence of the phase shift $\delta_{m\sigma}^0$ [Eq. (25)], implying that it can be expressed in terms of χ^{imp} , of the local static spin susceptibility at zero temperature [Eq. (29)]. In the scaling limit, this definition of T_K matches $B_{1/2}$ or $T_{1/2}$ up to prefactors, i.e., $B_{1/2}/T_K$ and $T_{1/2}/T_K$ are universal, N -dependent numerical constants, independent of the model's bare parameters.

In numerical work, however, the scaling limit is never fully realized, since the bandwidth is always finite. It may thus happen that a scaling collapse expected analytically is not found when the corresponding curves are calculated numerically. For example, if the Kondo temperature is defined,

EQUILIBRIUM FERMI-LIQUID COEFFICIENTS FOR THE ...

PHYSICAL REVIEW B **89**, 195131 (2014)

as seems natural, in terms of a purely local susceptibility, χ^{loc} , involving only the response of the local spin to a local field,

$$\frac{4S(S+1)}{3\pi T_K^{\text{loc}}} \equiv \chi^{\text{loc}} \equiv \frac{d}{dB} \langle S_z \rangle |_{B=0}, \quad (39)$$

then curves expected to show a scaling collapse actually do not collapse onto each other, as pointed out recently in Ref. [34] [see Figs. 2(d)–2(f) there]. That paper also showed how to remedy this problem: the static spin susceptibility used to calculate T_K has to be defined more carefully, and two slightly different definitions have to be used, depending on the context. The first option is needed when studying zero-temperature (i.e., ground state) properties as a function of some external parameter, such as the field dependence of the resistivity (needed for c_B). In this case, a corresponding susceptibility defined in terms of the response of the system's *total* spin to a local field should be used:

$$\frac{4S(S+1)}{3\pi T_K^{\text{FS}}} \equiv \chi^{\text{FS}} \equiv \frac{d}{dB} \langle S_z^{\text{tot}} \rangle |_{B=0}. \quad (40)$$

The superscript FS stands for ‘‘Friedel sum rule,’’ to highlight the fact that using this rule to calculate the linear response of $\langle S_z^{\text{tot}} \rangle$ to a local field directly leads to relation (29) between χ^{imp} and T_K . The second option is needed when studying dynamical or thermal quantities that depend on the system's many-body excitations for given fixed external parameters (e.g., fixed $B = 0$), such as the temperature dependence of the resistivity (needed for c_T), or the curvature of the Kondo resonance (needed for c_ε). In this case, one should use

$$\frac{4S(S+1)}{3\pi T_K^{\text{sc}}} \equiv \chi^{\text{sc}} \equiv 2\chi^{\text{FS}} - \chi^{\text{loc}}. \quad (41)$$

The superscript sc stands for ‘‘scaling,’’ to indicate that this definition of the Kondo temperature ensures [34] a scaling collapse of dynamical or thermal properties. Figure 2 demonstrates that a scaling collapse is indeed found when the field- or temperature-dependent resistivity, plotted versus B/T_K^{FS} or T/T_K^{sc} , respectively, is calculated for two different values of J_K (solid and dashed lines, respectively). Note that this works equally well for $N = 1, 2$, and 3. (For $N = 1$, such scaling collapses had already been shown in Ref. [34].)

We remark that the three Kondo temperatures defined in Eqs. (39)–(41) differ quite significantly from each other for the Kondo Hamiltonian of Eq. (1), with differences as large as 12%, 31%, and 55% for $N = 1, 2$, and 3, respectively, for the parameters used in Fig. 2. This indicates that although we have chosen bare parameters for which T_K/D is smaller than 10^{-4} , we have still not reached the scaling limit [in which the definitions Eqs. (39)–(41) of the Kondo temperature should all coincide numerically [34]]. We have checked that the differences between T_K^{loc} , T_K^{FS} , and T_K^{sc} decrease when νJ_K is reduced in an attempt to get closer to the scaling limit, but estimate that truly reaching that limit would require $\nu J_K < 0.01$ for the Kondo model, implying $T_K/D < 10^{-45}$. Thus, reaching the scaling limit by brute force is numerically unfeasible. Therefore, using T_K^{FS} and T_K^{sc} rather than T_K^{loc} is absolutely essential for obtaining scaling collapses. It is similarly essential for an accurate determination of the Fermi-liquid parameters. Correspondingly, for the results discussed below, we have used T_K^{FS} as definition of the Kondo

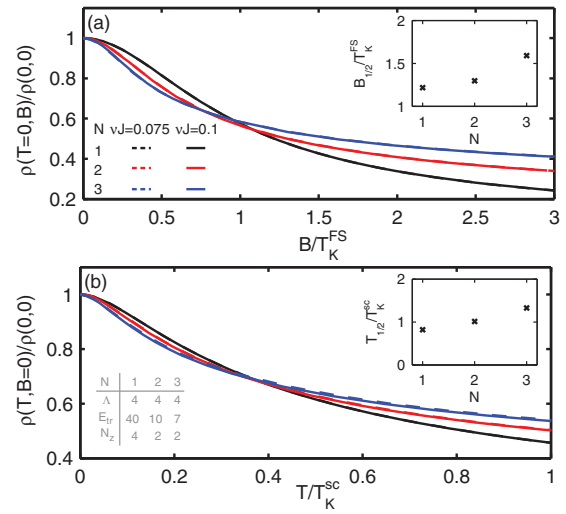


FIG. 2. (Color online) Scaling collapse of (a) the resistivity at zero temperature as a function of field, and (b) at zero field as a function of temperature, calculated for two different values of the bare coupling, νJ_K (dashed or solid), and for $N = 1, 2$, and 3. For each N , the dashed and solid curves overlap so well that they are almost indistinguishable. The insets compare the energy scales $B_{1/2}$ and $T_{1/2}$ at which the resistivity has decreased to half its unitary value [cf. Eq. (38)], to the scales T_K^{FS} and T_K^{sc} [cf. Eqs. (40) and (41)], respectively. The shown ratios are universal numbers of order unity, but not necessarily very close to 1, with a significant dependence on N : $B_{1/2}/T_K^{\text{FS}} = 1.22, 1.31, 1.60$ and $T_{1/2}/T_K^{\text{sc}} = 0.82, 1.02, 1.36$ for $N = 1, 2$, and 3, respectively. The legend in the lower left of panel (b) specifies the NRG parameters used for both panels.

temperature when extracting c_B , and T_K^{sc} when extracting c_T and c_ε .

C. Using unbroadened discrete data only

When one is interested in spectral properties, one typically has to broaden the discrete data. For the determination of the Fermi-liquid coefficients, however, where high numerical accuracy is required, it is desirable to avoid standard broadening. For the calculation of c_T and c_B this can be achieved [9] by directly inserting the Lehmann sum over δ functions for the spectral function $A_{m\sigma}(\varepsilon, T, B)$ [Eq. (37)] into the energy integral for $\rho(T, B)$ [Eq. (2)], resulting in a sum over discrete data points that produces a smooth curve. The curve is smooth because Eq. (2) in effect thermally broadens the δ peaks in the Lehmann representation. This is true even in the limit $T \rightarrow 0$, because in NRG calculations it is realized by taking T nonzero, but much smaller than all other energy scales.

For the determination of c_ε , in contrast, one faces the problem that $A_{m\sigma}(\varepsilon, 0, 0)$ is represented not as an integral of a sum over discrete δ functions, but directly in terms of the latter. To avoid having to broaden these by hand, it is desirable to find a way to extract c_ε from an expression involving an integral over the discrete spectral data, as for c_B and c_T . This can be achieved as follows. First, note that c_ε is, by definition, a coefficient in the general Taylor expansion of the normalized spectral function $A^{\text{norm}}(\varepsilon) \equiv A_{m\sigma}(\varepsilon, 0, 0)/A_{m\sigma}(0, 0, 0)$ for small

6.4 Equilibrium Fermi Liquid coefficients for fully screened Kondo models 165

M. HANL, A. WEICHELBAUM, J. VON DELFT, AND M. KISELEV

PHYSICAL REVIEW B **89**, 195131 (2014)

frequencies,

$$A^{\text{norm}}(\varepsilon) = \sum_{n=0}^{\infty} a_n (\varepsilon/T_K)^n, \quad c_\varepsilon = a_2. \quad (42)$$

Due to particle-hole symmetry, $a_n = 0$ for all n odd, and by definition $a_0 = 1$. To determine a_2 from an integral over discrete data, we consider a weighted average of $A^{\text{norm}}(\varepsilon)$ over ε ,

$$\bar{A}(\tau) \equiv \int d\varepsilon A^{\text{norm}}(\varepsilon) P_\tau(\varepsilon), \quad (43)$$

where $P_\tau(\varepsilon)$ is a symmetric weighting function of width τ and weight 1, and moments defined by

$$\int d\varepsilon (\varepsilon/\tau)^n P_\tau(\varepsilon) \equiv p_n \quad (44)$$

for integer $n \geq 0$ (with $p_0 = 1$). Here we use

$$P_\tau(\varepsilon) = \frac{1}{4\tau} \frac{1}{\cosh^2(\varepsilon/2\tau)} = -\frac{\partial f(\varepsilon, \tau)}{\partial \varepsilon}, \quad (45)$$

but other choices are possible, too (e.g., a Gaussian peak). Clearly, the leading τ dependence of $\bar{A}(\tau)$ for small τ reflects the leading ε dependence of $A^{\text{norm}}(\varepsilon)$ and allows for an accurate determination of a_2 . Indeed, using Eqs. (42)–(45), we obtain a power-series expansion for $\bar{A}(\tau)$ of the form $\bar{A}(\tau) = \sum_n a_n p_n (\tau/T_K)^n$. Thus, by fitting $\bar{A}^{\text{fit}}(\tau) = \sum_n f_n \tau^n$ to the NRG data for $\bar{A}(\tau)$, one can determine the desired coefficients in (42) using $a_n = T_K^n f_n / p_n$. In particular, the Fermi-liquid coefficient of present interest is given by $c_\varepsilon = a_2 = T_K^2 f_2 / p_2$.

D. Extraction of Fermi-liquid coefficients

Figures 3(a)–3(c) show our NRG data (heavy solid lines) for the resistivity plotted versus B/T_K^{FS} at zero temperature or plotted versus T/T_K^{sc} at zero field, and for the weighted spectral function plotted versus τ/T_K^{sc} , respectively. We determined the Fermi-liquid coefficients c_B , c_T , and c_ε from the quadratic terms of fourth-order polynomial fits to these curves. Including

TABLE I. Numerically extracted values of c_B , c_T , and c_ε , given here relative to the corresponding predictions from FLT of Eq. (7). The deviations between NRG and FLT values are $\leq 5\%$ in all cases. To numerically determine these coefficients, we used the quadratic coefficient of a fourth-order polynomial fit to the corresponding NRG data. Error bars were estimated by comparing the quartic fits to polynomial fits of different higher orders.

N	$c_B^{\text{NRG}}/c_B^{\text{FLT}}$	$c_T^{\text{NRG}}/c_T^{\text{FLT}}$	$c_\varepsilon^{\text{NRG}}/c_\varepsilon^{\text{FLT}}$
1	1.00 ± 0.01	1.00 ± 0.01	1.01 ± 0.03
2	1.02 ± 0.03	0.98 ± 0.03	0.99 ± 0.03
3	1.05 ± 0.05	1.01 ± 0.03	1.02 ± 0.07

the fourth-order term allows the fitting range to be extended towards somewhat larger values of the argument, thus increasing the accuracy of the fit. For each solid curve, the quadratic term from the fit is shown by heavy dashed lines; these are found to agree well with the corresponding predictions from FLT, shown by light lines of matching colors. The level of agreement is quite remarkable, given the rather limited range in which the behavior is purely quadratic: with increasing argument, quartic contributions become increasingly important, as reflected by the growing deviations between dashed and solid lines; and at very small values of the argument ($\lesssim 0.02$), the NRG data become unreliable due to known NRG artefacts.

Numerical values for the extracted Fermi-liquid coefficients are given in Table I; they agree with those predicted analytically to within $\leq 5\%$. This can be considered excellent agreement, especially for the numerically very challenging case of $N = 3$.

V. CONCLUSIONS

Our two main results can be summarized as follows. First, we have presented a compact derivation of three Fermi-liquid coefficients for the fully screened N -channel Kondo model, by generalizing well-established calculations for $N = 1$ to

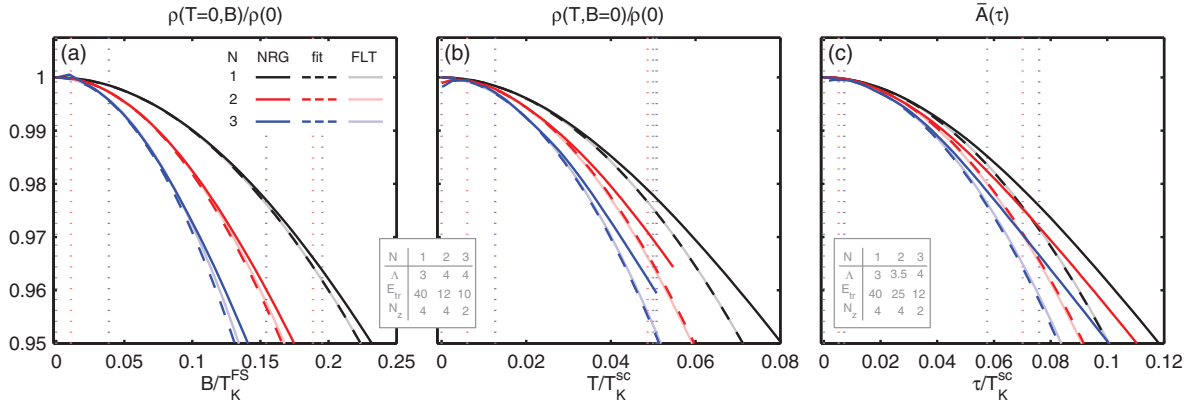


FIG. 3. (Color online) (a) Resistivity as function of magnetic field at $T = 0$, (b) resistivity as function of temperature at $B = 0$, and (c) the weighted spectral function $\bar{A}(\tau)$ [cf. Eq. (43)] at $T = B = 0$, all shown for $N = 1, 2, 3$. Each panel contains NRG data (heavy solid lines), the quadratic term from a fourth-order polynomial fit (heavy dashed lines) and the corresponding predictions from FLT of Eq. (7) for the quadratic term (light solid lines). Left and right vertical dotted lines in matching colors indicate the lower and upper borders of the fitting range used for each N . The boxed legends specify the NRG parameters used here.

general N . The corresponding calculations, building on ideas of Nozières, Affleck and Ludwig, and Pustilnik and Glazman, are elementary. We hope that our way of presenting them emphasizes this fact, and perhaps paves the way for similar calculations in less trivial quantum impurity problems that also show Fermi-liquid behavior, such as the asymmetric single-impurity Anderson Hamiltonian, or the 0.7 anomaly in quantum point contacts [45].

Second, we have established a benchmark for the quality of NRG results for the fully screened N -channel Kondo model, by showing that it is possible to numerically calculate equilibrium Fermi-liquid coefficients with an accuracy of better than 5% for $N = 1, 2$, and 3. To achieve numerical results of this quality, two technical ingredients were essential, both of which became available only recently: first, exploiting larger-rank non-Abelian symmetries in the numerics [11,12]; and second, carefully defining the Kondo temperature [34] in such a way that numerically calculated universal scaling curves are indeed universal, in the sense of showing a proper scaling collapse, despite the fact that the scaling limit $T_K/D \rightarrow 0$ is typically not achieved in numerical work.

ACKNOWLEDGMENTS

We acknowledge helpful discussions with K. Kikoin, C. Mora, A. Ludwig, and G. Zarànd. We are grateful to D. Schuricht for drawing our attention to Ref. [27], and for sending us a preprint of Ref. [46] prior to its submission. The latter work, which we received in the final stages of this work, also uses H_λ of Eq. (12) as starting point for calculating Fermi-liquid coefficients for the N -channel Kondo model, and its result for c_T is consistent with our own. We gratefully acknowledge financial support from the DFG (WE4819/1-1 for A.W., and SFB-TR12, SFB-631 and the Cluster of Excellence Nanosystems Initiative Munich for J.v.D., M.H., and A.W.)

APPENDIX

This Appendix offers a pedagogical derivation of the Hamiltonian H_λ given in Eq. (15) of the main text using the point-splitting regularization strategy, following AL (Appendix D of [26]). Its main purpose is to show how the relation $\alpha = 3\psi\nu = 1/T_K$ between Fermi-liquid parameters that NB had found by intuitive arguments [15] follows simply and

naturally from point splitting. For a detailed discussion of the point-splitting strategy, see Refs. [47–49].

According to AL, the leading irrelevant operator for the fully screened N -channel Kondo model has the form

$$H_\lambda = -\lambda : \vec{J}(0) \cdot \vec{J}(0) : . \quad (\text{A1})$$

Here $\vec{J}(x) = \sum_{m=1}^N : \vec{J}_m(x) :$ is the total (point-split) spin density from all channels at position x (the impurity or dot sits at $x = 0$), and

$$\vec{J}_m(x) = \frac{1}{2} \sum_{\sigma\sigma'} \Psi_{m\sigma}^\dagger(x) \vec{\tau}_{\sigma\sigma'} \Psi_{m\sigma'}(x) \quad (\text{A2})$$

is the corresponding (non-point-split) spin density for channel m . Here $: \dots :$ denotes point splitting,

$$: A(x)B(x) : \equiv \lim_{\eta \rightarrow 0} [A(x+\eta)B(x) - \underline{A(x+\eta)B(x)}], \quad (\text{A3})$$

a field-theoretic scheme for regularizing products of operators at the same point by subtracting their ground-state expectation value, $\underline{AB} = \langle AB \rangle$. (In most cases, point splitting is equivalent to normal ordering.) For present purposes, we follow AL [26] and take

$$\Psi_{m\sigma}(x) = \frac{1}{\sqrt{L}} \sum_k e^{-ikx} \psi_{km\sigma} \quad (\text{A4})$$

to be free fermion fields with linear dispersion ($\xi_k = k\hbar v_F$) in a box of length $L \rightarrow \infty$ (with $k \in 2\pi n/L$, $n \in \mathbb{Z}$), with normalization $\{\psi_{km\sigma}, \psi_{k'm'\sigma'}^\dagger\} = \delta_{kk'} \delta_{mm'} \delta_{\sigma\sigma'}$ and free ground-state correlators

$$\langle \Psi_{m\sigma}^\dagger(x) \Psi_{m'\sigma'}(0) \rangle = \langle \Psi_{m\sigma}(x) \Psi_{m'\sigma'}^\dagger(0) \rangle = \frac{\delta_{mm'} \delta_{\sigma\sigma'}}{2\pi i x}. \quad (\text{A5})$$

Note that we follow PG in our choice of field normalization, which differs from that used by AL [26] by $\Psi_{\text{here}} = \psi_{\text{AL}}/\sqrt{2\pi}$. Consequently, our coupling constant is related to theirs by $\lambda_{\text{here}} = (2\pi)^2 \lambda_{\text{AL}}$.

In the definition of H_λ , point splitting is needed because the product of two spin densities, $\vec{J}(x+\eta) \cdot \vec{J}(x)$, diverges with decreasing separation η between their arguments. To make this explicit, we use Wick's theorem,

$$: AB :: CD : = : ABCD : + : \underline{ABC} D : + : \underline{AB} CD : + : \underline{ABC} D : ,$$

to rewrite the product of spin densities as follows:

$$\vec{J}(x+\eta) \cdot \vec{J}(x) = \frac{1}{4} \sum_{m\sigma\sigma'} \sum_{m'\bar{\sigma}\bar{\sigma}'} : \Psi_{m\sigma}^\dagger(x+\eta) \vec{\tau}_{\sigma\sigma'} \Psi_{m\sigma'}(x+\eta) : : \Psi_{m'\bar{\sigma}}^\dagger(x) \vec{\tau}_{\bar{\sigma}\bar{\sigma}'} \Psi_{m'\bar{\sigma}'}(x) : \quad (\text{A6a})$$

$$= \frac{1}{4} \sum_{m\sigma\sigma'} \sum_{m'\bar{\sigma}\bar{\sigma}'} \vec{\tau}_{\sigma\sigma'} \cdot \vec{\tau}_{\bar{\sigma}\bar{\sigma}'} \left[: \Psi_{m\sigma}^\dagger(x+\eta) \Psi_{m\sigma'}(x+\eta) \Psi_{m'\bar{\sigma}}^\dagger(x) \Psi_{m'\bar{\sigma}'}(x) : \right. \\ \left. + \frac{\delta_{mm'}}{2\pi i \eta} (\delta_{\sigma'\bar{\sigma}} : \Psi_{m\sigma}^\dagger(x+\eta) \Psi_{m\bar{\sigma}'}(x) : + \delta_{\sigma\bar{\sigma}'} : \Psi_{m\sigma'}(x+\eta) \Psi_{m\bar{\sigma}}^\dagger(x) :) + \frac{\delta_{\sigma\bar{\sigma}'} \delta_{\sigma'\bar{\sigma}} \delta_{mm'}}{(2\pi i \eta)^2} \right]. \quad (\text{A6b})$$

The point-splitting prescription in Eq. (A1) subtracts off the $1/\eta^2$ divergence of the last term of Eq. (A6b). The contributions of the second and first terms to H_λ can be organized as $H_\lambda = H_1 + H_{\text{int}}$, describing single-particle elastic scattering and two-particle

6.4 Equilibrium Fermi Liquid coefficients for fully screened Kondo models 167

M. HANL, A. WEICHELBAUM, J. VON DELFT, AND M. KISELEV

PHYSICAL REVIEW B **89**, 195131 (2014)

interactions, respectively. Taking $x = 0$ and $\eta \rightarrow 0$, we find

$$H_1 = -\frac{\lambda}{8\pi i} \lim_{\eta \rightarrow 0} \sum_{m\sigma\sigma'} : \frac{1}{\eta} [\Psi_{m\sigma}^\dagger(\eta) \bar{c}_{\sigma\sigma'}^2 \Psi_{m\sigma'}(0) - \Psi_{m\sigma'}^\dagger(0) \bar{c}_{\sigma\sigma'}^2 \Psi_{m\sigma}(\eta)] : \quad (\text{A7a})$$

$$= -\frac{3\lambda}{8\pi i} \lim_{\eta \rightarrow 0} \sum_{m\sigma} : \left[\frac{1}{\eta} (\Psi_{m\sigma}^\dagger(\eta) - \Psi_{m\sigma}^\dagger(0)) \Psi_{m\sigma}(0) - \Psi_{m\sigma}^\dagger(0) \frac{1}{\eta} (\Psi_{m\sigma}(\eta) - \Psi_{m\sigma}(0)) \right] : \quad (\text{A7b})$$

$$= -\frac{3\lambda}{8\pi i} \sum_{m\sigma} : [(\partial_x \Psi_{m\sigma}^\dagger)(0) \Psi_{m\sigma}(0) - \Psi_{m\sigma}^\dagger(0) (\partial_x \Psi_{m\sigma})(0)] : , \quad (\text{A7c})$$

$$H_{\text{int}} = -\lambda \sum_{mm'} : \vec{J}_m(0) \cdot \vec{J}_{m'}(0) : . \quad (\text{A8})$$

To obtain Eq. (A7b), we used $\bar{c}_{\sigma\sigma'}^2 = 3\delta_{\sigma\sigma'}$ and subtracted and added $:\Psi_{m\sigma}^\dagger(0)\Psi_{m\sigma}(0):$ inside the square brackets. Now pass to the momentum representation, using Eq. (A4) and the shorthand notations (following PG [29])

$$\rho_{m\sigma}(0) = \frac{1}{L} \rho_{m\sigma}, \quad \rho_{m\sigma} = \sum_{kk'} \psi_{km\sigma}^\dagger \psi_{k'm\sigma}, \quad (\text{A9a})$$

$$\vec{J}_m(0) = \frac{1}{L} \vec{j}_m, \quad \vec{j}_m = \frac{1}{2} \sum_{kk'\sigma\sigma'} \psi_{km\sigma}^\dagger \bar{c}_{\sigma\sigma'} \psi_{k'm\sigma'}, \quad (\text{A9b})$$

for the conduction electron channel- m charge and spin densities at the impurity. This gives

$$H_1 = -\frac{\alpha_1}{2\pi v} \sum_{m\sigma k k'} (\xi_k + \xi_{k'}) : \psi_{km\sigma}^\dagger \psi_{k'm\sigma} : , \quad (\text{A10a})$$

$$H_{\text{int}} = -\frac{2\phi_1}{3\pi v^2} \sum_{mm'} : \vec{j}_m \cdot \vec{j}_{m'} : . \quad (\text{A10b})$$

Here $v = L/(2\pi \hbar v_F)$ is the extensive 1D density of states per spin and channel, and the prefactors were expressed in terms

of the constants

$$\alpha_1 = \phi_1 = \frac{3\lambda}{8\pi(\hbar v_F)^2} = \frac{1}{T_K}. \quad (\text{A11})$$

(This notation is consistent with that of Ref. [46], where H_λ served as a starting point for calculating Fermi-liquid corrections, too.) Checking dimensions, with $[H_\lambda] = \mathcal{E}$ and $[\Psi_{m\sigma}] = 1/\sqrt{\mathcal{L}}$ (\mathcal{E} stands for energy, \mathcal{L} for length), we see that $[\lambda] = \mathcal{E}\mathcal{L}^2$. Since $[v] = 1/\mathcal{E}$, $[\hbar v_F] = \mathcal{E}\mathcal{L}$, we have $[\alpha_1] = [\phi_1] = 1/\mathcal{E}$, thus, α_1 and ϕ_1 have dimensions of inverse energy. In the main text, they are identified with $1/T_K$; in fact, the numerical prefactor in Eq. (A11) is purposefully chosen such that the leading term in the expansion (25) of the phase shift $\delta_{m\sigma}(\varepsilon)$ turns out to take the form ε/T_K .

To elucidate how the case $N > 1$ differs from $N = 1$, we write $H_{\text{int}} = H_2 + H_3$ in the main text, with H_2 and H_3 given in Eqs. (15b) and (15c), respectively, where H_3 occurs only for $N > 1$.

-
- [1] W. J. de Haas, J. de Boer, and G. J. van den Berg, *Physica* **1**, 1115 (1934).
 [2] W. J. de Haas and G. J. van den Berg, *Physica* **3**, 440 (1936).
 [3] J. Kondo, *Prog. Theor. Phys.* **32**, 37 (1964).
 [4] T. A. Costi, L. Bergqvist, A. Weichselbaum, J. von Delft, T. Micklitz, A. Rosch, P. Mavropoulos, P. H. Dederichs, F. Mallet, L. Saminadayar, and C. Bäuerle, *Phys. Rev. Lett.* **102**, 056802 (2009).
 [5] M. Hanl, A. Weichselbaum, T. A. Costi, F. Mallet, L. Saminadayar, C. Bäuerle, and J. von Delft, *Phys. Rev. B* **88**, 075146 (2013).
 [6] F. Mallet, J. Ericsson, D. Maily, S. Ünlübayir, D. Reuter, A. Melnikov, A. D. Wieck, T. Micklitz, A. Rosch, T. A. Costi, L. Saminadayar, and C. Bäuerle, *Phys. Rev. Lett.* **97**, 226804 (2006).
 [7] K. G. Wilson, *Rev. Mod. Phys.* **47**, 773 (1975).
 [8] H. R. Krishna-murthy, J. W. Wilkins, and K. G. Wilson, *Phys. Rev. B* **21**, 1003 (1980).
 [9] A. Weichselbaum and J. von Delft, *Phys. Rev. Lett.* **99**, 076402 (2007).
 [10] R. Bulla, T. A. Costi, and T. Pruschke, *Rev. Mod. Phys.* **80**, 395 (2008).
 [11] A. Weichselbaum, *Ann. Phys.* **327**, 2972 (2012).
 [12] C. P. Moca, A. Alex, J. von Delft, and G. Zaránd, *Phys. Rev. B* **86**, 195128 (2012).
 [13] Ph. Nozières, *J. Low Temp. Phys.* **17**, 31 (1974).
 [14] Ph. Nozières, in *Proceedings of the 14th International Conference on Low Temperature Physics*, edited by M. Krusius and M. Vuorio (North-Holland, Amsterdam, 1974), Vol. 5, p. 339.
 [15] Ph. Nozières and A. Blandin, *J. Phys.* **41**, 193 (1980).
 [16] D. Cragg and P. Lloyd, *J. Phys. C* **11**, L597 (1978).
 [17] D. Cragg and P. Lloyd, *J. Phys. C* **12**, L215 (1979).
 [18] D. M. Cragg, P. Lloyd, and P. Nozières, *J. Phys. C* **13**, 243 (1980).
 [19] I. Affleck, A. W. W. Ludwig, H.-B. Pang, and D. L. Cox, *Phys. Rev. B* **45**, 7918 (1992).
 [20] Y. Nishikawa and A. C. Hewson, *Phys. Rev. B* **86**, 245131 (2012).
 [21] A. Yoshimori, *Prog. Theor. Phys.* **55**, 67 (1976).
 [22] L. Mihaly and A. Zawadowski, *J. Phys.* **39**, 483 (1978).
 [23] A. M. Tselick and P. B. Wiegmann, *Adv. Phys.* **32**, 45 (1983).

- [24] N. Andrei, K. Furuya, and J. H. Lowenstein, *Rev. Mod. Phys.* **55**, 331 (1983).
- [25] I. Affleck, *Nucl. Phys. B* **336**, 517 (1990).
- [26] I. Affleck and A. W. W. Ludwig, *Phys. Rev. B* **48**, 7297 (1993).
- [27] Y. Nishikawa, D. J. G. Crow, and A. C. Hewson, *Phys. Rev. B* **82**, 115123 (2010).
- [28] M. Pustilnik and L. I. Glazman, *Phys. Rev. Lett.* **87**, 216601 (2001).
- [29] M. Pustilnik and L. I. Glazman, *J. Phys.: Condens. Matter* **16**, R513 (2004).
- [30] L. Glazman and M. Pustilnik, in *Nanophysics: Coherence and Transport*, edited by H. Bouchiat *et al.* (Elsevier, Amsterdam, 2005), pp. 427–478.
- [31] C. Mora, *Phys. Rev. B* **80**, 125304 (2009).
- [32] C. Mora, P. Vitushinsky, X. Leyronas, A. A. Clerk, and K. Le Hur, *Phys. Rev. B* **80**, 155322 (2009).
- [33] A. K. Mitchell and E. Sela, *Phys. Rev. B* **85**, 235127 (2012).
- [34] M. Hanl and A. Weichselbaum, *Phys. Rev. B* **89**, 075130 (2014).
- [35] The Drude conductivity of a disordered metal has the form $\rho_{\text{tot}}^{-1} \propto \int d\varepsilon \tau(\varepsilon) [-\partial_\varepsilon f(\varepsilon, T)]$. In the presence of magnetic impurities (but neglecting phonons), the total scattering rate is the sum of the scattering rates due static disorder and magnetic impurities, $1/\tau(\varepsilon) = 1/\tau_{\text{st}} + 1/\tau_{\text{mag}}(\varepsilon)$, with $1/\tau_{\text{mag}}(\varepsilon) \propto \sum_{m\sigma} A_{m\sigma}(\varepsilon)$. Equation (2) is obtained [36] by expanding $\tau(\varepsilon)$ in powers of the ratio $\tau_{\text{st}}/\tau_{\text{mag}}(\varepsilon) \ll 1$, and correspondingly expanding the resistivity as $\rho_{\text{tot}} = \rho_{\text{st}} + \rho(T, B)$, where the second contribution, due to magnetic impurities, is much smaller than the first.
- [36] A. A. Abrikosov, *Physics* **2**, 5 (1965).
- [37] T. A. Costi, *Phys. Rev. Lett.* **85**, 1504 (2000).
- [38] A. Rosch, T. A. Costi, J. Paaske, and P. Wölfle, *Phys. Rev. B* **68**, 014430 (2003).
- [39] A. V. Kretinin, H. Shtrikman, D. A. Goldhaber-Gordon, M. Hanl, A. Weichselbaum, J. von Delft, T. A. Costi, and D. Mahalu, *Phys. Rev. B* **84**, 245316 (2011).
- [40] F. B. Anders and A. Schiller, *Phys. Rev. Lett.* **95**, 196801 (2005).
- [41] R. Peters, T. Pruschke, and F. B. Anders, *Phys. Rev. B* **74**, 245114 (2006).
- [42] A. Weichselbaum, *Phys. Rev. B* **86**, 245124 (2012).
- [43] A. Weichselbaum, *Phys. Rev. B* **84**, 125130 (2011).
- [44] L. N. Oliveira, V. L. Libero, H. O. Frota, and M. Yoshida, *Physica B* **171**, 61 (1991).
- [45] F. Bauer, J. Heyder, E. Schubert, D. Borowsky, D. Taubert, B. Bruognolo, D. Schuh, W. Wegscheider, J. von Delft, and S. Ludwig, *Nature (London)* **501**, 73 (2013).
- [46] C. B. M. Hørig, C. Mora, and D. Schuricht, *Phys. Rev. B* **89**, 165411 (2014).
- [47] I. Affleck, *Nucl. Phys. B* **265**, 409 (1986).
- [48] A. W. W. Ludwig, *Methods of Conformal Field Theory in Condensed Matter Physics: An Introduction to Non-Abelian Bosonization*, Lecture Notes, Trieste, 1992 (unpublished).
- [49] Jan von Delft, Ph.D. thesis, Cornell University, 1995.

7. Conclusions

This thesis contributed to the understanding of optical and transport related phenomena in quantum impurity systems. By comparing numerical calculations to experimental data, we showed that the Kondo effect has been observed with optical methods for the first time and that the system can be correctly described with numerical methods on a quantitative level. Going further into this direction, we theoretically examined how the line shape changes for strong optical coupling and discovered a new many body state, a hybridization of a Kondo state and a state with Rabi oscillations, which has a Kondo-like character on its own. It was also demonstrated that related experiments at self-assembled QDs concerning the phenomenon of the Fermi edge singularity can be understood on a quantitative level, too.

Regarding the field of transport, we presented a comprehensive study of the Kondo effect in an InAs-nanowire QD. We further identified the right model to describe iron impurities in gold and silver by comparing the magnetoresistivity and the dephasing rate from NRG-calculations for different models to experimental data, and we showed how to determine the Kondo temperature such that correct scaling is preserved in the presence of finite bandwidth. In the last project presented in this thesis, we calculated several Fermi liquid coefficients for fully screened Kondo models with different numbers of channels, both analytically and numerically.

The work presented in this thesis can also be seen as motivation and starting point for future experiments and calculations. One interesting experiment would be the observation of the predicted Rabi-Kondo state. This could be combined with the calculation of the non-equilibrium steady state density matrix, which would lead to an improved prediction of the emission line shape. Optical experiments with QDs also allow for time-resolved non-equilibrium measurements, like the build-up of the Kondo cloud after a quantum quench, or studying the effects of Anderson orthogonality in a tunable environment. Regarding transport, gold and silver with iron impurities could be taken as an exemplary experimental system to examine three-channel Kondo models. The strategy to identify the correct type of Kondo model, which was used here, could also be applied to other bulk materials with magnetic impurities to identify their underlying models. Such analyses could be combined with the measurement of the FL-coefficients, which constitutes a complementary method to identify the right type of Kondo model for an experimental system.

Part III.
Appendix

A. NRG Hamiltonian of impurity and hybridization in matrix form

It is very illustrative to see the NRG Hamiltonian of the impurity and the hybridization to the bath (i. e. the impurity and the 0th chain site) written out in matrix form. Since the impurity part of the SIAM (2.2a) is already diagonal, the corresponding Hamiltonian is simply given by:

$$H_{imp} = \begin{pmatrix} 0 & 0 & 0 & 0 \\ 0 & \varepsilon_e & 0 & 0 \\ 0 & 0 & \varepsilon_e & 0 \\ 0 & 0 & 0 & 2\varepsilon_e + U \end{pmatrix}. \quad (\text{A.1})$$

After adding the 0th chain site, according to Eq. (4.10) one obtains:

$$H = H_{imp} + V \sum_{\sigma} (e_{\sigma}^{\dagger} f_{0\sigma} + \text{h. c.}). \quad (\text{A.2})$$

When the state space of the new site is added, the operators $f_{0\sigma}^{(\dagger)}$ that act on the added site, are given in the local basis of a site. The Hamiltonian in Eq. (A.2) can therefore be expressed in terms of tensor products of operators in the basis of the impurity, and of operators in the local basis of the added site:

$$H = H_{imp} \otimes \mathbb{1} + V \sum_{\sigma} (e_{\sigma}^{\dagger} \otimes (Z f_{0\sigma}) + \text{h. c.}), \quad (\text{A.3})$$

with $Z = (-1)^n$, as defined in Sec. (4.3.1), where n is the number operator in the local basis of a site. Eq. (A.4) below shows the Hamiltonian written out in matrix form. It shows how the state space increases when a chain site is added and it also illustrates the sparsity of the matrix, which indicates the potential benefit of using symmetries (Secs. 4.4 and 4.5).

B. Publication for absorption in the presence of Kondo correlations

The following publication emerged from the work of my Diploma thesis. It describes the theory of absorption spectra with weak optical coupling in the presence of Kondo correlations. Its content is briefly discussed in adapted form in section [3.3](#), and has been added here in the appendix for completeness.

[indicated by wavy lines in Fig. 1(d)] can be tuned by magnetic field and gate voltage via their effects on the level occupancy.

Model.—We consider a QD, tunnel coupled to a FR, whose charge state is controllable via an external gate voltage V_g applied between a top Schottky gate and the FR [see Fig. 1(a) and 1(b)]. In a gate voltage regime for which the QD is initially uncharged, a circularly polarized light beam (polarization σ) at a suitably chosen frequency ω_L propagating along the z axis of the heterostructure will create a so-called neutral exciton [11] (X^0), a bound electron-hole pair with well-defined spins σ and $\bar{\sigma} = -\sigma$ ($\in \{+, -\}$) in the lowest available localized s orbitals of the QD's conduction- and valence bands (to be called e and h levels, with creation operators e_σ^\dagger and $h_{\bar{\sigma}}^\dagger$, respectively). The QD-light interaction is described by $H_L \propto (e_\sigma^\dagger h_{\bar{\sigma}}^\dagger e^{-i\omega_L t} + \text{H.c.})$. We model the system before and after absorption by the initial and final Hamiltonian $H^{i/f} = H_e^{i/f} + H_c + H_t$, where

$$H_e^a = \sum_\sigma \varepsilon_{e\sigma}^a n_{e\sigma} + U n_{e\uparrow} n_{e\downarrow} + \delta_{af} \varepsilon_{h\bar{\sigma}} \quad (a = i, f) \quad (1)$$

describes the QD, with Coulomb cost U for double occupancy of the e level, $n_{e\sigma} = e_\sigma^\dagger e_\sigma$, and hole energy $\varepsilon_{h\bar{\sigma}} (> 0$, on the order of the band gap). The e level's initial and final energies before and after absorption, $\varepsilon_{e\sigma}^a$ ($a = i, f$), differ by the Coulomb attraction $U_{\text{ch}} (> 0)$ between the newly created electron-hole pair, which pulls the final e level downward, $\varepsilon_{e\sigma}^f = \varepsilon_{e\sigma} - \delta_{af} U_{\text{ch}}$ [Fig. 1(b)]. This stabilizes the excited electron against decay into the FR, provided that $\varepsilon_{e\sigma}^f$ lies below the FR's Fermi energy $\varepsilon_F = 0$. Since $H^f \neq H^i$, absorption implements a quantum quench, which, as elaborated below, can be tuned by electric and magnetic fields. The term $H_c = \sum_{k\sigma} \varepsilon_{k\sigma} c_{k\sigma}^\dagger c_{k\sigma}$ represents a noninteracting conduction band (the FR) with half-width $D = 1/(2\rho)$ and constant density of states ρ per spin, while $H_t = \sqrt{\Gamma/\pi\rho} \sum_\sigma (e_\sigma^\dagger c_\sigma + \text{H.c.})$, with $c_\sigma = \sum_k c_{k\sigma}$, describes its tunnel coupling to the e level, giving it a width Γ . A magnetic field B along the growth-direction of the heterostructure (Faraday configuration) causes a Zeeman splitting, $\varepsilon_{e\sigma} = \varepsilon_e + \frac{1}{2} \sigma g_e B$, $\varepsilon_{h\sigma} = \varepsilon_h + \frac{3}{2} \sigma g_h B$ (the Zeeman splitting of FR states can be neglected for our purposes [12]). The electron-hole pair created by photon absorption will additionally experience a weak but highly anisotropic intradot exchange interaction [12]. Its effects can be fully compensated by applying a magnetic field fine-tuned to a value, say B_{ch}^σ , that restores degeneracy of the e level's two spin configurations [12]. Henceforth, B is understood to be measured relative to B_{ch}^σ . We set $\mu_B = \hbar = k_B = 1$, give energies in units of $D = 1$ throughout, and assume $T, B \ll \Gamma \ll U, U_{\text{ch}} \ll D \ll \varepsilon_{h\bar{\sigma}}$. The electron-hole recombination rate is assumed to be negligibly small compared to all other energy scales. We focus on the case, illustrated in

Figs. 1(a) and 1(b), where the e level is essentially empty in the initial state and singly occupied in the ground state of the final Hamiltonian, $\bar{n}_e^i \simeq 0$ and $\bar{n}_e^f \simeq 1$. (Here $\bar{n}_e^a = \sum_\sigma \bar{n}_{e\sigma}^a$, and $\bar{n}_{e\sigma}^a = \langle n_{e\sigma} \rangle_a$ is the thermal average of $n_{e\sigma}$ with respect to H^a .) This requires $\varepsilon_{e\sigma}^i \gg \Gamma$, and $-U + \Gamma \lesssim \varepsilon_{e\sigma}^f \lesssim -\Gamma$. The Kondo temperature associated with H^f is $T_K = \sqrt{\Gamma U/2} e^{-\pi|\varepsilon_{e\sigma}^f + U|/(2U\Gamma)}$. If $\varepsilon_{e\sigma}^f = -U/2$, so that $\bar{n}_e^f = 1$, then H^f represents the symmetric excitonic Anderson model, to be denoted by writing $H^f = \text{SEAM}$.

Absorption line shape.—Absorption sets in once ω_L exceeds a threshold frequency, ω_{th} . The line shape at temperature T and detuning $\nu = \omega_L - \omega_{\text{th}}$ is, by the golden rule, proportional to the spectral function (see [13])

$$A_\sigma(\nu) = 2\pi \sum_{mm'} \rho_m^i |{}_f \langle m' | e_\sigma^\dagger | m \rangle_i|^2 \delta(\omega_L - E_{m'}^f + E_m^i). \quad (2)$$

Here $|m\rangle_a$ and E_m^a are exact eigenstates and energies of H^a , depicted schematically in Fig. 1(c), and $\rho_m^i = e^{-E_m^i/T}/Z^i$ the initial Boltzmann weights. The threshold frequency evidently is $\omega_{\text{th}} = E_G^f - E_G^i$ (E_G^a is the ground state energy of H^a), which is on the order of $\varepsilon_{e\sigma}^f + \varepsilon_{h\bar{\sigma}}$ (up to corrections due to tunneling and correlations).

We calculated $A_\sigma(\nu)$ using the Numerical Renormalization Group (NRG) [14], generalizing the approach of Refs. [8,15] to $T \neq 0$ by following Ref. [16]. The inset of Fig. 2 shows a typical result: As temperature is gradually reduced, an initially rather symmetric line shape becomes highly asymmetric, dramatically increasing in peak height as $T \rightarrow 0$. At $T = 0$, the line shape displays a threshold, vanishing for $\nu < 0$ and diverging as ν tends to 0 from above. Figure 2 analyzes this divergence on a log-log plot, for the case that T , which cuts off the divergence, is smaller than all other relevant energy scales. Three distinct functional forms emerge in the regimes of ‘‘large’’, ‘‘intermediate’’ or ‘‘small’’ detuning, labeled (for reasons discussed below) FO, LM and SC, respectively, (given here for $H^f = \text{SEAM}$):

$$|\varepsilon_{e\sigma}^f| \lesssim \nu \lesssim D: \quad A_\sigma^{\text{FO}}(\nu) = \frac{4\Gamma}{\nu^2} \theta(\nu - |\varepsilon_{e\sigma}^f|); \quad (3a)$$

$$T_K \lesssim \nu \lesssim |\varepsilon_{e\sigma}^f|: \quad A_\sigma^{\text{LM}}(\nu) = \frac{3\pi}{4\nu} \ln^{-2}(\nu/T_K); \quad (3b)$$

$$T \lesssim \nu \lesssim T_K: \quad A_\sigma^{\text{SC}}(\nu) \propto T_K^{-1} (\nu/T_K)^{-\eta_\sigma}. \quad (3c)$$

The remarkable series of crossovers found above are symptomatic of three different regimes of charge and spin dynamics. They can be understood analytically using fixed-point perturbation theory (FPPT). To this end, note that at $T = 0$ the absorption line shape can be written as

$$A_\sigma(\nu) = 2 \text{Re} \int_0^\infty dt e^{i\nu t} \langle G | e^{i\bar{H}t} e_\sigma e^{-i\bar{H}t} e_\sigma^\dagger | G \rangle_i, \quad (4)$$

where $\bar{H}^a = H^a - E_G^a$ and $\nu_+ = \nu + i0_+$. Thus it directly probes the postquench dynamics, with initial state $e_\sigma^\dagger |G\rangle_i$,

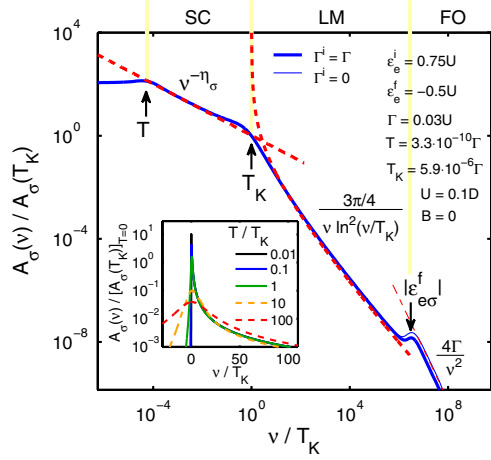


FIG. 2 (color online). Log-log plot of the absorption line shape $A_\sigma(\nu)$ for $T \ll T_K$, $B = 0$ and $H^f = \text{SEAM}$ (for which $\eta_\sigma = \frac{1}{2}$), showing three distinct functional forms for high, intermediate and small detuning, labeled FO, LM, and SC, respectively, according to the corresponding fixed points of the Anderson model. Arrows indicate the crossover scales T , T_K and $|\epsilon_{e\sigma}^f|$. Fixed-point perturbation theory [FPPT, red dashed lines, from Eq. (3)] and NRG (thick blue line for $\Gamma_i \neq 0$; thin blue line for $\Gamma_i = 0$) agree well. Inset: $A_\sigma(\nu)$ for five temperatures in semilog scale, obtained from FPPT for $\Gamma_i = 0$ [dashed lines, from Eq. (7)] and NRG (solid lines).

of a photogenerated e -electron coupled to a FR. Evidently, large, intermediate or small detuning, corresponding to ever longer time scales after absorption, probes excitations at successively smaller energy scales [see Fig. 1(c)], for which \bar{H}^f can be represented by expansions $H_r^* + H_r^f$ around the three well-known fixed points [14] of the AM: the free orbital, local moment and strong-coupling fixed points ($r = \text{FO, LM, SC}$), characterized by charge fluctuations, spin fluctuations and a screened spin singlet, respectively, as illustrated in Fig. 1(d).

Large and intermediate detuning—perturbative regime.—For large detuning, probing the time interval $t \lesssim 1/|\epsilon_{e\sigma}^f|$ immediately after absorption, the e level appears as a free, filled orbital perturbed by charge fluctuations, described by [14] the fixed-point Hamiltonian $H_{\text{FO}}^* = H_c + H_e^f + \text{const}$ and the relevant perturbation $H_{\text{FO}}^f = H_r$. Intermediate detuning probes the times $1/|\epsilon_{e\sigma}^f| \lesssim t \lesssim 1/T_K$ for which real charge fluctuations have frozen out, resulting in a stable local moment; however, virtual charge fluctuations still cause the local moment to undergo spin fluctuations, which are not yet screened. This is described by [14] $H_{\text{LM}}^* = H_c + \text{const}$ and the RG-relevant perturbation $H_{\text{LM}}^f = \frac{J(\nu)}{\rho} \vec{s}_e \cdot \vec{s}_c$. Here $\vec{s}_j = \frac{1}{2} \sum_{\sigma\sigma'} j_\sigma^\dagger \vec{\tau}_{\sigma\sigma'} j_{\sigma'}$ (for $j = e, c$) are spin operators for the e level and conduction band, respectively, ($\vec{\tau}$ are Pauli matrices), and $J(\nu) = \ln^{-1}(\nu/T_K)$ is an effective, scale-dependent dimensionless exchange constant.

For $r = \text{FO}$ and LM, $A_\sigma(\nu)$ can be calculated using perturbation theory in H_r^f . For $T = 0$, note that

$$A_\sigma(\nu) = -2 \text{Im}_i \langle G | e_\sigma \frac{1}{\nu_+ - \bar{H}^f} e_\sigma^\dagger | G \rangle_i, \quad (5)$$

set $\bar{H}^f \rightarrow H_r^* + H_r^f$ and expand the resolvent in powers of H_r^f . One readily finds (see [13])

$$A_\sigma^r(\nu) \simeq -\frac{2}{\nu^2} \text{Im}_i \langle G | e_\sigma H_r^f \frac{1}{\nu_+ - H_r^*} H_r^f e_\sigma^\dagger | G \rangle_i, \quad (6)$$

which reveals the relevant physics: Large detuning ($r = \text{FO}$) is described by the spectral function of the operator $H_r e_\sigma^\dagger$; the absorption process can thus be understood as a two-step process consisting of a virtual excitation of the QD resonance, followed by a tunneling event to a final free-electron state above the Fermi level. In contrast, intermediate detuning ($r = \text{LM}$) is described by the spectral function of $\vec{s}_c \cdot \vec{s}_e e_\sigma^\dagger$, i.e., it probes spin fluctuations. Evaluating these spectral functions is elementary since H_{FO}^* and H_{LM}^* involve only free fermions. For $B = 0$ and $|\epsilon_{e\sigma}^f| = \frac{1}{2}U$, we readily recover Eqs. (3a) and (3b) (see [13]), which quantitatively agree with the NRG results of Fig. 2.—Though the latter was calculated for $H^f = \text{SEAM}$, Eq. (3b) holds more generally as long as H^f remains in the LM regime, with $\bar{n}_e^f \simeq 1$; then $A_\sigma^{\text{LM}}(\nu)$ depends on $\epsilon_{e\sigma}^f$, U and Γ only through their influence on T_K , and hence is a universal function of ν and T_K .

The FPPT strategy for calculating FO and LM line shapes can readily be generalized to finite temperatures [12], using the methods of Ref. [17] (Section III.A) for finding the finite- T dynamic magnetic susceptibility [13]. For $|\nu| \ll |\epsilon_{e\sigma}^f|$ and $\max[|\nu|, T] \gg T_K$, we obtain

$$A_\sigma^{\text{LM}}(\nu) = \frac{3\pi}{4} \frac{\nu/T}{1 - e^{-\nu/T}} \frac{\gamma_{\text{Kor}}(\nu, T)/\pi}{\nu^2 + \gamma_{\text{Kor}}^2(\nu, T)}, \quad (7)$$

where $\gamma_{\text{Kor}}(\nu, T) = \pi T / \ln^2[\max(|\nu|, T)/T_K]$ is the scale-dependent Korringa relaxation rate [17]. It is smaller than T by a large logarithmic factor, implying a narrower and higher absorption peak than for thermal broadening.

Small detuning and Kondo-edge singularity—strong-coupling regime.—As ν is lowered through the bottom of the LM regime, $J(\nu)$ increases through unity into the strong-coupling regime, and $A_\sigma(\nu)$ monotonically crosses over to the SC regime. It was first studied for the present model (for $B = 0$) in Ref. [8], which found a power-law line shape of the form (3c), characteristic of a Fermi edge singularity, with an exponent η that followed Hopfield's rule [18]. The power-law behavior reflects Anderson orthogonality [19,20]: it arises because the final ground state $|G_f\rangle$ that is reached in the long-time limit is characterized by a screened singlet. The singlet ground state induces different phase shifts [as indicated in Fig. 1(d) by wavy lines] for FR electrons than the unscreened initial state just after photon absorption, $e_\sigma^\dagger |G_i\rangle$, and hence is orthogonal to the latter. It is straightforward to generalize

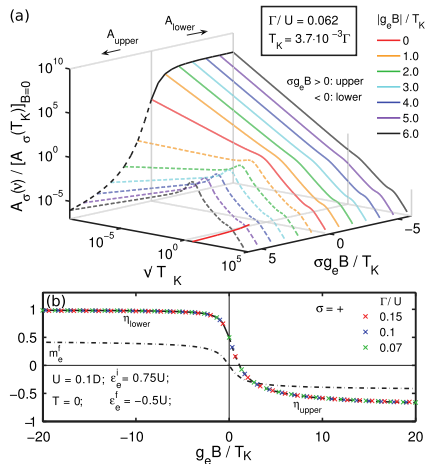


FIG. 3 (color online). Asymmetric magnetic-field dependence of the line shape for $H^f = \text{SEAM}$ and $T = 0$. (a) Depending on whether the electron is photoexcited into the lower or upper of the Zeeman-split e levels ($\sigma g_e B < 0$ or > 0 , solid or dashed lines, respectively), increasing $|B|$ causes the near-threshold divergence, $A_\sigma(\nu) \propto \nu^{-\eta_\sigma}$, to be either strengthened, or suppressed via the appearance of a peak at $\nu \approx \sigma g_e B$, respectively. (The peak's position is shown by the red line in the $\sigma g_e B$ - ν plane.) (b) Universal dependence on $g_e B / T_K$ of the local moment m_e^f (dash-dotted line), and the corresponding prediction of Hopfield's rule, Eq. (8), for the infrared exponents η_{lower} (solid line) and η_{upper} (dashed line) for $\sigma = +$. Symbols: η_+ values extracted from the near-threshold $\nu^{-\eta_+}$ divergence of $A_+(\nu)$. Symbols and lines agree to within 1%.

the arguments of Refs. [8,18] to the case of $B \neq 0$ (see [13]). One readily finds the generalized Hopfield rule

$$\eta_\sigma = 1 - \sum_{\sigma'} (\Delta n'_{e\sigma'})^2, \quad \Delta n'_{e\sigma'} = \delta_{\sigma\sigma'} - \Delta n_{e\sigma'}, \quad (8)$$

$\Delta n'_{e\sigma'}$ is the displaced charge of electrons with spin σ' , in units of e , that flows from the scattering site to infinity when $e_\sigma^\dagger |G_i\rangle$ is changed to $|G_f\rangle$, and $\Delta n_{e\sigma'} = \bar{n}_{e\sigma'}^f - \bar{n}_{e\sigma'}^i$ is the local occupation difference between $|G_f\rangle$ and $|G_i\rangle$.

According to Eq. (8), η_σ can be tuned not only via gate voltage but also via magnetic field, since both modify $\epsilon_{e\sigma}^a$ and hence $\Delta n'_{e\sigma'}$. This tunability can be exploited to study universal aspects of Anderson orthogonality physics. In particular, if the system is tuned such that $\bar{n}_e^i = 0$ and $\bar{n}_e^f = 1$ at $B = 0$, Eq. (8) can be expressed as $\eta_\sigma = \frac{1}{2} + 2m_e^f \sigma - 2(m_e^f)^2$, where the final magnetization $m_e^f = \frac{1}{2} \times (\bar{n}_{e+}^f - \bar{n}_{e-}^f)$ is a universal function of $g_e B / T_K$. The exponents η_σ then are universal functions of $g_e B / T_K$, with simple limits for small and large fields [see Fig. 3(b)]: $\eta_\sigma \rightarrow \frac{1}{2}$ for $|g_e B| \ll T_K$, while $\eta_{\text{lower/upper}} \rightarrow \pm 1$ for $|g_e B| \gg T_K$. Here the subscript ‘‘lower’’ or ‘‘upper’’ distinguishes whether the spin- σ electron is photoexcited into the lower or upper of the Zeeman-split pair ($\sigma g_e B < 0$ or > 0 , respectively). The sign difference ± 1 for η_σ arises since these cases yield fully asymmetric changes in local

charge: $\Delta n_{e,\text{lower}} \rightarrow 1$ while $\Delta n_{e,\text{upper}} \rightarrow 0$. As a result, Anderson orthogonality [19] is completely absent ($\Delta n'_{e\sigma'} = 0$) for photo-excitation into the lower level, since subsequently the e -level spin need not adjust at all. In contrast, it is maximal ($\Delta n'_{e\sigma'} = 1$) for photo-excitation into the upper level, since subsequently the e -level spin has to create a spin-flip electron-hole pair excitation in the FR to reach its longtime value. It follows, remarkably, that a magnetic field tunes the strength of Anderson orthogonality, implying a dramatic asymmetry for the evolution of the line shape $A_\sigma(\nu) \propto \nu^{-\eta_\sigma}$ with increasing $|B|$ [Fig. 3(a)].

Conclusions.—We have shown that optical absorption in a single quantum dot can implement a quantum quench in an experimentally accessible solid-state system that allows the emergence of Kondo correlations and Anderson orthogonality to be studied in a tunable setting.

A. I. and H. E. T. acknowledge support from the Swiss NSF under Grant No. 200021-121757. H. E. T. acknowledges support from the Swiss NSF under Grant No. PP00P2-123519/1. B. B. acknowledges support from the Swiss NSF and NCCR Nanoscience (Basel). J. v. D. acknowledges support from the DFG (SFB631, SFB-TR12, De730/3-2, De730/4-1), the Cluster of Excellence NIM and in part from NSF under Grant No. PHY05-51164. A. I. acknowledges support from an ERC Advanced Investigator Grant, and L. G. from NSF Grant No. DMR-0906498.

- [1] P. Nordlander *et al.*, *Phys. Rev. Lett.* **83**, 808 (1999).
- [2] M. Plihal, D. C. Langreth, and P. Nordlander, *Phys. Rev. B* **71**, 165321 (2005).
- [3] F. B. Anders and A. Schiller, *Phys. Rev. Lett.* **95**, 196801 (2005).
- [4] D. Lobaskin and S. Kehrein, *Phys. Rev. B* **71**, 193303 (2005).
- [5] T. V. Shahbazyan, I. E. Perakis, and M. E. Raikh, *Phys. Rev. Lett.* **84**, 5896 (2000).
- [6] K. Kikoin and Y. Avishai, *Phys. Rev. B* **62**, 4647 (2000).
- [7] A. O. Govorov, K. Karrai, and R. J. Warburton, *Phys. Rev. B* **67**, 241307 (2003).
- [8] R. W. Helmes *et al.*, *Phys. Rev. B* **72**, 125301 (2005).
- [9] J. M. Smith *et al.*, *Phys. Rev. Lett.* **94**, 197402 (2005).
- [10] P. A. Dalgarno *et al.*, *Phys. Rev. Lett.* **100**, 176801 (2008).
- [11] A. Högele *et al.*, *Phys. Rev. Lett.* **93**, 217401 (2004).
- [12] H. Tureci *et al.* (to be published).
- [13] See supplemental material at <http://link.aps.org/supplemental/10.1103/PhysRevLett.106.107402>.
- [14] H. R. Krishna-murthy, J. W. Wilkins, and K. G. Wilson, *Phys. Rev. B* **21**, 1003 (1980).
- [15] T. A. Costi, *Phys. Rev. B* **55**, 3003 (1997).
- [16] A. Weichselbaum and J. von Delft, *Phys. Rev. Lett.* **99**, 076402 (2007).
- [17] M. Garst *et al.*, *Phys. Rev. B* **72**, 205125 (2005).
- [18] J. Hopfield, *Comments Solid State Phys.* **2**, 40 (1969).
- [19] P. W. Anderson, *Phys. Rev. Lett.* **18**, 1049 (1967).
- [20] P. Nozières and C. T. De Dominicis, *Phys. Rev.* **178**, 1097 (1969).

EPAPS: Supplementary information
for “Many-Body Dynamics of Exciton Creation in a Quantum
Dot by Optical Absorption:
A Quantum Quench towards Kondo Correlations”

Hakan E. Türeci^{1,2}, M. Hanl³, M. Claassen², A. Weichselbaum³, T. Hecht³,
B. Braunecker⁴, A. Govorov⁵, L. Glazman⁶, A. Imamoglu² & J. von Delft³

¹ *Department of Electrical Engineering, Princeton University, Princeton, NJ 08544, USA*

² *Institute for Quantum Electronics, ETH-Zürich, CH-8093 Zürich, Switzerland*

³ *Arnold Sommerfeld Center for Theoretical Physics,
Ludwig-Maximilians-Universität München, D-80333 München, Germany*

⁴ *Department of Physics, University of Basel, Klingelbergstrasse 82, 4056 Basel, Switzerland*

⁵ *Department of Physics and Astronomy, Ohio University, Athens, Ohio 45701, USA*

⁶ *Sloane Physics Laboratory, Yale University, New Haven, CT 06520, USA*

We provide below some intermediate steps for the derivation of the main equations of the main text. For clarity, information contained in the main text is typeset in blue.

Spectral function

The origin of Eq. (2) for the absorption rate can be understood as follows [1]. We begin with a Hamiltonian slightly more general than those of the main text, in that it includes the hole degree of freedom: $H = H_{\text{eh}} + H_c + H_t$, where H_c and H_t are given in the main text, and

$$H_{\text{eh}} = \sum_{\sigma} (\varepsilon_{\text{e}\sigma} n_{\text{e}\sigma} + \varepsilon_{\text{h}\sigma} n_{\text{h}\sigma}) + U n_{\text{e}\uparrow} n_{\text{e}\downarrow} - \sum_{\sigma\sigma'} U_{\text{eh}} n_{\text{e}\sigma} n_{\text{h}\sigma'} \quad (\text{S1})$$

describes the QD, with e-level charging energy $U (> 0)$, e-h Coulomb attraction $U_{\text{eh}} (> 0)$, $n_{\text{e}\sigma} = e_{\sigma}^{\dagger} e_{\sigma}$, $n_{\text{h}\sigma} = h_{\sigma}^{\dagger} h_{\sigma}$. The hole energy $\varepsilon_{\text{h}\sigma} (> 0)$ is on the order of the band gap.

The QD-light interaction is described by $H_L \propto (e_{\sigma}^{\dagger} h_{\bar{\sigma}}^{\dagger} e^{-i\omega_L t} + \text{h.c.})$. Absorption sets in once ω_L exceeds a threshold frequency, say ω_{th} . According to Fermi's golden rule, treating H_L as harmonic perturbation, the absorption lineshape at temperature T and detuning $\nu = \omega_L - \omega_{\text{th}}$ is proportional to

$$A_{\sigma}(\nu) = 2\pi \sum_{mm'} \rho_m |\langle m' | e_{\sigma}^{\dagger} h_{\bar{\sigma}}^{\dagger} | m \rangle|^2 \delta(\omega_L - E_{m'} + E_m), \quad (\text{S2})$$

where the ρ_m are Boltzmann weights. Noting that the dynamics of the optically created hole is trivial, $[n_{\text{h}\sigma}, H] = 0$, we can write all initial states $|m\rangle$ as $|m\rangle_{\text{i}} \otimes |0\rangle_{\text{h}}$ and all final states $|m'\rangle$ in the form $|m'\rangle_{\text{f}} \otimes |\bar{\sigma}\rangle_{\text{h}}$, thus arriving at Eq. (2) from the main text:

$$A_{\sigma}(\nu) = 2\pi \sum_{mm'} \rho_m^{\text{i}} |\langle m' | e_{\sigma}^{\dagger} | m \rangle_{\text{i}}|^2 \delta(\omega_L - E_{m'}^{\text{f}} + E_m^{\text{i}}). \quad (\text{S3})$$

Here $|m\rangle_a$ ($a = \text{i, f}$) are the many-body eigenstates of the effective initial and final Hamiltonians, $H^{\text{i}} = {}_{\text{h}}\langle 0 | H | 0 \rangle_{\text{h}}$ and $H^{\text{f}} = {}_{\text{h}}\langle \bar{\sigma} | H | \bar{\sigma} \rangle_{\text{h}}$, that only include the QD and FR electronic

degrees of freedom. They are given by $H^{i/f} = H_e^{i/f} + H_c + H_t$, with $H_e^{i/f}$ given by Eq. (1):

$$H_e^a = \sum_{\sigma} \varepsilon_{e\sigma}^a n_{e\sigma} + U n_{e\uparrow} n_{e\downarrow} + \delta_{af} \varepsilon_{h\bar{\sigma}} \quad (a = i, f), \quad \text{with} \quad \varepsilon_{e\sigma}^a = \varepsilon_{e\sigma} - \delta_{af} U_{eh}. \quad (\text{S4})$$

To bring the spectral function into a resolvent form suitable for fixed point perturbation theory (FPPT), we use Dirac's identity

$$\delta(\omega_L - E_{m'}^f + E_m^i) = -\frac{1}{\pi} \text{Im} \left[\frac{1}{\omega_L - E_{m'}^f + E_m^i + i0^+} \right], \quad (\text{S5})$$

to rewrite Eq. (S3) as follows:

$$A_{\sigma}(\nu) = -2 \text{Im} \left[\sum_{mm'} \rho_m^i \langle m | e_{\sigma} \frac{1}{\omega_L - E_{m'}^f + E_m^i + i0^+} | m' \rangle_{f \leftarrow i} \langle m' | e_{\sigma}^{\dagger} | m \rangle_i \right]. \quad (\text{S6})$$

$$= -2 \text{Im} \left[\sum_m \rho_m^i \langle m | e_{\sigma} \frac{1}{\omega_L - H^f + E_m^i + i0^+} e_{\sigma}^{\dagger} | m \rangle_i \right]. \quad (\text{S7})$$

For the last step, we replaced $E_{m'}^f$ by H^f and used $\sum_{m'} |m'\rangle_{f \leftarrow i} \langle m'| = 1$.

Zero temperature:

At $T = 0$, the initial density matrix is $|G\rangle_i \langle G|$. With the definitions introduced in the text, $\bar{H}^a = H^a - E_G^a$, $\nu = \omega_L - E_G^f + E_G^i$ and $\nu_+ = \nu + i0_+$, Eq. (S7) reduces to Eq. (5) of the main text:

$$A_{\sigma}(\nu) = -2 \text{Im} \langle G | e_{\sigma} \frac{1}{\nu_+ - \bar{H}^f} e_{\sigma}^{\dagger} | G \rangle_i. \quad (\text{S8})$$

For the parameters considered in the main text, the ground state of H^i can be approximated by a free Fermi sea: $|G\rangle_i \simeq \prod_{\varepsilon_{k\sigma} < \varepsilon_F} c_{k\sigma}^{\dagger} |\text{Vac}\rangle$. Next comes the key step of FPPT: replace $\bar{H}^f \rightarrow H_r^* + H_r'$ and do a perturbation expansion in H_r' of the resolvent

$$\frac{1}{\nu_+ - \bar{H}^f} = \frac{1}{\nu_+ - H_r^*} + \frac{1}{\nu_+ - H_r^*} \hat{\mathcal{T}}_r \frac{1}{\nu_+ - H_r^*} \quad (\text{S9})$$

with the T-matrix given by

$$\hat{\mathcal{T}}_r = H_r' + H_r' \frac{1}{\nu_+ - H_r^*} H_r' + \dots \quad (\text{S10})$$

According to the main text, the free orbital (FO) regime is described by

$$H_{\text{FO}}^* = H_c + H_e^f - E_{\text{FO}} = \sum_{k\sigma} \varepsilon_{k\sigma} c_{k\sigma}^{\dagger} c_{k\sigma} + \sum_{\sigma} \varepsilon_{e\sigma}^f n_{e\sigma} + U n_{e\uparrow} n_{e\downarrow} - E_{\text{FO}}, \quad (\text{S11a})$$

perturbed by

$$H'_{\text{FO}} = H_t = \sqrt{\Gamma/\pi\rho} \sum_{\sigma} (e_{\sigma}^{\dagger} c_{\sigma} + \text{h.c.}), \quad (\text{S11b})$$

and the local moment (LM) regime by

$$H_{\text{LM}}^* = H_c - E_{\text{LM}} = \sum_{k\sigma} \varepsilon_{k\sigma} c_{k\sigma}^\dagger c_{k\sigma} - E_{\text{LM}}, \quad (\text{S12a})$$

perturbed by

$$H'_{\text{LM}} = \frac{J(\nu)}{\rho} \vec{s}_e \cdot \vec{s}_c, \quad (\text{S12b})$$

with e-level and conduction band spin operators given by $\vec{s}_j = \frac{1}{2} \sum_{\sigma\sigma'} j_\sigma^\dagger \vec{\tau}_{\sigma\sigma'} j_{\sigma'}$ (for $j = e, c$). The subtracted constants E_{FO} and E_{LM} correspond to the subtraction of E_{G}^f in the definition of $\tilde{H}^f = H^f - E_{\text{G}}^f \rightarrow H_r^* + H'_r$ (see the main text after Eq. (4)); they ensure that the ground state of H_r^* has eigenvalue 0. For both $r = \text{FO}$ and LM , this ground state is given by $|\sigma\rangle \equiv e_\sigma^\dagger |G_i\rangle$.

Now, when inserted into Eq. (S8), the first term in Eq. (S9) gives a $\delta(\nu)$ not relevant for the regime $\nu \gtrsim T_K$ that we are focusing on. The second term gives $-2\text{Im}\langle\sigma|\widehat{\mathcal{T}}_r|\sigma\rangle/\nu^2 = \text{Im}[\mathcal{T}_r^{(1)} + \mathcal{T}_r^{(2)} + \dots]/\nu^2$. For both $r = \text{FO}$ and LM , $\mathcal{T}_r^{(1)} = \langle\sigma|H'_r|\sigma\rangle = 0$ (for $B = 0$). Thus, to lowest non-zero order, we obtain Eq. (6) of the main text, namely

$$A_\sigma^r(\nu) = -2\text{Im}[\mathcal{T}_r^{(2)}]/\nu^2, \quad \mathcal{T}_r^{(2)} = \langle\sigma|H'_r \frac{1}{\nu_+ - H_r^*} H'_r|\sigma\rangle. \quad (\text{S13})$$

$\mathcal{T}_r^{(2)}$ can be evaluated straightforwardly using Wick's theorem, since $H'_r|\sigma\rangle$ produces a sum of uncorrelated free-fermion states, all of which are eigenstates of $\frac{1}{\nu_+ - H_r^*}$. For the free orbital regime, we obtain

$$\mathcal{T}_{\text{FO}}^{(2)} = \left(\sqrt{\Gamma/\pi\rho}\right)^2 \sum_{k_s, k'_s} \langle\sigma| \left(c_{k_s}^\dagger e_s + \text{h.c.}\right) \frac{1}{\nu_+ - H_{\text{FO}}^*} \left(c_{k'_s}^\dagger e_{s'} + \text{h.c.}\right) |\sigma\rangle \quad (\text{S14})$$

$$= \frac{\Gamma}{\pi\rho} \sum_k \left[\frac{(1 - f(\varepsilon_k))}{\nu_+ - (\varepsilon_k - \varepsilon_e^f)} + \frac{f(\varepsilon_k)}{\nu_+ - (-\varepsilon_k + \varepsilon_e^f + U)} \right], \quad (\text{S15})$$

where $f(\varepsilon) = \theta(-\varepsilon)$ stands for the Fermi function at zero temperature. Inserting this into Eq. (S13) we obtain (for $D \gg |\nu|$):

$$A_\sigma^{\text{FO}}(\nu) = \frac{2\Gamma}{\nu^2} \left[\theta(\nu - |\varepsilon_{e\sigma}^f|) + \theta(\nu - (\varepsilon_{e\sigma}^f + U)) \right]. \quad (\text{S16})$$

For the case of $H^f = \text{SEAM}$ (with $\varepsilon_e^f = -U/2$) considered in the main text, this reduces to Eq. (3a):

$$A_\sigma^{\text{FO}}(\nu) = \frac{4\Gamma}{\nu^2} \theta(\nu - |\varepsilon_{e\sigma}^f|). \quad (\text{S17})$$

The calculation for the local moment regime, $T_K \ll |\nu| \ll \min[|\varepsilon_{e\sigma}^f|, \varepsilon_{e\sigma}^f + U]$, is analogous.

Writing $\vec{s}_e \cdot \vec{s}_c = \frac{1}{2}(s_e^\sigma s_c^{\bar{\sigma}} + s_e^{\bar{\sigma}} s_c^\sigma) + s_e^z s_c^z$, we obtain

$$\mathcal{T}_{\text{LM}}^{(2)} = \left(\frac{J(\nu)}{\rho} \right)^2 \langle \sigma | \vec{s}_e \cdot \vec{s}_c \frac{1}{\nu_+ - H_{\text{LM}}^*} \vec{s}_e \cdot \vec{s}_c | \sigma \rangle \quad (\text{S18a})$$

$$= \frac{1}{4} \left(\frac{J(\nu)}{\rho} \right)^2 \left[\langle G_i | s_c^z \frac{1}{\nu_+ - H_{\text{LM}}^*} s_c^z | G_i \rangle + \langle G_i | s_c^{\bar{\sigma}} \frac{1}{\nu_+ - H_{\text{LM}}^*} s_c^\sigma | G_i \rangle \right] \quad (\text{S18b})$$

$$= \frac{3}{8} \left(\frac{J(\nu)}{\rho} \right)^2 \sum_{kq} \frac{f(\varepsilon_k) (1 - f(\varepsilon_q))}{\nu_+ - \varepsilon_q + \varepsilon_k}. \quad (\text{S18c})$$

Inserting Eq. (S18c) into Eq. (S13), with $J(\nu) = \ln^{-1}[\nu/T_K]$, we recover Eq. (3b):

$$A_\sigma^{\text{LM}} = \frac{3\pi}{4\nu} \frac{1}{\ln^2(\nu/T_K)}. \quad (\text{S19})$$

Nonzero temperature

For $T \neq 0$, the calculations are analogous, with only minor changes: The FPPT expansion in powers of H_r' is performed on Eq. (S7) (instead of Eq. (S8)), the Fermi occupation function is $f(\varepsilon) = 1/[e^{\varepsilon/T} + 1]$, and for the local moment regime the exchange coupling now takes the form $J(\nu) = \ln^{-1}[\max(|\nu|, T)/T_K]$. We consider only the local moment regime, with $|\nu| \ll \min[|\varepsilon_{e\sigma}^f|, \varepsilon_{e\sigma}^f + U]$ and $\max[|\nu|, T] \gg T_K$. Assuming (as before) that the initial level position lies so far above the Fermi surface ($\varepsilon_{e\sigma}^f \gg \Gamma$) that the initial density matrix contains no correlations between e-level and Fermi reservoir, we again arrive at Eq. (S18c), which now yields

$$A_\sigma^{\text{LM}} = \frac{3\pi}{4\nu} \frac{1}{1 - e^{-\nu/T}} \frac{1}{\ln^2[\max(|\nu|, T)/T_K]}. \quad (\text{S20})$$

For large positive detuning, $\nu \gg T$, we recover Eq. (S19), while the line-shape at large negative detuning, $\nu \ll -T$, is suppressed by an extra factor $e^{-|\nu|/T}$.

In the limit of small detuning, $|\nu| \ll T$, Eq. (S20) reduces to

$$A_\sigma^{\text{LM}}(\nu) = \frac{3\pi}{4\nu^2} \frac{T}{\ln^2[T/T_K]}. \quad (\text{S21})$$

The apparent ν^{-2} divergence indicates that in this limit, the expansion (S10) of \mathcal{T}_{LM} can not be truncated at second order, as done above, but must be summed to all orders. Instead of doing this explicitly, one may use methods which were applied to treat the dynamic magnetic susceptibility at finite temperature in Ref. [2]. These yield

$$A_\sigma^{\text{LM}}(\nu) = \frac{3\pi}{4} \frac{\nu/T}{1 - e^{-\nu/T}} \frac{\gamma_{\text{Kor}}(\nu, T)/\pi}{\nu^2 + \gamma_{\text{Kor}}^2(\nu, T)}, \quad (\text{S22})$$

(Eq. (7) of the main text), which contains a Lorentzian factor involving a frequency-dependent Korringa relaxation time,

$$\gamma_{\text{Kor}}(\nu, T) = \frac{\pi T}{\ln^2[\max(|\nu|, T)/T_K]}. \quad (\text{S23})$$

For $|\nu| \gg \gamma_{\text{Kor}}(\nu, T)$, Eq. (S22) reproduces Eq. (S20). For $|\nu| \ll T$ (but $T \gg T_K$), Eq. (S22) reduces to a pure Lorentzian

$$A_{\sigma}^{\text{LM}}(\nu) = \frac{3\pi}{4} \frac{\gamma_{\text{Kor}}/\pi}{\nu^2 + \gamma_{\text{Kor}}^2}, \quad (|\nu| \ll T) \quad (\text{S24})$$

of width $\gamma_{\text{Kor}} \simeq \pi T / \ln^2[T/T_K]$ (which is $\ll T$). This represents the properly regularized version of Eq. (S21), to which it reduces for $\gamma_{\text{Kor}} \ll |\nu| \ll T$.

Generalized Hopfield rule

The generalized Hopfield rule that holds when $\nu \ll T_K$ and arbitrary B is stated in Eq. (8) of the main text can be found as follows, using arguments similar to those in Refs. [1, 3]: First, write the $T = 0$ spectral function of Eq. (4) as

$$A_{\sigma}(\nu) = 2 \text{Re} \int_0^{\infty} dt e^{it\nu} \langle \psi_0 | \psi_t \rangle, \quad (\text{S25})$$

where $|\psi_0\rangle = e_{\sigma}^{\dagger} |G_i\rangle$ is the state just after photon absorption (at $t = 0^+$) and $|\psi_t\rangle = e^{-i\hat{H}t} |\psi_0\rangle$ its time-evolved version. In the $t \rightarrow \infty$ limit (relevant for $\nu \rightarrow 0$), the dynamics is governed by the final ground state, $|G_f\rangle$, characterized by a screened spin singlet. Once the latter begins to dominate (for $t \gtrsim 1/T_K$), the FR experiences the QD as a site of pure potential scattering (no spin-flips), just as at $t = 0^+$, but with changed strength. The adjustment of the FR to this changed potential (via changes in the scattering phase shifts of its single-particle wave-functions) causes an increasing Anderson orthogonality [4] between $|\psi_t\rangle$ and $|\psi_0\rangle$: their overlap decays as $\langle \psi_0 | \psi_t \rangle \sim t^{-\sum_{\sigma'} (\Delta n'_{e\sigma'})^2}$ [5], where, by Friedel's sum rule [7, 6], $\Delta n'_{e\sigma'} = \delta_{\sigma\sigma'} - \Delta n_{e\sigma'}$ is the *displaced charge* (of spin σ'), in units of e , that flows from the scattering site to infinity as $e_{\sigma}^{\dagger} |G_i\rangle$ evolves to $|G_f\rangle$, with $\Delta n_{e\sigma'} = \bar{n}_{e\sigma'}^f - \bar{n}_{e\sigma'}^i$ the local occupation difference between $|G_f\rangle$ and $|G_i\rangle$. Fourier-transforming $\langle \psi_0 | \psi_t \rangle$ according to Eq. (S25) yields the powerlaw-decay of Eq. (3c), with exponent

$$\eta_{\sigma} = 1 - \sum_{\sigma'} (\Delta n'_{e\sigma'})^2. \quad (\text{S26})$$

This is the generalized Hopfield rule, Eq. (8).

References

- [1] R. W. Helmes *et al.*, Phys. Rev. B **72**, 125301, (2005).
- [2] M. Garst, P. Wölfle, L. Borda, J. von Delft, L. Glazman, Phys. Rev. B **72**, 205125 (2005).
- [3] J. J. Hopfield, Comments Solid State Phys. **2**, 40 (1969).
- [4] P. W. Anderson, Phys. Rev. Lett. **18**, 1049 (1967).
- [5] P. Nozières and C. T. De Dominicis, Phys. Rev. **178**, 1097-1107 (1969).
- [6] D.C. Langreth, Phys. Rev. **150**, 516 (1966).
- [7] J. Friedel, Can. J. Phys., 1190, **34** (1956).

Part IV.

Miscellaneous

List of Figures

2.1. Conductance of quantum dots, dependence on source-drain-voltage, gate-voltage and temperature	13
3.1. Schematic picture of an absorption process at the excitonic Anderson model	18
3.2. Schematic picture of the absorption process leading to the Fermi edge singularity (FES).	20
3.3. Schematic picture of an absorption process at the excitonic Anderson model with Kondo correlations in the final state	23
3.4. Absorption line shape for weak optical coupling for zero temperature with a double logarithmic scale, and for different temperatures with a logarithmic y-scale.	24
3.5. Absorption line shapes for weak optical coupling for different magnetic fields, and B -field dependence of the local magnetization and of the low-frequency exponent.	25
3.6. Schematic picture of the transitions that yield the Mollow triplet and qualitative behavior of the resonance fluorescence spectrum	28
4.1. Discretized Anderson model and Wilson chain	32
4.2. Schematic energy spectra for several NRG iterations and flow diagram . . .	35
4.3. Schematic energy spectra and corresponding degeneracies obtained from the NRG algorithm	40
4.4. Beginning of the backward run to calculate the reduced density matrices and end of the following forward run for calculating the spectral function .	43

Bibliography

- [1] A. Altland and B. Simons, *Condensed Matter Field Theory*, Cambridge University Press, New York (2006)
- [2] P. W. Anderson, *More is different*, *Science* **4**, 393 (1972)
- [3] K. G. Wilson and J. Kogut, *The renormalization group and the ϵ expansion*, *Phys. Rep.* **12**, 75 (1974)
- [4] K. G. Wilson, *The renormalization group: Critical phenomena and the Kondo problem*, *Rev. Mod. Phys.* **47**, 773 (1975)
- [5] K. G. Wilson, *Renormalization group methods*, *Adv. Math.* **16**, 170 (1975)
- [6] K. G. Wilson, *The renormalization group and critical phenomena*, *Rev. Mod. Phys.* **55**, 583 (1983)
- [7] H. R. Krishna-murthy, J. W. Wilkins, and K. G. Wilson, *Renormalization-group approach to the Anderson model of dilute magnetic alloys. I. Static properties for the symmetric case*, *Phys. Rev. B* **21**, 1003 (1980);
- [8] H. R. Krishna-murthy, J. W. Wilkins, and K. G. Wilson, *Renormalization-group approach to the Anderson model of dilute magnetic alloys. II. Static properties for the asymmetric case*, *Phys. Rev. B* **21**, 1044 (1980)
- [9] R. Bulla, T. A. Costi, and T. Pruschke, *Numerical renormalization group method for quantum impurity systems*, *Rev. Mod. Phys.* **90**, 395 (2008)
- [10] L. Kouwenhoven and L. Glazman, *Revival of the Kondo effect*, *Phys. World* **14**, 33 (2001)
- [11] A. C. Hewson, *The Kondo problem to heavy Fermions*, Cambridge University Press, Cambridge (1993)
- [12] W. J. de Haas, J. de Boer, and G. J. van den Berg, *The electrical resistance of gold, copper and lead at low temperatures*, *Physica* **1**, 1115 (1934)
- [13] J. Kondo, *Resistance Minimum in Dilute Magnetic Alloys*, *Prog. Theor. Phys.* **32**, 37 (1964)

- [14] Ph. Nozières and C. T. De Dominicis, *Singularities in the X-Ray Absorption and Emission of Metals. III. One-Body Theory Exact Solution*, Phys. Rev. **178**, 1097 (1969)
- [15] K. D. Schotte and U. Schotte, *Threshold Behavior of the X-ray Spectra of Light Metals*, Phys. Rev. **185**, 509 (1969)
- [16] P. W. Anderson, *Infrared Catastrophe in Fermi Gases with Local Scattering Potentials*, Phys. Rev. Lett. **18**, 1049 (1967)
- [17] G. Zaránd, L. Borda, J. von Delft, and N. Andrei, *Theory of Inelastic Scattering from Magnetic Impurities*, Phys. Rev. Lett. **93**, 107204 (2004)
- [18] T. Micklitz, A. Altland, T. A. Costi, and A. Rosch, *Universal Dephasing Rate due to Diluted Kondo Impurities*, Phys. Rev. Lett. **96**, 226601 (2006)
- [19] L. D. Landau, *The Theory of a Fermi Liquid*, Soviet Phys. JETP **3**, 920 (1957)
- [20] L. Kouwenhoven and C. M. Marcus, *Quantum Dots*, Physics World **11**, 35 (1998)
- [21] S. M. Reimann and M. Manninen, *Electronic structure of quantum dots*, Rev. Mod. Phys. **74**, 1283 (2002)
- [22] R. J. Warburton, C. Schäfflein, D. Haft, F. Bickel, A. Lorke, K. Karrai, J. M. Garcia, W. Schoenfeld, and P. M. Petroff, *Optical emission from a charge-tunable quantum ring*, Nature **405**, 926 (2000)
- [23] A. Högele, S. Seidl, M. Kroner, K. Karrai, R. J. Warburton, B. D. Gerardot, and P. M. Petroff, *Voltage-Controlled Optics of a Quantum Dot*, Phys. Rev. Lett. **93**, 217401 (2004)
- [24] J. M. Smith, P. A. Dalgarno, R. J. Warburton, A. O. Govorov, K. Karrai, B. D. Gerardot, and P. M. Petroff, *Voltage Control of the Spin Dynamics of an Exciton in a Semiconductor Quantum Dot*, Phys. Rev. Lett. **94**, 197402 (2005)
- [25] P. W. Anderson, *Localized Magnetic States in Metals*, Phys. Rev. **124**, 41 (1961)
- [26] A. Georges, G. Kotliar, W. Krauth, and M. J. Rosenberg, *Dynamical mean-field theory of strongly correlated fermion systems and the limit of infinite dimensions*, Rev. Mod. Phys. **68**, 13 (1996)
- [27] J. R. Schrieffer and P. A. Wolff, *Relation between the Anderson and the Kondo Hamiltonians*, Phys. Rev. **149**, 491 (1966)
- [28] D. Goldhaber-Gordon, H. Shtrikman, D. Mahalu, D. Abusch-Magder, U. Meirav, and M. A. Kastner, *Kondo effect in a single-electron transistor*, Nature **391**, 156 (1998)
- [29] S. M. Cronenwett, T. H. Oosterkamp, and L. P. Kouwenhoven, *A Tunable Kondo Effect in Quantum Dots*, Science **281**, 540 (1998)

- [30] W. G. van der Wiel, S. De Franceschi, T. Fujisawa, J. M. Elzerman, S. Tarucha, and L. P. Kouwenhoven, *The Kondo Effect in the Unitary Limit*, *science* **289**, 2105 (2000)
- [31] P. W. Anderson, *A poor man's derivation for the scaling laws of the Kondo problem*, *J. Phys. C* **3**, 2436 (1970)
- [32] D. Haldane, *Scaling Theory of the Asymmetric Anderson Model*, *Phys. Rev. Lett.* **40**, 416 (1978)
- [33] P. B. Wiegmann and A. M. Tsvelik, *Exact Solution of the Anderson Model (I-II)*, *J. Phys. C* **16**, 2281 (1983)
- [34] T. A. Costi, A. C. Hewson, and V. Zlatić, *Transport coefficients of the Anderson model via the numerical renormalization group*, *J. Phys.: Condens. Matter* **6**, 2519 (1994)
- [35] I. Affleck, *The Kondo screening cloud: what it is and how to observe it* in *Perspectives of Mesoscopic Physics: Dedicated to Yoseph Imry's 70th Birthday*, edited by Amnon Aharony and Ora Entin-Wohlman, World Scientific, Singapore (2010)
- [36] Ph. Nozières, *A "fermi-liquid" description of the Kondo problem at low temperatures*, *J. Low Temp. Phys.* **17**, 31 (1974)
- [37] Ph. Nozières, in *Proceedings of the 14th International Conference on Low Temperature Physics*, edited by M. Krusius and M. Vuorio, North-Holland, Amsterdam (1974) Vol. 5, p. 339
- [38] M. Pustilnik and L. I. Glazman, *Kondo effect in Real Quantum Dots*, *Phys. Rev. Lett.* **87**, 216601 (2001)
- [39] M. Pustilnik and L.I. Glazman, *Kondo effect in quantum dots*, *J. Phys.: Cond. Mat.* **16**, R513 (2004).
- [40] L. I. Glazman and M. Pustilnik, *Coulomb blockade and Kondo effect in quantum dots, New Directions in Mesoscopic Physics (Towards Nanoscience)*, edited by R. Fazio, V. F. Gantmakher and Y. Imry, Kluwer Academic Publishers, Dordrecht (2003), p. 93-115
- [41] H. Bruus and K. Flensberg, *Many-Body Quantum Theory in Condensed Matter Physics: An Introduction*, Oxford University Press, New York (2004)
- [42] Y. Meir and N. S. Wingreen, *Landauer Formula for the Current through an Interacting Electron Region*, *Phys. Rev. Lett.* **68**, 2512 (1992)
- [43] T. Hecht, *Numerical Renormalization Group studies of Correlation effects in Phase Coherent Transport through Quantum Dots*, PhD thesis, LMU München (2008)
- [44] M. Pustilnik and L. I. Glazman, *Kondo effect induced by a magnetic field*, *Phys. Rev. B* **64**, 045328 (2001)

- [45] A. A. Abrikosov, *Electron scattering on magnetic impurities in metals and anomalous resistivity effects*, *Physics* **2**, 5 (1965)
- [46] Ph. Nozières and A. Blandin, *Kondo effect in real metals*, *J. Phys. (France)* **41** 193 (1980)
- [47] N. Andrei and C. Destri, *Solution of the Multichannel Kondo Problem*, *Phys. Rev. Lett.* **52**, 364 (1984)
- [48] A. M. Tsvelik and P. B. Wiegmann, *Exact solution of the multichannel Kondo problem, scaling and integrability*, *J. Stat. Phys.* **38**, 125 (1985)
- [49] N. Andrei, K. Furuya, and J.H. Lowenstein, *Solution of the Kondo problem*, *Rev. Mod. Phys.* **55**, 331 (1983)
- [50] I. Affleck and A. Ludwig, *Exact conformal-field-theory results on the multichannel Kondo effect: Single-fermion Green's function, self-energy, and resistivity*, *Phys. Rev. B* **48**, 7297 (1993)
- [51] A. K. Mitchell, M. R. Galpin, S. Wilson-Fletcher, D. E. Logan, and R. Bulla, *Generalized Wilson chain for solving multichannel quantum impurity problems*, *Phys. Rev. B* **89**, 121105(R) (2014)
- [52] D. L. Cox and A. Zawadowski, *Exotic Kondo effects in metals: magnetic ions in a crystalline electric field and tunneling centers*, *Adv. Phys.* **47**, 599 (1998)
- [53] P. Mehta, N. Andrei, P. Coleman, L. Borda, and G. Zaránd, *Regular and singular Fermi-liquid fixed points in quantum impurity models*, *Phys. Rev. B* **72**, 014430 (2005)
- [54] Y. Nishikawa and A. C. Hewson, *Hund's rule coupling in models of magnetic impurities and quantum dots*, *Phys. Rev. B* **86**, 245131 (2012)
- [55] A. H. Nevidomskyy and P. Coleman, *Kondo Resonance Narrowing in d- and f-Electron Systems*, *Phys. Rev. Lett.* **103**, 147205 (2009)
- [56] J. J. Hopfield, *Infrared Divergencies, X-Ray Edges, and all that*, *Comments Solid State Phys.* **II**, 1 (1969)
- [57] J. Friedel, *The distribution of electrons around impurities in monovalent metals*, *Phil. Mag.* **43**, 153 (1952)
- [58] J. Friedel, *On some electrical and magnetic properties of metallic solid solutions*, *Can. J. Phys.* **34**, 1190 (1956)
- [59] D. C. Langreth, *Friedel Sum Rule for Anderson's Model of Localized Impurity States*, *Phys. Rev.* **150**, 516 (1966)

- [60] W. Munder, A. Weichselbaum, M. Goldstein, Y. Gefen, and J. von Delft, *Anderson Orthogonality in the Dynamics After a Local Quantum Quench*, Phys. Rev. B **85**, 235104 (2012)
- [61] G. D. Mahan, *Excitons in Metals: Infinite Hole Mass*, Phys. Rev. **163**, 612 (1967)
- [62] L. N. Oliveira and J. W. Wilkins, *New approach to the x-ray-absorption problem*, Phys. Rev. B **24**, 4863 (1981)
- [63] A. Weichselbaum, W. Munder, and J. von Delft, *Anderson orthogonality and the numerical renormalization group*, Phys. Rev. B **84**, 075137 (2011)
- [64] H. E. Tureci, M. Hanl, M. Claassen, A. Weichselbaum, T. Hecht, B. Braunecker, A. Govorov, L. Glazman, A. Imamoglu, and J. von Delft, *Many-Body Dynamics of Exciton Creation in a Quantum Dot by Optical Absorption: A Quantum Quench towards Kondo Correlations*, Phys. Rev. Lett. **106**, 107402 (2011)
- [65] M. Garst, P. Wolfle, L. Borda, J. von Delft, and L. Glazman, *Energy-resolved inelastic electron scattering off a magnetic impurity*, Phys. Rev. B **72**, 205125 (2005)
- [66] Y. Yamamoto and A. Imamoglu, *Mesoscopic Quantum Optics*, Wiley, New York (1999)
- [67] B. R. Mollow, *Power Spectrum of Light Scattered by Two-Level Systems*, Phys. Rev. **188**, 1969 (1969)
- [68] B. Sbierski, *Resonance fluorescence from a Kondo exciton*, Diploma thesis, TU Munchen (2012)
- [69] C. Cohen-Tannoudji, J. Dupont-Roc, and G. Grynberg, *Atom-Photon Interactions: Basic Processes and Applications*, Wiley, New York (1992)
- [70] T. A. Costi, *Kondo effect in a magnetic field and the magnetoresistivity of Kondo alloys*, Phys. Rev. Lett. **85**, 1504 (2000)
- [71] A. Rosch, T. A. Costi, J. Paaske, and P. Wolfle, *Spectral function of the Kondo model in high magnetic fields*, Phys. Rev. B **68**, 014430 (2003)
- [72] R. Žitko and T. Pruschke, *Energy resolution and discretization artifacts in the numerical renormalization group*, Phys. Rev. B **79**, 085106 (2009)
- [73] A. Weichselbaum, *Discarded weight and entanglement spectra in the numerical renormalization group*, Phys. Rev. B **84**, 125130 (2011)
- [74] A. Weichselbaum and J. von Delft, *Sum-Rule Conserving Spectral Functions from the Numerical Renormalization Group*, Phys. Rev. Lett. **99** 076402 (2007)
- [75] M. Yoshida, M. A. Whitaker, and L. N. Oliveira, *Renormalization-group calculation of excitation properties for impurity models*, Phys. Rev. B **41**, 9403 (1990)

- [76] R. Bulla, A. C. Hewson, and T. Pruschke, *Numerical renormalization group calculations for the self-energy of the impurity Anderson model*, J. Phys.: Condens. Matter **10**, 8365-8380 (1998)
- [77] A. Weichselbaum, F. Verstraete, U. Schollwöck, I. Cirac, and J. von Delft, *Variational matrix-product-state approach to quantum impurity models*, Phys. Rev. B **80** 165117 (2009)
- [78] O. Sakai, Y. Shimizu, and T. Kasuya, *Single-Particle and Magnetic Excitation Spectra of Degenerate Anderson Model with Finite f-f Coulomb Interaction*, J. Phys. Soc. Jpn. **58**, 3666 (1989)
- [79] R. Bulla, T. A. Costi, and D. Vollhardt, *Finite-temperature numerical renormalization group study of the Mott transition*, Phys. Rev. B **64**, 045103 (2001)
- [80] W. Hofstetter, *Generalized Numerical Renormalization Group for Dynamical Quantities*, Phys. Rev. Lett. **85**, 1508 (2000)
- [81] F. B. Anders and A. Schiller, *Real-Time Dynamics in Quantum-Impurity Systems: A Time-Dependent Numerical Renormalization-Group Approach*, Phys. Rev. Lett. **95**, 196801 (2005)
- [82] F. B. Anders and A. Schiller, *Spin precession and real-time dynamics in the Kondo model: Time-dependent numerical renormalization-group study*, Phys. Rev. B **74**, 245113 (2006)
- [83] R. Peters, T. Pruschke, and F. B. Anders, *Numerical renormalization group approach to Green's functions for quantum impurity models*, Phys. Rev. B, **74**, 245114 (2006)
- [84] W. Mündler, *Matrix product state calculations for one-dimensional quantum chains and quantum impurity models*, PhD thesis, LMU München (2011)
- [85] A. Weichselbaum, *Non-abelian symmetries in tensor networks: a quantum symmetry space approach*, Ann. Phys. **327**, 2972-3047 (2012)
- [86] A. I. Tóth and G. Zaránd, *Dynamical correlations in the spin-half two-channel Kondo model*, Phys. Rev. B **78**, 165130 (2008)
- [87] A. Alex, M. Kalus, A. Huckleberry, and J. von Delft, *A numerical algorithm for the explicit calculation of $SU(N)$ and Clebsch-Gordan coefficients*, J. Math. Phys. **52**, 023507 (2012)
- [88] C. P. Moca, A. Alex, J. von Delft, and G. Zaránd, *$SU(3)$ Anderson impurity model: A numerical renormalization group approach exploiting non-Abelian symmetries*, Phys. Rev. B, **86**, 195128 (2012)

- [89] I. Affleck, *A current algebra approach to the Kondo effect*, Nucl. Phys. B **336**, 517 (1990)
- [90] J. J. Sakurai, *Modern Quantum Mechanics*, Addison-Wesley, Boston (1994)
- [91] A. O. Govorov, K. Karrai, and R. J. Warburton, *Kondo excitons in self-assembled quantum dots*, Phys. Rev. B **67**, 241307 (2003)
- [92] R. W. Helmes, M. Sindel, L. Borda, and J. von Delft, *Absorption and emission in quantum dots: Fermi surface effects of Anderson excitons*, Phys. Rev. B **72**, 125301 (2005)
- [93] P. A. Dalgarno, M. Ediger, B. D. Gerardot, J. M. Smith, S. Seidl, M. Kroner, K. Karrai, P. M. Petroff, A. O. Govorov, and R. J. Warburton, *Optically Induced Hybridization of a Quantum Dot State with a Filled Continuum*, Phys. Rev. Lett. **100**, 176801 (2008)
- [94] W. J. de Haas and G. J. van den Berg, *The electrical resistance of gold and silver at low temperatures*, Physica **3**, 440 (1936)
- [95] T. A. Costi, L. Bergqvist, A. Weichselbaum, J. von Delft, T. Micklitz, A. Rosch, P. Mavropoulos, P. H. Dederichs, F. Mallet, L. Saminadayar, and C. Bäuerle, *Kondo Decoherence: Finding the Right Spin Model for Iron Impurities in Gold and Silver*, Phys. Rev. Lett. **102**, 056802 (2009)
- [96] F. Mallet, J. Ericsson, D. Mailly, S. Ünlübayir, D. Reuter, A. Melnikov, A. D. Wieck, T. Micklitz, A. Rosch, T. A. Costi, L. Saminadayar, and C. Bäuerle, *Scaling of the Low-Temperature Dephasing Rate in Kondo Systems*, Phys. Rev. Lett. **97**, 226804 (2006)
- [97] G. M. Alzoubi and N. O. Birge, *Phase Coherence of Conduction Electrons Below the Kondo Temperature*, Phys. Rev. Lett. **97** 226803 (2006)

List of Publications

The work presented in this thesis has been published in the following papers:

1. *Quantum quench of Kondo correlations in optical absorption*
C. Latta, F. Haupt, M. Hanl, A. Weichselbaum, M. Claassen, W. Wuester, P. Fallahi, S. Faelt, L. Glazman, J. von Delft, H. E. Türeci, and A. Imamoglu, Nature (London) **474**, 627 (2011)
2. *Spin- $\frac{1}{2}$ Kondo effect in an InAs nanowire quantum dot: Unitary limit, conductance scaling, and Zeeman splitting*
A. V. Kretinin, H. Shtrikman, D. Goldhaber-Gordon, M. Hanl, A. Weichselbaum, J. von Delft, T. Costi, and D. Mahalu, Phys. Rev. B **84**, 245316 (2011)
3. *Iron impurities in gold and silver: Comparison of transport measurements to numerical renormalization group calculations exploiting non-Abelian symmetries*
M. Hanl, A. Weichselbaum, T. A. Costi, F. Mallet, L. Saminadayar, C. Bäuerle, and J. von Delft, Phys. Rev. B **88**, 075146 (2013)
4. *Proposed Rabi-Kondo Correlated State in a Laser-Driven Semiconductor Quantum Dot*
B. Sbierski, M. Hanl, A. Weichselbaum, H. E. Türeci, M. Goldstein, L. I. Glazman, J. von Delft, and A. Imamoglu, Phys. Rev. Lett. **111**, 157402 (2013)
5. *Nonequilibrium dynamics in an optical transition from a neutral quantum dot to a correlated many-body state*
F. Haupt, S. Smolka, M. Hanl, W. Wuester, J. Miguel-Sanchez, A. Weichselbaum, J. von Delft, and A. Imamoglu, Phys. Rev. B **88**, 161304(R) (2013)
6. *Local susceptibility and Kondo scaling in the presence of finite bandwidth*
M. Hanl and A. Weichselbaum, Phys. Rev. B **89**, 075130 (2014)
7. *Equilibrium Fermi-liquid coefficients for the fully screened N-channel Kondo model*
M. Hanl, A. Weichselbaum, J. von Delft, and M. Kiselev, Phys. Rev. B **89**, 195131 (2014)

The following paper emerged from the work of my Diploma thesis and can be found in the appendix.

8. *Many-Body Dynamics of Exciton Creation in a Quantum Dot by Optical Absorption: A Quantum Quench towards Kondo Correlations*
H. E. Türeci, M. Hanl, M. Claassen, A. Weichselbaum, T. Hecht, B. Braunecker, A. Govorov, L. Glazman, A. Imamoglu, and J. von Delft, Phys. Rev. Lett. **106** 107402 (2011)

Acknowledgements

First, I want to thank my advisor Jan von Delft for his advice during my PhD studies. I benefited not only from his academic knowledge, but also from his way of looking at things. Learning how to work out the gist of a problem is an ability which is useful not only in science. I also appreciate his ability to motivate his chair members and spreading enthusiasm.

Further, I want to thank Andreas Weichselbaum for fruitful discussions and who provided me with his NRG code. He also always took the time for answering questions and imparting background knowledge about physical and numerical problems.

Most of the studies presented in this thesis benefited from the knowledge and experience of my collaborators: Atac Imamoglu, Theo Costi, Mikhail Kiselev, Christopher Bäuerle, Christian Latta, Björn Sbierski and Florian Haupt.

Special thanks goes to Wolfgang Munder from whom I learnt a lot about all kinds of things and with whom I had the greatest time.

I also want to thank all members from the group and all office mates who made my PhD a nice time: Stefan Kehrein, Florian Marquardt, Oleg Yevtushenko, Andreas Holzner, Markus Heyl, Korbinian Paul, Annika Wöhner, Ireneusz Weymann, Wael Chibani, Peter Fritsch, Alois Dirnaichner, Constantin Tomaras, Francesco Alaimo, Arvid Kingl, Jiang Qiang, Björn Kubala, Max Ludwig, Georg Heinrich, Clemens Neuenhahn, Hamed Saberi, Huaizhi Wu, Michael Möckel, Pablo Dominguez, Ferdinand Helmer, Benjamin Abel, Jad Halimeh, Katharina Eissing, Kevin Jägering, Dimitri Pimenov and Lukas Weidinger.

Special thanks to Cheng, Olga, Dennis, Ari, Arne, Alex and Philipp also for discussions about life and the universe, Max and Oli for funny stories from everyday life, Theresa for giving me an introduction to NRG, Katharina for explaining her work to me, Wei for discussions about soccer and Florian, Jan, Benedikt, Niels and Frauke for being up to date with the latest news.

Thanks also go to the members of Prof. Schollwöck's chair, especially to those with whom I often went to lunch together, for discussions about physics and everything else.

Thanks also to the RBG for keeping the computers running.

I am glad that I could write this thesis at the Arnold Sommerfeld Center for Theoretical Physics (ASC), which provided lots of talks from great speakers and a productive working atmosphere.

I acknowledge funding from the DFG through the Sonderforschungsbereich 631 and the "Nanosystems Initiative Munich" (NIM) from the German Excellenz Initiative.